Development of a novel CD52 functionalised nanoparticle for the targeting of Chronic Lymphocytic Leukaemia

Submitted by

Laura Christine Kickham

A thesis submitted for the degree of Doctor of Philosophy

Under the supervision and direction of

Dr Adriele Prina-Mello,

Dr Anthony McElligott,

Professor Yuri Volkov,

Professor Paul Browne

Department of Clinical Medicine

Trinity College, The University of Dublin

2019

Declaration

I declare that this thesis has not been submitted as an exercise for a degree at this or any other university and it is entirely my own work. I have read, and I understand the plagiarism provisions in the General Regulations of the University Calendar for the current year, found at: http://www.tcd.ie/calendar.

I agree to deposit this thesis in the University's open access institutional repository or allow the Library to do so on my behalf, subject to Irish Copyright Legislation and Trinity College Library conditions of use and acknowledgement.

I consent to the examiner retaining a copy of the thesis beyond the examining period, should they so wish (EU GDPR May 2018).

Signed: Laura Christine Kickham   Date: 26th July 2019

Acknowledgements

I would like to express my sincere thanks to my supervisor's, Dr Adriele Prina-Mello, Dr Tony McElligott, Professor Yuri Volkov and Professor Paul Browne, for the opportunity to undertake this research. Together they provided me with constant support, guidance, encouragement and most importantly freedom of research; and I will be forever grateful to them.

I would like to thank Professor Elisabeth Vandenberghe for the provision of patient-derived cells, and Dr Fiona Quinn of the Cancer Molecular Diagnostics Laboratory, St James's Hospital, for kindly providing patient cytogenetic data.

To all members of the Nanomedicine and Molecular Imaging group, both past and present, for all of their assistance and support over the years: Dr Ciarán Maguire, Dr Dania Movia, Dr Omar Mahfoud, Dr Tatsiana Rakovich, Dr Kieran Crosbie-Staunton and Mr Gareth Clarke. Massive thank you to Dr Sarah Brophy of the John Durkan Leukaemia laboratory for all of her assistance and support, and most importantly friendship.

To all of my friends in the 0.72 reading room: Dr Ayokunmi Ajetunmobi, Mr Melad Aswisi, Dr Sarah Brophy, Mr Gareth Clarke, Dr Kieran Crosbie-Staunton, Dr Susan Heavey, Dr Aidan Toner and Ms Alexandra Tuzova, thank you for being such wonderful office buddies and for the memories I will never forget.

Special thanks to my wonderful boyfriend Ayokunmi, without whom I would certainly be lost. Thank you for all of your support, and for always lending a

shoulder when times became tough. Thank you to your lovely family who have always been there to cheer me on.

I would like to thank all of my family and friends, in particular Mary and Patrick, who have always provided me with a true home away from home.

And last, but certainly not least, thank you to my amazing family: Mom, Dad, Michelle (and Java), for always being there, showing unwavering support and unconditional love. Thank you for always encouraging me to follow my dreams - I hope that I will always continue to do you all proud.

I dedicate this thesis to my late grandfather, Maurice "Mossie" Kickham – a true lover of education and learning.

Abstract

Nanomedicine has been recognised as a next-generation technology for the treatment and management of many disease states, including blood cancers. The term "nanotechnology" was first coined in 1974 and, is at the interface of biology, chemistry and physics nanomedicine has transformed over the past two decades to a $40 billion market. Chronic lymphocytic leukaemia (CLL) is a highly heterogeneous B cell malignancy, with a variable clinical course; dependent on patient characteristics and the presence of relevant prognostic markers. Though there has been significant progress in the clinical translation of therapies for the management of CLL, frontline therapies consist of chemoimmunotherapies targeting CLL cell surface markers such as CD20 and CD52. CD52 is a long-established CLL therapeutic target; with the anti-CD52 monoclonal antibody alemtuzumab being approved as a targeted therapy in the management of CLL in 2001. Here, we propose the development of a novel, anti-CD52 functionalised nanoparticle for the treatment of CLL as a proof-of-concept therapeutic model. We propose CD52 as a suitable cell surface marker for therapeutic targeting in CLL, and utilising characterisation techniques such as Nanoparticle Tracking Analysis (NTA), scanning electron microscopy (SEM) and flow cytometry demonstrate successful functionalisation and characterisation of Fe_2O_3 nanoparticles with anti-CD52 monoclonal antibody (Fe_2O_3@CD52). Qualitatively and quantitatively, we demonstrate enhanced interaction and uptake of Fe_2O_3@CD52 nanoparticles in CLL cells when compared to normal B cells. The data suggests clathrin-mediated endocytosis as a possible mechanism of uptake of nanoparticles by CLL cells. Additionally, we report the reduction in adherence of patient-derived CLL cells following

treatment with nanoparticles to endothelial monolayers under physiologically-relevant fluid shear flow conditions. Finally, we demonstrate that my novel nanoparticle can significantly induce apoptosis in patient-derived CLL cells over 8 and 24 hours, when compared to non-functionalised (Fe_2O_3@APTES) nanoparticles. We report that Fe_2O_3@CD52 is equally potent in inducing apoptosis in cells with favourable or poor prognostic markers. Additionally, we demonstrate that the inclusion of the purine analogue, fludarabine; or the addition of an additional targeting monoclonal antibody (yielding double-functionalised nanoparticles) to the surface of Fe_2O_3@CD52 does not enhance its activity.

In conclusion, this thesis aims to bridge the gap between haemato-oncology and nanotechnology to provide some of the insights required to address the unmet need for a targeted nanotherapeutic in the management of blood cancers, and CLL in particular. Using multiple validated technologies, here we present the findings of a robust study with the potential to contribute to the ever-expanding fields of both nanotherapeutics and haemato-oncology by providing the opportunity for the further progress and development of novel, targeted therapeutics for haematological malignancies.

Table of Contents

List of figures

Chapter 1: Introduction

Chapter 2: Materials and Methods

Chapter 3: Characterisation and assessment of the effects of bare Fe_2O_3 nanoparticles on B cells

Chapter 4: Development, characterisation and investigation of functionalised Fe$_2$O$_3$ nanoparticles in patient-derived CLL cells and the I-83 cell line

Chapter 5: Functional effects of Fe2O3@CD52 on patient-derived CLL cells

List of tables

Chapter 4: Development, characterisation and investigation of functionalised Fe_2O_3 nanoparticles in patient-derived CLL cells and the I-83 cell line

Chapter 5: Functional effects of Fe_2O_3@CD52 on patient-derived CLL cells

List of abbreviations

μg, microgram

μL, microlitre

μm, micrometer

μs, microsecond

ADCC, antibody-dependent cellular cytotoxicity

Akt, protein kinase B

ALL, acute lymphoblastic leukaemia

AML, acute myeloid leukaemia

APTES, (3-aminopropyl) triethoxysilane,

ATM, ataxia-telangiectasia-mutated

BCR, B cell receptor

BET, Brunauer, Emmett and Teller theory

BMSC, bone marrow stem cells

BTK, Bruton's Tyrosine Kinase

CAP, cyclophosphamide/ doxorubicin/ prednisone combination

CD, cluster of differentiation

CDC, complement-dependent cytotoxicity

CHOP, cyclophosphamide/ doxorubicin/ vincristine/ prednisone combination

CLL, chronic lymphocytic leukaemia

DLS, dynamic light scattering

DNA, deoxyribonucleic acid

dPBS, Dulbecco's phosphate-buffered saline

EDC, 1-ethyl-3-(-3-dimethylaminopropyl) carbodiimide hydrochloride

EDTA, ethylenediaminetetraacetic acid

EGFR, epidermal growth factor receptor

EMA, European Medicines Agency

EPR, enhanced permeability and retention

FBS, foetal bovine serum

FCR, fludarabine/cyclophosphamide/rituximab combination

FDA, Food and Drug Administration

FL, follicular lymphoma

GC, germinal centre

HDLEC, human dermal lymphatic endothelial cell

HER2, human epidermal growth factor receptor 2

HEV, high endothelial venules

HIV, human immunodeficiency virus

HMDS, hexamethyldisilazane

HSC, haematopoietic stem cells

HUVEC, human umbilical vein endothelial cell

Ig, immunoglobulin

IGHV, immunoglobulin variable region heavy chain

IR, infrared

ITAM, immunoreceptor tyrosine-based activation motif

ITIM, immunoreceptor tyrosine-based inhibition motif

ITP, immune thrombocytopenia

kDa, kilodalton

kV, kilovolts

MAC, membrane attack complex

MASP 1/2, mannose-associated serine protease 1

MBL, mannose-binding lectin

MDS, myelodysplastic syndromes

MHC, major histocompatibility complex

mL, millilitre

MNP, magnetic nanoparticle

MRI, magnetic resonance imaging

mRNA, messenger RNA

MUC-1, mucin 1, cell surface associated

NF- κB, nuclear factor kappa-light-chain-enhancer of activated B cells

NHL, Non-Hodgkin lymphoma

NLC, nurse-like cell

NLS, nuclear localisation signal

nm, nanometer

nM, nanomolar

NTA, nanoparticle tracking analysis

ORR, objective response rate

pA, picoampere

PBMC, peripheral blood mononuclear cell

PBS, phosphate-buffered saline

PCR, polymerase chain reaction

PDT, photodynamic therapy

PEG, poly(ethylene) glycol

PFS, progression-free survival

PI3K, phosphoinositide-3 kinase

PS, phosphotidylserine

PTK, protein-tyrosine kinase

PTT, photothermal therapy

QELS, quasi-electric light scattering

RGD, arginylglycylaspartic acid

RNA, ribonucleic acid

SEM, scanning electron microscopy

SHP-1, Src homology region 2 domain-containing phosphatase-1

SPION, super paramagnetic iron oxide nanoparticle

TD, T cell dependent

TNF, tumour necrosis factor

VCAM, vascular cell adhesion protein 1

VEGF, vascular endothelial growth factor

Communications

Publications

Hutchinson D, Müller J, McCarthy JE, Gun'ko YK, Verma NK, Di Cristo L, Kickham L, Movia D, Prina-Mello A, Volkov Y. Cadmium nanoparticles citrullinate cytokeratins within lung epithelial cells: cadmium as a potential cause of citrullination in chronic obstructive pulmonary disease. *Int J Chron Obstruct Pulmon Dis.* 2018; 13:441-449.

Kickham, L.C., McElligott A.M., Vandenberge, E.A., Volkov. Y., Browne, P.V. "Interrogating the Interaction of CD52 functionalised Metallic Nanoparticles with Malignant B Lymphocytes" *Blood* 2015; 126(23):A4437.

Oral and poster presentations

"An Interrogation into the Interaction of Metallic Nanoparticles with Malignant B Lymphocytes" – Laura Kickham, Anthony M. McElligott, Adriele Prina-Mello, Yuri Volkov and Paul Browne. InterReg 4A Irish Presidential Meeting, Swansea University, October 2014.

Invited Speaker - "An Interrogation into the Interaction of Metallic Nanoparticles with Malignant B Lymphocytes" – Laura Kickham, Anthony M. McElligott, Yuri Volkov and Paul Browne. *Haematological Association of Ireland*, Clarion Hotel Sligo, October 2014.

"Nanoparticle uptake by Malignant B Cells: The Potential of Nanomedicine in the Diagnosis and Treatment of Haematological Malignancies" – Laura Kickham, Anthony M. McElligott, Adriele Prina – Mello, Elisabeth Vandenberghe, Yuri Volkov and Paul Browne. *Haematological Association of Ireland Annual Meeting*, Europa Hotel Belfast, 18-19 Oct 2013.

"Applications of Nanomaterials in the Diagnostics of Haematological Malignancies" – Laura Kickham, Omar Kazem Mahfoud, Dania Movia, Tony McElligott, Paul Browne, Adriele Prina – Mello and Yuri Volkov. *Euronanoforum*, Convention Centre Dublin, 18-20 June 2013.

"Nanoparticle Uptake by Malignant B-Cells: The Potential of Nanomedicine in the Diagnosis and Treatment of Haematological Malignancies" - Laura Kickham, Dania Movia, Alan P. Bell, Anthony M. McElligott, Adriele Prina-Mello Elisabeth Vandenberghe, Paul V. Browne and Yuri Volkov. *Institute of Molecular Medicine* 16th Annual Meeting, November 2013.

1. Introduction

1.1 Nanotechnology and applications in medicine

1.1.1 Nanotechnology and nanoparticles

Nanotechnology has been defined as the "intentional design, characterisation, production and applications of materials, structures, devices and systems by controlling their size and shape in the nanoscale range (1-100nm)" though this term has also been used in reference to materials up to 500nm and rarely exceeding 700nm (Mody *et al.*, 2010). The European Commission first adopted the definition of a nanomaterial in 2011 and has since then reviewed several times to ensure reflection of the evolving landscape of these materials. They can be defined as "A natural, incidental or manufactured material containing particles, in an unbound state or as an aggregate or as an agglomerate and where, for 50% or more of the particles in the number size distribution, one or more external dimensions is in the size range 1 nm - 100 nm" (European Commission, 2011).

 A nanoparticle can be classed as such if it is of a single dimension and on the nanoscale in size (Powers et al., 2007). Within a biological context, they are comparable in size to viruses (20-300 nm) and significantly smaller than cells (30 to 300 μm). Upon reaching the nanoscale, the properties of the bulk material can become altered. This is as a result of nanoparticles having a greater surface area to volume than larger particles, meaning their small diameter provides a large and available surface area, often causing the nanoparticle to be more reactive than the bulk material (Mahdavi, et al., 2013). The importance of this property was realised when researchers found that size can

influence the physicochemical properties of a material, such as surface charge and dispersion stability (Duan & Li, 2013). Nanotechnology is by no means a recent advancement in the scientific field, having been presented by Nobel Laureate Richard P. Feynman in 1959 during a talk entitled "There is plenty of room at the bottom" (Feynman, 1960), though its potential for the advancement of the scientific field is only more recently becoming clear. During this talk, Feynman described how in order to fully understand "big science", scientists should also understand the scientific phenomena on the smaller scale (Feynman, 1960). The term "nanotechnology" was then first coined by Norio Taniguchi in 1974, (Taniguchi, 1974) for which the European Society for Precision Engineering and Nanotechnology awarded him the Lifetime Achievement Award in 1999.

Nanotechnology has demonstrated its implications across a variety of branches of science and industries, including: biotechnology and medicine, the food industry, agriculture, textiles environmental science and electronics (Figure 1.1). The crossover of the use of nanotechnology has resulted in the significant advancement of manufacturing processes, engineering and healthcare, to name but a few. As of 2018, the global nanotechnology market value was estimated at approximately $40 billion, with a projected growth rate of 17%, meaning that by 2021 this market could be worth over $90 billion globally (Koshovets & Ganichev, 2016) (McWilliams, 2016) (Markets, 2018). The use of nanotechnology for the advancement of medicine and healthcare is known as nanomedicine.
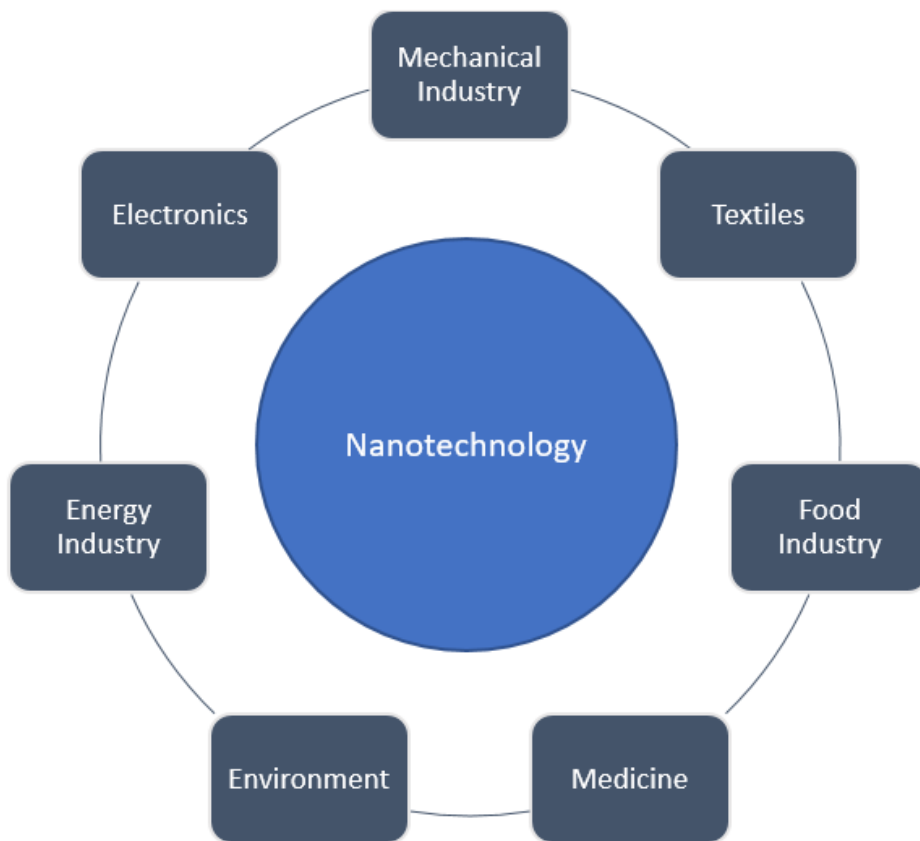
Figure 1.1: Nanotechnology is widely used across a variety of sectors. This field continues to advance, with economic impact growing annually.

1.1.2 Nanomedicine

Nanomedicine forms the epicentre of the convergence of physics, chemistry and biology (Figure 1.2). This convergence of technologies has allowed for the combination of differing approaches from scientists of various backgrounds to tackle problems directly related to the medical and biological fields.
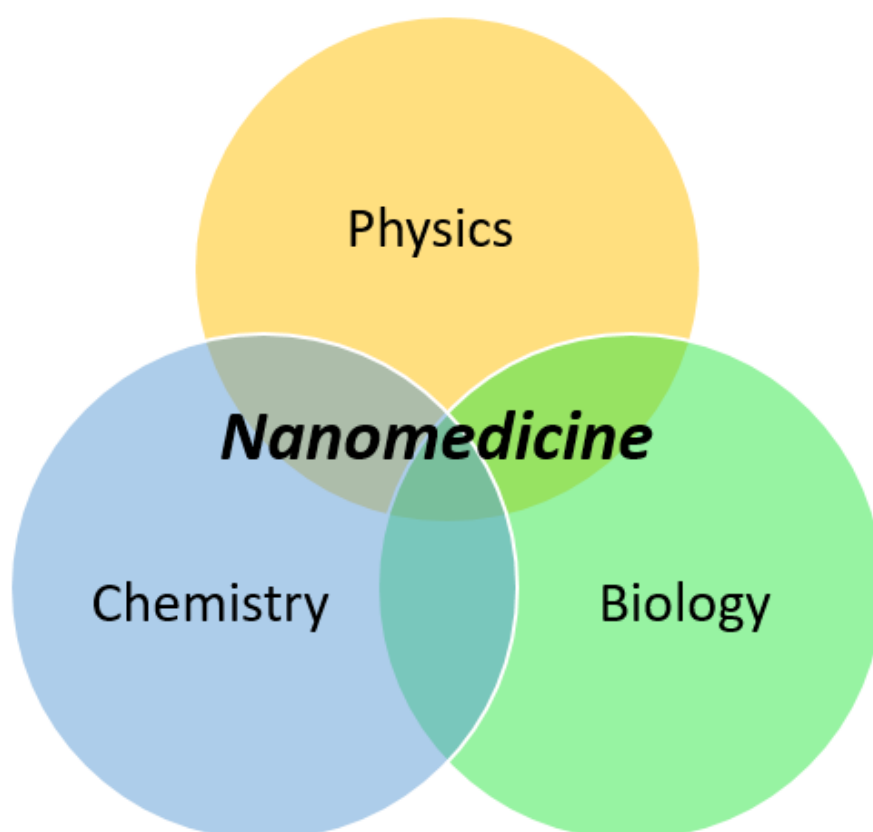
Figure 1.2: Nanomedicine is at the epicentre of the convergence of biology, physics, and chemistry, allowing for a multi and inter-disciplinary collaborative approach to be taken towards new medicinal projects.

Interestingly, the application of nanoparticles, as carriers or vectors, has been shown to be of great potential in the field of targeted therapies for a range of disordered and diseased states, and there are now more than 50 nanomedicinal products available for clinical use (Bobo et al., 2016)

(Sanna et al., 2014) (Tran, DeGiovanni *et al*., 2017)(European Medicines Agency, 2018). A selection of the most commonly used FDA approved nanoparticles is summarised in Table 1.1 below.

Table 1.1: List of FDA-approved nanomedicines detailing material, indication(s), advantages gained from using each product and the year(s) each material was approved. Adapted from Bobo et al. 2016, European Medicines Agency and Tran *et al.* 2017**.**

Name	Material description	Advantage	Indication(s)	Year(s) approved
Nanotherm® (MagForce)	Iron oxide	Allows for cellular uptake and introduces superparamagnetism	Glioblastoma	2010
Feraheme™/ ferumoxytol (AMAG pharmaceuticals)	Ferumoxytol SPION with polyglucose sorbitol carboxymethyl ether	Magnetite suspension allows for prolonged release, decreasing dose number	Anaemia in chronic kidney disease	2009
Venofer® (Luitpold Pharmaceuticals)	Iron sucrose	Allows for increased dosage	Anaemia in chronic kidney disease	1999
INFeD® (Sanofi Avertis)	Iron dextran (low MW)	Allows for increased dosage	Anaemia in chronic kidney disease	1957
Ferrlecit® (Sanofi Avertis)	Sodium ferric gluconate	Allows for increased dosage	Iron deficiency in chronic kidney disease	1999
Feridex®/Endorem® (AMAG pharmaceuticals)	SPION coated with dextran	Introduces superparamagnetism	Imaging agent	1996/ 2008
GastroMARK™; umirem® (AMAG pharmaceuticals)	SPION coated with silicone	Introduces superparamagnetism	Imaging agent	2001/ 2009
DepoDur® (Pacira Pharmaceuticals) Visudyne® (Bausch and Lomb)	Liposomal Verteporfin	Increased delivery to site of diseased vessels; photosensitive release	Macular degeneration, It age-related; myopia; ocular histoplasmosis	2000
Doxil®/Caelyx™ (Janssen)	Liposomal doxorubicin	Improved delivery to site of disease; decrease in systemic toxicity of free drug	Karposi's Sarcoma; Ovarian cancer; multiple myeloma	1995/ 2005/ 2008

Estrasorb™ (Novavax)	Micellar Estradiol	Controlled delivery of therapeutic	Menopausal therapy	2003
Abraxane®/ABI-007 (Celgene)	Albumin-bound paclitaxel nanoparticles	Improved solubility; improved delivery to tumour	Breast cancer, NSCLC, pancreatic cancer	2005/ 2012/ 2013
MM-398 (Onivyde)	Lipsomal 5-fluorouracil and leucovorcin	Increased potency allows for reduced dosage	Metastatic pancreatic cancer	2015
Fulphila	PEGylated filgrastim	Decreased elimination allows for fewer treatments	Neutropenia infection control in non-myeloid malignancy patients	2018

Although enormous advances have been made in nanotechnology, many of these have not yet achieved either an industrial development or translation to an available therapy. Some nanoparticles have been shown to potentially improve the pharmacokinetics and pharmacodynamics of drugs; they may provide a platform in which to deliver an increased concentration of a therapeutic agent than would normally be permissible, and they can improve the affinity of the drug within the blood stream through evasion of the reticuloendothelial system (RES) and providing the ability to solubilise hydrophobic drugs. Nanoparticle evasion of the RES is a highly attractive feature in many applications, and attributed to the lack of serum proteins on the surface of functionalised nanoparticles, resulting in minimal uptake by macrophages and subsequent increased longevity in the bloody stream (Bae & Park, 2012) (Ferrari, 2008). Additionally, nanoparticles provide the opportunity for controlled, directed release of drugs at a site or target using environmental or an external signal, and importantly possess the ability to accumulate in tumours through the phenomenon known as the enhanced permeability and retention (EPR). (Onoue *et al.*, 2014) (Islam, *et al.*, 2018).

1.1.3 Nanoparticles in cancer

There are several limitations to conventional cancer therapies, such as low to moderate therapeutic efficacy, drug resistance and poor delivery resulting in low concentrations of the therapeutic at the site of action (Lammers *et al.*, 2012). This has resulted in a call for novel and combined cancer therapeutics, with nanoparticles being extensively studied to fulfil this purpose. First-generation nanoparticles have proven relatively easy to synthesise and were designed for use in diagnostics and imaging solely. A newer generation of nanoparticles have multi-functional characteristics and are designed for combined therapeutic and diagnostic applications, known as theranostics (Li, Nejadnik, & Daldrup-Link, 2017) (Gobbo *et al.*, 2015). This means that the characteristics of nanoparticles that may have been originally developed for solely diagnostic purposes or therapeutic purposes have been combined, resulting in a nanoparticle suitable for both diagnostics and therapeutics. This has been successfully demonstrated with magneto-polymeric nanohybrids for both the detection and the targeted treatment of breast cancer (Yang *et al.,* 2007).

Iron oxide nanoparticles have been used for several years as an imaging contrast agent for MRI. This allows healthcare practitioners to image the specific area where the tumour resides within the body, with magnetic particles combined with MRI scanning resulting in greater imaging contrast (Ebrahimi *et al.*, 2016) (Gobbo *et al.*, 2015). In addition to their proven use as contrast agents, magnetic iron oxide nanoparticles have also shown the potential in drug delivery. These nanoparticles can be surface functionalised in order to make them

suitable for such drug conjugation and delivery. Surface functionalisation relates to the modification of the surface of a nanoparticle using one or more of a vast array of ligands, proteins, functional groups or compounds which can enhance the properties of the bare material. The use of iron oxide nanoparticles as a drug delivery system can help to overcome the issues of conventional chemotherapeutics, and potentially even immunotherapeutics by offering increased specificity, crossing biological barriers and offering controlled release. In addition, a controlled and specific drug delivery utilising techniques such as MRI targeting or a tissue/cell surface marker targeting ligand could increase the retention of the drugs at the site of the tumour cells, potentially avoiding over-dosage and decreasing the notable chemotherapeutic side effects (Li, Nejadnik, & Daldrup-Link, 2017) (Lima-Tenorio *et al.*, 2015). In addition to their use as a contrast agent or drug delivery system, iron oxide nanoparticles are also used in magnetic hypothermia therapy, for solid tumour treatment. For this, nanoparticles are localised to the solid tumour tissue and energy absorption by the nanoparticles in alternating magnetic field results in localised heating of the cells inducing cell death (Askari *et al.*, 2016)(Kossatz, *et al.*, 2015). A more detailed discussion of the uses of nanoparticles and their biomedical applications can be found in section 1.2.

1.1.4 Nanoparticles and the tumour microenvironment

Control in particle size, in combination with appropriate surface coating may also allow a stealth-effect against the body's immune system. However, the complexity of *in vivo* systems poses multiple barriers that

may severely inhibit efficiency and these barriers must be overcome in order to fully exploit the theoretical potential of nanoparticles. (Tiwari, *et al.*, 2012) For instance, the endothelial cells which line the interior of the entire vascular system represent a major barrier for therapeutic agents travelling from the bloodstream to the target tissues. These endothelial gaps can vary in size considerably, dependent on the tumour type, and therefore result in non-uniform extravasation into the tumour site. Additionally, nanoparticle extravasation can also be governed by particle size, with smaller nanoparticles demonstrating enhanced penetration of the tumour matrix compared to larger nanoparticles. In an attempt to address this, several groups have shown that a degradable nanoparticle with the ability to reduce in size upon extravasation results in an increased accumulation of nanoparticles at the desired site (Tong *et al.,* 2012) (Tong *et al.,* 2013). However, the mononuclear phagocyte system (MPS), consisting of monocytes and macrophages will often sequester the majority of administered nanoparticles, where the cells will then process and degrade components of the administered nanoparticle, often rendering them non-functional (Parambath, 2018). This approach has as of yet not been investigated clinically. Over 40,000 studies published in the last 10 years have focused on nanoparticle targeting strategies and substantial progress has been made toward our understanding of how nanoparticles interact with cells and tissues (Rosenblum *et al.,* 2018)(Li, *et al.*, 2016)

In order to maximise the functionality of the nanoparticle, it is therefore desirable to develop a therapeutic that can passively or actively target cancer cells and achieve the desired effect. There have been many

major advances in the use of nanomaterials in medicine, including the use of magnetic nanoparticles such as iron oxide, gold and silver nanoparticles, nanoshells and nanocages. Liposomes have also been shown to be of great benefit in the field of nanomedicine (Bozzuto & Molinari, 2015). One of the more exciting and important developments in the realm of nanomedicine was the introduction of antigen-specific functionalised nanoparticles. This involves the conjugation of an appropriate ligand that demonstrates a specific binding activity towards the targeted cell type (Bozzuto & Molinari, 2015).

1.2 Nanoparticles and their biomedical applications

Nanoparticles have demonstrated their role in healthcare and medicine for many years, and as a result have been extensively studied as both a direct therapeutic agent and as a carrier for biologically relevant agents (Bobo *et al.,* 2016) (Wagner *et al.,* 2006) (Caruso *et al.,* 2012) (Sanvicens & Pilar Marco, 2008). Although nanoparticles are ubiquitous in the environment, prior to the release of any new nanoparticle-containing product, each constituent and product must undergo intense scrutiny and study in order to assess their safety and efficacy, dependent on the desired function of the biomedical nanoparticle. Because of their small size, many nanoparticles can easily enter the body and cross many barriers, potentially gaining access to many tissues and organs, where they have the potential to cause a number of different issues. It has been postulated that nanoparticles less than 10nm in size have the potential to act similarly to gases, and separate studies have shown that nanoparticles that are either inhaled or

ingested can reach the liver, heart, spleen, gastrointestinal tract, lungs and even the brain (Bahadar *et al.,* 2016). Targeted therapeutics employing the use of nanoparticles have been shown to have the potential to revolutionise healthcare, and the way in which we approach the management of different disease states (Revia & Zhang, 2016) (Yong *et al.,* 2009) (Zhang, *et al.*, 2008). The properties and use of nanoparticles, including those that contribute to the use of nanoparticles in biomedical applications are discussed in further detail below.

1.2.1 Iron (III) oxide nanoparticles (SPIONs)

Iron (III) oxide (Fe_2O_3) is an inorganic compound of paramagnetic nature. Superparamagnetic iron oxide nanoparticles, or SPIONs, have generated a large amount of interest as a potential candidate in nanomedicine, both as potential therapeutics and as diagnostic tools, due to their inherent biocompatibility and magnetic properties (Gobbo *et al.,* 2015)(Senapati *et al.,* 2018). Superparamagnetism refers to the nanoparticles ability to randomly switch, or flip, direction when under the influence of temperature, and where the typical time between two flips is known as the Neel relaxation time. When no magnetic field is applied, and the time taken to measure the magnetisation of the nanoparticles is longer than the Neel relaxation time (where the average value of magnetisation appears as zero), the nanoparticles are said to be in the superparamagnetic state. While in this state, an external field can magnetise the nanoparticles (Marghussain, 2015). The concept of superparamagnetism was first proposed and described by Frenkel and Doefman in 1930 (Frenkel & Doefman, 1930). Some of the benefits of superparamagnetism include a lack of magnetic memory meaning the

nanoparticles do not retain any net magnetisation following removal of the external magnetic field, making them easily controllable in MRI, and retention of stability upon immersion into fluid, making them ideal for use in biological settings (Kolhatkar *et al.,* 2013).

The potential uses of Fe_2O_3 nanoparticles as MRI contrast agents has been an area of intense interest for many years and was a pivotal step towards the realisation of these materials for biomedical use. In 2009, this was accelerated with the FDA approval of ferumoxytol, the first Fe_2O_3 nanoparticle approved for clinical use, indicated for the treatment of iron deficiency anaemia in adults with chronic kidney disease (McCullough *et al.,* 2012). SPIONs have since demonstrated their use in various applications such as malignant hyperthermia, imaging and magnetic separation techniques such as those used for cellular separation and DNA sequencing (Sabale, *et al.,* 2017). As therapeutic agents, SPIONs have drawn increasing attention due to their potential in gene therapy and targeted drug delivery (Gupta & Gupta, 2005) (Mody *et al.,* 2010). This wide range of potential bio-applications of SPIONS is heavily influenced by the particles physical, chemical and magnetic properties, in addition to its shape and size (Patil, *et al.,* 2018). The inherent characteristics of SPIONs may be exploited for image-guided therapies and multimodal theranostics, where more than one treatment strategy is employed, such as with photothermal therapy (PTT), photodynamic therapy (PDT), magnetic hyperthermia and immunotherapy (Saeed *et al.,* 2018). PTT is a non-invasive cancer treatment approach, utilising visible of infrared (IR) light where, in the presence of photo-absorbers such as SPIONs previously administered

to the disease area, the laser energy is converted into thermal energy which can then be used for tumour ablation (Revia & Zhang, 2016). PDT is a technique that destroys cancer cells using the combination of photo-sensitisers, such as SPIONs, and a laser source. This combination results in the release of reactive oxygen species, along with sufficient cellular oxygen, which stimulates apoptosis within the tumour cells (Revia & Zhang, 2016) (Gobbo *et al.,* 2015). However, an as of yet insurmountable drawback of both PDT and PTT is the irrevocable damage to the normal tissue types in their surrounding environment resulting from the penetration of photosensitiser beams. Whilst this is an area which has drawn much attention and resulted in the use of highly size-specific photosensitiser beams, it still remains a concern (Gobbo *et al.,* 2015).. As previously discussed, magnetic hyperthermia is an approach which exploits the ability to heat SPIONs when placed in an external alternating magnetic field. The resultant heat then acts as a tumour ablator. This approach is one of the older multimodal approaches in the treatment of tumours using SPIONS, having been first demonstrated intracellularly in 1979 by Gordon *et al.* (Gordon *et al.,* 1979) (Saeed *et al.,* 2018). The use of PDT, PTT and magnetic hyperthermia has demonstrated great potential in the treatment of solid tumours, though the scalability of these technologies remain to be seen. Another important use of iron oxide nanoparticles is their use in nano-based immunotherapy. The proven biocompatibility and adaptable nature of iron oxide nanomaterials have identified them as useful tools in the generation of novel immunotherapies. A detailed discussion as to the generation and use of nanoimmunotherapies can be found later

within this section. The method employed in the generation of these SPIONs can however be pivotal to ensuring their suitability for use.

1.2.1.1 Synthesis of SPIONs

There are a wide variety of methods in which to develop SPIONs of the correct size and shape for their intended use. These include sol-gel synthesis, electrospray synthesis, hydrothermal reactions, hydrolysis and co-precipitation of iron salts. Co-precipitation is an extremely common method in the synthesis of SPIONs as this technique results in a high nanoparticle yield. This technique, however, allows the producer very limited control over the size distribution, meaning that there may be additional purification steps following synthesis, dependent on the intended use of the SPIONs. The size distribution of SPIONs, and the synthesis of uniform-sized SPIONs is very important as the behaviour and properties depend largely on the dimensions of the particle. (Mahdavi, *et al.*, 2013) (Mody *et al.,* 2010) However, another characteristic of nanoparticles such as SPIONs is their large surface-to-volume ratio with high surface energies, resulting in their common aggregation and tendency to accumulate in one location. Additionally, as with their bulk material, SPIONs have a high reactivity tendency and are therefore easily oxidised, resulting in a loss of magnetism and dispersal. For these reasons, it is vital in the successful generation of SPIONs for biomedical purposes to provide the most suitable surface coating for the SPIONs, in order to maximise the abilities of this materials in biomedical applications (Mahdavi, *et al.*, 2013). SPIONs can be used as scaffolds for the conjugation of a range of biologically and clinically relevant materials including: drugs, proteins, enzymes,

antibodies and nucleotides. The release and distribution/diffusion mechanism, bioavailability and biodegradation rate are important factors in the development of these so-called functionalised SPIONs. In order to generate these functionalised nanoparticles, SPIONs first need to be coated with a surfactant, polymer or conjugation material. This may consist of oleic acid, dextran, chitosan or poly(ethylene glycol) (PEG), or they may need to be silanised using (3-aminopropyl) triethoxysilane, referred to herein as APTES (Mahdavi, *et al.*, 2013). APTES is an aminosilane commonly used in the process of the generation of functionalised nanoparticles, including SPIONs, and it acts as a bonding agent for the adhesion of appropriate molecules to the surface of materials. A representative illustration of a multi-layered functionalised SPION is shown in Figure 1.3. SPIONs are categorised into two main categories based on their hydrodynamic diameter: standard SPIONs (50 to 150nm) and ultrasmall SPIONs (<50nm in size). Most studies looking at the use of SPIONs for biomedical use focus on the use of SPIONs in the range of 10 to 100nm. SPIONs with a hydrodynamic radius of >200nm or <10nm tend to be sequestered by the spleen, or removed through renal clearance (Singh *et al.,* 2010) (Flias & Tsourkas, 2009).

However, the potential toxicity of SPIONs towards normal cells has somewhat hindered their successful implementation as a clinically approved therapeutic agent. Whilst the nanoscale properties demonstrated by SPIONs have proven to be of great potential benefit in the furthering of nanomedicine, these same properties (a large surface area coupled with an enhanced reactivity and an increase in the

propensity to diffuse across biological membranes) can potentially result in an increase in cytotoxicity (Singh *et al.,* 2010). In addition to the direct toxicity and clinical responses of the biological system requiring intense scrutiny, the degradation and accumulation of SPIONs following administration is a key point of study (Patil, *et al.*, 2018). Exposure to SPIONs has been associated with toxic effects such as inflammation, apoptosis, impaired mitochondrial function, the generation of reactive oxygen species (ROS) and an increase in micronuclei (an indicator of significant chromosomal damage, and hence an indicator of genotoxicity) (Singh *et al.,* 2010). However, SPIONs have been shown to demonstrate low toxicity *in vivo* (Hussain *et al.,* 2005) (Kim, *et al.,* 2006). Additionally, a large study comparing the toxicity of several SPIONs *in vitro* demonstrated that Fe_2O_3 were safe and non-cytotoxic below 100µg/mL (Karlsson *et al.,* 2008). The precise mechanism of toxicity is strongly influenced by the size and shape of the SPION, the surface coating; and the mechanism of uptake of the SPION by the cell type.
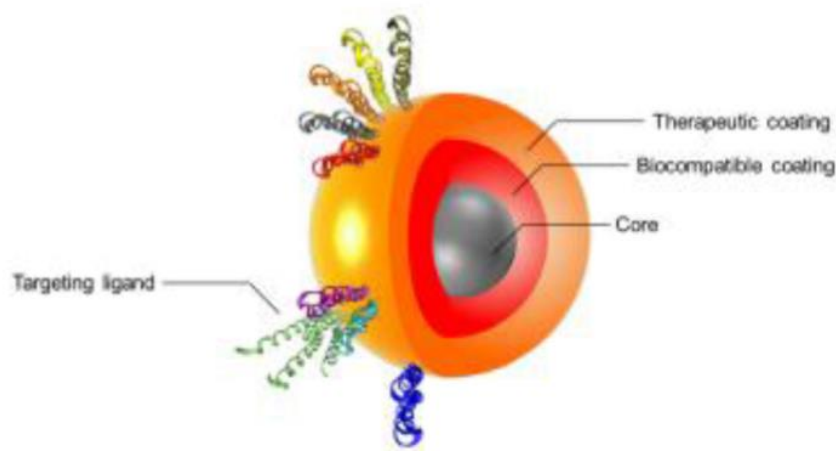
Figure 1.3: **Schematic of a multi-layered magnetic nanoparticle for use in personalised medicine**. Figure depicts iron oxide core for use as a carrier or for imaging purposes, a biocompatible coating, a therapeutic coating for use in cellular

toxicity and a targeting ligand, often an antibody, for cellular targeting. Reproduced with permission from Handbook of Clinical Nanomedicine: Nanoparticles, Imaging, Therapy and Clinical Applications (Movia D, Poland C, Tran L, Volkov Y, Prina-Mello A. Multi-layered Nanoparticles for Personalized Medicine: Translation into Clinical Markets).

1.2.1.2 Surface functionalisation of SPIONs

One of the most notable uses of nanoparticles in biomedical applications is their ability to be used as a "scaffold" or "carrier" for other biologically relevant components. This involves a strategy known as surface functionalisation and involves the incorporation of material(s) on to the surface of the nanoparticle (briefly discussed in section 1.2.1.1). Whilst there are a number of methods in which this end goal can be achieved, the "core-shell" approach is very commonly utilised. This usually involves surface functionalisation as a separate step to the synthesis of the SPION itself (Wu *et al.,* 2015). This "core-shell" approach to surface functionalisation can be achieved through a number of bioconjugation strategies including covalent conjugation and electrostatic conjugation (El-Boubbou, 2018).

Organic materials such as dextran, PEG, chitosan and hyaluronic acid are amongst some of the most commonly used surface modifiers in the development of SPIONs for biomedical applications. SPIONs with such a surface coating have been developed for potential use as MRI agents, magnetic cell separation, magnetic recording and gene delivery (Uthaman *et al.,* 2015) (Wu *et al.,* 2015).

One of the more intricate methods of surface functionalisation includes the addition of particular functional groups to the surface of the SPION. This can include the addition of groups such as hydroxyl groups (-OH), carboxyl groups (-COOH), thiol groups (-SH) or an amine group ($-NH_2$).

The addition of such groups renders the surface of the SPION easily modifiable, allowing for the easy attachment of differing biologically relevant molecules. Aminosilane is a small molecule that is often used to modify the surface of SPIONs, resulting in available functional groups (i.e. amine groups) on the surface of the SPION, which are then available for further functionalisation APTES is an aminosilane which is commonly used in the process of silanisation, and results in the anchoring of the -NH_2 group to the surface of the SPION (Wu *et al.,* 2015). Following on from silanisation of SPIONs, it is then possible to attach a drug/molecule or antibody to the surface of these SPIONs using a carbodiimide compound such as 1-ethyl-3-(-3-dimethylaminopropyl) carbodiimide hydrochloride (EDC) (El-Boubbou, 2018). This process acts through the activation of the carboxyl groups, allowing for their direct conjugation to the available -NH_2 groups. Such techniques have resulted in the generation of anti-EGFR SPIONs, anti-HER2 SPIONs, prostate-specific antigen SPIONs and MUC-1 SPIONs, amongst many others in generation (Mu, *et al.*, 2015) (Mu, *et al.*, 2015) (Bates *et al.,* 2014) (Aghanejad *et al.,* 2018). As mentioned previously, the majority of these SPIONs have been generated as diagnostic or imaging agents, but there is considerable research ongoing in the field of biologically-active nanomedicines (El-Boubbou, 2018).

1.2.2 Nanoparticle characterisation techniques, protocols and methodologies

Nanoparticles, including those with a potential for use in nanomedicine, display novel physicochemical properties (Lin *et al.,* 2014)(Gioria, *et al.,* 2018). This is a feature of nanoparticles that presented them as such an

attractive choice for novel medicinal approaches, but also means that the advancement of their use as a novel nanomedicinal requires a step-wise and thorough characterisation. These novel physicochemical properties have the potential for implications on their physiological interactions, but due to the novelty of these technologies, and the rapid advancement in this field, there is a lack of standardised characterisation methods for nanoparticles and nanomedicines (Lin *et al.,* 2014). These physiological interactions may be influenced by a number of factors, including: the biodistribution of the nanomedicine and the phagocytosis and endocytosis of the nanodrug. There are a number of nanoparticle parameters that may need to be considered such as pH and solubility. Additionally, there is a special emphasis placed on nanoparticle parameters such as size, surface area, shape, charge and aggregation state (Prina-Mello *et al.,* 2013). To date, there have been no stringent guidelines developed for the characterisation of nanoparticles for diagnostic or therapeutic use. However, the US Food and Drug Administration (US FDA) has issued guidelines for the characterisation of materials for the food and cosmetic industries, including the characterisation of drug products, including biological products that contain nanomaterials (Food and Drug Administration (FDA), 2017). Over the past two years, efforts have been made in instigating official legislation for the use of nanomaterials in biomedical applications. To date, these materials are currently subject to the same legislation as chemical substances and require applicable safety and risk assessment methods during manufacturing.

In the production and characterisation of nanoparticles, size is one of the most critical factors. This characteristic is responsible for the regulation and circulation of nanomaterials in the bloodstream, their penetration across physiological barriers, localisation and the induction of cellular response. (Lin *et al.,* 2014) (Ferrari, 2008) (Jiang *et al.,* 2008). It has been reported that the response of a nanoparticle to its surrounding environment is largely size dependent, due to the size of the surface area interacting with the surrounding environment (Jiang *et al.,* 2008) (Tsao *et al.,* 2011). There are a number of different methods that may be employed in the characterisation of the size of nanoparticles. These include nanoparticle tracking analysis (NTA), scanning electron microscopy (SEM), transmission electron microscopy (TEM), Helium Ion Microscopy (HIM) and dynamic light scattering (DLS). Below is a detailed description of NTA technology and DLS. A detailed discussion surrounding microscopy techniques in the context of nanoparticle investigations can be found in Chapter 2.3. Within this chapter, we will discuss the use of NTA, SEM and DLS as a means to confirm the size, dispersion state and aggregation rate of Fe_2O_3 nanoparticles.

1.3 B lymphocytes and Chronic Lymphocytic Leukaemia

In 1890, Emil von Behring first established the functional importance in circulating antitoxins in the immunity to diphtheria and tetanus (Von Behring & Kitasato, 1890) (Kaufmann, 2017). From this evolved the first acknowledgement of cells known as the B cell where, in 1967, Paul Ehrlich proposed that these "antitoxins" were produced by antibody receptors. He proposed that an immune cell bearing several different antibody receptors could be stimulated by the binding of an antigen to produce and release this receptor which was complementary to the antigen (Ehrlich, 1967) (Cooper, 2015). Over the past century, there has been significant knowledge garnered in the understanding of what we now know as the B cell, including the understanding of the antibody-antigen relationship in the 1930s (Tiselius & Kabat, 1939) and the determination that antibody production correlates with immunisation (Fagraeus, 1948). It was not until 1965 that the distinct lineages of the B cell and the T cell became apparent (Cooper *et al.,* 1965) (Cooper, 2015).

Early B cell development is the ordered rearrangement of the immunoglobulin (Ig) H and L chain loci, with Ig proteins playing a vital role in the regulation of this error-prone process (LeBien & Tedder, 2008). In addition to the expression of specific cell surface and cytoplasmic markers, V(D)J recombination distinguishes the subpopulations of developing B cells. Ig are heterodimeric proteins that are composed of four chains: two heavy (H) chain and two light (L) chains. Functionally, these chains can be separated further again: variable (V) domains which are responsible for binding of antigens; and

constant (C) domains that will specify effector functions like complement or the binding to Fc receptors (Figure 1.4) (Schroeder & Cavacini, 2013).
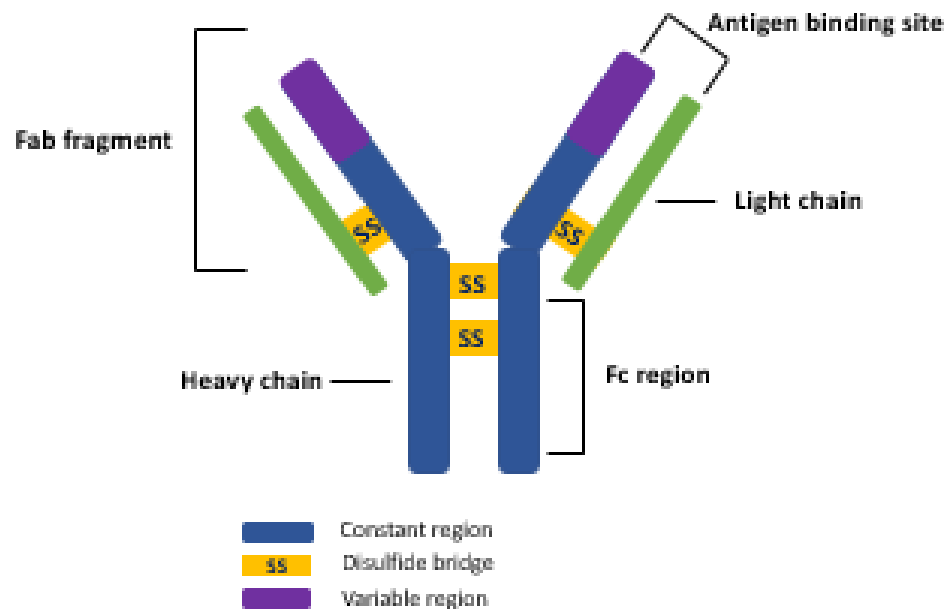
Figure 1.4: **Schematic illustrating the basic structure of immunoglobulin.** Blue regions depict the constant regions, purple depicts the variable regions and yellow bridges depict the disulfide bridges linking each region. Schematic also highlights antigen binding sites within the Fab fragment and the Fc region (or tail region), which is responsible for binding to the Fc receptors on the surface of certain cells. Adapted from Janeway *et al.* 2001. (Janeway Jnr, Travers, Walport, & Shlomchik, 2001).

B cell development begins in the foetal liver but continues in the bone marrow. At this point in the B cell lineage, the immature cell is easily killed upon contact with an antigen, and therefore must develop into a mature cell. B cell development begins as the lymphoid progenitor cells receive signals from the bone marrow stromal cells. The somatic recombination process responsible for the joining of these V, D and J segments of the H chain and the VJ segments of the L chain is catalysed

by two recombinases encoded by the recombination activating genes – *RAG1* and *RAG2* (Eibel, 2015). Cells then undergo D-J joining on the H chain, becoming early pro-B cells where they then begin to express CD45 and MHC Class II molecules. The late pro-B cell stage is then complete upon the attachment of the V segment to the D-J$_H$ component. From here, the pro-B cell will then become a pre-B cell upon the expression of the membrane Ig light chains in their pre-B cell receptor. Within this pre-B cell receptor complex are Igα Igβ signal transduction molecules, containing ITAMs (immunoreceptor tyrosine activation motifs) which will become phosphorylated in response to antigen binding with the B cell receptor (BCR) (more can be found about the B cell receptor in Chapter 1.3.2). It is at this point in the B cell lineage that division occurs, with recombination being halted and B cell clones being produced all producing the same Ig chains, and the B cell being known as the large pre-B cell. A schematic depicting B cell development can be found in Figure 1.5 (LeBien & Tedder, 2008). Small pre-B cells are B cells which are no longer dividing. These cells undergo V-J joining on the L chain expressing the Ig chain on the cell surface, where it is known as an immature B cell. These cells will express the Ig δ chain and membrane IgD. At this point in the B cell lineage, the cell is known as a mature naïve B cell (LeBien & Tedder, 2008).

	Stem cell	Early pro-B cell	Late pro-B cell	Large pre-B cell	Small pre-B cell	Immature B cell	Mature B cell
H-chain genes	Germline	D-J rearranging	V-DJ rearranging	VDJ rearranged	VDJ rearranged	VDJ rearranged	VDJ rearranged
L-chain genes	Germline	Germline	Germline	Germline	V-J rearranging	V-J rearranged	V-J rearranged
Surface Ig	Absent	Absent	Absent	μ chain found transiently on cell surface as part of pre-B cell receptor	Intracellular	IgM now expressed on cell surface	IgD and IgM on cell surface

Figure 1.5: **Development of B cells from stem cell and the importance of VDJ rearrangement in the successful development and expression of surface immunoglobulins**. Image shows that throughout B cell lineage and subsequent VDJ rearrangement, surface Ig will be presented on the surface of the immature B cell. Adapted from Janeway *et al*. 2001.

1.3.1 The role of the B cell

Human B lymphocytes constitute a massively diverse cell population - at the forefront of the immune system. Each B cell is clonally diverse producing a single species of antibody, and collectively these antibodies are known as immunoglobulins. Antibodies produced by B cells are vital in our defence against infection, where their binding to an antigen results in the employment of the complement system, initiating an immune response (Nicholson, 2016) (Sarvaria *et al.,*2017). The production of antibodies is the principal function of B cells, and these molecules can be broken down into their different isotypes and classes. Antibodies (immunoglobulins) are glycosylated protein molecules, either present on the surface of the cell (surface immunoglobulins) where they serve as antigen receptors, or they can be secreted into the extracellular space, where they will bind and neutralise their target antigens. An antibody molecule consists of four protein chains, two "heavy" chains which are linked together by disulphide bonds. There are five antibody classes, or isotypes, distinguished according to the C-terminus regions of the heavy chains (which are constant and therefore do not participate in antigen binding): IgM, IgG, IgD, IgA and IgE (Hoffman *et al.,*2016).

In addition to their role in humoral immunity, B cells are also responsible for the mediation of many other essential functions involved in immune homeostasis, including the initiation of T cell immune responses. It is likely that the antigen-specific interactions between B and T cells require the antigen to first become internalised by the BCR, processed and prepared and then presented in an MHC-manner to the T cell. The

responsibility for this role is shared with dendritic cells (LeBien & Tedder, 2008).

B cells are not only critical for the normal development of the immune system, they are also vital to its maintenance. One way in which this occurs is through the release of immunomodulatory cytokines that can influence a variety of T cell, dendritic cell and antigen-presenting cell functions,.. B cells have been shown to function as cytokine-producing effector cells, influencing T cell differentiation (Harris, *et al.*, 2000). In addition to these functions, they can also regulate lymphoid tissue organisation and neogenesis, help to regulate wound healing and facilitate regulation of tissue transplantation rejection, in addition to influencing tumour development and tumour immunogenicity (LeBien & Tedder, 2008).

1.3.2   The surface of the B cell

The surface of the B cell is a complex and molecule-rich environment. The B cell surface is home to B cell surface receptors (BCR) and a variety of cell surface markers. BCRs are heterodimeric protein complexes, which are composed of two identical immunoglobulin (Ig) heavy-chains (IgH) and two identical Ig light-chain proteins. The BCR genes consist of multiple distinct gene segments which correspond to the variable (V), diversity (D) and joining (J) regions, and they undergo site-specific V(D)J recombination. During this recombination, a series of events including protein rearrangement and random deletion significantly increases the BCR diversity. The majority of the receptors on the surface of the B cell are responsible for the regulation of

development and function, facilitation of communication with the extracellular environment and to interpret BCR signals. CD79a (Igα) and CD79b (Igβ) are non-covalently associated with the BCR complex. Their cytoplasmic domains contain highly conserved motifs for both tyrosine phosphorylation and Src family kinase docking, both of which are essential for the initiation of BCR signalling and B cell activation (LeBien & Tedder, 2008). A schematic depiction of the BCR can be seen in Figure 1.6. In addition to the complexities of the BCR, the surface of the B cell is also home to a number of other cell surface markers which are preferentially expressed by B cells. Some of the cell surface markers which are preferentially expressed by B cells are described below.
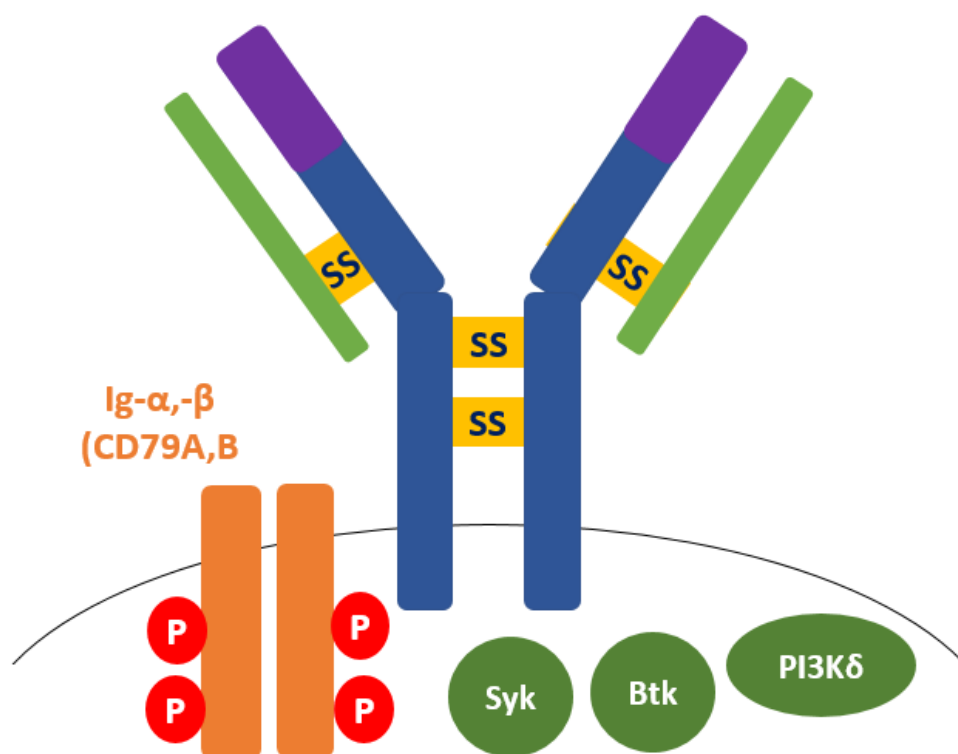
Figure 1.6: **Schematic of the B cell receptor (BCR) and the other components involved in its upstream signalling.** The BCR consists of antigen-binding heavy chains IgH and light chains IgL, that are non-covalently associated with CD79A (Ig-α) and CD79B (Ig-β) signalling units. Upon BCR clustering following an antigen encounter, tyrosine phosphorylation of ITAMs by the Src-family kinases occurs. Syk is responsible for the triggering of a signalling cascade engaging several kinases including Bruton's tyrosine kinase (BTK) and PI3Kδ. Adapted from Burger *et al.* 2013. (Burger & Chiorazzi, 2013)

1.3.3.1 CD19

The CD19 antigen is a 95kDa transmembrane glycoprotein, encoded by the short arm of chromosome 16. CD19 was first identified in 1983 by Nadler and colleagues, and can be detected on all normal, mitogen-stimulated and malignant B cells, excluding the plasma cell.(Nadler *et al.*, 1983) (Kim, *et al.,* 2000) (Wang *et al.,* 2012). CD19 is involved in the antigen-independent development and immunoglobulin-induced activation of B cells (Nadler *et al.*, 1983) (Wang *et al.,* 2012). CD19 is known to work in complex with the B cell receptor to allow both the indirect and the direct recruitment of down-stream protein kinases, in addition to being required for optimal MHC class II-mediated signalling, through its modulation of tyrosine phosphorylation and Akt kinase signalling (Wang *et al.,* 2012). CD19 is commonly employed in the identification of B cells within a cellular suspension, as a rapid means to differentiate from other haematological cells in suspension (Scheuermann & Racila, 1995). CD19 was initially identified as a B cell specific antigen and considered as a potential BCR co-receptor because it was found to co-modulate with the BCR. CD19 functions as a signal receptor via a PTK-dependent pathway. CD19 has been found to be associated with the cell membrane in complex with the complement receptor CD21, and the tetraspanin CD81, with this complex thought to facilitate cellular signalling. CD19 is important to humoral immunity, through its interaction and co-ligation with the BCR, lowering BCR-mediated activation thresholds and enhancing primary B cell responses through signal amplification. Additionally, mouse studies have shown that the IgG response to antigens is considerably compromised by the

absence of CD19 on the cell surface, and normal germinal centre development in response to immunisation with antigens is compromised, and though there is a germinal centre response to the infection, normal B cell memory does not develop. This demonstrates the important role of CD19 in normal adaptive humoral response. CD19 has been found to be expressed in almost all B cell malignancies - acute lymphoblastic leukaemia (ALL), chronic lymphocytic leukaemia (CLL) and B cell lymphomas all show expression of CD19 at normal to high levels. Additionally, other forms of lymphoma such as follicular lymphoma show lower levels of CD19. For this reason, CD19 expression levels have proven to be a useful tool in the diagnosis of leukaemia's and lymphomas (Bishop *et al.,* 2003).

1.3.3.2 CD5

CD5 is a monomeric cell surface glycoprotein expressed on the surface of thymocytes, mature T cells and a subset of B cells, including B-CLL cells and mantle cell lymphoma (Martin *et al.*, 1980). It is thought that CD5+ B cells are likely involved in antigen presentation and tolerance induction, and they have been shown to represent a subpopulation of B cells which have unmutated Ig variable region genes. CD5 expression is commonly used as a marker for CLL using flow cytometric analysis, in combination with CD19 positivity, allowing for clear differentiation from CD5+ T cells in the cell population (Masuda & Kishumoto, 2016) (Bashford-Rogers, *et al.*, 2017). It has been demonstrated that there is heterogeneity of CD5 expression within CLL clones from individual patients, indicating that the state of CD5 expression is a dynamic and fluid expression throughout the lifetime of the disease. Additionally, it

has been recently demonstrated that CD5 expression in CLL correlates with differences in expression of CD45 and CD81 cell surface expression and CD5+ B cells may play a role in immunosuppression, perhaps providing an insight into their excessive proliferation in malignancies (Raveche, 1990) (Masuda & Kishumoto, 2016) (Bashford-Rogers, *et al.*, 2017).

1.3.3.3 CD20

CD20 is a 33kDa, non-glycosylated tetraspanin of the membrane with two extracellular loops containing the epitopes for anti-CD20 antibodies, and a B cell differentiation antigen widely expressed in B cells, from the early pre-B cell until the mature B cell stage. However, CD20 expression is lost in plasma cells (Tedder *et al.*, 1988). It contains four highly conserved membrane spanning regions and was one of the first B cell differentiation antigens described. It is one of the most well-known B cell antigens due to its role as a target for monoclonal antibodies in the treatment of B cell malignancies and some autoimmune diseases, such as rheumatoid arthritis (Marshall *et al.,* 2017).

The function of CD20 is largely unknown; however, it is postulated to be involved in B cell activation, growth regulation and possibly acting as a calcium ion channel, as demonstrated in CD20-deficient mouse cells (Riley & Sliwkowski, 2000). CD20 has also been shown to play an important role in enabling B cells to respond optimally to T-cell independent antibody responses (Kujipers *et al.*, 2010). These cells have been shown to exhibit decreased calcium signalling downstream of BCR engagement, and human B cells are also shown to be unable to

initiate calcium signalling in the absence of the BCR signalling in the absence of the BCR despite CD20 crosslinking (Marshall *et al.,* 2017) (Riley & Sliwkowski, 2000).

1.3.3.4 CD38

CD38 is a single chain transmembrane molecule of approximately 45kDa. CD38 tends to associate with other human B cell molecules, including the CD19/CD81 complex, the chemokine receptor CXCR4, and adhesion molecules such as CD49d (Vences-Catalan, *et al.*, 2012)(Kontani, *et al.*, 1993). CD38 is also found in membrane vesicles secreted by B cells and is likely to be an important factor in intracellular communication. CD38 is expressed at high levels by B cells lineage progenitors in the bone marrow, and by B lymphocytes in the germinal centre, in activated tonsils and by terminally differentiated plasma cells. It is expressed at low levels on memory B cells. CD38 has also been shown to be expressed in pancreatic cells, smooth muscle cells, osteoclasts and in regions of the brain; though generally in these cases CD38 is located in either the cytosol or the nucleus (Malavasi F , *et al.*, 2008) (Malavasi F., *et al,* 2011).

CD38 expression can act to identify two subgroups of CLL with two distinct clinical outcomes. These two groups can differ clinically in several ways, including overall survival, time to first treatment, number of leukaemic cells with atypical morphology and absolute lymphocyte count, where a higher burden of CD38+ CLL cells has been shown to result in such clonal aggressiveness and a worse clinical outcome. CD38 in combination with other markers such as ZAP-70 and CD49d

can successfully provide prognostic information. ZAP-70 is a signalling molecule in T and NK cells, is structurally homologous to spleen tyrosine kinase (SYK) and has been shown to enhance BCR signalling with patients displaying high levels of ZAP-70 protein having a more aggressive clinical course (ten Hacken & Burger, 2016). Interestingly, the genetic signature of CD38+ and CD38- members of the same CLL clone revealed a higher VEGF and Mcl-1 levels in the CD38+ CLL cells, which could indicate a survival advantage from microenvironmental stimuli (Pepper, *et al.*, 2007) (Malavasi F. , *et al.*, 2011).

1.3.3.5 CD52

CD52 is a glycosylphosphatidylinositol (GPI)-anchored glycoprotein, 29kDa in size, comprised of 12 amino acids with a large carbohydrate domain. CD52 is expressed on most haematopoietic cells at different levels: low levels on stem cells and high levels on lymphocytes and malignant B cells, in addition to expression on spermatocytes (Hale, 1983). The biological function of CD52 remains poorly understood, however its presence on the surface of spermatocytes indicates that it may play a role in anti-adhesion (Hale & Waldmann, 2000) (Vojdeman, *et al.,* 2017). Additionally, CD52 has been postulated to participate in cell-cell interactions, regulatory T cell function and the regulation of activated T cells (Turner, *et al.*, 2016).

The high levels of surface expression of CD52 antigen in malignant B cells has given rise to its use as a therapeutic target for the treatment of CLL using anti-CD52 monoclonal antibodies (alemtuzumab). It has also demonstrated high efficacy in the treatment of prolymphocytic

leukaemia (PLL), and remains a target of great interest in targeting of not just CLL cells, but other malignant lymphocytes (Dearden *et al.*, 2011).

Other CLL cell surface receptors not expanded upon here include: CD21, which synergises with the BCR to play an important role in B cell activation; CD22, an important adhesion molecule in the interaction of B cells with T cells, in addition to being involved in BCR-mediated B cell activation; CD32 which functions as an inhibitory receptor preventing excessive cellular proliferation; and CD40 which is involved in cell cycle regulation of CLL cells.

1.4 Chronic lymphocytic leukaemia

Chronic Lymphocytic Leukaemia (CLL) is the most common form of leukaemia across North America and Europe, with a median age of onset of 72 years of age and about 10% of patients reported to be younger than 55 years of age. In Ireland, CLL is the most common form of leukaemia, making up 41% of all leukaemia diagnoses in men, and 37% in women. Each year, approximately 110 individuals in Ireland will be diagnosed with this disease (National Cancer Registry, Ireland). CLL is generally characterised by an absolute lymphocytosis, or presence in the peripheral blood, of 5 x 10^9/L mature CD5+ lymphocytes in the blood, bone marrow and spleen; and blood smears that demonstrates characteristically small cell size and with a dense nucleus and aggregated chromatin with a corresponding immunophenotype distinguishing it from other diseases frequently mimicking CLL, such as mantle cell lymphoma and splenic marginal-zone lymphoma (Kipps, *et al.*, 2017) (Hallek, 2017). The clinical progression of CLL is heterogenous and ranges from patients who require therapeutic intervention immediately after diagnosis to those who may not require therapy for years, if ever, with the average time to first treatment being 4 to 5 years from the time of diagnosis (Kipps, *et al.*, 2017). Approximately 25% of patients will not require any intervention at the time of diagnosis, and approximately 30% of patients will never require treatment for their disease (Gribben, 2010). It has recently been reported that the capacity for the generation of clonal B cells might be acquired at the haematopoietic stem cell (HSC) stage, implying that the primary event in CLL might involve these multipotent, self-renewing

HSCs. Upon initiation of malignant transformation, B cells retain much of their key features, including specific characteristics of the particular differentiation stages. Studies have shown that the germinal centre B cell of origin carry somatically mutated Ig V genes and show intraclonal diversity (Seifert *et al.,* 2013). The interesting aspect of the development of CLL cells is the fact that CLL clones use either mutated or unmutated IGHV genes, and that this feature can distinguish patient subgroups with very distinct clinical courses. This finding resulted in many suggesting that the cell of origin in the pathogenesis of differentiating forms of B cell leukaemia's arise from differing cells of origin (Seifert *et al.,* 2013). An analysis of numerous studies has concluded that the majority of B cell lymphomas are derived from the germinal centre or post-germinal centre B cells. This has been an important finding, especially given that approximately half of all B cells are naïve B cells, and that B cells tend to only reside in the germinal centre for a few days or weeks. A potential reason for the production of transformed B cells may be the rate of cellular proliferation in the germinal centre. In addition, the processes of somatic hypermutation and class switching are mutagenic processes, both of which increase the risk for a B cells to undergo malignant transformation (Seifert *et al.,* 2013) (Chiorazzi & Ferrarini, 2011). Much work has been done on the characterisation of the molecular and cellular markers which could play a role in prediction and disease progression, with mutation status and abnormalities being of particular benefit in disease prognosis. These prognostic factors include genetic abnormalities (17p,11q and immunoglobulin heavy chain variable (IGHV) abnormalities), and biochemical and cell surface markers

(serum thymidine kinase, β2-microglobulin, CD49d, CD38, and ZAP-70) (Chen & Puvvada, 2016). Several factors contributing to the events leading up to the generation of neoplastic B cell conditions resulting in CLL have been identified. These transforming events include genomic aberrations, gene mutations and deregulated micro RNAs. All of these factors are of prognostic relevance (Georgiadis, *et al.*, 2017). It has also recently been reported that the loss or addition of large chromosomal material may be involved in the initiation of CLL, and this is followed by the additional mutations that may render the disease more aggressive. Deletions on the long arm of chromosome 13 (e.g. *13q14* deletion) are the single most frequently observed aberration in CLL, detected in over 50% of all cases. This aberration is characterised by a benign disease course, and loss of the miRNAs located in the important region of *del(13q14)* have been seen to induce a CLL-like disorder in animal models (Klein, *et al.*, 2010) (Hallek, 2017). Deletions in the long arm of chromosome 11 (*del(11q)*) are found in approximately 25% of chemotherapy-naïve patients with advanced disease, and in approximately 10% of patients in early stage disease (Hallek, 2017). These deletions are often found on band *11q23* harbouring the gene ATM, a gene responsible for the encoding of the proximal DNA damage response kinase ATM. In addition to this, patients carrying such a deletion typically show a bulky disease lymphadenopathy, rapid disease progression and reduced overall survival. Deletions of the short arm of chromosome 17 *del(17p)* are found in approximately 5-8% of chemotherapy-naïve patients. These deletions almost always include band 17p13, where the prominent tumour suppressor gene *TP53* is

located. Patients with a carrying this deletion have shown a marked resistance against genotoxic chemotherapies that cannot be overcome by the addition of anti-CD20 antibodies. Mutations in the TP53 gene are found in approximately 4-37% of patients with CLL and have been shown to be associated with very poor prognosis. TP53 mutations with a lack of (del(17p)) are considerably more rare and have been shown to have a detrimental effect on chemotherapeutic response and overall survival (Hallek, 2017).

The B cell receptor plays a pivotal role in the pathogenicity of CLL. Within CLL, both ligand dependent and independent BCR signalling have been described. The B cell receptor inventory is increased by the introduction of somatic mutations in the germinal centre. Whilst functional BCRs are expressed in most B cell lymphomas, the surface expression of BCR in CLL is generally weak (Kono, *et al.*, 2013). Although the BCR is poorly expressed at the membrane level in CLL, transcription and intracellular synthesis of the constituents of the BCR are at normal levels. However, these components cannot be assembled and transported from the endoplasmic reticulum to the cell surface due to a defect in the folding and glycosylation of the CD79A chain, but not of the CD79B chain. The same folding defect of the CD79A chain is also responsible for the poor expression of CD22 in CLL (Carrasco & Batista, 2006). That being said, the BCR remains a huge topic of study based on the hypothesis that it is responsible for huge amount of crosstalk between signalling pathways involved in the pathogenesis of CLL. This area of research has resulted in a rapid clinical development of novel therapeutics aimed at targeting BCR pathway components and has

demonstrated high response rates and durable remissions (Burger & Chiorazzi, 2013) (Georgiadis, *et al.*, 2017).

1.4.1 The importance of the microenvironment in CLL

The leukaemia microenvironment is proving pivotal in the understanding of CLL biology, and to the design of new and emerging therapies. CLL cells recirculate between the peripheral blood and the secondary lymphoid organs, where they then proliferate in distinct tissue areas, known as pseudofollicles (ten Hacken & Burger, 2016). External cues and signals from surrounding cells in the microenvironment have been shown to not only increase survival rates of CLL cells, but are of pivotal importance to the homing of CLL cells, and much work is now being performed using co-cultures as opposed to a single cell type, for instance, using bone marrow stromal cells (BMSCs) and endothelial cells in order to better mimic or model this interaction (Fiorcari, *et al.*, 2013). BMSCs have been shown to provide a comforting niche for CLL cells in circulating, providing shelter from toxic agents and abundant attachment sites. These cells have also been shown to be of importance in the migratory behaviour of CLL cells in aggressive disease states. The adhesive properties of CLL cells have been the topic of much discussion in recent years, given the importance of this adhesion in the homing of CLL cells in addition to the pro-survival benefits of adhesion for CLL cells (Fiorcari, *et al.*, 2013) (Hartmann, *et al.*, 2009). *In vitro* culture with follicular dendritic cells have been shown to rescue CLL cells from spontaneous apoptosis by direct cell contact, dependent on the ligation of CD44 on CLL cells and subsequent up-regulation of

myeloid cell leukaemia-1 (Mcl-1), a member of the BCL2 family of anti-apoptotic proteins.

Nurse-like cells (NLCs) have been shown to be a critical component of the CLL microenvironment. This cell type is capable of spontaneously differentiating in vitro from monocytes in high-density cultures of CLL peripheral blood mononuclear cells (PBMCs). NLCs have been shown to activate the BCR and NF-κB signalling pathways in CLL cells. Additionally, NLCs have been shown to induce chemotaxis and promote the survival of CLL cells through the secretion of chemokines CXCL12 and CXCL13, and the expression of TNF family members activating factor (BAFF). Interestingly, NLCs also express CD31, the ligand for CD38, expressed on the surface of CLL cells. Additional studies have also demonstrated that monocytes protect CLL cells from *in vitro* apoptosis by secreting soluble CD14, activating NF-κB in CLL cells and induce gene expression profile changes in CLL cells including inflammatory cytokine production (ten Hacken & Burger, 2016).

CLL cell trafficking and homing to the tissue microenvironment is highly controlled and involves the activation of both chemokine receptors and adhesion molecules on the CLL cells. Chemotaxis towards the stromal cells in the environment is promoted predominantly by CXCL12, secreted by both BMSCs and NLCs. CLL cells which display higher levels of ZAP-70, CD38 and VLA-4 have been shown to display a higher degree of chemotaxis towards CXCL12, and a higher degree of extravasation. High levels of the CXCL12 receptor, CXCR4, on CLL cells have been associated with a higher risk of lymphoid organ infiltration and poorer disease outcome, as well as higher

responsiveness to BCR stimulation. Additionally, activated CLL cells have been shown to secrete high levels of the chemokines CCL3 and CCL4, following BCR stimulation or after co-culture with NLCs. These chemokines then likely recruit T cells and monocytes/macrophages to tissue sites for interactions with CLL cells (ten Hacken & Burger, 2016).

The possibility of controlling and hindering adhesion of CLL cells to cells in their microenvironment could be of great benefit in the prevention of anti-apoptotic status and increased cell death. Recently, Farahani and colleagues demonstrated that CLL cells also secrete microvesicles which have been shown to transfer the phosphor-receptor tyrosine kinase Axl to nearby stromal cells, creating a "homing and nurturing environment". There has been a great amount of work and research into the targeting of the microenvironment in CLL. This has included the use of CXCR4/CXCL12 inhibitors and targeting of BCR-associated kinases using novel small molecule inhibitors such as ibrutinib and idelalisib. The complexity of the cross-talk between the microenvironment and CLL cells, as well as the mechanisms of drug resistance and treatment failure still need to be better defined and are the subject of much investigation (ten Hacken & Burger, 2016).

A key process in CLL homing and trafficking to lymph nodes and the bone marrow is the adhesion of CLL cells to the endothelial cells in high endothelial venules (HEVs). HEVs are normally only found in lymphoid organs, with the exception of the spleen, but malignancy can cause their development in non-lymphoid tissues resulting in the infiltration of high numbers of lymphocytes to these tissues (Martinet *et al.*, 2011). A number of protein families, in particular selectins and integrins

expressed on the homing lymphocytes, and sialylated carbohydrates, integrin ligands and chemoattractants expressed in the HEVs are crucial to the migration process. Initial adhesion and migration to the HEVs occurs as a multistep adhesion cascade (Rosen, 2004)(Umemoto *et al.,* 2006). Carbohydrate and mucin-like molecules line the HEVs and are recognised by selectin molecules expressed on homing lymphocytes, and this initial interaction allows for the slowing and rolling of lymphocytes along the endothelial layer, beginning this multistep adhesion cascade. Chemokines within the HEV then activate integrins which then mediate the adherence of lymphocytes to the HEV endothelial cells. After this initial adhesion, additional integrins that then strengthen this adherence include integrins CD11b/18, CD11c/18 and CD49d. Following this, lymphocytes then transmigrate between endothelial cells (diapedesis) using other adhesion molecules including CD38 and CD31 (Kinashi, 2005). This trafficking of CLL cells between the peripheral blood and secondary lymphoid organs is important in the pathogenesis of CLL (ten Hacken & Burger, 2016). A schematic depicting this process can be found below in Figure 1.7.
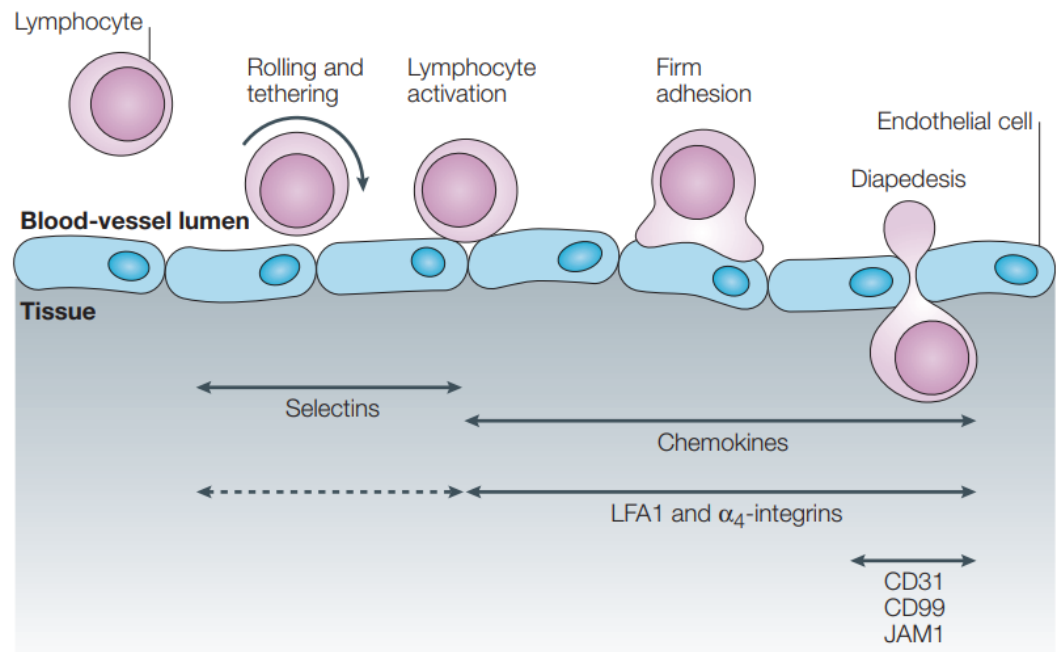
Figure 1.7: Multistep process of lymphocyte adhesion and migration. Under shear flow, lymphocytes will begin to roll and tether to the endothelial cells lining the HEV, using selectin molecules. After this initial adherence, chemokines then activate integrins and further adhesion molecules then enable the adhesion and transmigration of lymphocytes (Kinashi, 2005).

1.4.2 Current approaches and outlook in the treatment of CLL

The clinical staging systems for the classification of CLL were developed by Rai and Binet and remain to be a cornerstone in the clinical assessment and staging of patients with CLL. This classification system can enable clinicians to separate those patients with early stage disease (Rai stage 0-II or Binet stage A) from those with advanced-stage disease (Rai III-IV or Binet stage B or C). This classification is primarily on a symptomatic basis of the development of anaemia and/or the presence of thrombocytopenia, in addition to lymph node enlargement and spleen involvement; or bulky disease at advanced stages. These classification systems were developed prior to the establishment of prognostic genetic and molecular characterisation, and therefore are not suitable for use as a prognostic indicator of disease progression in individual, or cohorts of patients, but act as a means of risk stratification by which to determine initiation of treatment or utilisation of "watch and wait" approach (Buger & O'Brien, 2018). Improvements in next-generation sequencing have allowed for the determination of cohorts of CLL patients who would respond favourably to certain treatment regimes, and indeed those who would display a chemorefractory clinical course. Over 50% of patients diagnosed with CLL will display clinically relevant molecular and genetic markers, and it is these that are now most commonly be used as guidance for treatment initiated (Foa, *et al.*, 2013). As discussed earlier, these clinically relevant molecular markers include genetic abnormalities (17p,11q and immunoglobulin heavy chain variable (IGHV) abnormalities), and biochemical and cell surface

markers (serum thymidine kinase, β2-microglobulin, CD49d, CD38, and ZAP-70) (Chen & Puvvada, 2016). Patients presenting with a 17p deletion or another TP53 mutation are recommended venetoclax or ibrutinib as first line treatment. Those presenting with a high level of cell surface markers may benefit from targeted therapy such as with monoclonal antibody therapy (Foa, *et al.*, 2013).

Patients are generally only treated following disease progression, and the current frontline treatment for patients who are considered fit and in generally good health is combination therapy including fludarabine and cyclophosphamide (FC regimen, further discussed below) in addition to anti-CD20 therapy such as with rituxumab (Eichhorst , *et al.*, 2016). This treatment approach tends to be higher in intensity with the goal of inducing a durable remission and the achievement of minimal residual disease (MRD) negativity at the end of treatment, and as such is the frontline therapeutic strategy as issued by the National Institute of Care and Excellence (Thompson & Wierda , 2016). Patients who are considered to fall into the frailer category (a common find given the median age of onset of CLL) are commonly treated with low-intensity therapy including an alkylating agent (such as chlorambucil) and anti-CD20 antibody (such as rituxumab), or some such combination. The goal of such treatments is to alleviate symptoms and to treat anaemia or thrombocytopenia associated with disease progression (Buger & O'Brien, 2018).

The FC regimen was developed for CLL patients who were previously untreated or who has previously been treated with fludarabine as a single agent. Those patients who were not refractory to fludarabine (or

another alkylating agent) demonstrated an overall response rate of over 80%. Further studies into the synergy between these two agents showed that even patients refractory to fludarabine at point of entry achieved a 38% response rate (Skarbnik & Faderl, 2017).

Over the last decade, there have been significant advancements in the treatment of patients with CLL. These advancements in treatment approaches have resulted in improved response rates and overall survival for many patients with this disease, particularly those with chemorefractory disease with a 17p deletion. Chronic lymphocytic leukaemia can be treated using a regimen of drugs, biological therapies and in some cases, bone marrow transplantation. These treatment regimen combinations often include fludarabine, cyclophosphamide and rituximab (FCR); pentostatin, cyclophosphamide and rituximab; fludarabine and rituximab; and fludarabine and alemtuzumab, though the FCR regime has demonstrated complete response rates as high as 70% as a frontline therapy (Kay *et al.,* 2006). Treatment with monotherapies have traditionally served as initial, front-line therapy for CLL, with chlorambucil serving as the gold standard for many years. Chlorambucil has many advantages as a treatment: it demonstrates low toxicity, it has a low cost, has the convenience of an oral medication. However, it has also been shown to not generate a complete response rate in patients and induces several side effects after prolonged use. It is for these reasons that chlorambucil is predominately reserved for palliative treatment of the elderly and frail patients, where an inexpensive drug is one of the goals of the therapy. There are three common purine analogues used in the treatment of CLL. These include

the aforementioned fludarabine, pentostatin and cladribine. Fludarabine is the most studied and understood of these three in CLL and has been shown to result in superior overall response rates when compared to other treatment regimens. Additionally, fludarabine has been shown to induce more remissions and complete remissions (between 7% and 40%) than other chemotherapeutic regimens such as CHOP (cyclophosphamide, doxorubicin, vincristine, prednisone) and CAP (cyclophosphamide, doxorubicin, prednisone), but had little success in improving overall survival when used as a single agent (Hallek, 2017).

The central issue with these treatments is a lack of specificity to the malignant cell types, therefore highlighting a massively unmet need for more targeted and specific therapies in the field of haematological malignancy. These treatments, whilst demonstrating response rates in number of patient cohorts, lack the specificity required in the treatment of B cell malignancies and can often result in acute toxicity to the patient (Bagacean *et al.,* 2016). The BCR has emerged as a target for CLL therapies. Idelalisib is a reversible p110δ isoform-specific phosphoinositide-3 kinase (PI3K) inhibitor. The δ isoform of this oral therapeutic is specific for B cells meaning that this inhibitor has specific targeting abilities for CLL cells, whilst displaying limited effects on other cells in the environment. Idelalisib acts through the potent inhibition of PI3K signalling within the microenvironment, which bears great importance in the survival and proliferation of CLL cells (Fiorcari, *et al.,* 2013). Idelalisib is approved for administration in conjunction with rituximab (anti-CD20 monoclonal antibody) for the treatment of relapsed/refractory CLL. Ibrutinib is a selective and reversible inhibitor

of Bruton Tyrosine Kinase (BTK), an enzyme involved in the activation of mast cells and B cell maturation. BTK acts through the inhibition of BCR signalling which then prevents lymphocyte adhesion and homing, again inhibiting these protective effects of the tumour microenvironment. This treatment regime is commonly employed in the treatment of relapsed/refractory CLL displaying a *del(17p),* or 17p deletion, genotype (Forconi, 2015) (Byrd, *et al.*, 2015). Additional novel therapies include venetoclax, a selective inhibitor of BCL2, an anti-apoptotic protein. Venetoclax acts as an antagonist to BCL2 and its analogues, resulting in increased apoptotic events of CLL cells (Byrd, *et al.*, 2015).

1.4.2.1 Monoclonal antibody therapies

One approach which has shown great promise in a large percentage of patients is monoclonal antibody therapies. Expression of the cell surface molecules often become overexpressed as the B lymphocytes become cancerous, resulting in an abundance of potential targetable molecules (McLeod *et al.,* 1998). The use of rituxumab or alemtuzumab has been shown to result in response rates of greater than 90% of patients (Christian & Lin, 2008).

Monoclonal antibody therapy may result in the initiation of at least one of three main cell death pathways: programmed cell death (apoptosis), complement-dependent cytotoxicity (CDC) or antibody-dependent cellular cytotoxicity (ADCC).

Apoptosis is induced by one of two pathways: the intrinsic pathway and the extrinsic pathway. The intrinsic pathway occurs when the cell self-destructs due to cell stresses in the environment. The extrinsic pathway

occurs when the cell self-destructs as a result of signals from external cells (Elmore, 2007). There are several events that occur in cells that are undergoing apoptotic events. These can include chromatin condensation, cell blebbing and shrinkage, nuclear fragmentation and mRNA decay. Direct apoptosis following treatment with monoclonal antibodies may be induced upon the interference of the antibody with signals and modulators involved in cell growth and proliferation, perhaps acting as a calcium channel resulting in an increase of intracellular Ca^{2+}; or through the activation of caspase-3 and caspase-9. Other monoclonal antibodies have also been shown to be involved in direct induction of apoptosis through the targeting of the family of tumour necrosis factor receptors (Ludwig *et al.,* 2003). CDC is employed when a target antibody, which has become bound to the surface of the target cell, is recognised by the C1q component of the C1 complex of the classical pathway of complement activation. Upon binding of the C1q with the antibody on the surface, the subsequent complement cascade leads to the formation of the membrane attack complex (MAC) on the surface of the target cell. Alternatively, the mannose-binding lectin (MBL) pathway is initiated when plasma MBL and MBL-associated protease MASP-1/2 bind to mannose and fructose residues on the surface of pathogens detected. The alternative pathway of CDC displays spontaneous autoactivation, identifying potential pathogens. All three pathways result in the assembly of the MAC pathway. When the MAC is inserted into the cell membrane of the target cell, and remains open, it results in the induction of cell lysis through an influx of ions and water leading to fatal colloid-osmotic swelling (Zhou *et al.*, 2008) (Beum, *et al.*, 2008) (Kishore

& Reid, 2000). Antibody-dependent cellular cytotoxicity (ADCC) is a mechanism of cell death whereby Fc receptor- (the antibody receptor involved in antigen recognition) bearing effector cells recognise and kill cells bearing the antibody target, or pathogenic target on their surface. In the majority of studies, these effector cells are commonly found to be NK cells, however it should be noted that macrophages, neutrophils and eosinophils may also mediate ADCC (Herberman *et al.*, 1979). There are four main stages involved in ADCC of target cells: (1) the recognition of the target cell, and subsequent cross-linking of the surface of these cells, (2) the phosphorylation of ITAMs by cellular kinases within the effector cells, (3) the triggering of downstream signalling pathways in the effector cells and the (4) subsequent cell death of the target cells through the perforin/granzyme cell death pathway (Bleesing & Oliveira, 2013) (Herberman *et al.*, , 1979) (Wang *et al.,* 2015).

There are a number of novel monoclonal antibody therapies that have recently shown great promise in the treatment of CLL, against a range of CLL cell surface receptors. Some of these include monoclonal antibodies directed against CD20, CD52, CD38 and, more recently, CD19.

1.4.2.1.1 Anti-CD20 monoclonal antibodies

Anti-CD20 therapy has become a part of the standard of care regimen in the management of CLL, having been shown to improve patient outcome when combined with the chemotherapeutics fludarabine and cyclophosphamide, known as the FCR regimen (Byrd, *et al.*, 2005) (Badoux, *et al.*, 2011) (Feugier, 2015). Most anti-CD20 monoclonal

antibodies are categorised as either Type I or Type II antibodies. The classification of these antibodies into one of these categories is based on their ability to induce the translocation of CD20 into large lipid microdomains known as lipid rafts, a process which is responsible for the enhancement of the recruitment and activation of complement (Janas *et al.,* 2005) (Klein, *et al.,* 2013). This translocation ability contributes to not only the mechanism of the induction of cell death, but also the binding capacity of anti-CD20 antibodies by B cells. Type I anti-CD20 monoclonal antibodies redistribute CD20 in the insoluble membrane lipid rafts and activate complement potently. Type II anti-CD20 antibodies can only weakly activate complement but can more potently activate programmed cell death, or apoptosis (Alduaij & Illidge, 2011). Type I antibodies have been found to exert potent CDC and the ability to bind twice as many B cells when compared to the binding ability of Type II antibodies. However, Type II antibodies have been shown to demonstrate higher cell death induction as a result of their ability to induce ADCC (Klein, *et al*, 2013). Monoclonal antibody recognising CD20 on the surface of the B cell has shown great success in the clinic has been shown to induce rapid cell death in malignant B cells through CDC. Type II antibodies have also demonstrated the ability to induce direct cell death upon binding to their respective antigens on the cell surface.

Rituximab is a chimeric IgG1 and anti-CD20 monoclonal antibody, binding to amino acids 170-173 and 182-185 on CD20, and was licensed in the US in 1997, and in 1998 by the EMA for the evaluation of medical products. It is a Type I antibody and acts to stabilise the CD20

on lipid rafts which promotes antibody-dependent cellular toxicity and complement-dependent cytotoxicity. In combination with chemotherapy, rituximab has shown significantly improved response rates and progression-free survival in addition to an improvement in overall survival in some patients, when compared to other standard of care approaches (response rates of up to 72% and progression-free survival of up to 4.8 years) (Feugier, 2015). Rituximab is generally well-tolerated, though as with other chimeric antibodies can result in cytokine mediated reactions such as low blood pressure. In addition to this, rituximab can result in an increase in susceptibility to developing viral and bacterial infections, due to resultant lymphopenia (Feugier, 2015).

The successes of rituximab have led to the production of many more anti-CD20 antibodies, including those of second, and now even third generation, each of which have been designed to build upon the successes of rituximab, increasing potency, lengthening dissociation rates and improving overall efficacy. Rituximab is less commonly employed as a single agent in CLL than in follicular lymphoma, unless very high doses are used. However, a combination of rituximab with traditional chemotherapies have proven to be very efficacious therapies for CLL (Badoux, *et al.*, 2011) (Bagacean *et al.,* 2016).

Ofatumumab is a fully humanised antibody targeting a unique CD20 epitope. This results in an increase in binding affinity to CD20, a prolonged dissociation rate and an increase in cell death due to an increase in CDC activity. Ofatumumab has been approved as a monotherapy in patients that are fludarabine and alemtuzumab refractory and displays a toxicity profile similar to that of rituximab with

ORRs seen up to 58%, with a median PFS of approximately 6 months (Byrd, *et al.*, 2014) (Hallek, 2017).,.

Obinutuzumab (GA101) is a humanised glycoengineered monoclonal antibody, which has shown impressive results in vitro with higher rates of apoptosis in B cells when compared with rituximab. The engineering of obinutuzumab has led to its higher affinity binding to CD20, an increase in ADCC, low CDC and increased direct cell death induction (Hallek, 2017). Single-agent obinutuzumab in clinical trials have shown ORRs of between 30% and 62%, and a median response duration of 8.9 months (Cartron , *et al.*, 2014). In combination with chlorambucil, obinutuzumab has shown significantly improved PFS when compared to rituximab combination (Goede, *et al.*, 2014).

Daratumumab is a novel, high affinity, therapeutic human monoclonal antibody that has been raised against a unique CD38 epitope, noted for its ability to induce complement-dependent cytotoxicity in multiple myeloma cells. Recent studies have implicated its potential use in a variety of haematological malignancies, including CLL (de Weers, *et al.*, 2011).

1.4.2.1.2 Anti-CD19 monoclonal antibodies

In addition to their importance as a cell surface marker, CD19 monoclonal antibodies have been shown to be of potential benefit as a therapy. Several studies are on-going with the use of anti-CD19 as a potential therapy, including unconjugated antibody for the treatment of progressive B cell lymphoma, as an adjuvant therapy for the treatment of non-Hodgkin's lymphoma and as an antibody-drug conjugate for the

treatment of CD19+ B cell lymphoma. Additionally, BiTE®, a bi-specific T cell engaging antibody has been developed to direct cytotoxic T cells to B cells that are expressing CD19. BiTE® is currently being explored as a viable therapy option for CD19+ B cell malignancies by Amgen (Wang *et al.,* 2012). Additionally, the adoptive transfer of T cells engineered to express chimeric antigen receptor (CAR-T) targeting CD19 has recently emerged as a powerful targeted immunotherapy, which has shown complete remission responses in patients with relapsed/refractory ALL and remains an evolving landscape in the management of haematological malignancies (Maude *et al.*, 2015).

1.4.2.1.3 Anti-CD52 monoclonal antibodies

CD52 is targeted by alemtuzumab, and levels of CD52 have been proposed as a marker for minimal residual disease, and as such, a correlation between CD52 expression levels and the effect of alemtuzumab has been sought. CAMPATH-1, the precursor to alemtuzumab was initially created as a means of depleting mature T lymphocytes from bone marrow grafts in order to reduce the incidence of graft versus host disease (Hale *et al.*, 1983). CD52 is an excellent therapeutic target because of both its abundant surface expression and its apparent lack of regulation, and as such anti-CD52 therapy has been employed in the treatment of CLL (Lundin, *et al.*, 2002). In 2001, alemtuzumab attained initial FDA approval for B-CLL and full approval was attained in 2007. Under current National Comprehensive Cancer Network (NCCN) guidelines, alemtuzumab may be used as a single agent or in combination with rituximab for the treatment of CLL with *17p* deletion or in the case of relapsed/refractory cases (Wierda, *et al.*,

2017). The clinical trial that led to the subsequent approval of alemtuzumab, CAM 307, was an open-label, international, multicentre, randomised trial designed to demonstrate the longer progression-free duration with alemtuzumab than with chlorambucil, in patients with previously untreated CLL experiencing progression of their disease (Hillmen, *et al.*, 2007). The data showed that treatment with alemtuzumab led to an 88 day longer median progression-free survival than when compared to chlorambucil and a 42% longer time to disease progression or death. The overall response rate for alemtuzumab treatment was 83% and the complete response rate was 24% (Hillmen, *et al.*, 2007). Further trials identified that treatment with alemtuzumab resulted in an overall response rate rage between 31% and 54%, with complete response rates of 5%-35%. The median response rates ranged from between 7.7 months and 10 months in the case of progression-free survival, and 12 to 19.1 months in the case of overall survival (Warner & Arnason, 2012) (Schweighofer & Wendtner, 2010).

Overall, monotherapy with alemtuzumab has been shown to produce response rates of 33-53%, with a median duration of response ranging from 8.7 to 15.4 months in patients with advanced CLL who were previously treated with an alkylating agent. Additionally, it has shown to have proven effects in patients who have high-risk genetic markers such as *del(11q)* or *del(17p)*, and TP53 mutations; meaning that anti-CD52 monoclonal therapy may be a suitable treatment option for patients with poor prognostic features. However, intravenous transfusion of alemtuzumab was soon found to results in high rates of transfusion reactions including fevers, rigors, rash and nausea. As with other

chimeric antibodies such as CD20, alemtuzumab is associated with significantly increased risks for opportunistic infections, particularly the reactivation of cytomegalovirus (Vojdeman, *et al.*, 2017). Due to its observed potential as a treatment in the autoimmune disease, it was approved for the treatment of multiple sclerosis (Ruck *et al.,* 2015).

To date, little is known as to how alemtuzumab exerts its effects *in vivo*, though *in vitro* studies have demonstrated that anti-CD52 antibodies mediate CDC and ADCC (discussed further above). Additional *in vitro* studies have shown that CD52 exerts differing cytotoxic effects on either T cells or B cells. The ligation of CD52 with alemtuzumab and a secondary cross-linking antibody has been shown to lead to activation and proliferation of T cells *in vitro*, however the same has been shown to result in cell death and growth arrest in B cells *in vitro* (Rowan *et al.,* 1998) (Zent, *et al.*, 2004). Additionally, studies have been performed as to the possibility of cell death of CLL cells in the absence of ADCC or CDC, suggesting direct alemtuzumab-mediated killing in some studies (Mone, *et al.*, 2006)**.**

1.4.3 Nanotherapeutic approaches in haematological malignancies

Traditional approaches for the management and treatment of leukaemia's and lymphomas tend towards point of care diagnostics and therapeutics, often designed for a wide range of patients and disease stages (Friedman *et al.,* 2015). Many of these approaches have been developed as a result of the identification of biomarkers and molecular profiles generated from patients of the same disease profile and staging, as discussed earlier. This molecular characterisation of disease profiles has proven to be of great importance in the development and standardisation of chemotherapeutic protocols in clinical settings, and have allowed for the development of precision oncology, where treatment strategies and regimes can be tailored to individual patients or small subgroups of patients (Zaimy, *et al.*, 2017) (Vinhas *et al.,* 2017).

Nanoparticles have been used in the development of cancer biomarker probes (for example, quantum dots and gold nanoparticles) for several years now, but much work has been focused on the development of such nanoparticles for the treatment of these complex diseases (Allen & Cullis, 2004). One of the main obstacles in the successful treatment of haematological malignancies is the low therapeutic index of many anticancer drugs, their lack of specificity and the large volumes of distribution involved in treatment, in addition to the complexities of the tumour microenvironment. Additionally, many anti-cancer therapies infer a high dosage associated toxicity, nontargeted accumulation, fast elimination, poor solubility, and a short *in vivo* half-life. One strategy to circumvent the problem is the direct, targeted delivery of the therapeutic

agent directly to the tumour cells, using innovative drug delivery systems or drug conjugates (Allen & Cullis, 2004).

Among available nanotherapeutics, the most common formulations are liposomes and polymer-based nanoparticles. These nanoparticles can be modified in a number of different ways in order to desirably increase their *in vivo* properties, including increasing bioavailability and stability of the carrier. Table 1.2 below highlights a selection of some of the most commonly utilised nanotherapeutics in the treatment of haematological malignancies.

Table 1.2: Summary of the most commonly utilised nanotherapeutics in haematological malignancies. Adapted from Visani *et al.* 2014, Ventola *et al.* 2017.

System	Name	Characteristics	Bioactive compound	Indication
PEGylated liposome	Caelyx/Doxil (Scheringh-Plough, NJ, USA)	Biocompatible, amphiphilic; biodegradability; targeting potential; low toxicity	Doxorubicin	Multiple myeloma, lymphoma
Non-PEGylated liposome	Myocet (TEVA)	Biocompatible, amphiphilic; biodegradability; targeting potential; low toxicity	Cytarabine and daunorubicin	Lymphoma, AML and MDS
Liposomal carrier	Nanobins	Biocompatible, amphiphilic; biodegradability; targeting potential; low toxicity	Arsenic trioxide	Lymphoma
Micelle + pluronic block copolymer	SP1049C (Supratek Pharma)	Suitable carrier for water insoluble drugs; biocompatible, self-assembling, biodegradable; ease of functional modification; targeting potential	Doxorubicin	AML
Magnetic iron oxide nanoparticles	Fe_3O_4-MNP/DNR	Biocompatibility; superparamagnetic behaviour; chemical stability	Daunorubicin	AML

Liposomal formulations have been shown to provide substantial increases in anti-tumour efficacy when compared with free drug regimens (Bulbake *et al.,* 2017). This area is a growing area; however, the most common formulations of liposomes include the use of either doxorubicin (Doxil) or daunorubicin (Fe_3O_4-MNP/DNR), a chemotherapeutic commonly employed in the treatment of AML and ALL. One of the major advantages of using liposomal nanotherapeutics is their potential for reduced opsonisation, reduction in cardiotoxicity and an improvement in circulation time and drug accumulation (Bulbake *et al.,* 2017).

Whilst great strides have been achieved in the clinical development of liposomes for haematological malignancies, polymeric nanoparticles have demonstrated superior stability *in vivo* when compared to liposomes, have a high drug load capacity and have the ability for controlled and triggered release of drug (ud Din, *et al.*, 2017). Pluronic P85 are a commonly used polymeric nanotherapeutic that act to sensitise drug resistant tumours to several anti-cancer agents including doxorubicin and paclitaxel (Sharma, *et al.*, 2008). A polymeric micelle formulation of doxorubicin with Pluronic block copolymers, SP1049C, has been shown to generate high objective response rates and increased median survival and decreased the tumorigenicity and aggressiveness of cancer cells, reducing their colony formation ability and the frequency of cancer stem cells (Valle, *et al.*, 2011).

Iron oxide nanoparticles have been of considerable interest in the development of nanotherapeutics such as size, large surface area, magnetic capabilities and drug loading capacity. These nanoparticles

are FDA approved (e.g. Sienna+ or ferumoxytol and others), and given the naturally operating metabolic pathways of iron in the body increases their inherent biocompatibility. In addition to these inherent properties, these nanoparticles can be coated with a variety of materials, including polymers, other metals and a multitude of ligands (Revia & Zhang, 2016). Of particular interest is surface functionalisation of SPIONs using 3–aminopropyltriethoxysilane (APTES) due to the biological benefits over their bare counterparts, including biocompatibility, surface activity, stability and chemical simplicity (Ranmadugala *et al.,* 2017). Amino functionalisation can increase the chance of binding negatively charged SPIONs to the cell membrane, in addition to providing a suitable surface for the anchoring of ligands, such as antibodies (Ranmadugala *et al.,* 2017).

Over the last two decades, work in the development of both diagnostic and therapeutic SPIONs for use in haematological malignancies has been advancing. There has been a move towards the use of magnetite (Fe_3O_4) as opposed to maghemite (Fe_2O_3), the oxidised form, though both forms of iron oxide are found freely within the body and have been shown to display similar properties from a nanomedicinal perspective (Muzquiz-Ramos *et al.,* 2015). Many of these SPIONs received FDA approval a number of years ago as either an iron deficiency therapeutic or an imaging agent, including Feraheme®, Feradex® and Gastromark® (see Table 1.1).

SPIONs have also proven to be of particular use in the diagnosis and monitoring of leukaemia and lymphoma, as nanodiagnostic tools. Traditionally, these disease states are diagnosed and monitored using

one of, or a combination of, microarrays, flow cytometry, fluorescence *in situ* hybridisation, PCR and DNA sequencing. However, due to the often-aggressive nature of these cancer types, coupled with the low neoplastic cell numbers in the early stages of the disease, early and accurate detection of malignant cells is extremely important. A number of different metallic nanoparticle diagnostic strategies have been developed, with the goal of amplifying this signal and potentially increasing the chances of earlier disease detection, which are outlined below in Table 1.3.

Table 1.3: Summary of the available nanoparticles used in the diagnosis and monitoring of leukaemia and lymphoma. Adapted from Vinhas *et al*. 2017.

Nanoparticle	Tumour type	Target	Approach
Aptamer-conjugated Au-coated magnetic NPs	AML	PTK7	Aptamer (Sgc8) recognising PTK7 on graphene-nitrogen nanosheet electrode *in vitro* cells and in human blood plasma
Hollow core photonic crystal silver NPs	AML	Leukaemia cells	Portable monitoring of leukemic cells *in vitro*, using NPs for SERS
Aptamer-functionalized fluorescent silica NPs	ALL	PTK7	Sgc8-FSNPs specifically recognise leukemic cells via fluorescence *in vitro* and *in vivo*
Anti-CD20-polymeric NPs	CLL	CD20	*In vivo* imaging Cy5.5-labeled-probe for CD20-expressing tumours based on fluorescence intensity
PEG-coated SERS AuNPs	Malignant B-cells (leukaemia/lymphoma)	CD45, CD19 and CD20	Triplex spectra for SERS flow cytometry detecting anti-CD20 SERS probes in clinical samples (*ex vivo*)
Anti-CD20 antibody-conjugated MNPs	Lymphoma cells	CD20	CTC detection and isolation *in vitro* using SPIONs functionalised with anti-CD20

1.4.3.1 Recent advancements in novel nanotherapeutics for CLL

There have been very few recent advancements in the development of a novel nanotherapeutic for the treatment of CLL. Of those advancements, the majority focus on the use of antigen targeting, such as CD19 and CD20, with some exceptions. The use of gold nanoparticles impregnated with anti-VEGF antibodies were presented by Mukherjee *et al.* in 2007, where it was observed that the cytotoxic response to these gold-anti-VEGF nanoparticles was greater than when CLL cells were exposed to anti-VEGF alone, with gold nanoparticles displaying an insignificant induction of apoptosis in the CLL population tested (Mukherjee, *et al.*, 2007). In 2013, Yu *et al.* ascertained that anti-CD37 monoclonal antibody infused immunoliposomes can be successfully utilised as a targeted agent for CLL cells. A proof-of-concept B cell specific antibody (anti-CD19 or anti-CD20 monoclonal antibody) was combined with anti-CD37, and demonstrated increased delivery efficacy and apoptosis induction, when compared to that of the monoclonal antibodies alone (Yu, *et al.*, 2013) (Samir *et al.,* 2015)**.**

However, as of yet there remain limited studies demonstrating the use of nanotechnology towards the treatment of CLL. This niche in the market is one showing great promise, but likely hinges on the optimal understanding of both haematological malignancies and nanotechnology to develop the most optimal nanotherapeutic. These findings provide the rationale and the scope for the development of a targeted nanotherapeutic for the treatment of CLL.

1.5 Hypothesis

Based on the literature and state-of-the-art findings presented above, we hypothesise that the functionalisation of an iron oxide metallic nanoparticle with a therapeutic monoclonal antibody, anti-CD52, will result in increased interactions and subsequent toxicity in chronic lymphocytic leukaemia cells, when compared to an anti-CD52 antibody alone.

Within this thesis, we will show:

1. Characterisation of commercially-available Fe_2O_3 nanoparticles using a range of techniques including nanoparticle tracking analysis and scanning electron microscopy, in order to determine appropriate nanoparticle size.

2. Screening of cell surface markers to identify a suitable cell surface target on malignant B cells using a flow cytometric panel.

3. Functionalisation of Fe_2O_3 nanoparticles with a range of biologically-relevant monoclonal antibodies, and a purine analogue intended to interact with normal and malignant B lymphocytes; to identify the most appropriate functionalised nanoparticle in a novel approach for the treatment of CLL.

4. Investigation of the interaction and uptake of Fe_2O_3@CD52 nanoparticles by B lymphocytes, using qualitative and quantitative methods, to determine successful targeting.

5. Investigation of the potential toxicity and induction of apoptosis by Fe_2O_3@CD52 in both cell lines and patient-derived CLL cells.

6. Investigation of the interactions of the Fe_2O_3@CD52 nanoparticles with patient-derived CLL cells with an endothelial monolayer under physiologically relevant shear flow conditions, using a custom-built microfluidics system.

2. Materials and methods

2.1 Materials

50 nm superparamagnetic iron oxide nanoparticles were purchased from Sigma Aldrich (Sigma-Aldrich Ireland Ltd., Arklow, Ireland; Catalogue Number 544884). This nanoparticle was used as the core nanoparticle in all experimentation.

Cell culture media RPMI-1640, phosphate buffered saline and foetal bovine serum (FBS) and TrypLE was purchased from Gibco (Biosciences Ltd., Dublin, Ireland). Endothelial Cell Growth Medium 2 (Catalogue Number C-22011) and Accutase (Catalogue Number C-41310) were purchased from Promocell GmbH (PromoCell GmbH, Sickingenstrasse, Heidelberg, Germany).

Antibodies used in this study are detailed below in Table 2.1.

Table 2.1: List of antibodies used in this work. All antibodies in this list, and throughout this work, were sourced from Biolegend, UK, unless otherwise specified. This table also serves to highlight the role of each monoclonal antibody within this study.

Monoclonal antibody	Biolegend product code	Study purpose
anti-CD5 – AlexaFluor® 647	300616	Cell surface marker verification
anti-CD19 - AlexaFluor® 488	302219	Cell surface marker verification
anti-CD20– AlexaFluor® 488	302316	Cell surface marker verification
anti-CD52 (097) - AlexaFluor®647	338205	Cell surface marker verification/ uptake & interaction quantification
anti-CD52 (097) - FITC	338204	Fluorophore control
anti-CD52 (HI 186) - FITC	316003	Clonality control
anti-CD52 (097)	338201	Fluorophore control
Mouse IgM	401602	Isotype control

Normal blood samples were obtained from the Irish Blood Transfusion Service (National Blood Centre, St James Hospital, Dublin 8, Ireland)

following donation from consenting, healthy adults. All samples were handled with respect to the policies and practices of Good Research Practices as set out by the Irish Blood Transfusion Service and Trinity College Dublin.

The CLL cell line, I-83, was originally established in 1994 from the peripheral blood of a 75-year-old male presenting with chronic lymphocytic leukaemia and subjected to immortalisation by Epstein-Barr virus. The I-83 cell line is a suspension cell line and is also $CD19^+$, $CD20^+$ and $CD52^+$. Aliquoted vials of the I-83 cell lines were stored in 1mL aliquots at -80°C. The human umbilical vein endothelial cell (HUVEC) originates from the endothelium of the umbilical cord. HUVECs are an adherent, primary, endothelial cell type and exhibit a rapid proliferation rate. The human dermal lymphatic endothelial cell (HDLEC) originates from human dermal tissue and are an adherent, primary endothelial cell.

Primary CLL cells were obtained from the SJH/TCD Blood Cancer Biobank under the clinical direction of Prof. Elisabeth Vandenberghe, St. James' Hospital, Dublin 8, Ireland. In brief, CLL cells were isolated from peripheral blood following informed consent from patients presenting at clinic following a diagnosis of chronic lymphocytic leukaemia. Peripheral blood mononuclear cells (PBMCs) were isolated by Lymphoprep® density centrifugation and were cryopreserved in liquid nitrogen in 90% FCS + 10% DMSO until required. This study was approved by the Tallaght University Hospital/St. James' Hospital Joint Research Ethics Committee.

Diagnosis of CLL requires monoclonal B cells with a characteristic immunophenotype based on guidelines by the European Society of Medical Oncology, National Comprehensive Cancer Network and International Workshop on Chronic Lymphocytic Leukaemia (Eichhorst , *et al.*, 2015) (Hallek, *et al.*, 2008). The Immunophenotyping Laboratory of St. James's hospital performed flow cytometric analysis on CLL samples. Whole Blood staining of fresh CLL samples for flow cytometry was performed by Mr. David O'Brien and the Immunophenotyping Laboratory, Department of Haematology, St. James's Hospital as described in section 24.2. IGHV mutational status was performed by the Cancer Molecular Diagnostics, St. James's Hospital. Clinical assessment and information were supplied by Prof. Elisabeth Vandenberghe. Samples were processed and stained by whole-blood staining and the following characteristics of the B cell population are indicative of CLL: CD200 positive, IgM weak to negative expression, FMC7 negative, CD20 weak, CD10 negative, CD22 weak, CD23 positive and CD79b negative expression. The clinical characteristics, IGHV mutational status, CD38 and CD49d expression, NOTCH1 mutational status, cytogenetics (del13q, trisomy 12, del11q, and del17p), Binet stage and bulky disease state for the patient cohort used in this study are shown in Table 2.2. Patients were either untreated for CLL or had not undergone treatment in the previous 2 years. No patients were previously treated with antiCD52 therapeutics. A description of investigations performed on each CLL patient samples used within this study can be found in Table 2.3.

Table 2.2: Details of the clinical characteristics of CLL patient samples used within this study.

CLL Number	Male/Female (M/F)	Binet Stage	WBC (10⁹/L)	CD19+	CD19+/CD5+	IGVH Mutation %	IGVH M/UM	NOTCH1	Flow cytometry markers CD38	Flow cytometry markers CD49d	Cytogenetics Del13q	Cytogenetics Trisomy 12	Cytogenetics Del11q	Cytogenetics Del17p
1	F	C	74.7	97	97	99.5	UM	M	N	N	N	N	N	N
2	M	C	387	93	100	100	UM	UM	P	N	P	N	P	N
3	M	B	37.6	98	100	94	M	UM	N	N	P	N	N	N
4	F	A	58.3	94	100	94.17	M	M	N	ND	P	N	N	N
5	M	A	63.4	95	96	100	UM	UM	P	P	N	N	N	N
6	F	A	NA	92	58	100	UM	UM	N	N	P	N	N	N
7	M	A	183.5	97	94	ND	ND	UM	N	P	N	N	P	N
8	F	A	28.1	97	96	99.51	UM	UM	N	P	N	N	N	P
9	F	A	103.7	96	51	ND	ND	ND	ND	N	ND	ND	ND	ND
10	F	A	50.1	92	98	100	UM	M	N	ND	N	N	N	N
11	M	B	47.9	93	97	100	UM	M	P	ND	N	N	P	N
12	M	C	138.6	97	99	95.79	M	UM	N	P	ND	ND	ND	ND
13	F	B	34	97	99	100	UM	M	P	P	N	N	N	P
14	M	C	141.7	97	100	100	UM	M	P	ND	P	N	N	N
15	F	A	33.1	95	98	92	M	UM	N	ND	P	N	P	N
16	M	C	19.9	61	98	100	UM	M	P	P	N	N	N	N
17	M	B	171	97	99	99.5	UM	UM	P	ND	N	N	P	N

NA, not available; ND, not defined; M, mutated; UM, unmutated; P, positive; N, negative

71

Table 2.3: Details a quick reference guide as to the chronic lymphocytic leukaemia patient sample used in each experiment within this study.

CLL Number	Quick guide to sample use within this study					
	Toxicity testing	Surface marker profile	Shear flow	Confocal microscopy	Uptake studies	HIM
1	x	x	x	x	x	x
2	x	x	x			
3		x	x	x		x
4	x	x		x	x	x
5	x	x				
6	x	x				
7	x	x	x			
8	x	x		x		x
9	x	x		x	x	x
10	x	x				
11	x	x				
12	x					
13	x					
14	x			x		x
15	x		x			
16			x			
17	x					

2.2 Methods

2.2.1 Nanoparticle functionalisation

Fe_2O_3 nanoparticles were selected as the most appropriate core nanoparticle carrier for use in this study, for reasons extensively discussed in the introduction. These nanoparticles were previously size-determined to be of 50nm in diameter using Brunauer, Emmett and Teller (BET) Theory by the manufacturer, Sigma Aldrich. The 50nm nanoparticles were functionalised with a range of stabilising agents and antibodies, including anti-CD19, anti-CD20 and anti-CD52, and the chemotherapeutic agent fludarabine through the formation of amide bonds using (3-Aminopropyl)triethoxysilane (APTES, Sigma Aldrich Catalogue Number 440140) and 1-Ethyl-3-(3-dimethylaminopropyl) carbodiimide (EDC, Sigma Aldrich Catalogue Number E6383) coupling. Successful functionalisation was determined using flow cytometric analysis measuring the shift in fluorescence of fluorophore conjugated to each antibody (with successful functionalisation being determined at >95% functionalisation). A similar method was employed in order to determine stability of functionalisation of each nanoparticle. Briefly, the samples were washed thrice in PBS before being re-suspended once again in PBS. An aliquot of each sample was taken and the shift in fluorescence as read by flow cytometry was compared against bare, non-functionalised nanoparticles. Nanoparticle samples showing a > 95% fluorescent shift were considered successfully functionalised and stable. This process was repeated on each sample up to a period of one month, where stability studies ceased. All samples were analysed in this fashion prior to use.

73

2.2.1.1 Preparation of amino-terminated silanised nanoparticles (Fe$_2$O$_3$ @ APTES)

APTES (10µL, 99%) and ammonium (10µL, ≥99%) were each added to 900µL of isopropanol, prepared immediately prior to use. Amine functional groups were introduced on to the surface of stock nanoparticles (500µl, 1mg/mL) by the addition of above APTES solution (500µL). Stock nanoparticles were allowed to react with APTES solution for 24 hours at 4°C and subsequently washed thrice through magnetic separation in dPBS and finally dispersed in dPBS by sonication. Magnetic separation was performed by applying a uniform magnet to the surface of one side of the microfuge tube, and gently running the silanised nanoparticles suspension across this magnetic field. This resulted in the capture of the nanoparticle to the side of the tube, allowing for the gentle removal of the supernatant using a pipette. Once the supernatant had been removed, the captured nanoparticles were again dispersed in 500µL of dPBS, and the process repeated (Zhou, Bai, & Wang, 2017). Sonication for silanisation was performed for 10 minutes within a sonicated water bath. Fe$_2$O$_3$@ APTES nanoparticles were then stored at 4°C until use (≤48 hours in all cases).

2.2.1.2 Preparation of antibody functionalised nanoparticles using APTES and EDC coupling (Fe$_2$O$_3$@CD19/CD20/CD52)

Fe$_2$O$_3$ @ APTES (see above, 2.1.2) were subsequently conjugated to antibodies mentioned in above Table 2.1. The method employed for said conjugation was the same for each antibody. Following surface modification using APTES, Fe$_2$O$_3$ @ APTES nanoparticle suspension

and antibody (50μL, 2mg/mL) were pre-activated with EDC (500μL, 1mg/mL) for 20 minutes at room temperature with gentle mixing. The suspension was then incubated overnight at 4°C, again with gentle mixing. The suspension was then washed thrice using dPBS using magnetic separation (as discussed above in Section 2.2.1.1) and stored at 4°C until required.

Double functionalisation of Fe_2O_3 nanoparticles was also performed in order to determine if the addition of a second targeted monoclonal antibody may result in increased efficacy though these nanoparticles are far more difficult to characterise. This is due to the difficulty in quantifying and distinguishing the surface antibodies, and therefore distinguishing the antibody to which the efficacy may be attributed. Briefly, anti-CD19 and anti-CD52 were simultaneously conjugated to the surface of silanised nanoparticles Fe_2O_3 @ APTES (see above, 2.2.1.1) using EDC cross-linker techniques discussed above, with a total antibody volume of 50μL at a ratio of 1:1 (25μL of 2μg/mL of each antibody used).

Fe_2O_3 nanoparticles functionalised with a range of control antibodies for use in uptake measurement studies were also prepared, in the same manner as above. These antibodies are described in Table 2.1 above and include an isotype control of Mouse IgM; anti-CD52 monoclonal antibody of clone 097, with either FITC, AlexaFluor647 or no fluorophore as fluorophore controls; and anti-CD52 of clone HI 186 as a clonality control.

2.2.1.3 Preparation of fludarabine functionalised nanoparticles (Fe$_2$O$_3$ @ fludarabine)

Fe$_2$O$_3$ @ APTES (as described above, 2.2.1.1) were electrostatically coupled to fludarabine through adsorption on to the surface of nanoparticles (Wang, Hu, & Xiang, 2016). For this process, a suspension of Fe$_2$O$_3$ @ APTES was sonicated for 10 minutes to ensure dispersion of nanoparticles. To this an equal volume of 5mM fludarabine was added and the suspension subsequently incubated at 37°C overnight. Following incubation, Fe$_2$O$_3$ @ fludarabine were then washed thrice as mentioned above using dPBS and stored at 4°C until use (electrostatically-couple nanoparticles were not stored for any longer than 24 hours as stability was undetermined). Immediately prior to use, nanoparticles were again washed using magnetic separation with dPBS (as presented in section, 2.2.1.1).

2.2.1.4 Preparation of fludarabine - antibody functionalised nanoparticles using APTES and EDC coupling (Fe$_2$O$_3$ @ fludarabine – CD19/CD20/CD52)

Fe$_2$O$_3$@ CD19/CD20/CD52 were electrostatically coupled to fludarabine through adsorption on to the surface of the functionalised nanoparticles (Wang *et al.,* 2016). In brief, the suspension of Fe$_2$O$_3$@ CD19/CD20/CD52 nanoparticles were washed through magnetic separation (section 2.2.1.2). Nanoparticles were then re-suspended in a 5mM solution of fludarabine (Sigma Aldrich, Catalogue Number F9813) and subsequently incubated at 37°C overnight (section 2.2.1.3). Following incubation, Fe$_2$O$_3$@fludarabine – CD19/CD20/CD52 were

washed thrice as before using magnetic separation and dPBS and stored at 4°C until use (section 2.2.1.2).

2.2.1.5 Preparation of fluorescent pH sensitive doped Fe_2O_3 nanoparticles (Fe_2O_3@ STP ester)

A solution of 0.5mM amine-reactive pH sensitive green STP ester dye (pHRodo Green STP Ester, Life Technologies, Catalogue Number P35369) was prepared in dH_2O. Previously silanised nanoparticles (1mg/mL; Fe_2O_3@ APTES, see above 2.1.2) were washed three times using magnetic separation and dPBS and re-suspended in 0.5mM amine-reactive pH sensitive green STP ester dye to a total volume of 500µL. This suspension was incubated for 1 hour at room temperature, protected from light. Following this, the pH sensitive doped nanoparticles were washed three times in dH_2O to ensure complete removal of any excess dye. These doped nanoparticles remain stable, stored at 4°C, protected from light, until use (no more than 24 hours).

As above, in order to prepare antibody coupled fluorescent pH sensitive-doped Fe_2O_3 nanoparticles (Fe_2O_3 @STP ester – CD19/CD20/CD52), solution of 0.5mM amine-reactive pH sensitive green STP ester dye (pHRodo Green STP Ester, Life Technologies, Catalogue Number P35369) was prepared using dH_2O. Previously functionalised nanoparticles (Fe_2O_3@ CD19/CD20/CD52, see above 2.2.1.2) were washed three times using magnetic separation and dPBS and re-suspended in 0.5mM amine-reactive pH sensitive green STP ester dye to a total volume of 500µL. This suspension was incubated for 1 hour at room temperature, protected from light. Following this, the pH sensitive

77

doped nanoparticles were washed three times in dH2O to ensure complete removal of any excess dye. These doped nanoparticles remain stable, stored at 4°C, protected from light, until use (no more than 24 hours).

For a complete list of each antibody used throughout these functionalisation reactions and the rationale for their selection, please see Table 2.1.

2.3 Nanoparticle characterisation

Several nanoparticle candidates have been identified as potential carriers for antibody coupling or drug loading, as mentioned in the introduction. Nanoparticle characterisation was carried out for fingerprinting of the prepared nanoparticle. Nanoparticles, due to their inherent shape, are suitable for both dry and liquid characterisation techniques covered here - Nanoparticle Tracking Analysis and Scanning Electron Microscopy. Other nanomaterials, such as rods or wires, are not suitable for Nanoparticle Tracking Analysis due to their shape and subsequent light scattering properties, and so depend upon more traditional techniques such as Scanning Electron Microscopy.

2.3.1 Nanoparticle Tracking Analysis

Nanoparticles, both non-functionalised and functionalised, were characterised using Nanoparticle Tracking Analysis (NTA), a system developed by Nanosight Malvern Ltd. First commercialised in 2006, this is a technology which is rapidly becoming commonly utilised in the characterisation of materials in the 20nm – 2000nm size range, popular in the studies of nanomaterials, exosome and protein aggregation

studies (Filipe, Hal, & Jiskoot, 2010). NTA is a technology that obtains individual particle size distribution of samples in suspension through the combination of light scattering and Brownian motion. The technology functions through the passing of a laser beam through a prism-edged glass sheet which is housed within the sample chamber. The wavelength of laser beam used in NTA is not of critical importance, but is often one of either 405 nm, 488 nm, 532 nm or 635 nm. The angle and refractive index of this glass sheet is designed such that upon convergence of the laser with both the glass sheet and the liquid sample layer above, the laser beam is refracted. Any particles that are contained within the path of this beam then scatter light which is easily visualised using the mounted optical microscope configured with a 20x microscope objective and recorded using a mounted camera, recording 30 frames per second, within a predefined field of view. Brownian motion is the random movement of particles within a liquid suspension and can be captured and recorded using the NTA software which calculates, using the Stokes-Einstein equation where sample temperature and solvent viscosity are known, the hydrodynamic diameter of the particles in suspension. From these calculations, the NTA software can then calculate the diffusion coefficient of the particles. Unlike many other techniques, including the commonly used DLS approach, NTA is not biased towards larger particles or aggregates in suspension. This is as a result of the mechanism of tracking employed by the software works to measure individual particles, resulting in other peaks potentially being present within the resultant data sets, which may go undetected using other traditional measurement techniques (Hole, *et al.,* 2013).

The nanoparticles analysed using this method were previously measured by the manufacturer (Sigma Aldrich) using the Brunauer-Emmett-Teller theory (BET), a technique which allows for the specific measurement of the surface area of a material using the physical adsorption of gas molecules on a solid surface (Zhu, *et al.*, 2011). NTA was carried out using a NS500 system which has been equipped with a 405nm laser. The system utilises NTA software version 3.1. All particles were dispersed in 100nm filtered ultrapure water. Six 60 second videos were recorded with 200 completed tracks per video for statistical significance, with each video capturing between 20-100 nanoparticle per frame. This procedure has been developed during multiple rounds of interlaboratory comparison studies with Nanosight Ltd. and twelve other European and US research institutes and centres. (Hole, *et al.*, 2013) Finite track length adjustment was incorporated into analysis to improve upon resolution and accuracy of the size distribution profiles.

Figure 2.1: **The Malvern NS500-NTA system, which tracks and records the movement of nanoparticles under Brownian motion and subsequently calculates the mean and mode particle size, generates particle size distribution**

graphs and calculates nanoparticle per ml concentrations. Image of Malvern NS500-NTA available at Malvern.com, accessed 2017.

Nanoparticles were diluted in ultrapure water to a concentration of 1µg/mL and vortexed to disperse. The sample was then attached to the sample inlet pump and the fluidics system then loads the sample into the chamber within the machine. Once the appropriate focus level has been selected and recording the required number of videos, the software will then analyse the videos and tracks the movement of each nanoparticle on screen.

2.3.2 Scanning Electron Microscopy

In order to be adequately prepared and proficient at performing electron microscopy, full training (basic and advanced) and provision of educational materials was provided by the Advanced Microscopy Laboratory, CRANN, TCD. As part of this training, and to ensure competency in more than standard spherical nanoparticles, 3nm, 13nm and 35nm silver nanowires were prepared at a working concentration (1µg/mL) in isopropanol. 100µl of this suspension was dropped onto a borosilicate glass coverslip (Fisher Scientific, Ireland), allowed to air dry and mounted onto a standard 13um SEM imaging stub (Agar Scientific, product code: AGG301-S-50) using a carbon tab (Agar Scientific, product code: AGG3111). Samples of Fe_2O_3@APTES nanoparticles were prepared identically. Fe_2O_3@APTES nanoparticles are a more suitable candidate for scanning electron microscopy in this instance as they may be imaged without a sputter-coat (further discussed in Chapter 1), allowing for visualisation of the actual nanoparticles). To prevent overcharging of the samples, conductive silver paint (Agar Scientific,

Product code: AG16062-15) was applied from the outer rim of the sample on the borosilicate coverslip down to the surface of the sample stub. All samples were imaged using the Carl Zeiss Ultra at a working distance of 3.1mm and an acceleration voltage of 1 kV. Nanowire dimensions were measured using Carl Zeiss Ultra profile overlay. Measurements were repeated a minimum of 6 times for each sample for statistical significance. A detailed description of the use of SEM in nanoparticle characterisation can be found in Section 3.1.

2.3.3 Dynamic Light Scattering

Dynamic light scattering (DLS) is a technique that has been employed for many years for the study of nanoparticle size and stability. This method of characterisation has benefits over electron microscopy techniques in that it measures the size of the nanoparticles in suspension, providing a more accurate representation of the size and stability potential of these nanoparticles when used in *in vitro* studies. DLS, also known as Quasi-Electric Light Scattering (QELS), is a frequently used and cost-effective means of measuring the scattering of light of particles moving under Brownian motion, by recording the fluctuations in these parameters. DLS originates from a combination of the proposed theories of light scattering; Brownian motion; and stochastic process and density fluctuations, put forward by Lord Rayleigh, Albert Einstein and Marian Smoluchowski, respectively (Cichocki, Ekiel-Jezewska, & Wajnryb, 2015). The first experimentation employing the properties of dynamic light scattering began in the 1960s, and these led to the implementation of DLS as well-established characterisation and measurement process (Stetefeld, McKenna, &

Patel, 2016). The mode of action of DLS in the characterisation of nanoparticles is such that particles are suspended in a suitable measurement medium, where a monochromatic light source is directed through the sample, resulting in this light becoming scattered at differing intensities and directions, as a function of time. This light scattering is directed correlated to the size distribution of the particles undergoing analysis and using the DLS software the size of the particles in suspension can then be calculated. However, in some cases, the interpretation of the results from DLS can be ambiguous as the analysis in DLS is weighted more towards larger particle size, meaning that nanoparticle aggregates in suspension will also be integrated into size averaging, and result in inaccurate size determination. Additionally, DLS is unable to detect subtle differences in size between nanoparticles (Fissan, Ristig, Kaminski, Asbach, & Epple, 2014) (Pecora, 2000). Similar to the analysis performed by the Nanosight NS500, DLS yields a hydrodynamic radius calculated via the Stoke-Einstein equation from the measurements taken (Murdock, Braydich-Stolle, Schrand, Schlager, & Hussain, 2008).

DLS was carried out using the Malvern Zetasizer Nano ZS instrument, utilising software version 7.1. The zetasizer utilises a laser which is passed through the sample and in turn measures the velocity of the particles in an electric field. Samples were prepared in a similar fashion utilised for NTA measurements (see 2.3.1). Dilutions of Fe_2O_3@APTES (100µg/mL, 10µg/mL, 1µg/mL) in Dulbecco's Modified Eagle Medium at pH7.4. The samples were then vortexed to disperse nanoparticles within the solution and sonicated immediately before use. Prior to analysis of

nanoparticle samples, 1.5mL of Dulbecco's Modified Eagle Medium was loaded into a glass cuvette and data was collected by the system in order to establish a baseline measurement. 1.5mL of each sample was then transferred to a cuvette prior to analysis. For sample analysis, when prompted, each sample cuvette was loaded into the cuvette holder within the machine and once the correct working temperature had been reached (detected by Zetasizer), the samples were read for dispersity index, size and concentration using the pre-set Fe_2O_3 Standard Operation Procedure (SOP). This SOP is based on automated detection of the backscattering of the light source through the selected cuvette. The software then generates a detailed report of analysis for your sample.

2.4 Biological investigations of nanoparticles

2.4.1 Ethical approval

Ethical approval was obtained from the Research Ethics Committee of the School of Medicine, Trinity College Dublin. Normal B lymphocytes were isolated from surplus blood donations obtained from healthy donors presenting at the Irish Blood Transfusion Service. All samples were collected and processed for research purposes in accordance with ethical and legislative guidelines, following informed patient consent. Primary CLL cells were isolated from a patient cohort presenting at clinic for treatment of chronic lymphocytic leukaemia, following full ethical and legislative guidelines and informed patient consent. CLL patient characteristics are further described in Section 2.1.

2.4.2 Cell Culture

Chronic Lymphocytic Leukaemia – like cell line I-83, was cultured using RPMI-1640 (supplemented with 2nM L-glutamine, 10% FBS and 1% 5,000U/mL penicillin/streptomycin, Gibco, Thermo Fisher Scientific). Cells were incubated at 37°C in a humidified atmosphere with 5% CO_2. Passages were restricted to between 6 and 12 throughout the study. Upon reaching 80% confluency (approximately every 48 hours), the contents of the flask were transferred to a 30mL sterile tube, cells pelleted using centrifugation at 1200Xg for 10 minutes. The cell pellet was then re-suspended in 5mLs with 1mL of this suspension being transferred to a new tissue culture flask containing 24mLs fresh RPMI-1640 (supplemented with 2nM L-glutamine, 10% fetal bovine serum and 1% 5,000U/mL penicillin/streptomycin), warmed to 37°C prior to use.

Peripheral blood mononuclear cells (PBMCs) were isolated using density centrifugation. Briefly, the acquired buffy coat (50mL) was diluted with 50mL dPBS and gently mixed. 20mL Lymphoprep (StemCell Technologies, Catalogue Number 07851) was added to each of 4 50mL centrifuge tubes and the diluted buffy coat was gently layered on top of the Lymphoprep, ensuring no mixing of the layers occurs. Tubes were then centrifuged for 20 minutes at 19°C, 1200 x g, with no brake to ensure careful and undisturbed separation of the buffy coat. PBMCs were collected using a Pasteur pipette, transferred to two 30mL tubes and re-suspended to 25mLs using dPBS. The cell suspension was then washed twice for 5 minutes at 600 x g, room temperature, using dPBS. 5mLs 1 x red blood cell lysis buffer (Biolegend, UK, Catalogue Number 420301) was added to each tube and allowed to stand for approximately 5 minutes, with the purpose to lyse any remaining red blood cells. Cells were then washed twice in 10mLs dPBS and the final cell pellets were re-suspended in 5mLs of supplemented RPMI-1640 medium (supplemented with 2nM L-glutamine, 10% fetal bovine serum and 1% 5,000U/mL penicillin/streptomycin). In order to remove monocytes and macrophages from isolated cell suspension, the cell suspension was added to a large cell culture flask containing 30mLs supplemented RMPI-1640 (as above) and incubated at 37°C, 5% CO_2 for 2 hours in order to allow any adherent cells to adhere to the flask. After 2 hours, the flask was gently rocked by hand to remove any adhered B and T cells from the adherent layer of monocytes and macrophages and the contents of the flask in suspension were transferred to a fresh large tissue culture flask and the washing step repeated once again, for 2

hours. Following this incubation, the suspension cells were removed from the flask, cells were collected by centrifugation at 1200X g for 5 minutes for further use.

B cells were isolated from the PBMC population using Miltenyi Biotech MACS B Cell Isolation Kit II, human (Miltenyi Biotech, product number 130-091-151). Following isolation of PBMCs, the cells are were counted and re-suspended in $40\mu L/10^7$ cells of cell separation buffer (freshly prepared dPBS supplemented with 0.5% BSA bovine serum albumin and 2mM EDTA). To this, $10\mu L$ of the biotin-antibody cocktail/10^7 was added, mixed well and incubated at 4°C for 5 minutes. $30\mu L/10^7$ cells buffer was then added in addition to $20\mu L/10^7$ cells anti-biotin microbeads, with the sample then being mixed well and again incubated at 4°C. For magnetic separation, the MACs MS column (Miltenyi Biotech, product number: 130-042-201) was mounted to the VarioMACS™ Separator and prepared for use by washing with 500μL of sample buffer. Following this, the labelled cells were then applied into the column, and flow-through containing unlabelled B cells were collected. The column was then washed three times using sample buffer, to ensure all flow through B cells have been collected.

Cryopreserved samples were rapidly thawed at 37°C, resuspended in RPMI media containing 10% FBS and incubated at ~ $1x10^7$ cells/mL for at least 1 hour, to allow cells to recover prior to use. CLL cell selection was performed on samples that were <90% CD19 positive as identified by immunophenotyping (Table 2.2). Selection was performed using EasySep™ Human B Cell Enrichment Kit without CD43 Depletion (Stemcell Technologies, product code: 19154). After isolation of

PBMCs, cells were counted and re-suspended in the recommended buffer (PBS, 1mM EDTA, 2% FBS) at a concentration of 5×10^7 cells/ml. 50μl of selection cocktail was added per ml of sample and incubated at room temperature for 10 minutes. 50μl of magnetic particles was added per ml of sample and incubated at room temperature for ten minutes. The required volume of buffer was added to a final volume of 2.5ml and the tube was incubated in the EasySep Magnet (Stemcell Technologies, product code: 18000) for 5 minutes. The enriched cells were poured into a new tube by inverting the magnet and 2.5ml of buffer was added to the tube. The remaining cells were added to the new tube. Cells were stained with CD19 antibodies and purity was confirmed using flow cytometry on an aliquot of enriched cells.

Unless otherwise specified, CLL patient samples, the I-83 cell line and normal B cells were each cultured using RMPI-1640 supplemented with 2nM L-glutamine, 10% fetal bovine serum and 1% 5,000U/mL penicillin/streptomycin.

Human Umbilical Vein Endothelial Cells (HUVECs) and Human Dermal Lymphatic Endothelial Cells (HDLECs) were cultured using Endothelial Growth Medium II (PromoCell, Catalogue Number C-22011), supplemented with Endothelial Cell Growth Supplement (0.02mL/mL FBS, 5ng/mL epidermal growth factor, 10ng/mL basic fibroblast growth factor, 20ng/mL insulin-like growth factor, 0.5ng/mL vascular endothelial growth factor 165, 1μg/mL ascorbic acid, 22.5μg/mL heparin, 0.2μg/mL hydrocortisone; PromoCell, product code C-39216). Cells were incubated at 37°C and 5% CO_2. Passages were restricted to 6 throughout the study. Upon reaching 80% confluency (approximately

every 48/72 hours for each of HUVEC and HDLEC, respectively), the contents of the flask were detached from the flask, transferred to a 30mL sterile tube, cells pelleted using centrifugation at 1200xg for 10 minutes. The cell pellet was then re-suspended in 5mLs with 2.5mL of this suspension being transferred to a new tissue culture flask containing 22.5mLs of fresh Endothelial Growth Medium II, warmed to 37°C prior to use.

Mycoplasma and phenotypic responses were checked regularly for contamination as part of the laboratory GLP using MycoProbe® Mycoplasma Detection Kit (R & D Systems, product code: CUL001B).

2.4.3 Whole Blood Flow Cytometry Diagnostic Panel

Whole Blood Flow cytometry was performed by the Immunophenotyping Laboratory, St. James's Hospital. This method allows the staining of leukocytes from fresh, whole blood. 5 15ml Falcon tubes were labelled and antibody mixes were prepared as per Table 2.4. The peripheral blood was diluted to 2×10^6 cells/ml in CellWASH (BD, Switzerland) and 100µl of whole blood was added to each tube. Tubes were placed in a BD FACS Sample Prep Assistant III and cells were washed by adding 2ml of CellWASH was added to tubes 1 and 2 from Table 2.4 (IgM, kappa/lambda) and vortexed and centrifuged. The supernatant was removed, and this was repeated twice more. The appropriate monoclonal antibodies were added to each individual tube and cells were vortexed and incubated at room temperature in the dark for 5 minutes. Tubes were then placed in the BD FACS Lyse Wash Assistant and 2ml of Pharm Lyse (10X buffered ammonium chloride diluted 1:10

with distilled water) (BD, Switzerland) was added to each tube, vortexed and incubated, in the dark at room temperature for 15 min. 1ml of CellWASH was added to the tubes and they were vortexed and centrifuged to remove lysed antibody and unbound Fluorochrome. The supernatant was removed, and cells were re-suspended in 0.5ml CellWASH before running on the BD FACS Canto II flow cytometer (BD, Switzerland).

Table 2.4: Chronic B Lymphoproliferative flow cytometry panel

Tube	Antibody	Fluorochrome	Volume (µl)
1	CD5 FITC	FITC	20
	CD3 PE	PE	20
	CD19 PerCP-Cy5.5	PerCP-Cy5.5	20
	CD45 APC-H7	APC-H7	5
2	Kappa /Lambda	FITC/PE	20
	CD19	PerCP-Cy5.5	20
	CD38	APC	5
3	CD43	FITC	20
	CD200	PE	20
	CD19	PerCP-Cy5.5	20
	IgM	APC	20
4	FMC7	FITC	20
	CD20	PE	20
	CD19	PerCP-Cy5.5	20
	CD10	APC	5
5	CD22	FITC	20
	CD23	PE	20
	CD19	PerCP-Cy5.5	20
	CD79b	APC	20

2.4.4 Determination of appropriate cell surface marker for targeting of nanoparticles.

Normal B lymphocytes and malignant B lymphocytes were isolated from patient blood samples as previously described in section 2.4.1. The I-83 cell line was maintained as described above. Cells were counted and subsequently seeded at a density of 1×10^5 cells/well in a 96 well plate. Each well containing cells were incubated with 5µL of one of either CD5-

AlexaFluor 633, CD19 – AlexaFluor 488, CD20 – AlexaFluor 488 and
CD52 – AlexaFluor 633 (all antibody products sourced from BioLegend,
UK). Each cell suspension was allowed to stain at room temperature,
protected from light for 30 minutes prior to flow cytometric analysis.

2.4.4.1 Gating strategy

For all surface molecule flow cytometry experiments, cells were gated
on single, live cells, excluding cell debris and cell doublets (if present).
This was performed using the BD Accuri C6 flow cytometry. First,
forward scatter – side scatter analysis of the unstained population, three
samples of which were analysed for each surface marker stained. Each
surface marker was stained for individually and gated for in a similar
fashion. Upon selecting the correct population for flow cytometric
analysis, this population (referred to as P1, below Figure 2.2) was used
for further analysis and to observe any fluorescent shifts within the cell
population. An example of the gating population used can be seen
below in Figure 2.2.

Further flow cytometric analysis gating strategies throughout this body
of work were performed in an identical manner, using live gating for
single cells on CD19+ population.
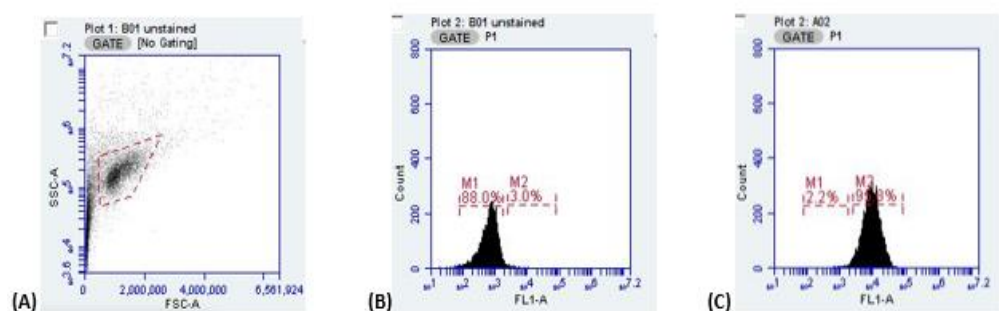
**Figure 2.2: Gating strategy undertaken for flow cytometric analysis within this
thesis**. All cells were gated for on the single cell, CD19+ population. Figure panel (A)
shows the unstained live CLL cell population as gated using forward scatter vs. side
scatter. Figure panel (B) shows the unstained count vs. FL1 (fluorescent channel for
CD19) of the selected P1 population. Figure panel (C) shows count vs. FL1 of the
stained population, and the shift in positive populations from the M1 to the M2 gating.

2.4.5 Determination of successful functionalisation of Fe$_2$O$_3$ with anti-CD52 antibody and theoretical loading of antibody to nanoparticles

Following functionalisation procedure of nanoparticles (see above 2.2), it is necessary prior to use to ensure successful functionalisation of the nanoparticles. Briefly, each sample was washed three times following the functionalisation reaction and re-suspended in dPBS. 10µL of 1mg/mL functionalised nanoparticles was then taken and added to 1.5mL of dPBS in an amber microcentrifuge tube (allowing protection from light degradation) resulting in a considerable dilution. The anti-CD52 antibody chosen for functionalisation studies and subsequent toxicity testing was anti-CD52 AlexaFluor® 647. Using the BD Accuri C6, the software was set to read forward scatter on the Y-axis versus 'FL3' (corresponding to the filter set required for analysis of fluorophores in the far-red region of the spectrum), with samples analysed for 10,000 events. Gating was set on the scatter of the bare, non-functionalised nanoparticles and subsequent shifts in this scatter are then quantifiable upon loading of the functionalised nanoparticle sample. Samples with a functionalisation (corresponding to a shift in the fluorescent scatter) of greater than 95% were considered successfully functionalised.

For further toxicity and characterisation experiments, a control of free anti-CD52 antibody was incorporated into each study. This control aims to replicate the use of monoclonal antibody therapy utilising anti-CD52.

The concentration chosen for these control studies was 10µg/mL, a concentration commonly used in similar studies as found in previous literature studies (Nuckel *et al.,* 2005). For the covalent linkage of this monoclonal antibody to the surface of Fe_2O_3, the theoretical loading yield was calculated, by calculating the quantity of antibody used in these reactions, relative to the concentration of the antibody used. The potential maximum amount of anti-CD52 antibody present at each concentration of Fe_2O_3@CD52 nanoparticle suspension, as calculated based on the amount of anti-CD52 used in each functionalisation reaction, as shown in Table 2.5.

Table 2.5: Shows the maximum binding potential of anti-CD52 antibody to the surface of Fe_2O_3 nanoparticles as calculated using the amount of anti-CD52 used in each functionalisation reaction.

Fe_2O_3 @ CD52 concentration	Amount of anti-CD52 antibody present
200µg/mL	0.5µg/mL
100µg/mL	0.25µg/mL
50µg/mL	0.125µg/mL
25µg/mL	0.06µg/mL

2.4.6 Measuring the interaction and uptake of nanoparticles by CLL cell line, I-83, and patient derived malignant B CLL cells and normal B cells.

Interaction with the cell surface, internalisation, trafficking and transport of nanoparticles is a vital part of nanomedicinal research and there are a variety of methods to investigate such events. Uptake measurements and quantification of nanoparticle interaction and internalisation was performed utilising two techniques. Qualitative measurement of cell-nanoparticle interactions and uptake was performed using laser scanning confocal microscopy. Quantitative measurements were

obtained by doping nanoparticles with a fluorescent pH sensitive dye (see 2.2.1). As these doped nanoparticles become associated with the cell membrane and become internalised, and the pH of the environment begins to drop, the dye will fluoresce more brightly. This drop in pH can be attributed to the position within the cell. For example, the pH of the buffered cell media is pH7.4, the pH of the cell membrane and intracellular pH dropping to approximately pH6-6.8 due to the internal production of acids (Maouyo *et al.,* 2000).

2.4.7 Preparation of poly L-lysine coated borosilicate glass coverslips.

Poly L-lysine (Sigma Aldrich) coated coverslips were prepared on the day of use by inserting sterilised borosilicate glass coverslips into the wells of 24 well plates using sterile forceps. The glass coverslips were then coated with 200µl of 0.1% (w/v) poly L-lysine and gently placed at 37°C to incubate for 10 minutes. After 10 minutes the plates were removed, and the poly L-lysine removed from the glass coverslip. The plates were then allowed to dry at room temperature for approximately 15 minutes. Following this, the coverslips are ready for use. All poly L-lysine coverslips were prepared on the day of use in order to ensure maximum efficiency of the poly L-lysine.

2.4.8 Quantitative assessment of the interaction of malignant cells with fluorescent pH sensitive doped Fe_2O_3 nanoparticles.

The I-83 cell line CLL patient samples and normal B cells were cultured in RPMI-140 media (supplemented with 2nM L-glutamine, 10% fetal

bovine serum and 1% 5,000U/mL penicillin/streptomycin) as discussed above. Cells were then seeded at a cell density of 200,000 cells/well in a 96 well plate (Nunclon, Thermo Fisher Scientific) at a final volume of 200µl/well. Cells were then exposed to pH sensitive doped non-functionalised and functionalised Fe_2O_3 nanoparticles (see below, Table 2.6) at a concentration ranging from 10µg/mL to 100µg/mL. Non-functionalised nanoparticles were used as a control in each study in order to demonstrate the targeting capabilities of functionalised nanoparticles. A negative control of untreated cells was also plated, and all experiments were performed in triplicate and each with technical repeats. Cells treated were then incubated at 37°C and 5% CO_2 for 24 hours. Following incubation, plates were then read in a fluorescence plate reader (Biotek FLx800) at λ_{exc} = 505nm; λ_{emm} = 525nm. A standard curve was also prepared using doped nanoparticles in solutions of varying pH in order to ensure assay reproducibility.

Table 2.6: Shows fluorescently doped, pH sensitive functionalised nanoparticles used in uptake and interaction studies and their individual purpose within this study. Characters within brackets (097) (HI 186) identify different clones of anti-CD52 antibody used in this work.

Functionalised Nanoparticle	Purpose of inclusion in this study
Non-functionalised Nanoparticles	Demonstrate minimal nanoparticle interaction
anti-CD52 (097) - AlexaFluor® 647	Demonstrate targeted interaction and internalisation
anti-CD52 (097) – FITC	Fluorophore control
anti-CD52 (097)	Fluorophore control
anti-CD52 (HI 186) – FITC	Clonality control
Mouse IgM	Isotype control

2.4.9 Qualitative assessment of the interaction of Fe_2O_3 nanoparticles with normal and malignant B cells using laser scanning confocal microscopy.

Both primary B lymphocytes and CLL patient samples were seeded at a density of 2×10^5 cells/well onto poly L-lysine coated coverslips (see 2.4.6). The cells were allowed to adhere to borosilicate surface at 37°C for approximately 1 hour. Cell supernatant and remaining unadhered cells were gently removed using a Pasteur pipette and remaining adherent cells were treated with concentrations of Fe_2O_3 nanoparticles ranging from 10µg/mL to 100µg/mL and incubated at 37°C for 24 hours in a total of 200µL RPMI-1640 cell medium (supplemented with 2nM L-glutamine, 10% fetal bovine serum and 1% 5,000U/mL penicillin/streptomycin).

Following incubation, the cells were immediately fixed using 4% paraformaldehyde for 10 minutes at room temperature. Following fixation, the cells were washed with dPBS to remove all traces of paraformaldehyde to decrease chances of subsequent permeabilisation of the cells and stained for nucleus and F-actin using 5µL of 1mg/mL Hoechst 33342 (nuclei stain; Life Technologies, product code: H3570) and 60µL of 6.6µM rhodamine Phalloidin (F-actin stain; Life Technologies, product code: R415), respectively. The specimens were allowed to stain for 2 hours at room temperature, protected from light, and subsequently followed by washing of coverslips twice with dPBS. The coverslips were then mounted onto glass slides using Dako mounting medium and visualised using the confocal microscope. Confocal microscopy analysis was performed using a ZEISS 510 Meta

confocal microscope equipped with ZEISS LSM 5 software for subsequent analysis (Carl Zeiss, Germany, below Figure 2.3). Nucleus stained using Hoechst 33342 could be visualised λ_{exc} 405nm, F-actin could be visualised λ_{exc} 561nm. Fe_2O_3 nanoparticles could be detected using reflectance mode. Localisation of nanoparticles within the cell could be confirmed using Z-stack analysis. Figure 2.3 below shows the confocal microscope set-up within the laboratory.

Figure 2.3: Image shows set-up of the confocal microscopy workspace.

2.4.10 Qualitative assessment of the interaction of Fe_2O_3 nanoparticles with normal and malignant B cells using epifluorescence microscopy.

During the process of the investigation of the interaction of nanoparticles with malignant B lymphocytes, treated cell suspensions were routinely visualised using epifluorescence and brightfield microscopy, prior to additional experimentation. I-83 cells were seeded at a density of 2×10^5 cells/well and treated with 25µg/mL and 100µg/mL Fe_2O_3 nanoparticles to a total volume of 200µL/well and incubated for 24 hours at 37°C and subsequently visualised using brightfield microscopy on the Nikon Eclipse TE300. This serves to understand on a basic level the

interaction of this cell type with nanoparticles for future experiments. Images of these cellular interactions may then be taken and stored as a future reference material.

2.4.11 Assessment of the mechanism of internalisation of functionalised nanoparticles.

The experimental procedure here is similar to that of internalisation quantification with the addition of inhibitors that act to prevent internalisation of nanoparticles by the cells. Chlorpromazine acts as a clathrin-mediated endocytosis inhibitor through the inhibition of clathrin protein disassembly and receptor localisation to the plasma membrane, a key event in this form of endocytosis (dos Santos *et al.,* 2011). Amiloride hydrochloride acts as a macropinocytosis inhibitor through its inhibition of membrane Na^+/H^+ exchange (Franca, *et al.,* 2014).

The CLL cell line I-83 was seeded at a cell density of 2×10^5 cells per well in a 96 well plate, to a total volume of 100μL. Cells were treated for quantitative analysis of uptake using Fe_2O_3@ CD52 as described above (see 2.4.7). Additional samples were prepared concurrently with the purpose of investigating nanoparticle uptake inhibition. For inhibition of macropinocytosis, cells were treated with amiloride hydrochloride (Santa Cruz Biotechnology, Catalogue Number sc-3578) at a final concentration of 100μM. For inhibition of clathrin-dependent endocytosis, cells were treated with chlorpromazine to a final concentration of 50μM. In each case, cells were treated with inhibitors for 1 hour prior to treatment with nanoparticles.

2.4.12 Imaging and recording the interactions of Fe_2O_3 nanoparticles with normal and malignant B lymphocytes, utilising helium ion microscopy.

Nanoparticle interaction with the cell surface and the effect on the surface morphology of the cells can be investigated using helium ion microscopy (HIM, Advanced Microscopy Laboratory, CRANN). The HIM microscope itself functions similarly to the SEM based on a field ion microscope which operates in a highly vacuumed environment using a cryogenically cooled Tungsten tip. It is at this tip, that the He ions are introduced. The tips' structure is such that there is a trimer of helium atoms (three helium atoms) which emit at a low voltage which means that the He gas which is then displaced to the Tungsten tip can only interact with a few atoms at a time. As the helium ion beam interacts with the sample it is capable of providing an image of extremely high resolution, with quite a high secondary electron yield, which is responsible for the intricacy of the image produced, in contrast to traditional electron microscopy techniques which employ the use of photons or electrons for the imaging process. The field of view, intricacy of imaging, and the size of the sample required to be imaged can all be taken in to consideration by changing the pressure of the gas from femtoampere to picoampere (Joens, *et al.*, 2013).

2.4.12.1 The effects of pre-processing on the morphology of the B lymphocyte as investigated with Helium Ion Microscopy.

It has been a topic of debate for decades, but it is fundamental to any morphological study or analysis that one is certain that the results that are being obtained are true, and to minimise the possibility of artefacts caused during sample preparation. In order to investigate the effects of different combinations of fixation and dehydration protocols on normal B cells and CLL patient samples, the most common fixation and dehydration methods were preformed, and comparisons were made between the methods. The most common methods of fixation and dehydration can be seen below in Table 2.7.

Table 2.7: Shows differing fixation protocols and dehydration protocols which can be utilised to prepare samples for electron microscopy.

Fixation Protocol 1:	2.5% Glutaraldehyde overnight at 4°C
Fixation Protocol 2:	2.5% Glutaraldehyde + 0.1M Sodium Cacodylate overnight at 4°C
Fixation Protocol 3:	4% Paraformaldehyde overnight at 4°C
Dehydration Protocol A:	Gradient of ethanol followed air drying
Dehydration Protocol B:	Gradient of ethanol followed by 30% HMDS (5 mins), 60% HMDS (5 mins), 100% HMDS (10 mins)
Dehydration Protocol C:	Gradient of ethanol followed by 100% HMDS (3 mins)
Dehydration Protocol D:	Gradient of ethanol followed by followed by 60% HMDS (3 mins)
Dehydration Protocol E:	Gradient of ethanol followed by 100% acetone (3 mins)

Normal B lymphocytes isolated from healthy donors were utilised in this work. Following isolation of B lymphocytes, cells were prepared for helium ion microscopy using protocols described in the above table, in order to demonstrate the effects of differing combinations of the above fixation and dehydration protocols. For this optimisation experiment, the three different fixation methods were combined with the different dehydration protocols, in order to establish the optimal protocol for cellular preparation for HIM, as follows:

1. 2.5% Glutaraldehyde overnight at 4°C followed by a gradient of ethanol followed by 30% HMDS (5 mins), 60% HMDS (5 mins), 100% HMDS (10 mins)

2. 2.5% Glutaraldehyde overnight at 4°C and followed by a gradient of ethanol and 60% HMDS (3 mins)

3. 4% Paraformaldehyde overnight at 4°C followed by a gradient of ethanol and by 100% acetone (3 mins)

4. 2.5% Glutaraldehyde + 0.1M Sodium Cacodylate overnight at 4°C followed by a gradient of ethanol and by 100% acetone (3 mins)

5. 2.5% Glutaraldehyde overnight at 4°C followed by a gradient of ethanol followed air drying

Glutaraldehyde acts as an excellent fixative as it preserves the cross-linking within the tissue more so than that of other fixatives. Its acts through the slow penetration of the surface of the cells when compared to other common fixatives, and in this manner provides excellent structural preservation (Eltoum *et al.,* 2001). The ethanol gradient used throughout these comparisons can be found below in Table 2.8.

Following preparation of samples, all samples were stored for Helium Ion microscopy performed in the days after sample preparation. The HIM was operated at an imaging voltage of 30kV, with a dwell time of 0.5μs and a blanker current of 0.9pA. The working distance and field of view varied slightly between each image in order to produce optimal imaging conditions.

2.4.13 Morphology of B lymphocytes as investigated using He Ion Microscopy.

Following isolation, the normal human B lymphocytes and patient derived CLL cells were seeded onto prepared borosilicate glass coverslips coated with poly L-lysine at a density of 5×10^5cells/ml, as described above in section 2.4.6. The cells were allowed to set down for 1 hour and then immediately fixed using 2.5% glutaraldehyde (Sigma Aldrich) overnight at 4°C. Following fixation, cells were then prepared for electron microscopy using a dehydration process involving incremental increases of ethanol followed by cell scaffolding integrity fixation using hexamethyldisilazane HMDS; (Sigma Aldrich, catalogue number 440191) as described in Table 2.8 below. Following dehydration, the coverslips were mounted onto SEM mounting stubs using carbon tabs. The cells were observed using helium ion microscopy (HIM), seen below in Figure 2.4. The HIM was operated at an imaging voltage of 30kV, with a dwell time of 0.5μs and a blanker current of 0.9pA. The working distance and field of view varied slightly between each image in order to produce optimal imaging conditions.

Table 2.8: **Sets out steps for the careful preparation of biological samples for Helium ion microscopy.** *All steps utilising HMDS should be performed in the fume hood with care.*

Step	Reagent	Concentration	Time	Temperature
Fixation	Glutaraldehyde	2.5%	Overnight	4°C
	dPBS		10 minutes	RT
Dehydration	Ethanol	30%	10 minutes	RT
	Ethanol	50%	10 minutes	RT
	Ethanol	70%	10 minutes	RT
	Ethanol	90%	10 minutes	RT
	Ethanol	100%	20 minutes	RT
	Ethanol	100%	20 minutes	RT
	Ethanol	100%	20 minutes	RT
	HMDS	30% in EtoH	5 minutes	RT
	HMDS	60% in EtOH	5 minutes	RT
	HMDS	100%	10 minutes	RT
Samples should be allowed to dry overnight in fume hood.				

Figure 2.4: Image shows Zeiss Orion Helium Ion Microscope. Samples are dehydrated in preparation for imaging and images, before being inserted into vacuum chamber.

2.4.14 Effects of Fe₂O₃ nanoparticles on the morphology of B Lymphocytes, as investigated using Helium Ion Microscopy.

As previously described, primary normal B lymphocytes, I-83 cells and patient derived CLL cells were seeded onto poly L-lysine coated coverslips. The cells were allowed to adhere for approximately 1 hour and were then subsequently treated with iron oxide nanoparticles. The cells were treated with 25µg/mL Fe_2O_3 in a total volume of 200µL/well and incubated at 37°C overnight. The cells were then immediately fixed using 2.5% glutaraldehyde overnight at 4°C. Following fixation, cells were then prepared for HIM, as discussed above. The samples, on the borosilicate glass coverslip, is then mounted on to a standard 13um SEM imaging stub using a carbon tab and the samples were imaged using HIM. The HIM was operated at an imaging voltage of 30kV, with a dwell time of 0.5µs and a blanker current of 0.9pA. The working distance and field of view varied slightly between each image in order to produce optimal imaging conditions.

.

2.4.15 Determination of toxicity of non-functionalised and functionalised Fe₂O₃ nanoparticles on CLL cells

A preliminary determination of the levels of cell death resultant from the treatment of the I-83 cell line with non-functionalised and functionalised nanoparticles was conducted using ethidium bromide-acridine orange cell staining. For this, $3x10^5$ cell/well I-83 cells were treated with one of either bare Fe_2O_3, Fe_2O_3@APTES or Fe_2O_3@CD52, at concentrations

of 0, 0.3, 1.0, 10, 30, 100 and 300µg/mL in a 24 well plate for 24 hours at 37°C. Following treatment, cells were recovered from the wells using gentle pipetting, and 10µl of the cell suspension was stained with 10µl of ethidium bromide-acridine orange, whilst protected from the light, and immediately visualised using fluorescent microscopy and cell counting using a standard haemocytometer. The number of cells undergoing cell death were recorded.

In order to determine the apoptotic effects of non-functionalised and functionalised nanoparticles, cells were stained for both Annexin V-FITC and propidium iodide following treatment with nanoparticles. The basis of this assay is to study the series of cellular events which are known to occur during the stages of apoptosis and necrosis. Briefly, early stage apoptosis can be observed through the changes in the cellular surface, whereby the translocation of phosphotidlyserine (PS) from the inner side of the plasma membrane to the outer side occurs. Annexin V is a calcium-dependent phospholipid binding protein displaying high affinity for PS and therefore serves as the ideal probe for PS translocation and thus apoptosis analysis. The important distinction between apoptosis and necrosis can be used using an additional stain of propidium iodide (PI). During the onset and process of necrosis, the cell membrane becomes compromised and therefore leaky. PI is a fluorescent dye that acts as an intercalating agent and is used during apoptosis/necrosis assays due to its binding affinity for nucleic acids. Upon initiation of apoptosis/necrosis assays using these dyes, annexin V can therefore be used as an indicator of the onset of apoptosis (translocation of PS) and PI as an indicator of necrosis/late

stage apoptosis (leaky, compromised cell membrane) (Cummings *et al.,* 2004).

For this assay, 3×10^5 cell/well I-83 cells were treated with one of either bare Fe_2O_3, Fe_2O_3@APTES or Fe_2O_3@CD52, at concentrations of 10, 25 and 100µg/mL in a 24 well plate for 24 hours at 37°C. Cells were collected through centrifugation at 300X g for 10 minutes. Cells were re-suspended in ice cold 1 x annexin V binding buffer (Biolegend UK, United Kingdom, Catalogue number 422201) and washed twice in same buffer. 5µL of annexin V-FITC was added to each sample and samples gently vortexed and incubated for 15 minutes on ice to stain. 400µL of annexin V binding buffer was then added to each tube in preparation for flow cytometry. Immediately prior to flow cytometric analysis, 10µl of PI solution was added to each tube (to a final concentration of 1µg/mL) and samples run on the flow cytometer. Samples Were analysed for annexin V-FITC staining (λ_{exc} 488nm, λ_{emm} 350nm) and PI staining (λ_{exc} 535nm, λ_{emm} 617nm) using the BD Accuri C6, using filter sets 2 and 3 for each stain, respectively. The use of appropriate controls is fundamental for successful assessment of apoptosis and necrosis of cells following treatment.

Recommended controls for Annexin V – PI staining are outlined below in Table 2.9.

Table 2.9: **Table demonstrates the variety of controls implemented in each flow cytometric analysis of Annexin V-PI staining for the study of apoptotic events in cell samples**. Above controls were utilised in each experiment.

Sample	Annexin V Stain Present	Propidium Iodide Stain Present
Untreated cell suspension		
Untreated cell suspension	X	
Untreated cell suspension		X
Untreated cell suspension	X	X
Nanoparticle Suspension		
Annexin V Stain	X	
Propidium Iodide Stain		X

Next, we investigated whether the presence of the both targeting and toxic agent, anti-CD52, combined with an antibody directed at the pan-B cell marker CD19 (anti-CD19) might increase efficacy of the functionalised nanoparticle. Also included in this work was nanoparticles functionalised with anti-CD20, also known as rituximab, another commonly used monoclonal antibody therapeutic with B cell targeting capabilities. This experimental procedure was performed in the same manner as mentioned above. Briefly, the I-83 cell line was seeded at a density of 3×10^5 cells per well in a 24 well plate and incubated with 5 differing functionalised nanoparticles for 8 hours at 37°C. Functionalised nanoparticles used in this study were: Fe_2O_3@APTES, Fe_2O_3@CD19, Fe_2O_3@CD20, Fe_2O_3@CD19-CD52 and Fe_2O_3@CD52. Following this, the cells were recovered using centrifugation and prepared for Annexin V-PI staining and cell viability assessment as discussed above.

In order to determine the effects of functionalised nanoparticles (Fe_2O_3@ CD52, Fe_2O_3@ fludarabine – CD52) on patient-derived malignant B lymphocytes, CLL cell isolates were treated with a previously determined range of functionalised nanoparticle and cellular

toxicity effects were observed using flow cytometric analysis above. Briefly, CLL patient samples were seeded at a cell density of 3 x 10^5 cells per well in a total volume of 200µL, allowed to recuperate for 1 hour at 37°C, and subsequently incubated with functionalised nanoparticles, namely Fe_2O_3@APTES, Fe_2O_3@ CD52 and Fe_2O_3@ Fludarabine – CD52, for 8 hours and 24 hours in order to obtain a time and dose-dependent response using flow cytometric analysis of induced apoptosis and necrosis. In addition to incubation with this novel drug and monoclonal antibody delivery vehicle, cell suspensions were also incubated with controls using 10µg/mL anti-CD52 monoclonal antibody and 20µM fludarabine.

Following treatment with either Fe_2O_3@APTES, Fe_2O_3@ CD52 or Fe_2O_3@ Fludarabine – CD52, cell suspensions were then prepared for Annexin V-PI staining for analysis of induction of apoptosis and necrosis as discussed above.

2.4.16 The effects of shear stress on B lymphocytes and their interactions with endothelial cells in a shear flow environment.

Cell adhesion and migratory behaviour under shear flow conditions was investigated and recorded using an in-house, custom built microfluidics system utilising neMESYS (Cetoni, Germany) microfluidics platform and Cellix Vena8 Fluoro+ biochips coated with VCAM-1 and Endothelial+ biochips seeded with Human Umbilical Vein Endothelial Cells (HUVECs) and Human Dermal Lymphatic Endothelial Cells (HDLECs).

These cell types were chosen so as to mimic, as closely as possibly, both the lymphatic and vascular environment encountered by CLL cells. The microfluidics system utilised was based on the use of an epifluorescent microscope modified through a series of tubing connected to a controlled pump, where the microscope allows visualisation of the biochip chambers and events occurring within. Much optimisation was performed on this including flow rates, cell densities, chamber location variations and syringe diameter. The microscopy instrumentation utilised is equipped with both a temperature and humidity-controlled chamber for continuous live imaging where shear flow experiments were performed at 37°C. This home-built microfluidics system can be seen below in Figure 2.5. The differing factors that need to be considered upon the generation of such a device are shown below in Figure 2.6. An example as to the visualisation of patient-derived CLL cells across the endothelial monolayer using above microfluidics system can be seen in Figure 2.7.
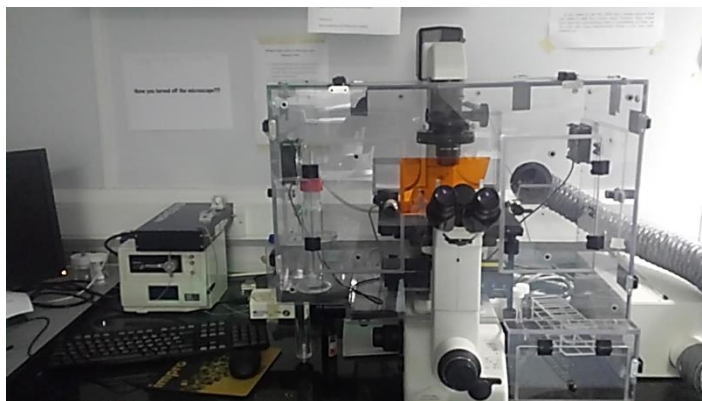
Figure 2.5: Set-up of the self-assembled and optimised microfluidics workspace, complete with temperature and CO_2-controlled chamber and associated epifluorescent microscope.
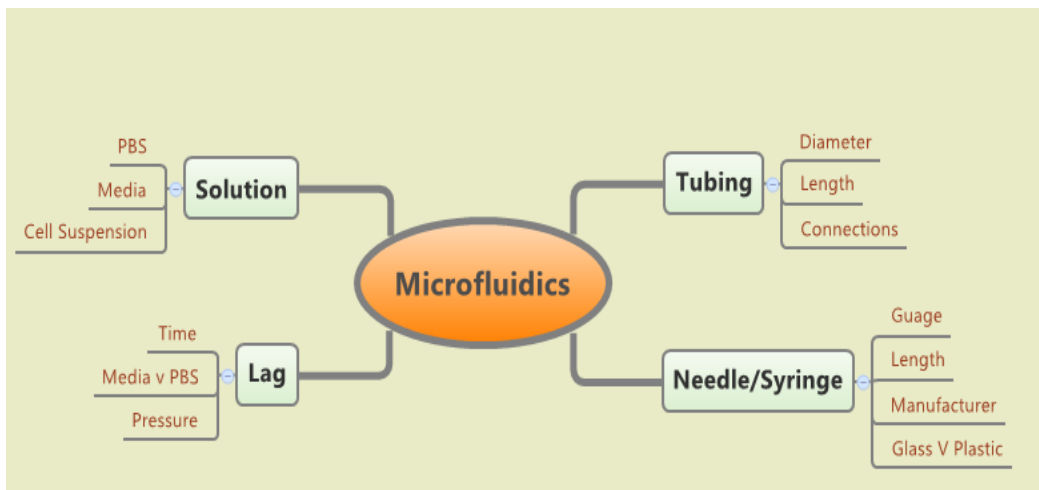
Figure 2.6: Schematic highlighting the variety of implicating factors in the generation of a microfluidics system in the study of complex multifactorial diseases such as CLL.

Direction of flow
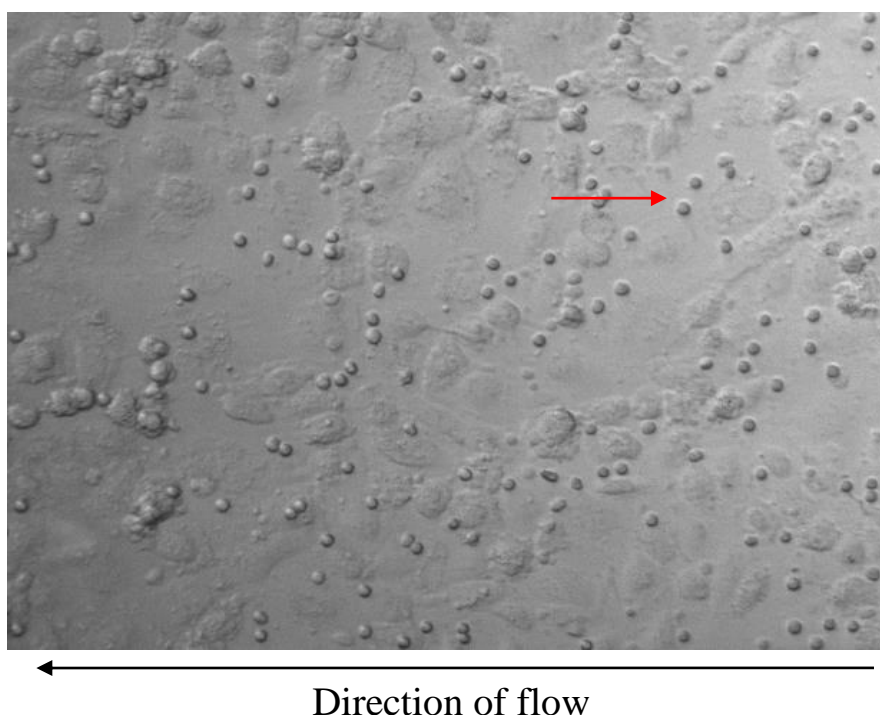
Figure 2.7: Representative image of cells under shear flow. Red arrow shows malignant cell isolated from patient with CLL. Channel of Cellix Vena8 Endothelial+ chip coated with monolayer of human umbilical venous endothelial cells (HUVECs).

2.4.16.1 Comparison of toxicity responses of malignant B lymphocytes following treatment with nanoparticles under static and shear conditions.

The I-83 cell line suspension was prepared at a concentration of 2×10^5 cells/mL in RPMI-1640 and (supplemented with 2nM L-glutamine, 10% FBS and 1% 5,000U/mL penicillin/streptomycin). Cells were seeded into wells of a 96 well plate at a volume of 100µl per well and cell suspensions were treated with 25µg/mL bare Fe_2O_3 nanoparticles. For this study, bare Fe_2O_3 nanoparticles were chosen as Fe_2O_3@APTES nanoparticles display little to no toxicity and would yield little information. Treated cell suspension was immediately run through the microfluidics system at a shear force rate of 0.5 Dynes/cm^2 and 0.08 Dynes/cm^2 for 30 minutes at a continuous flow rate. The time point of 30 minutes was selected as enough time was required to elapse for a toxicity effect to be induced in the static assay. These two flow rates were chosen to simulate venous shear stress (0.5 Dynes/cm^2) and a rate of 0.08 Dynes/cm^2 chosen to simulate lymphatic shear stress, flow rates both commonly described in the literature and of importance in the pathogenesis of CLL (Voyvodic, *et al.*, 2014) (Frueh, *et al.*, 2013) (Harker, Jivan, McWhorter, Liu, & Lodoen, 2014) (Woo, Dutta, Patel, Kresge, & Feranchak, 2008). Following exposure to the nanoparticles, cell suspension was collected, and viability was immediately assessed using Trypan Blue (0.4% solution; Gibco, Thermo Fisher Scientific, product code: 15250061). For this, a 1:1 (20µL:20µL) ratio of gently mixed cell suspension and 0.4% Trypan Blue solution was added to a tube, and Trypan Blue exclusion tests were performed using

haemocytometer-based light microscopy cell counting, as described by Strober, 2001 (Strober, 2001). In tandem to the microfluidics work, cells treated as above were allowed to sit in the 96 well plate in the chamber for 30 minutes in accordance with traditional experimental procedure. Cell viability was recorded following microfluidics using Trypan Blue dye exclusion test. Nanoparticle suspension and untreated cell suspension stained with Trypan Blue was used as a control.

2.4.16.2 Adherence of I-83 cells and CLL patient samples to endothelial cells, and the effect of nanoparticles, in a shear flow environment

Biochip channels were incubated with 5µL VCAM-1 (Promokine, product code: C-60064) per channel at 4°C in a humidified environment 24 hours prior to experimental work. A T25 flask of HUVECs and HDLECs that had reached 90-100% confluency were then stimulated with 50ng/mL of TNF-α (Promokine, product code: C-63719) 24 hours prior to use, and incubated at 37°C. HUVECs were the endothelial cells used for the investigations at 0.5 Dynes/cm^2 and 0.25 Dynes/cm^2. HDLECs were the endothelial cell of choice for 0.08 Dynes/cm^2, to mimic lymphatic flow. 4 hours prior to use, HUVECs were gently detached from the tissue culture flask using 10mLs of accutase (Promokine, product code: C-41310) incubated at 37°C for 15 minutes. The flask of HUVEC cells was then centrifuged down and re-suspended in a total of 50µL of RPMI-1640 media (supplemented with 2nM L-glutamine, 10% fetal bovine serum and 1% 5,000U/mL penicillin/streptomycin). 5µl of the HUVEC suspension was seeded into each of the biochip channels ensuring a minimum density of 2 x10^4 per

channel and allowed to adhere and form a monolayer before use (approximately 4 hours). I-83 cell line suspension and patient sample suspension was prepared at a concentration of 1 x 10^6 cells/mL and 2 x 10^6 cells/mL, respectively in RPMI-1640 (supplemented with 2nM L-glutamine, 10% FBS and 1% 5,000U/mL penicillin/streptomycin). Patient-derived CLL cells were seeded into wells of a 96 well plate at a volume of 100µl per well and cell suspensions were treated with 25µg/mL Fe_2O_3 NPs for 30 minutes prior to analysis. Untreated cells were used as control. Cell suspension was immediately run through the microfluidics system. For this study, three different rates of flow were investigated: 0.5 Dynes/cm^2, 0.25 Dynes/cm^2 and 0.08 Dynes/cm^2. 0.5 Dynes/cm^2 and 0.25 Dynes/cm^2 to simulate venous shear stress and 0.08 Dynes/cm^2 simulates lymphatic shear stress (Voyvodic, et al., 2014) (Frueh, et al., 2013) (Harker, Jivan, McWhorter, Liu, & Lodoen, 2014) (Woo, Dutta, Patel, Kresge, & Feranchak, 2008). Cell adhesion was monitored, and number of adherent cells was recorded after 2 minutes and 15 minutes.

Here, we also investigated the effect of bare Fe_2O_3, Fe_2O_3@APTES and Fe_2O_3@CD52 functionalised nanoparticles on the adherence of CLL patient samples to the HUVEC monolayer. For this, CLL patient samples were run through the microfluidics system at a rate of 0.5 Dynes/cm^2 for 2 minutes and 15 minutes, following treatment with 25µg/mL of either bare Fe_2O_3, Fe_2O_3@APTES or Fe_2O_3@CD52 functionalised nanoparticles at 37°C for 30 minutes prior to analysis. The microfluidics chip and HUVEC cells were prepared as discussed above. A control of

untreated cells, and 10µg/mL of anti-CD52 monoclonal antibody were also used (Jantus Lewintre, *et al.*, 2004) (Cheney, *et al.*, 2014).

2.4.17 Statistical analysis

Statistical analysis was conducted using GraphPad Prism software, with $p<0.05$ considered statistically significant (GraphPad Software, Inc., La Jolla, CA, USA). Error bars represent mean ± standard error of the mean. The appropriate test used in each experiment is indicated at the presentation of each result section.

Chapter 3: Characterisation and assessment of the effects of bare Fe_2O_3 (non-functionalised) nanoparticles on B cells

3.1 Introduction

Nanoparticles, particularly iron (III) oxide nanoparticles (Fe_2O_3) have been widely used in medicine for many years now, demonstrating their use in the field of imaging, drug and gene delivery and the treatment of malignant hyperthermia (Banobre-Lopez, Teijeiro, & Rivas, 2013) (Nune, Gunda, Thallapally, Lin, & Berkland, 2009) (Cho, Wang, Nie, Chen, & Shin, 2008). This is due in part to their magnetic properties, and to their relative ease of modification. Fe_2O_3 commonly exists in nature as rust and offers an attractive choice of material in the generation of nanoparticles due to their prevalence, wide use and low cost. Like many other nanoparticles, Fe_2O_3 nanoparticles exhibit a high surface to volume ratio. This allows for an increase in reactivity and involvement in biochemical activities. The structural and optical properties of Fe_2O_3 nanoparticles are size-dependent and the respective synthesis method can affect both the nanoparticles size and crystal structure, ultimately altering the nanoparticles suitability for their intended purpose (Ali, *et al.*, 2016) (Wu, Wu, Yu, Jiang, & Kim, 2015). The synthesis of Fe_2O_3 is generally conducted using one of two main techniques: physical methods and chemical methods. Chemical preparation of Fe_2O_3 nanoparticles is a very common approach, where the methods are relatively simple and efficient in addition to maintaining control over the size, composition and the shape of the resultant nanoparticles (Laurent, *et al.*, 2008). Chemical synthesis of Fe_2O_3 nanoparticles is often conducted through the coprecipitation of Fe^{2+} to Fe^{3+} by the addition of a base. Here, the size and shape of the nanoparticle is controlled based on the type of salt used in the reaction, the ratio of Fe^{2+} to Fe^{3+}, the pH

and the ionic strength (Laurent, *et al.*, 2008) (Kumar Gupta & Gupta, 2005). A more detailed description of the various techniques that may be employed in the synthesis of Fe_2O_3 nanoparticles may be found in Chapter 1.

Fe_2O_3 nanoparticles with bare surfaces also tend to form aggregations due to their strong magnetic properties and van der Waals forces (Ali, *et al.*, 2016). Bare Fe_2O_3 nanoparticles may also undergo significant surface opsonisation with non-specific proteins in their environment, particularly serum proteins, making them considerably more "visible" to phagocytic cells, in addition to often high levels of uptake and retention within the reticuloendothelial system (RES) (Nie, 2010). Both of these processes can contribute to high levels of ultimate clearance *in vivo*, resulting in difficulties in nanoparticle targeting and penetration of solid tumours. Encapsulation of Fe_2O_3 nanoparticles has been shown to result in decreased clearance by the RES, increased preferential uptake and targeting, longer blood circulation times and improved pharmacokinetic properties (Cisterna, *et al.*, 2016). In addition to the method employed in Fe_2O_3 nanoparticle synthesis, stabilisation or encapsulation of Fe_2O_3 nanoparticles can be of great importance (Lu, Salabas, & Schuth, 2007). The use and choice of stabilising agent will generally be dictated by the ultimate intended purpose of the Fe_2O_3 nanoparticles. Stabilisation agents in nanomedicine will be discussed in Chapter 4.

One of the most important aspects in the characterisation of nanoparticles is the ability to accurately measure the size and distribution of the particles, both in their anhydrous prepared state and

in their subsequent state in suspension. The size of a nanoparticle can directly relate to, and effect, the particles ability to penetrate and permeate across a variety of barriers and membranes within the body (Barua & Mitragotri, 2014) (Hoshyar, *et al.* 2016). The size of nanoparticles can also impact upon the loading capability of nanoparticles and the capacity of the nanoparticles to either contain or carry molecules including drugs, biologics and targeting agents. The distribution of nanoparticles within their suspended state, both during their preparation and *in vivo*, can affect the bioavailability of any agents that may be contained within, or indeed loaded onto the surface, of the nanoparticles. Nanoparticles that display a significant propensity to aggregate within solution may not be an ideal choice as a vehicle for drug delivery or targeted agents, as aggregation may limit delivery to the site of interest (Faure, *et al.*, 2013).

As stated in the materials and methods and introduction, there are many methods that may be employed to measure the dimensions, dispersion state and subsequent suitability of use of nanoparticles, including: nanoparticle tracking analysis (NTA), scanning electron microscopy (SEM), and dynamic light scattering (DLS).

NTA technology has been commercialised for just over a decade now, since 2006. (Filipe, Hal, & Jiskoot, 2010) Such validation of this technique has resulted in the consolidation of the technique across a number of areas of application, including exosome characterisation, nanoparticle characterisation, drug delivery, assay development, vaccine characterisation and nanotoxicology (Hole, *et al.*, 2013). Further information about NTA technology can be found in Chapter 2.3.1.

Within this work, we have consolidated the data generated toward the standardisation of NTA characterisation for particle sizing. However, over the past few years, the list of parameters along with the number of adjustable settings for each parameter has been honed, and these settings are not automated. This has created an SOP which has been provided to several laboratories for robustness testing for each user and laboratory (Filipe, Hal, & Jiskoot, 2010) (Hole, *et al.*, 2013).

The study of the interaction of nanoparticles with cells within is another pivotal point in the overall understanding of the role of said nanoparticle as a potential therapeutic. Nanoparticle-nanoparticle interactions have been measured for decades, with nanoparticle-cell interactions using a vast range of techniques. One of the best methods for understanding the interactions, and hence functional effects of nanoparticles on cells in the environment remains microscopy. Microscopy allows for not only the visualisation, but also real-time analysis of cells and nanoparticles in their environment and can also allow for a greater understanding into the interactions of nanoparticles with the cell surface and cellular uptake of nanoparticles (Rothen-Ruthishauser, *et al.*, 2014)(Park, *et al.*, 2015) (Shang, *et al.*, 2014) (Kang, *et al.,* 2015)(Villa, *et al.,* 2016).

Microscopy techniques such as light microscopy allow for the user to visualise the interactions of cells with nanoparticles under brightfield conditions. This has many advantages as it allows the user to visualise cells over a prolonged period, without any concerns for phototoxicity and photobleaching (Selinummi, *et al.*, 2009). This technique is however limited to visualisation of the outer portions of cells, and the surrounding environment. This has given rise to the popular use of laser scanning

confocal microscopy (LSCM) in the study of the interaction of nanoparticles with their cellular environment.

Within this study, several microscopy techniques were used for the observation and recording of cell-nanoparticle interactions and surface or uptake behaviour. These included: epifluorescence microscopy, laser scanning confocal microscopy and helium ion electron microscopy.

The use of LSCM can provide the user with an in-depth understanding of these interactions at the individual cellular scale (Paddock, 2000) (Jonkman & Brown, 2015) (Paddock & Eliceiri, 2013). Typically, samples fated for LSCM are stained prior to imaging in order to easily identify major cellular components, such as nucleus and cytoskeleton. DAPI or Hoechst stain for nucleus, and phalloidin stain for actin (F or G) enable visualisation of the nucleus and cytoskeleton (Paddock & Eliceiri, 2013) (Paddock, 2000). Following treatment of cells with nanoparticles, this approach can allow for the identification of the location of nanoparticles within the cell; and in some cases, a further understanding into the mechanisms of uptake employed. This can be further evaluated using a specific method of imaging on the LSCM, known as reflectance imaging. This imaging technique is not widely used in most biological studies, but commonly employed in the study of metallic nanoparticle interactions with cellular material. It relies on the use of an available fluorescent channel during imaging, which can be focused for the reflection of the laser beam from the metallic surface as backscatter towards the pinhole. This allows the user to record this interaction, resulting in the imaging of the optically dense particle against the cell (Jain, El-Sayed, & El-Sayed, 2007). Within this chapter, we assessed

the interaction of the bare Fe_2O_3 nanoparticle with both the I-83 cell line and normal B cells, using laser scanning confocal microscopy.

Advances in microscopy are ever-growing, and recently the helium ion microscope has proven its use in the study of nanoparticles and their interaction with cellular materials (Bell, 2009). Helium ion microscopy, or HIM, is an advanced form of electron microscopy that allows for the visualisation of cellular material without the need for prior sputter-coating, as is the case in SEM. The HIM itself functions similarly to the SEM; based on a field ion microscope which operates in a highly vacuumed environment using a cryogenically cooled Tungsten tip. It is at this tip, that the He ions are introduced. The tips structure is such that there is a trimer of helium atoms which emit at a low voltage which means that the helium gas which is then displaced to the Tungsten tip can only interact with a few atoms at a time. As the helium ion beam interacts with the sample it can provide an image of extremely high resolution, with quite a high secondary electron yield, which is responsible for the intricacy of the image produced, in contrast to traditional electron microscopy techniques which employ the use of photons or electrons for the imaging process (Joens, *et al.*, 2013). When utilising electron microscopy, the visualisation of organic material and surface structures can be considerably more difficult as often biological material requires sputter-coating due to the hydrated nature of the cellular material (see introduction section 1.6). In contrast, HIM can yield useful information about the surface of cells as it does not require prior cell sputter-coating. When using HIM as a tool to investigate the interactions of organic materials with inorganic materials (in this case,

cells with nanoparticles), it is important to have an in-depth understanding of the workings of such a piece of equipment.

As with any form of electron microscopy, there are a number of pre-processing steps employed in order to render the sample suitable for analysis. B lymphocytes are a non-adherent, non-static cell type and the method of pre-processing is vital to ensure an accurate representation of the native B cell. Processing of the sample for helium ion microscopy requires similar steps as for any form of electron microscopy, including the dehydration of sample material, as the sample will then be loaded into a vacuum. If a biological sample, however small, is loaded into a vacuum chamber without complete dehydration, gas molecules from the samples will interfere with the recording of electrons emitted from the sample. Fixation of the sample can be performed using one of several possible fixatives, including 4% paraformaldehyde overnight at 4°C, 2.5% glutaraldehyde overnight at 4°C and 2.5% glutaraldehyde containing 0.1M sodium cacodylate at 4°C overnight. Sodium cacodylate is often used in this process as it provides additional buffering capacity and can therefore help to retain the integrity of the cell structure overnight during fixation. Paraformaldehyde is a common fixative in microscopy, acting to solidify the bonds within the cells and functioning similar to a glue. However, excessive fixation with paraformaldehyde can result in cell destruction and loss of surface structures. Glutaraldehyde acts to preserve the cross-linking within the tissue, acting through the slow penetration of the surface of the cells when compared to other common fixatives, and in this manner provides excellent structural preservation (Eltoum, Fredenburgh, Myers, &

Grizzle, 2001) (Eltoum, Fredenburgh, & Grizzle, 2001). The dehydration process of biological samples for HIM is relatively consistent within the literature, using a gradual increase in ethanol concentration (Zhang, *et al.*, 2017). The final step in the preparation protocol of samples for electron microscopy is the sample drying process, including either air-drying overnight, or matrix solidification using hexamethyldisalazane (HMDS). HMDS acts to draw out any remaining liquid, bringing the cells to the same state of dehydration as can be obtained with critical point drying. It has gained notable focus in the past decade for this attribute, though its classification as both highly toxic in its liquid and gaseous form and its low flash point have increased reservations surrounding its use (Hazrin-Chong & Manefield, 2012). Determining the most appropriate combination of these protocols is an important step prior to the undertaking of any study using electron microscopy, in order to minimise the appearance of artefacts within your cell type. Work herein focused on a comparison of the morphology of normal B cells compared to patient derived CLL cells, using a range of microscopy techniques including brightfield/epifluorescence microscopy, LSCM and HIM, and the interaction of these cell types with bare Fe_2O_3 nanoparticles.

Another important consideration in the generation of a nanoparticle for therapeutic purposes is the characterisation of the toxicity of the bulk material, i.e. the bare Fe_2O_3 nanoparticle. Whilst there is much research on the toxicity of Fe_2O_3 nanoparticles on numerous differing cell lines and primary tissue types; and both *in vitro* and *in vivo,* we are unaware of any such studies in B lymphocytes. Much work into the study of the toxic effects of Fe_2O_3 nanoparticles on differing tissues results from the

use of such nanoparticles in MRI contrast imaging, as further discussed in Introduction Section 1.2. There are several advantages to the use of cell lines as an initial tool for research in the investigation of toxicity of nanoparticles on cell and tissue types (Ray, Yu, & Fu, 2009). This initial approach can reveal effects on the target cells without the presence of secondary effects such as inflammation, that may mask findings. It can allow for the identification of the effects of the nanoparticle on just the cell or tissue type of interest, without the nanoparticle being subjected to systemic effects which may interfere with the initial effects and findings. One of the most beneficial aspects of using cell lines and *in vitro* studies is that it allows for rapid results, which are efficient and cost-effective, and the results of such studies can be used to translate for use in cell samples which may be more limited in supply or difficult to obtain, such as *ex vivo* patient samples (Huang, Wu, & Aronstam, 2010). Previous studies have shown that bare Fe_2O_3 nanoparticles induces inflammation in lung liver and kidney tissues, in addition to inducing dose-dependent oxidative stress and a reduction in cell viability (Hanini, *et al.*, 2011) (Wu, Tan, Mao, & Zhang, 2010). Prior to the generation of a functionalised nanotherapeutic for the targeting of CLL cells, it is important to determine the levels of toxicity induced by the bare, bulk nanomaterial. This approach allows for the identification of any acute toxicities induced by the bare material, given that subsequent functionalisation may not always successfully encapsulate 100% of the nanoparticles in the suspension. This further allows nanomedicinal researchers to more thoroughly understand the levels of toxicity induced by the nanoparticle suspensions. This chapter will investigate the effects

of the bare Fe_2O_3 nanoparticle on the I-83 cell line. Within this study, we assessed cell death via apoptosis/necrosis induction through the well-established technique of annexin-V propidium iodide staining and flow cytometric analysis, across a large range of concentrations, in order to determine the most appropriate nanoparticle treatment concentration. This cell death assay was chosen as the most appropriate means of assessing cell death given the number of samples to be assessed in this proof-of-concept toxicity assessment.

Aims

In keeping with the hypothesis laid out, the aim of this chapter was to characterise, and subsequently use the bare Fe_2O_3 nanoparticles as a candidate for functionalisation. This is to enhance the investigation of the interactions of these nanoparticles with B lymphocytes. This was achieved by:

- determination of the size of commercially available Fe_2O_3 nanoparticles using nanoparticle tracking analysis, in order to ensure suitability for use in this study.

- investigation of the morphology of B lymphocytes and subsequently the interaction of these bare Fe_2O_3 nanoparticles using microscopy techniques including brightfield microscopy, laser scanning confocal microscopy and helium ion microscopy.

- examination of the toxic effects of bare Fe_2O_3 nanoparticles on B lymphocytes using acridine orange/ethidium bromide staining to visualise nuclear changes and apoptotic body formation and flow cytometric analysis of annexin V-PI staining to assess cells undergoing apoptosis and necrosis, in order to fully understand the toxicity induced by both the bare and subsequently functionalised nanoparticles.

3.2 Results

3.2.1 Nanoparticle Tracking Analysis

Nanoparticle Tracking Analysis (NTA) was used to determine the initial Fe_2O_3 nanoparticle size distribution and dispersion quality, establish the size of the nanoparticle suspended in ultrapure water and determine the aggregation/clustering state. Figure 3.1 (A) shows the size distribution of the Fe_2O_3 nanoparticles, where the hydrodynamic radius was determined to have a mode of 210 ± 12.2 nm and a mean of 252.6 ± 8.0nm (n=6). As NTA measures the hydrodynamic radius of a nanoparticle, this larger size accounts for adsorption of solution to the nanoparticle surface whilst in suspension. The second, smaller peak, indicated by red arrow below in Figure 3.1 (B), presents the secondary aggregation of the nanoparticles in solution. Table 3.1 shows the additional parameters measured using NTA, including the total concentration of nanoparticles measured per frame and the average drift velocity of the nanoparticles. Determining the aggregation state of nanoparticles in solution can be of particular benefit when subsequent functionalisation of nanoparticles is intended. In addition to size and dispersity determination using NTA analysis, DLS was utilised to determine the particle size mode and polydispersity index (PDI), where Fe_2O_3 nanoparticles were suspended in Dulbecco's Modified Eagle Serum at a biologically relevant pH of 7.4. As DLS is performed in individual cuvettes, and not a free tubing system, the equipment is optimised to use cell media in order to assess the state of nanoparticles in suspension. A PDI of greater than 0.7 indicates that the sample has a very broad size distribution and is not suitable for DLS analysis

(Pecora, 1985). In this analysis, the PDI was determined to be 0.761 and therefore accurate determination of the size and dispersity could not be accurately obtained (results available in the Appendix 8.1).
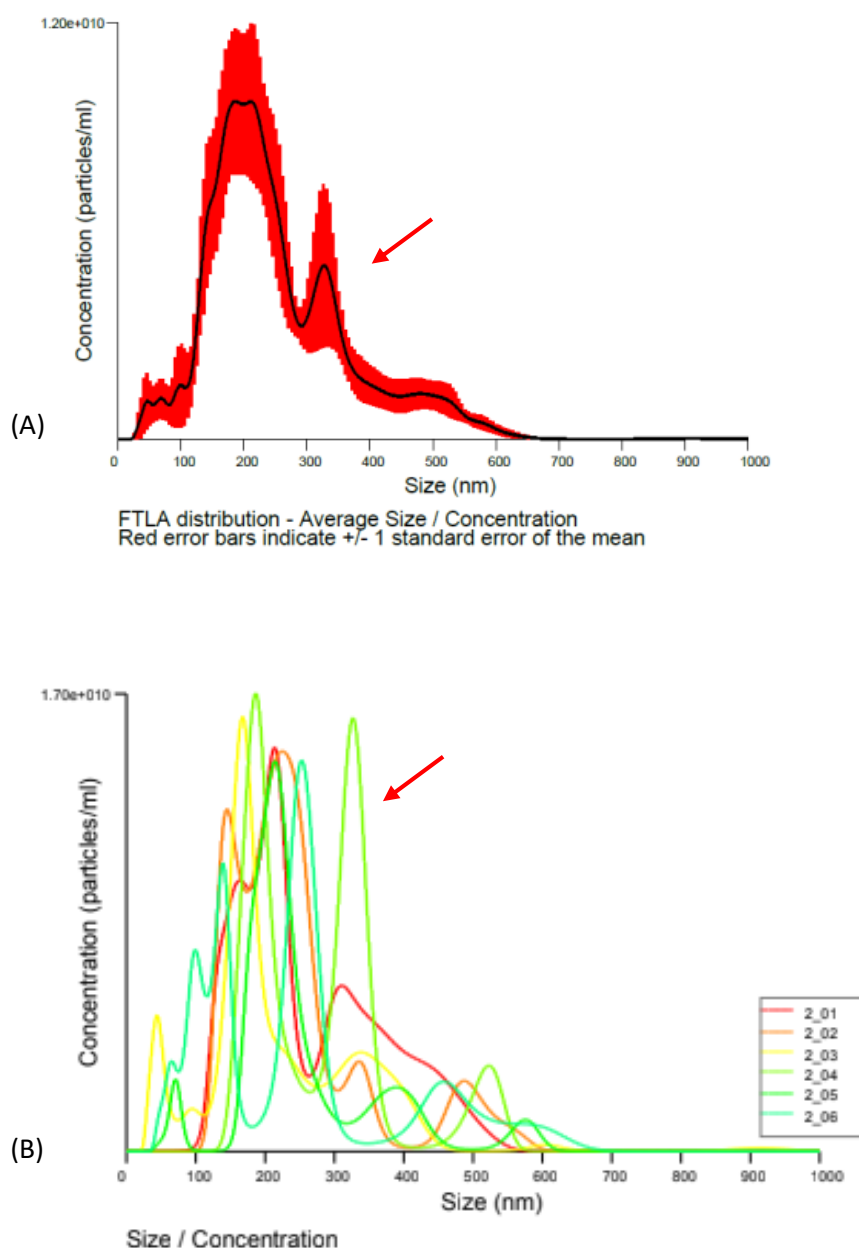
Figure 3.1: NTA analysis of bare Fe$_2$O$_3$ nanoparticles in ultra-pure water. 1µg/mL Fe$_2$O$_3$@APTES were dispersed in ultra-pure dH$_2$0 at 22°C and analysed by NTA. Six, 60 second videos were recorded per sample. (A) Solid black line represents the average of six 60 second recorded videos. Primary peak shown at ~200nm and secondary aggregation is recorded at ~320nm (as indicated by red arrow). Red error bars indicate ± 1 SEM. (B) Illustrates each of the individual six 60 second video represented in Figure 3.1(A). In each sample run, the primary peaks can be seen at ~200nm. A secondary notable peak is observed at ~320nm (as indicated by red arrow).

Table 3.1: Shows the various parameters recorded during NTA analysis of Fe$_2$O$_3$ nanoparticles. The recorded size of nanoparticles in suspension was consistent across readings (n=6).

Parameter	Result
Size distribution as measured by NTA (Mean)	252.6 +/- 8.0 nm
Size distribution as measure by NTA (Mode)	210 +/- 12.2 nm
Dilution factor	10,000
Total concentration per frame	13.23 ± 0.97nm particles/frame
Total concentration per mL	1.91x10^{12} ± 1.39x10^{11} particles/mL
Average drift velocity	563 nm/s
Temperature	24.0°C

3.2.2 Qualitative assessment of the interaction of Fe_2O_3 nanoparticles with the I-83 cell line using epifluorescence microscopy

The CLL cell line, I-83, was imaged using brightfield/epifluorescence microscopy in order to assess the interaction of this cell type with bare Fe_2O_3 nanoparticles. Micrographs show that I-83 cells demonstrate characteristic clumping in culture *in vitro* (shown in Figure 3.1A). These cellular aggregates were determined to be approximately 342 ± 34µm in size (n=3). Following treatment with 25µg/mL bare Fe_2O_3 nanoparticles for 24 hours, results show that I-83 cells form clumps and some smaller cellular aggregates in the presence of nanoparticles (Figure 3.2). These smaller clusters were determined to be approximately 279 ± 25µm in size (n=3). The smaller cell aggregates present in the surrounding media were determined to be approximately 59.1 ± 11µm in size (n=10), and present in each sample imaged. These smaller cellular aggregates were not visualised in the untreated I-83 cell population.
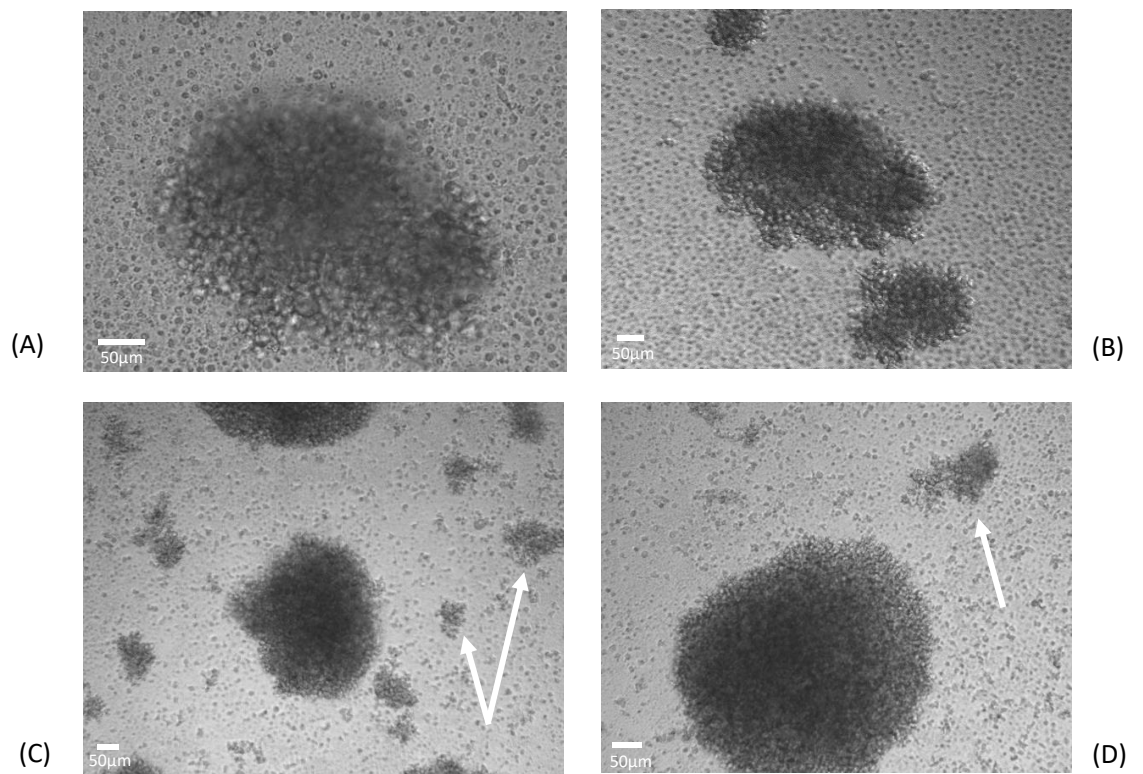
Figure 3.2: The I-83 cell line demonstrates considerable aggregation when cultured in suspension, and treatment with bare Fe₂O₃ nanoparticles effects cell aggregation.
Figure 3.2A and B shows untreated I-83 cells, and Figure 3.2C and D show I-83 cells treated with 25µg/mL bare Fe₂O₃ over 24 hours. Smaller cellular aggregates following treatment with bare 25µg/mL bare Fe₂O₃ are indicated by white arrows.

3.2.3 Qualitative assessment of the interaction of Fe_2O_3 nanoparticles with the I-83 cell line, normal B cells and CLL patient samples, using laser scanning confocal microscopy

Initial uptake of bare Fe_2O_3 NPs by the CLL patient samples, the I-83 cell line and B lymphocytes isolated from healthy donors was next qualitatively measured using laser scanning confocal microscopy. For this work, cells were treated with a concentration of 25µg/mL Fe_2O_3 NPs for 24 hours at 37°C. Nucleus and F-actin were stained with Hoechst 33342 and Rhodamine phalloidin, respectively.

Laser scanning confocal microscopy (LCSM) shows the large nucleus with minimal cytoplasm, characteristic of B cells, to be present in each of the normal B cells, the I-83 cells and CLL patient samples, both prior to, and following treatment with 25µg/mL of NPs for 24 hours.

LSCM micrographs of normal B cells before and after treatment with 25µg/mL of bare Fe_2O_3 NPs is shown in Figure 3.3 where Figure 3.3(A) and Figure 3.3(B) show the untreated normal B cells with a large nucleus and little cytoplasm, and the presence of F-actin proteins surrounding the cell. Figure 3.3(C) shows the normal B cell following 24-hour treatment with 25µg/mL bare Fe_2O_3 NPs. Interaction of the nanoparticles with the cell surface of the normal B cells can be seen, as indicated using white arrow.

The untreated I-83 cells, again with a large nucleus and little cytoplasm as characteristic of B cells are shown in Figure 3.4(A) and Figure 3.4(B). The presence of F-actin proteins surrounding the cell comparable to that of the normal B cells was noted. The I-83 cell following 24-hour

treatment with 25µg/mL bare Fe_2O_3 NPs is shown in Figure 3.4(C). Interaction of the NPs with the cell surface and localisation of the nanoparticles towards the cytoplasmic region can be observed, as indicated using white arrow.

The untreated CLL patient sample cells with the characteristic large nucleus and little cytoplasm is highlighted in Figure 3.5(A) and Figure 3.5(B). The pattern of F-actin presence is again comparable to that of the normal B cells. Figure 3.5(C) shows the CLL patient sample cell following 24-hour treatment with 25µg/mL bare Fe_2O_3 NPs. Interaction of the NPs with the cell surface and localisation of the nanoparticles towards the surface can be observed, as indicated using white arrows. The interaction of NPs with the surface of the CLL patient sample cells is noted to be lower than that of the other two cell types.

Results of this study of nanoparticle interaction with the cells indicate that nanoparticles interact with the surface of and can be internalised by each of the above cell types (shown in Figures 3.3, 3.4 and 3.5). Of note, no nanoparticles were visualised within the nucleus of the cells in any of the three cell types.
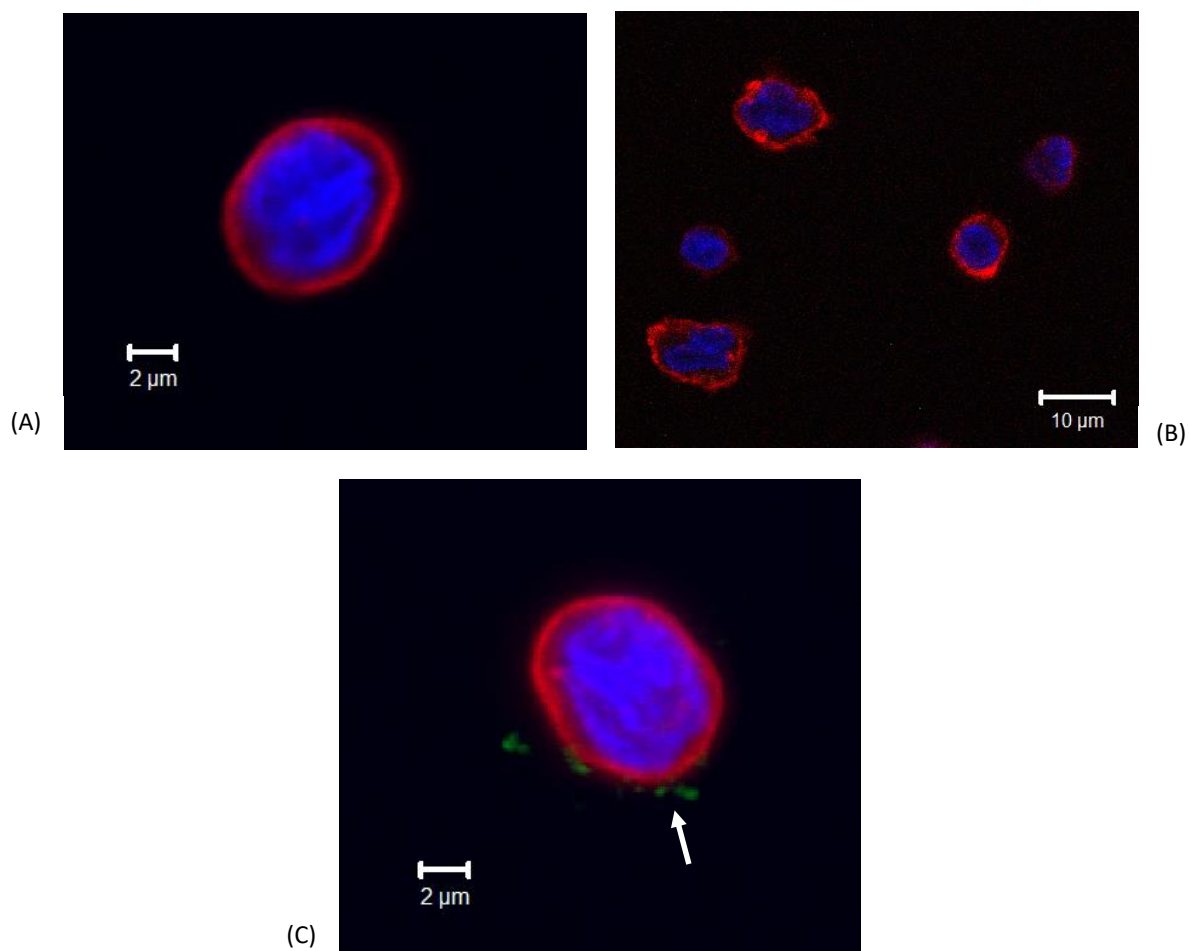
Figure 3.3: B lymphocytes interact with bare Fe₂O₃ nanoparticles following 24 hours incubation. 2×10^5 normal B cells were treated with 25µg/mL bare Fe₂O₃ NPs and the interactions measured using LSCM. Confocal micrographs show cells following staining for nucleus (Hoechst 33342, blue), F-actin (rhodamine phalloidin, red) and green colour indicates the presence of nanoparticles, as visualised using reflectance. Micrographs show untreated normal B cells (Figure 3.3(A) and Figure 3.3(B)). Figure 3.3(C) shows normal B cells following treatment with nanoparticles, as indicated above (n=6).
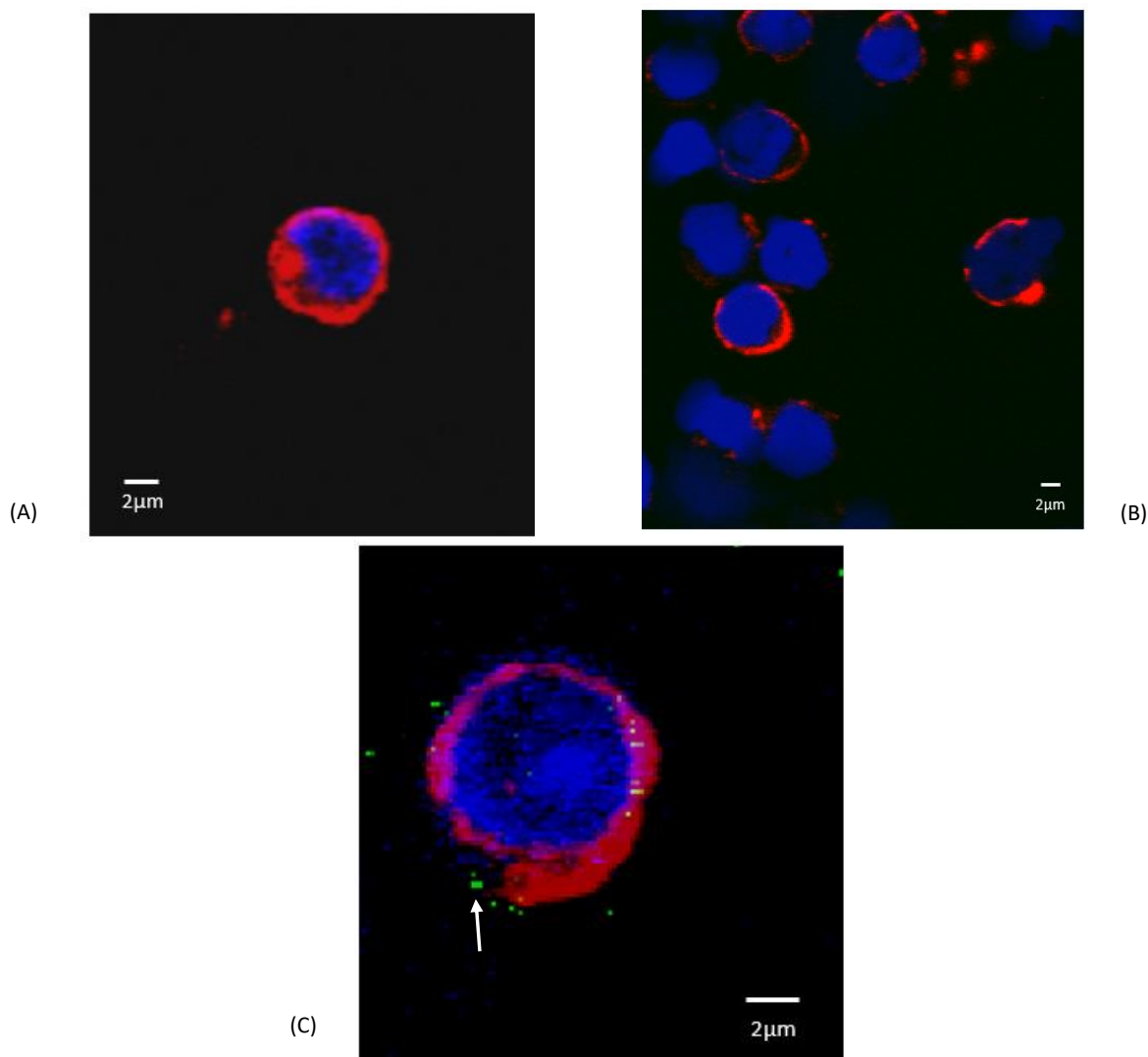
Figure 3.4: I-83 cells interact with bare Fe$_2$O$_3$ nanoparticles following 24 hours incubation. 2×10^5 I-83 cells were treated with 25µg/mL bare Fe$_2$O$_3$ NPs and the interactions measured using LSCM. Confocal micrographs show cells following staining for nucleus (Hoechst 33342, blue), F-actin (rhodamine phalloidin, red) and green colour indicates the presence of nanoparticles, as visualised using reflectance. Micrographs show untreated I-83 cells (Figure 3.4(A) and Figure 3.4(B)). Figure 3.4(C) shows I-83 cells following treatment with nanoparticles, as indicated above. White arrow indicated nanoparticle interaction with the cell surface (n=6).
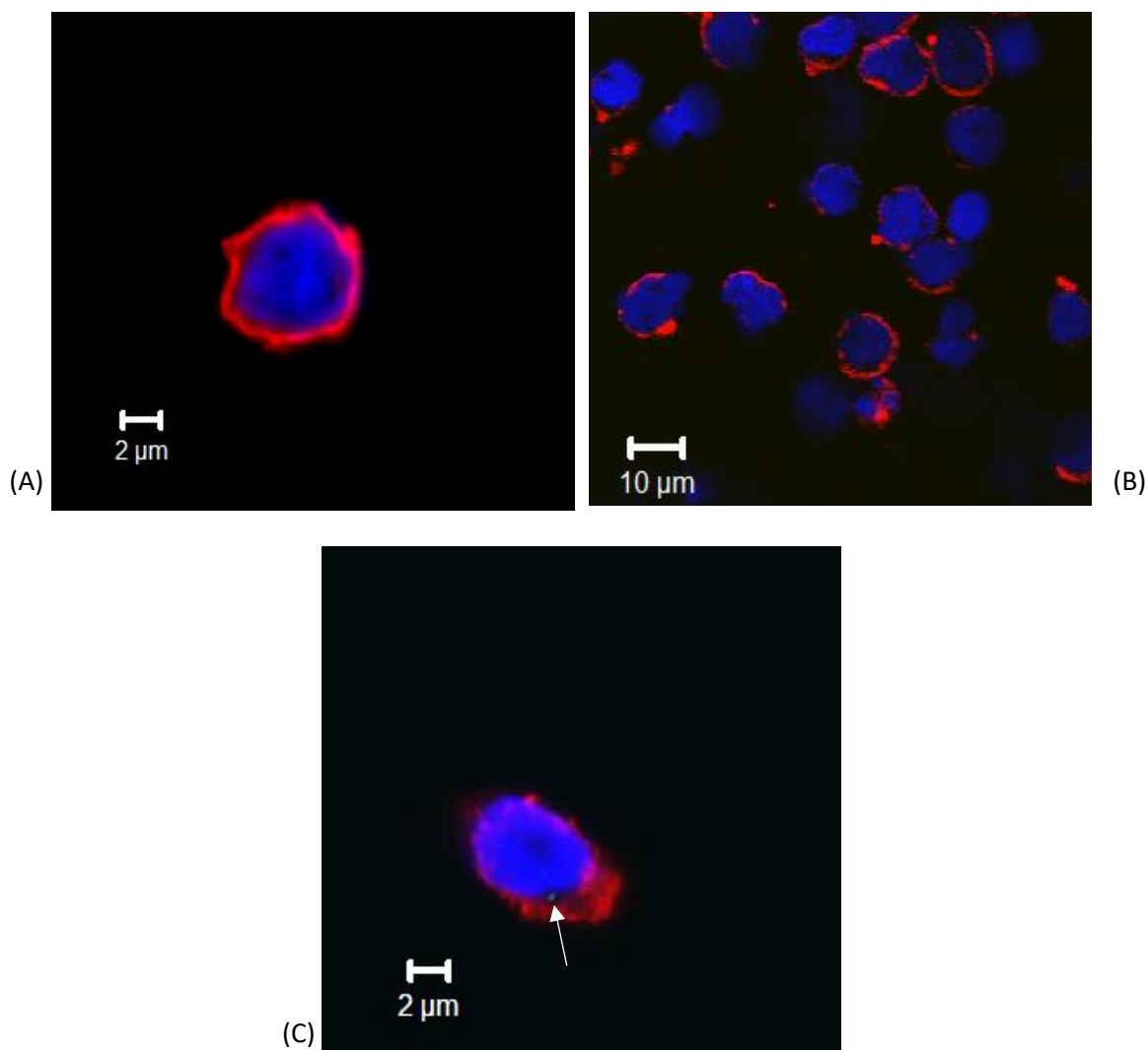
Figure 3.5: P**atient-derived CLL cells will interact and internalise bare Fe$_2$O$_3$ nanoparticles following 24-hour incubation.** 2×10^5 patient-derived CLL cells were treated with 25µg/mL bare Fe2O3 NPs and the interactions measured using LSCM. Confocal micrographs show cells following staining for nucleus (Hoechst 33342, blue), F-actin (rhodamine phalloidin, red) and green colour indicates the presence of nanoparticles, as visualised using reflectance. Micrographs show untreated CLL cells (Figure 3.5(A) and Figure 3.5(B)). Figure 3.5(C) shows CLL cells following treatment with nanoparticles, as indicated above. Nanoparticle internalisation within the cytoplasmic region can be observed in green, as indicated by white arrow (n=6).

3.2.4 Optimisation of fixation and preservation of B lymphocytes for Helium ion microscopy

To further investigate the interaction of nanoparticles with cells, we used helium ion microscopy (HIM). Prior to undertaking this investigational method, we assessed the effects that pre-processing can have on the imaging of B cells, and thus the effect that this pre-processing may have on the investigation of the interactions of nanoparticles with B cells. In order to ensure the optimum fixation and preservation method of cells, both prior to and following treatment with nanoparticles, a number of different methods were employed (see Section 2.4.11). The methods for fixation, dehydration and drying used are discussed in-depth in Section 2, but briefly include:

1. 2.5% Glutaraldehyde overnight at 4°C followed by a gradient of ethanol followed by 30% HMDS (5 mins), 60% HMDS (5 mins), 100% HMDS (10 mins)

2. 2.5% Glutaraldehyde overnight at 4°C and followed by a gradient of ethanol and 60% HMDS (3 mins)

3. 4% Paraformaldehyde overnight at 4°C followed by a gradient of ethanol and by 100% acetone (3 mins)

4. 2.5% Glutaraldehyde + 0.1M Sodium Cacodylate overnight at 4°C followed by a gradient of ethanol and by 100% acetone (3 mins)

5. 2.5% Glutaraldehyde overnight at 4°C followed by a gradient of ethanol followed air drying

Normal B cells with several villi-like projections from the cell body is reported in Figure 3.6(A). Preparation of these cells using protocol 1 above resulted in little morphological disturbances to the cell membrane. Figure 3.6(B) shows the results of preparation using protocol 2 above, with the normal B cells displaying a more smoothened surface morphology, with less contrast between the cell body and the mounting substrate. Cells remained adherent to the mounting substrate and appeared to retain microvilli projections. Figure 3.6(C) confirms that preparation with protocol 3 above (utilising 4% paraformaldehyde) results in the destruction of the cell membrane of several of the cells imaged with the presence of cell debris evident in all samples, and with the majority of samples imaged displaying evidence of whole intact cells. The addition of 0.1M sodium cacodylate to 2.5% glutaraldehyde appeared to again reduce the incidence of ruptured cell membranes, is shown in Figure 3.6(D). This resulted in a smoothening of the cell surface comparable to that of cells observed in Figure 3.6(B). Figure 3.4(E) shows fixation using 2.5% glutaraldehyde overnight at 4°C, dehydration using stepwise ethanol increments as discussed above and air-drying, where the cells appear to have again retained much of their morphological characteristics as visualised in other images, but with a slight smoothing noted on the surface of the cells when compared to that of Figure 3.6A. However, these cells did demonstrate a notable roughening of the surface when compared to that of Figures 3.6(B) and 3.6(D).

The drying step employed following the dehydration protocol appeared to have the most profound consequences on the cell prior to imaging.

Air drying appeared to result in slight rounding of the cells, whilst drying with acetone resulted in an appearance of the lack of integrity of the cell membrane and less ease of visualisation of the cells on their mount of borosilicate glass. Drying with HMDS appeared to result in the increased maintenance of integrity of the cell membrane with visible cellular protrusions and the distinct visualisation of the cell body when compared to the mount of the borosilicate glass coverslip. Furthermore, results indicate that lymphocytes that are fixed prior to mounting on coverslips appeared rounded and smooth, and therefore not representative of the native B lymphocyte (Alexander, Sanders, & Braylan, 1976).
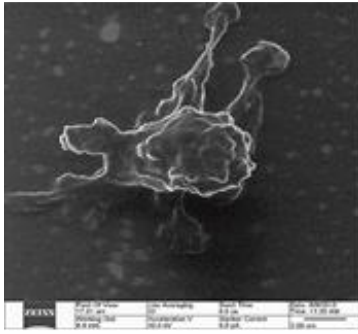
(A)
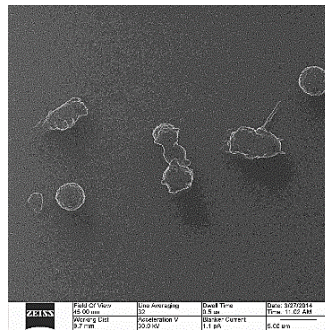
(B)
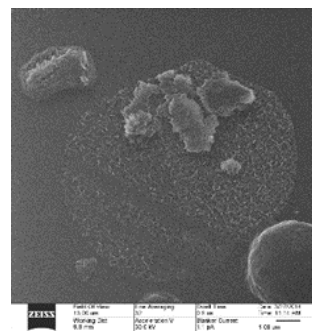
(C)
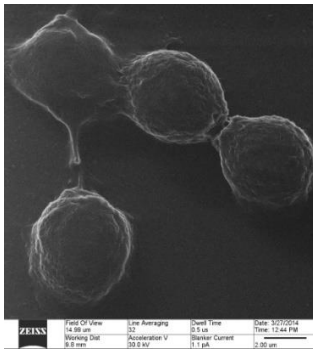
(D)
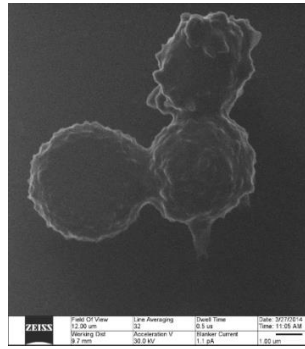
(E)

Figure 3.6: Helium ion micrographs showing the effects of pre-processing on normal B lymphocytes. Figure 3.6(A) shows that fixation using 2.5% glutaraldehyde and final drying using HMDS gradients allow the visualisation of cellular, villous-like projections, with a roughening of the surface morphology apparent. Figure 3.6(B) shows fixation using 2.5% glutaraldehyde and drying using 60% HMDS results in the retention of surface morphology though with a notable smoothening of the cell surface. Microvilli projections were apparent in all samples visualised. Figure 3.6(C) shows fixation using 4% paraformaldehyde followed by drying with 100% acetone, where the cells are observed to have undergone membrane destruction and significant cellular damage. This result was only noted in samples prepared using this protocol. Figure 3.6(D) shows fixation using 2.5% glutaraldehyde supplemented with 0.1M sodium cacodylate overnight at 4°C and subsequent drying using 100% acetone, which has resulted in again loss of membrane retention and loss of surface structures, providing little contrast between the imaging surface and the biological material. Figure 3.6(E) shows fixation using 2.5% glutaraldehyde overnight at 4°C, and subsequent air-drying, where the cells appear to have retained much of their surface morphology, with a slight ruffling of the surface being noted. Images are representative images of 3 dehydration protocol investigations. Scale bars and imaging parameters can be seen along the bottom right of each image (n=22 patients).

3.2.5 Imaging and recording the interactions of Fe_2O_3 nanoparticles with B lymphocytes, utilising helium ion microscopy.

Nanoparticle interaction with the surface of both normal B cells and patient derived CLL cells was investigated using HIM. As this technique works based on ion diffraction, organic materials of a mid-range surface area generally yield a lighter appearance than the substrate on which they are based. Similarly, particles within the nanoscale range appear as even lighter (close to white) due to the extent of ion diffraction. Normal B cells and patient-derived CLL cells were treated with 25μg/mL of bare Fe_2O_3 nanoparticles for 24 hours. and prepared for helium ion microscopy using protocol 1 (see section 2.4.11 above). Patient-derived CLL cells were first determined as CD19+ following flow cytometric analysis, in order to ensure a pure population of CLL cells (Figure 3.7 below).
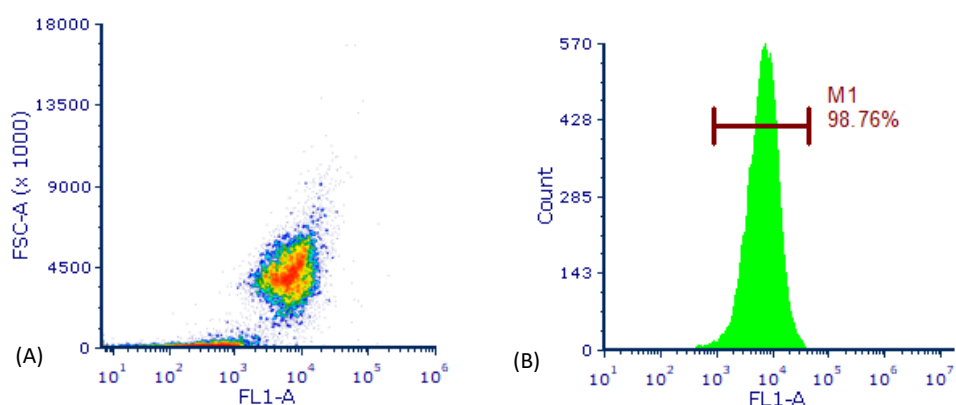
Figure 3.7: **Normal B cells isolated from healthy donors were determined as ≥95% CD19+. PBMCs were isolated from the peripheral blood by density gradient centrifugation and the B cell population was purified by MACs B cell Isolation kit. Cells were stained with anti-CD19 AlexaFluor488 and analysed by flow cytometry.** Representative flow cytometry plots illustrating CD19 positivity of >95% of the normal B cell population. (A) Dot plot shows the FSC/SSC plot and the identification of the lymphocyte population. (B) Histogram shows the percentage of CD19+ cells within the lymphocyte population (n=3).

Similar to morphology noted in previous section, normal B cells have a ruffled cell surface with numerous large microvilli which appear to interact with adjacent cells (Figure 3.8 (A)(B)(C). Normal B cell were treated for 24 hours with 25µg/mL Fe_2O_3 nanoparticles and analysed by helium ion microscopy (HIM). Several cells were observed having less features and an absence of microvilli was noted in untreated cells (Figure 3.8(D), nanoparticles indicated by white arrow). This effect on cells was only visualised in the cases of cells that had undergone treatment with Fe_2O_3 nanoparticles. The treated B cells were visualised to be a similar size to that of the untreated B cells, with nanoparticles interacting with the surface of the cell type (Figure 3.8(E)). Additionally, normal B cells were found to be of approximately 7µm in size.

Patient-derived CLL cells were also visualised in the same manner as described. CLL cells were seen to display a more smoothened appearance with an absence of a network of microvilli, compared to that present on normal B cells (Figure 3.9(A), (B), (C)). Following treatment with 25µg/mL Fe_2O_3 nanoparticles, there were little surface morphological changes observed in the patient-derived CLL cells. Nanoparticles were noted to interact with and adhere to the cell surface (Figure 3.9(D)(E). Additionally, patient-derived CLL cells were found to be of approximately 5µm in size.
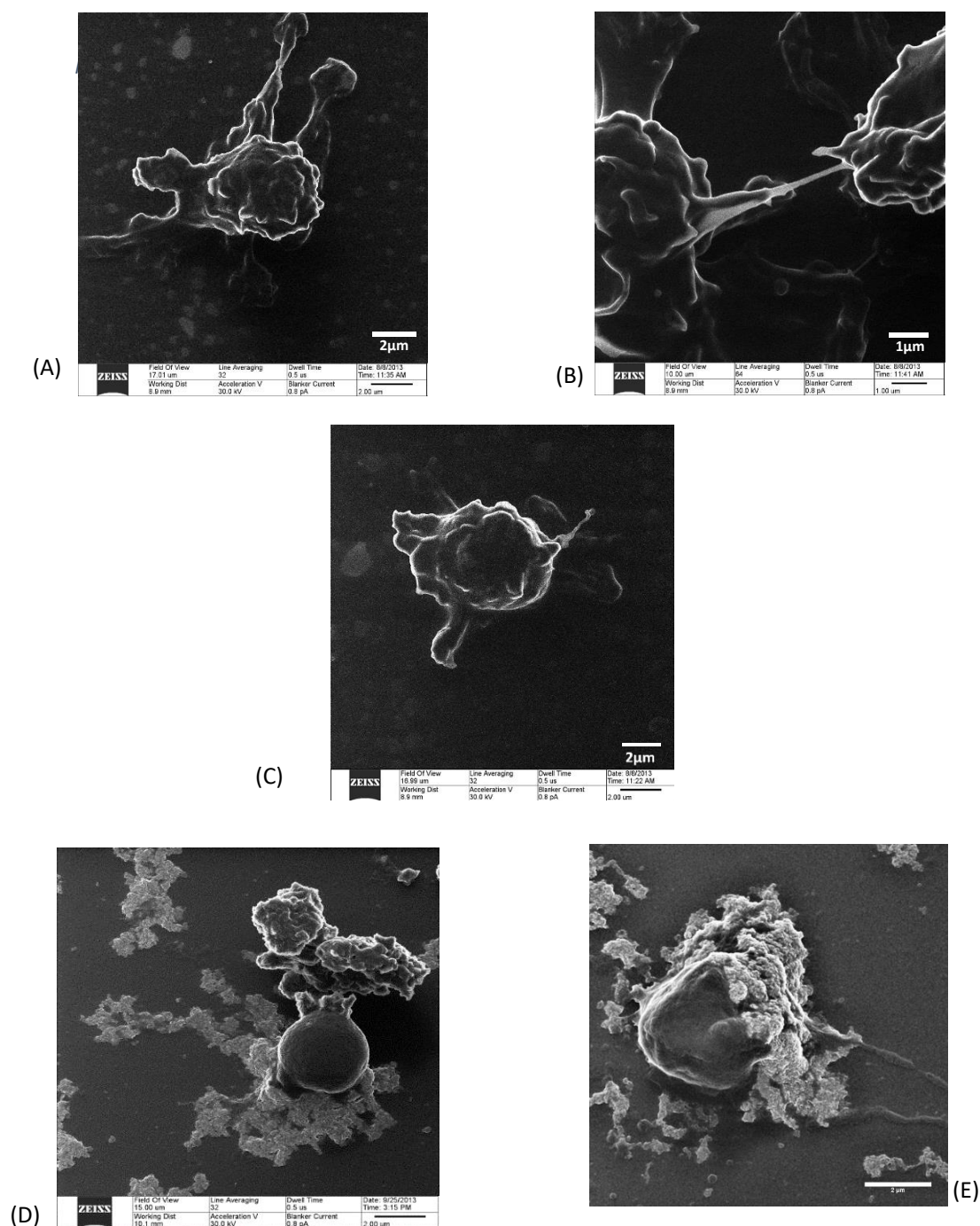
Figure 3.8: **HIM of normal B cells.** Images are representative HIM micrographs of normal B lymphocytes isolated from healthy donors (n=12). Image panel (A) shows microvilli projections from the cell surface interacting with the borosilicate glass surface. Image panel (B) shows that these villi projections from the surface of normal B lymphocyte appear to be in contact with one another. This was observed in a number of normal B cells imaged. Figure panel (C) shows normal B cells with felr microvilli projections from the cell body. Image panel (D) and (E) shows B cells following treatment with 25µg/mL Fe_2O_3 nanoparticles for 24 hours. Each normal B cell population was determined as >95% CD19 positive by flow cytometry following isolation using MACs B cell isolation kit (n=22).
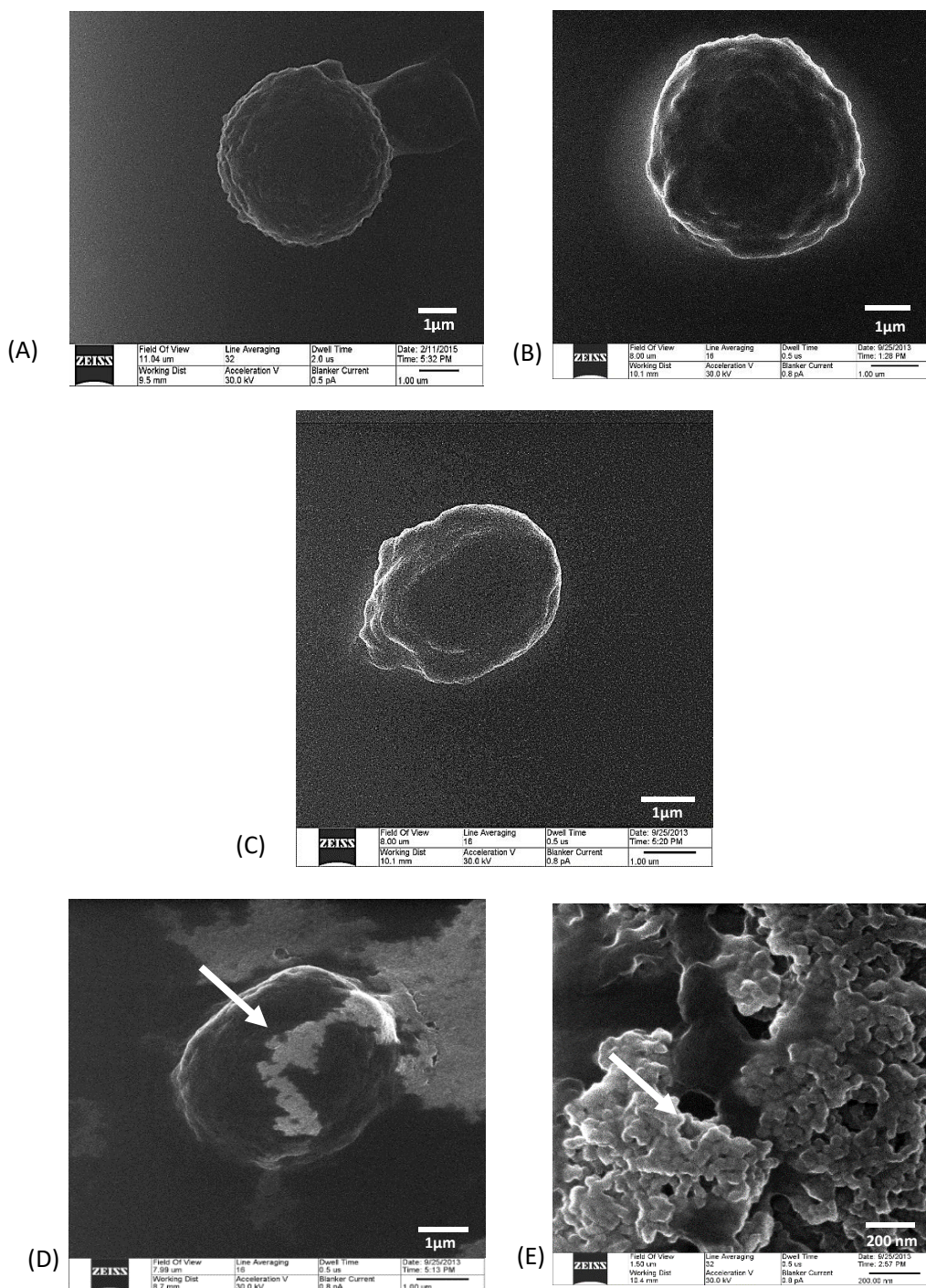
Figure 3.9: Patient-derived CLL cells appear as a smoothened surface morphology, with a spherical shape. Representative HIM micrograph of CLL patient samples prior to treatment with nanoparticles, shown in Figure panels (A)(B)(C). Figure panel (D) shows the interaction of Fe_2O_3 nanoparticles on the surface of CLL patient sample cells, following treatment for 24 hours with 25μg/mL Fe_2O_3 nanoparticles. Figure panel (E) shows the same cell as shown in Figure panel (D) at an increased magnification (200nm scale), showing the interaction of the Fe_2O_3 nanoparticles with the cell surface. Area observed in grey (as indicated by white arrows) shows the coating and dispersion of nanoparticles over the surface of the cell (n=6). In each of the below micrographs, inorganic material (the nanoparticles) appear in a much lighter grey colour (also indicated by white arrows), as can be seen in (D), where the nanoparticles can be seen dispersed across the surface of the CLL patient sample (n=6).

144

3.2.6 Determination of toxicity of bare Fe_2O_3 nanoparticles on the I-83 cell line

In order to determine the levels of cell death induced in I-83 cells following treatment with bare Fe_2O_3 nanoparticles, cells were stained with ethidium bromide-acridine orange (EtO) cell stain following treatment with 0.3-300µg/mL bare Fe_2O_3 NPs for 24 hours and cell death was assessed using fluorescence microscopy (Figure 3.10). The IC50 of bare Fe_2O_3 nanoparticles on the I-83 cell line was determined as approximately 18.6µg/mL, using GraphPad Prism analysis software. Significant levels of cell death were observed following treatment with greater than 30µg/mL of bare Fe_2O_3 nanoparticles, when compared to the no treatment sample (n=3; $p<0.001$).
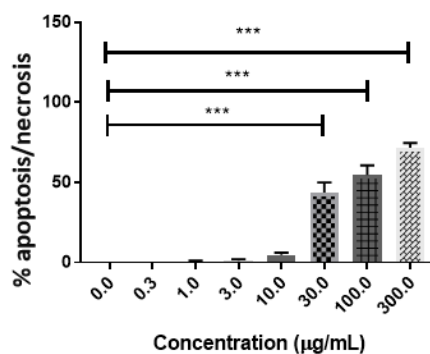
Figure 3.10: **Treatment with bare Fe_2O_3 nanoparticles significantly effects the viability of I-83 cells, as measured by ethidium bromide-acridine orange staining.** $3x10^5$ cells/well I-83 cells were treated with bare Fe_2O_3 nanoparticles for 24 hours over a range of concentrations as indicated, and cell viability was assessed using ethidium bromide-acridine orange staining followed by analysis using fluorescent microscopy (n=3; $p<0.001$; one-way ANOVA with multiple comparisons and Dunnet's post-test).

Next, we assessed whether the NP induced cell death was as a result of apoptosis or necrosis. I-83 cells were treated with bare Fe_2O_3 nanoparticles at a concentration range of 0, 10, 25, 50 and 100µg/mL; stained with annexin-V and PI and analysed by the flow cytometer for apoptosis/necrosis. Briefly, early stage apoptosis can be observed through the staining of phosphatidylserine (PS) on the surface of cells (utilising Annexin V stain) and late stage apoptosis/necrosis can be observed through staining with PI, which is taken up by dead cells (as can be seen in Figure 3.14 below).

Bare Fe_2O_3 nanoparticles were found to induce significant levels of apoptosis/necrosis following treatment with a concentration greater than 25µg/mL over 24 hours in each of the I-83 cell line, as shown in Figure 3.11 (n=3; $p<0.001$). Following treatment with 10µg/mL bare Fe_2O_3 NPs over 24 hours, approximately 4% apoptosis/necrosis was observed. Following treatment with 25µg/mL bare Fe_2O_3 NPs over 24 hours, approximately 17% apoptosis/necrosis was observed, with approximately 39% apoptosis/necrosis observed following treatment with 50µg/mL and 100µg/mL bare Fe_2O_3 NPs. Representative flow cytometric plots of both untreated I-83 cells and I-83 cells following treatment with 100µg/mL bare Fe_2O_3 NPs (Figure 3.14) demonstrate that I-83 cells undergo apoptosis/necrosis following treatment, with the majority of these cells determined to be in the early apoptotic phase at 24 hours.

Bare Fe$_2$O$_3$ nanoparticle treatment significantly impacts the cell viabilityof I-83 cells at 24 hours
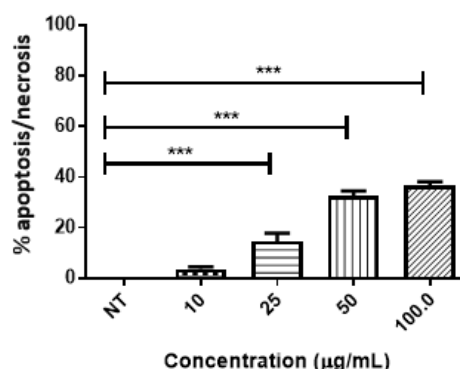
Figure 3.11: **Treatment with bare Fe$_2$O$_3$ nanoparticles induces significant levels of apoptosis/necrosis in I-83 cells, as measured by annexin V-PI staining.** 3×10^5 cells/well I-83 cells were treated with bare Fe$_2$O$_3$ nanoparticles for 24 hours over a range of concentrations as indicated. Apoptosis/necrosis was assessed using Annexin V-PI staining and subsequent flow cytometric analysis. Significant cell death was observed following treatment with 25µg/mL of bare Fe$_2$O$_3$ nanoparticles (n=3; $p<0.001$; one-way ANOVA with multiple comparisons and Dunnett's post-test).

Following on from a determination as to the levels of apoptosis/necrosis induced in the I-83 cell line following treatment with bare Fe$_2$O$_3$ NPs at 24 hours, we assessed the levels of apoptosis/necrosis induced in normal B cells following the same treatment. As these cells are a primary cell type, we eliminated treatment with 10µg/mL Fe$_2$O$_3$ NPs from the treatment range given its demonstrated lack of efficacy in the I-83 cells.

Normal B cells were treated with bare Fe$_2$O$_3$ nanoparticles at a concentration range of 0, 25, 50 and 100µg/mL; stained with annexin-V and PI and analysed by the flow cytometer for apoptosis/necrosis. Bare Fe$_2$O$_3$ nanoparticles were found to induce significant levels of apoptosis/necrosis following treatment with a concentration greater than 25µg/mL over 24 hours in the normal B cells, as shown in Figure 3.12 (n=3; $p<0.001$). Following treatment with 25µg/mL bare Fe$_2$O$_3$ NPs over

24 hours, approximately 40% apoptosis/necrosis was observed, with approximately 61% and 82% apoptosis/necrosis observed following treatment with 50μg/mL and 100μg/mL bare Fe_2O_3 NPs, respectively. Representative flow cytometric plots of both untreated normal B cells and normal B cells following treatment with 100μg/mL bare Fe_2O_3 NPs (Figure 3.14) demonstrate that normal B cells undergo apoptosis/necrosis following treatment, with the majority of these cells determined to be in the late apoptotic/early necrotic phase at 24 hours.
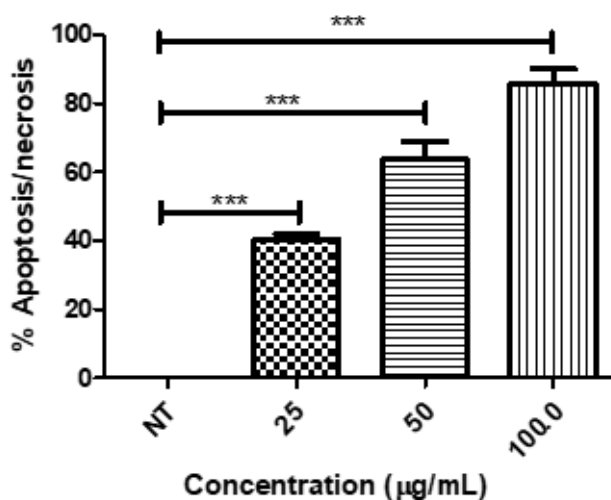
Figure 3.12: **Treatment with bare Fe_2O_3 nanoparticles induces significant levels of apoptosis/necrosis in normal B cells, as measured by annexin V-PI staining.** $5x10^5$ cells/well normal B cells were treated with bare Fe_2O_3 nanoparticles for 24 hours over a range of nanoparticle concentrations as indicated above, and cell viability was assessed using Annexin V-PI staining and subsequent flow cytometric analysis. Significant cell death was observed following treatment with 25μg/mL of bare Fe_2O_3 nanoparticles (n=3; $p<0.001$, one-way ANOVA with multiple comparisons and Dunnett's post-test).

Following on from a determination as to the levels of apoptosis/necrosis induced in both the I-83 cell line and normal B cells following treatment with bare Fe_2O_3 NPs at 24 hours, we assessed the levels of apoptosis/necrosis induced in patient-derived CLL cells, following the same treatment. As was the case in normal B cells above, as these cells are a primary cell type we eliminated treatment with 10µg/mL Fe_2O_3 NPs from the treatment range given its demonstrated lack of efficacy in the I-83 cells.

Patient-derived CLL cells were treated with bare Fe_2O_3 nanoparticles at a concentration range of 0, 25, 50 and 100µg/mL; stained with annexin-V and PI and analysed by the flow cytometer for apoptosis/necrosis. Bare Fe_2O_3 nanoparticles were found to induce significant levels of apoptosis/necrosis following treatment with a concentration greater than 25µg/mL over 24 hours in the patient-derived CLL cells, as shown in Figure 3.13 (n=3; $p<0.001$). Following treatment with 25µg/mL bare Fe_2O_3 NPs over 24 hours, approximately 39% apoptosis/necrosis was observed, with approximately 60% and 79% apoptosis/necrosis observed following treatment with 50µg/mL and 100µg/mL bare Fe_2O_3 NPs, respectively. Representative flow cytometric plots of both untreated patient-derived CLL cells and patient-derived CLL cells following treatment with 100µg/mL bare Fe_2O_3 NPs (Figure 3.14) demonstrate that normal B cells undergo apoptosis/necrosis following treatment, with the majority of these cells determined to be in the late apoptotic/early necrotic phase at 24 hours.

Bare Fe$_2$O$_3$ nanoparticle treatment induces signficant levels of apoptosis/necrosis in malignant CLL patient samples
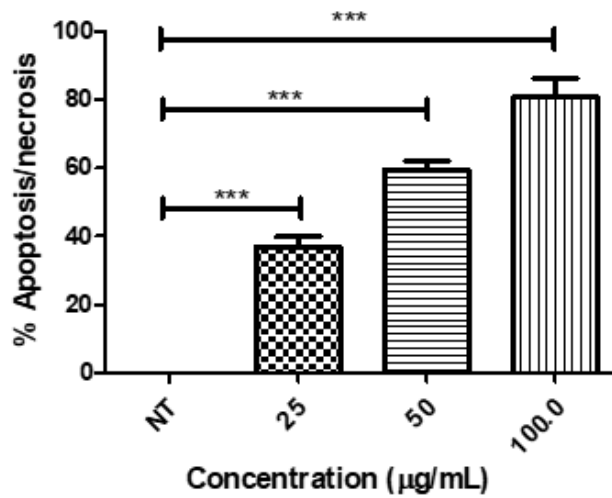
Figure 3.13: **Treatment with bare Fe$_2$O$_3$ nanoparticles induces significant levels of apoptosis/necrosis in CLL patient sample cells, as measured by annexin V-PI staining.** 5x10^5 cells/well patient-derived CLL cells were treated with bare Fe$_2$O$_3$ nanoparticles for 24 hours over a range of nanoparticle concentrations as indicated above, and cell viability was assessed using Annexin V-PI staining and subsequent flow cytometric analysis. Significant cell death was observed following treatment with 25µg/mL of bare Fe$_2$O$_3$ nanoparticles (n=3; $p < 0.001$; one-way ANOVA with multiple comparisons and Dunnett's post-test).
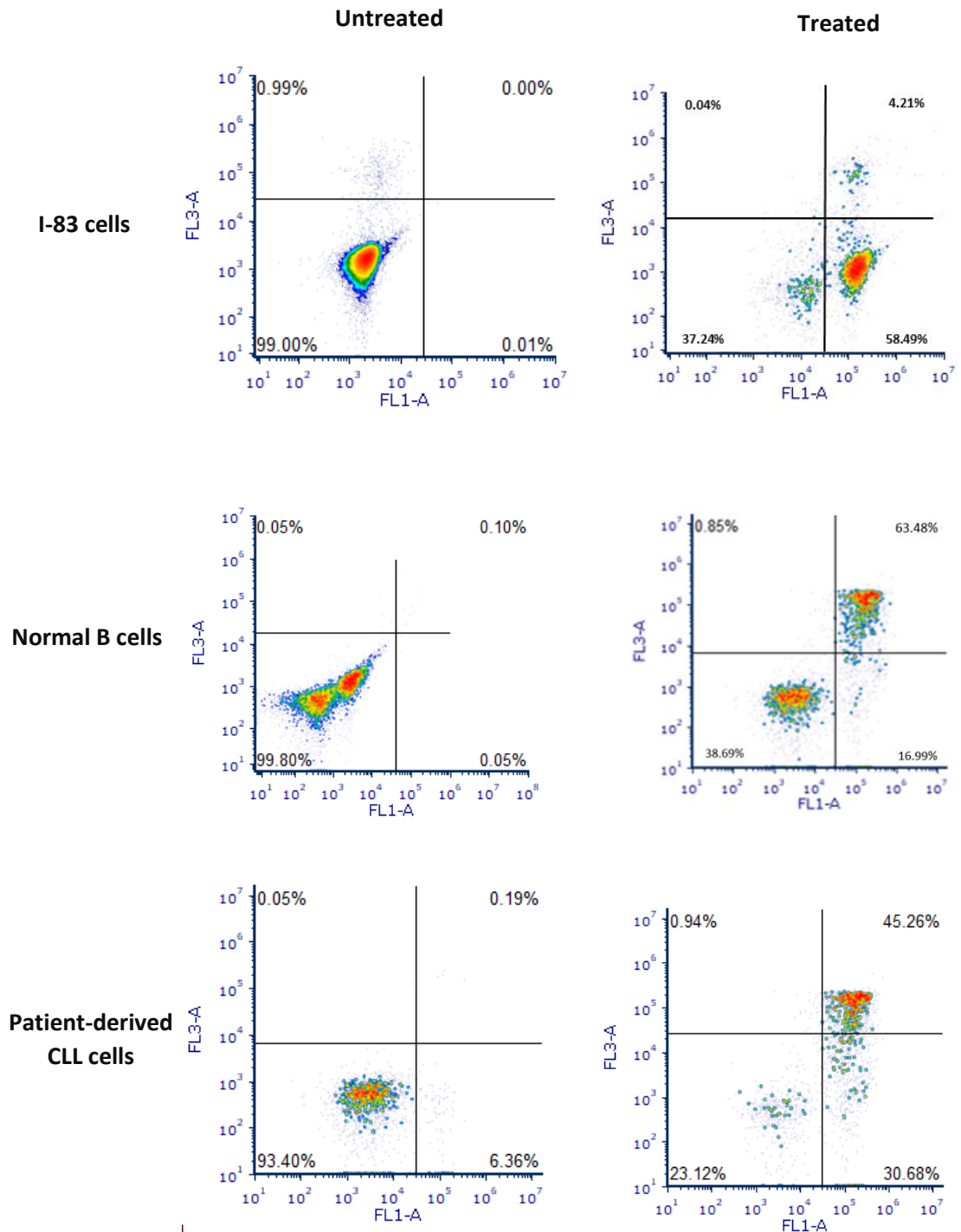
Figure 3.14: **Representative flow cytometric density plots of annexin V-propidium iodide staining of both untreated and Fe₂O₃ treated I-83 cells, normal B cells and patient-derived CLL cells with 100μg/mL Fe₂O₃ nanoparticles.** Each cell type discussed above was treated with 100μg/mL Fe₂O₃ NPs for 24 hours. Treatment with NPs resulted in the induction of apoptosis/necrosis in each cell type, as indicated by an increase in annexin V-PI positive cells within the cell populations. Flow cytometric plots show density plots of annexin V (X-axis) and PI (Y-axis) staining. In each plot, the lower right quadrant represents annexin V-PI negative cells. The lower left quadrant represents annexin V positive, PI negative cells; an indicator of early apoptosis. The upper right quadrant represents annexin V-PI positive cells; an indicator of late apoptosis/necrosis. The upper left quadrant represents annexin V negative, PI positive cells; an indicator of necrosis.

3.3 Discussion

There is much work ongoing in the field of nanotechnology and nanomedicine, investigating the use of nanoparticles in a wide variety of applications. For an accurate and reproducible investigation to be conducted in this field, it is important to understand the various techniques that may be employed in this investigation and their relative role and suitability in the investigation of the nanoparticle of interest. 50nm Fe_2O_3 nanoparticles employed throughout the course of this body of work were purchased commercially, in order to ensure consistency and uniformity of nanoparticle size (report displaying size determination using BET analysis may be found in the Appendix 8.2, as measured by Sigma Aldrich).

NTA is a robust and validated technique that has been employed in the investigation of nanoparticle size and stability for many years. A large interlaboratory comparison resulting from an industry-academia collaboration between TCD and Malvern has allowed for the generation and refinement of stringent SOPs to be developed for the use of Nanosight the characterisation of nanoparticles (Hole, *et al.*, 2013). Thus, NTA was employed as a first-line method in the verification of the size of commercially-available Fe_2O_3 nanoparticles. Results of NTA show the hydrodynamic radius of bare Fe_2O_3 nanoparticles measuring at a mean of 252.6 ± 8nm. This increase in size of the bare nanoparticles is consistent with other reports, and can be attributed to hygroscopicity, or the adsorption and creation of a thin water film on the surface of the nanoparticles (Yesilbas & Boily, 2016) (Park, Kim, & Miller, 2009). Size determination and stability in solution is an important measurement in

the assessment of nanoparticles intended for *in vitro* use, as it provides an understanding into the potential behaviour and interactions of nanoparticles in an aqueous environment. A critical finding from this investigation is an understanding of the aggregation state, and stability of these nanoparticles. Results of NTA show that the aggregation state of Fe_2O_3 nanoparticles in solution is minimal, demonstrating the potential suitability of these nanoparticles for subsequent functionalisation due to the availability and provision of access to the surface of the nanoparticles, and an increased understanding as to the approach that will be required for the functionalisation of these nanoparticles. One outlier peak was observed during one of six NTA assessments, providing a secondary peak in our analyses. The provision of secondary peak detection is a beneficial aspect of NTA that is often not available with other conventional nanoparticle characterisation techniques, such as DLS; a technique which is weighted towards large particles and provides just an average size (Hole*, et al.*, 2013). A hydrodynamic radius of approximately 200nm, as shown here, would provide a suitable size for the subsequent functionalisation and is of a suitable size for future cellular uptake studies (Behzadi, *et al.*, 2017).

Having shown the average hydrodynamic radius of Fe_2O_3 nanoparticles in ultra-pure water, an investigation into the average hydrodynamic diameter of bare Fe_2O_3 nanoparticles suspended in DMEM supplemented with 10% FBS at a biologically relevant pH of 7.4 was conducted using DLS. During the course of these measurements, the Zetasizer, the instrument used to perform DLS, was unable to determine

the size or stability of these particle suspensions. Several error reports were generated and the PDI reading was extremely high at 0.761. A PDI reading of greater than 0.7 may be indicative of a broad range of particle size, or the presence of a high percentage of aggregation within the sample. High levels of aggregation of nanoparticles upon exposure to serum-containing media have been regularly reported within the field (Romer, *et al.*, 2011) (Moore, *et al.*, 2015) (Keller, *et al.*, 2010). It is for this reason, that alternate methods of size determination of nanoparticles in suspension has been preferred over DLS in recent years (Hole, *et al.,* 2013). The use of NTA in determining the size of nanoparticles dispersed in serum-containing media has been shown to yield successful results (Hole, *et al.,* 2013). The nanoparticles will adsorb proteins to their surface creating the protein corona, and measurements will therefore yield larger size results (Nguyen & Lee, 2017). Additionally, aggregation state may also be seen and measured, with little or no bias to the larger aggregates, as is often reported with DLS measurements (Moore, *et al.,* 2015). Future work here may assess the size of our nanoparticles dispersed in cell media, a measurement which can be of great use in in-depth analyses of uptake mechanisms and when particularly interested in the effects of size on toxicity and uptake of nanoparticles. Of note, one disadvantage with the use of NTA in the analysis of nanoparticles dispersed in cell media is the absorption of cell serum proteins to the surface of the tubing within the NTA machine (Hole, *et al.*, 2013). This can affect the workings of the machine and future analyses focusing on the analysis of nanoparticles dispersed

in ultra-pure water, and given the cost of these pieces of equipment, is the rationale for not having assessed this within this thesis.

Whilst NTA has been shown to be of great use in the determination of the hydrodynamic size of nanoparticles, particularly in validation studies investigating the possible fate of a nanoparticle *in vivo,* this method of measurement alone may not be sufficient when the interest of the study is subsequent functionalisation. For this reason, it is important to consider further analysis of the nanoparticle population following the employment of any coating or preparation for subsequent functionalisation. Subsequent investigative methods such as microscopy – both brightfield and fluorescent, can be of great use in the investigation of the interaction of nanoparticles with cells (Egerton, 2005) (Bell, 2009) (Paddock, 2000).

Whilst each microscopy technique has its own advantages and disadvantages, when used in conjunction with one another they can provide a level of detail that can be of huge benefit in the study of nanoparticle/cell interactions. Large cellular aggregates are typical of the I-83 cell line in culture, however, treatment with bare nanoparticles results in reduced cellular aggregation. This could possibly be as a result of nanoparticles on the surface of the cells preventing the cells from forming their usual large aggregates. This effect has been reported previously in other cell types and with other particle types (Kong, *et al.,* 2008) (Huang, *et al.*, 2012) (Verma & Stellacci, 2010) (Safi, *et al.,* 2011).

The method undertaken in the pre-processing of cells prior to imaging can have an effect on the results of studies, and in some cases has

been shown to result in artefacts (Butt, *et al.*, 1990) (Watson, 1997) (Ayache *et al.* 2010). The production of artefacts such as effects to the cell membrane, or destruction of cells, as a direct result of the pre-processing of cells is particularly problematic in the case of electron microscopy as this method of imaging is dependent on the actual visualisation of material, and not in the detection of fluorophores and stains (Thompson *et al.* 2016).

For our studies, we used cell fixative prior to adherence of the cells to the borosilicate glass coverslip, as has been conducted by others (Zhang, *et al.,* 2017). We proceeded to investigate the effects of differing combinations of fixative and dehydration procedures on cells for electron microscopy. We found that the use of paraformaldehyde resulted in artefacts such as discussed above, with rounding of the cells and destruction of whole cells being observed. This is thought to be likely as a result of the permeabilisation effects of paraformaldehyde, an artefact which has been described in the literature. Additionally, fixation with paraformaldehyde (at any stage in the imaging preparation process) has been shown to result in antigenicity loss from the cell surface. Both of these factors are a potentially important factors in the decision of which fixative route to choose in the visualisation of B cells (Hagedorn *et al.* 2006) (Hallden *et al.* 1989) (Melan & Sluder, 1992). We determined that fixation of cells that have been allowed to adhere to the surface of the borosilicate glass is best conducted using glutaraldehyde. Throughout this comparison study, we found that that fixation of cells using glutaraldehyde was a suitable fixative for imaging, and that a step-wise dehydration process using increasing concentrations of ethanol

followed by drying with HMDS yield robust and reproducible results, when compared to the use of other fixatives or drying methods.

Helium ion microscopy (HIM) was then employed to investigate the morphology of, and interactions of our nanoparticles, with normal B cells and CLL patient sample cells. We show normal B cells display a roughened appearance, with several microvilli, in contrast to normal B cells that have undergone treatment with bare Fe_2O_3. Interestingly, we observed cells in close proximity being either connected or interacting through these microvilli. Such microvilli have been shown by SEM to be present on the surface of circulating lymphocytes. Here we show findings similar to that which can be found within the literature, though with perhaps more prominent evidence of these microvilli on the cell surface (Majstoravich, *et al.,* 2004). This may be due to the sample preparation method employed in either study, or the lack of sputter coating required in the preparation of cell within this study.

We have shown that patient-derived CLL cells have much less pronounced microvilli compared to normal cells (Oscier, *et al.,* 2016) (Kim, *et al.,* 2000). The cytoskeletal organisation of CLL cells is different to that of normal B cells, with lower detectable levels of F-actin and less cytoskeletal integrity than that of normal B cells (Davids & Burger, 2012). This aberrant cytoskeleton formation has been capitalised upon in the diagnosis of CLL, whereby blood smears of patients with CLL show what have commonly become known as 'smudge cells'. These 'smudge cells' are CLL cells that have been damaged during the physical stresses of the blood smear preparation (Scielzo, *et al.*, 2010) *(*Caligaris-Cappio*, et al.,* 1986). This identifiable morphology of CLL cells have allowed for the

differentiation of CLL cells from other forms of B cell leukaemia's and lymphomas (Caligaris-Cappio, *et al.*, 1986) (Caligaris-Cappio & Hamblin, 1999). Our HIM findings support previous morphological studies using other techniques; with CLL cells being observed as smaller and their cytoskeleton appearing as less dynamic, likely as a result of lower levels of F-actin (Hutchinson, *et al.*, 2014) (Herishanu *et al.* 2014). Other studies have shown cytoskeletal defects in patient-derived CLL cells. The lower levels of actin present in the cytoskeleton of CLL cells may also contribute to the more dynamic appearance and motile cytoskeleton of their normal B cell counterpart, in keeping with our findings here (Hutchinson, *et al.*, 2014). Here, we present a study comparing the morphologies of CLL cells compared to that of normal B cells using helium ion microscopy, the first use of HIM in the study of CLL that we are aware of. We propose HIM as a useful tool in the morphological characterisation of CLL cells and would propose that further studies conducted in this could provide clarification in studies predominantly relying on other microscopy tools, such as laser scanning confocal microscopy or scanning electron microscopy.

Following treatment of cells with bare nanoparticles, the normal B cells appeared to remain relatively unchanged, however a loss in microvilli structure was observed in approximately 10% of cells. The appearance of this morphology was not observed in the untreated normal B cells. This could possibly be as a result of uptake of nanoparticles, though given our further uptake studies we have concluded this to be the less likely scenario, and more likely either an artefact of the interaction with nanoparticles or possibly the initiation of toxic events, as has been

reported in other cell types (Jurkowitz-Alexander, *et al.*, 1992) (Rock & Kono, 2011).

Interestingly, CLL patient samples that had undergone treatment with nanoparticles however appear to have become coated with the nanoparticles in their vicinity, with far less nanoparticles being seen in the surrounding environment (i.e. the borosilicate glass coverslip). Nanoparticles also appeared to be interacting with the surface of the CLL cell at an increased level when compared to that of the normal B cell, indicating that nanoparticles may display a greater affinity for CLL cells and therefore may be a useful tool in the targeting of CLL cells, and this interaction was observed in almost all of the CLL patient sample cells imaged. The reasons behind this increased affinity are currently unclear and might warrant further investigation in future work. We postulate some possible reasons for this; the accumulation of nanoparticles on the surface of the CLL cells may also be as a result of electrostatic forces between the more static nature of the CLL cell membrane and the nanoparticles (Engin, *et al.*, 2017) Or possibly the smoothened appearance of the CLL cell membrane may provide a more suitable surface for adhesion of NPs. Further highlighting the differences between CLL cells and normal B cells, no change in CLL cell morphology was observed following treatment with NPs.

Additionally, LSCM studies were performed on each of the I-83 cells, normal B cells and CLL patient sample cells, both prior to and following treatment with bare Fe_2O_3 nanoparticles. Results of this study demonstrate that bare nanoparticles do interact with and become internalised within each of the cell types assessed, but that interactions

appear to be primarily localised to just the cytoplasmic regions of the cells and do not penetrate the nucleus. Each of the cell type appeared to interact with the bare nanoparticles at a similar level. The interaction and internalisation of the bare nanoparticles within the cells is likely a passive interaction given the low level of interaction and internalisation, and that B cells are not a phagocytic cell type but rely predominantly on clathrin-dependent, or receptor-mediated, endocytosis (Salisbury *et al.,* 1980). The lack of penetration of the nucleus with non-targeted nanoparticles has also been reported in the A549 lung cell line, human breast cancer cells line (MCF7, MCF10A and MDA-MB231) and the PC12 neural cell line using confocal microscopy (Treuel, Jiang, & Nienhaus, 2013) (Chaves, *et al.*, 2017) (Marcus, *et al.*, 2016). It has been reported that in the case of A549 cells, bare NPs can be seen to localise extensively to the lysosomes (Treuel *et al.* 2013).

Subsequent experiments (presented in further chapters) will aim to assess and quantify these cellular interactions, and of importance, assess whether or not it is possible to significantly increase this interaction level which could potentially provide a strong and importance basis in the generation of a targeted nanotherapeutic.

An initial investigation into the levels of cell death induced by bare Fe_2O_3 nanoparticle in each of the I-83 cell line, normal B cells and malignant CLL patient samples, as measured using ethidium bromide staining, demonstrated that there is a significant induction of cytotoxicity following treatment with 30µg/mL, over 24 hours. Following on from this work, we then established that the cell death observed following treatment with bare Fe_2O_3 is a result of apoptosis – both early and late stage apoptosis,

using flow cytometry to measure staining of annexin V-PI. Interestingly, We found that there was little difference in the level of apoptosis/necrosis between any of the three cell types assessed following lower dose treatment (up to 25µg/mL treatment), though the levels of apoptosis and necrosis initiated following treatment with bare NP were found to be lower in the I-83 cell line following treatment with greater than 50µg/mL when compared to that of the normal B cells. Additionally, following treatment with nanoparticles and assessment using annexin v-PI, we observed primarily early stage apoptosis in the I-83 cell line. This finding supports the lower levels of toxicity observed in the I-83 cell line compared to the primary cell types. This provides a robust rationale for the use of flow cytometric analysis of cells stained with Annexin V-PI as a measurement of toxicity of future nanoparticles. Much work has been conducted on the toxic effects of Fe_2O_3 nanoparticles, though few studies have focused on the effects of these nanoparticles on lymphocytes. Many cancer cell lines have been employed in these studies as *in vitro* toxicity models, however it is generally agreed that toxicity data generated can be conflicting and inconsistent, with many of these data generated being only applicable to other identical parameters studied (Bahadar *et al.* 2016). The findings we report here are consistent with the findings of the toxic effects of bare Fe_2O_3 as noted in the literature (approximately 25-200µg/mL), with our findings of an IC50 of 18.6µg/mL being lower than that of bare Fe_2O_3 reported in the literature (~25-200µg/mL) (Jeng & Swanson, 2006) (Gaharwar, Meena, & Rajamani, 2017). These groups utilised microscopic assessment and induction of DNA damage as a

measurement of toxicity, which may account for the differences noted in the induction of cellular toxicity. As discussed in the introduction, there are limited available studies assessing the toxic effects of Fe_2O_3 nanoparticles in B lymphocytes, with the majority of these studies being in T lymphocytes or animal-derived lymphocyte populations (Rajiv, *et al.*, 2016) (Naserzadeh, *et al.,* 2018) (Laffon, *et al.,* 2018) (Gaharwar, *et al.,* 2017). In fact, to date we are unaware of any studies assessing the toxicity of Fe_2O_3 nanoparticles on B lymphocytes, either cell-line or primary derived. Whilst this lack of published work means that there are limited available comparators as to the results of our studies, it does provide additional verification as to the novelty of the work contained within this thesis. Having obtained a deeper understanding of the effects of bare Fe_2O_3 nanoparticles on B lymphocytes, further work within this thesis will focus on the use of this bare Fe_2O_3 nanoparticle in the development of an Fe_2O_3 nanoparticle targeted to CLL cells.

Chapter 4: Development, characterisation and investigation of functionalised Fe_2O_3 nanoparticles in CLL cells

4.1 Introduction

Following the characterisation of the bulk, bare Fe_2O_3 nanoparticle, we proceeded to generate a functionalised nanoparticle targeted towards CLL cells. In addition to the methods employed in Fe_2O_3 nanoparticle synthesis discussed in Chapter 3, the coating (also commonly referred to encapsulation) of Fe_2O_3 nanoparticles can also be of great importance in the successful generation of a functionalised nanoparticle (Lu, Salabas, & Schuth, 2007), with use and choice of stabilising agent will generally be dictated by the ultimate intended purpose of the Fe_2O_3 nanoparticles. Additionally, Fe_2O_3 nanoparticles with bare surfaces also tend to form aggregations due to their strong magnetic properties and van der Waals forces (Ali, *et al.*, 2016), an event that can be minimised using surface coatings. Bare Fe_2O_3 nanoparticles may also undergo significant surface opsonisation with non-specific proteins in their environment, particularly serum proteins, making them considerably more "visible" to phagocytic cells, in addition to often high levels of uptake and retention within the reticuloendothelial system (RES) (Nie, 2010). These processes can contribute to high levels of ultimate clearance *in vivo*, resulting in difficulties in nanoparticle targeting and penetration of solid tumours (Nie, 2010). Encapsulation of Fe_2O_3 nanoparticles has been shown to result in decreased clearance by the RES, increased preferential uptake and targeting, longer blood circulation times and improved pharmacokinetic properties (Cisterna, *et al.*, 2016).

There are a number of coatings or stabilising agents that can be incorporated onto the surface of Fe_2O_3 nanoparticles. These include the

commonly used polyethylene glycol (PEG), dextran, chitosan, gelatin and (3-Aminopropyl) triethoxysilane (APTES). PEG, gelatin and dextran coatings have been shown to improve the biocompatibility of the nanoparticle, improve blood circulation time and improve the stabilisation of the colloidal solution. Chitosan is a linear polysaccharide obtained from the exoskeleton of shellfish and has been shown to be of great benefit in the generation of nanoparticles as a non-viral gene delivery system and is widely used in the biotechnology industry for other applications, given its inherent biocompatibility and biodegradability (Ali, *et al.*, 2016). APTES coated, or silanised, Fe_2O_3 nanoparticles provide an ideal intermediate in the subsequent generation of Fe_2O_3 nanoparticles functionalised with bioactive molecules, due to their terminal amino group. In addition, APTES coated Fe_2O_3 nanoparticles have been shown to increase biocompatibility through the decrease or prevention of free ion leakage from the Fe_2O_3 nanoparticles (Nie, 2010) (Ali, *et al.*, 2016) (Bini *et al.,* 2012). Given the advantages detailed above, APTES stabilised Fe_2O_3 nanoparticles were used in this study. Following the encapsulation of our bare Fe_2O_3 nanoparticles with APTES, it was then important to characterise these nanoparticles for both size and shape, using techniques as discussed in Chapter 2.3. These included the use of nanoparticle tracking analysis (NTA) and microscopy using scanning electron microscopy (SEM). SEM was chosen here for use with Fe_2O_3@APTES as the APTES coating provides sufficient insulation of the sample to avoid over-charging of the samples (when compared to bare Fe_2O_3 nanoparticles) but provides greater resolution than that of some other microscopy techniques such

as brightfield microscopy. Additionally, SEM is more commonly utilised in the investigation of non-organic samples, when compared to the use of HIM, meaning that the process of imaging takes a considerably longer time than that of SEM. For this reason, SEM was an ideal tool for the assessment of nanoparticles alone., without the presence of organic materials.

Due to the characterisation of cell surface markers in CLL, a nanotherapeutic targeted to one of these antigens could be of great benefit in the management of this disease, further supported by the importance of anti-CD20 therapeutics in the field. Traditionally, standard of care in the treatment of CLL typically centred around the use of combination chemo-immunotherapeutic regimens and the management of patient symptoms (Pettijohn & Ma, 2017). With significant advances in the diagnosis of this disease, and a further understanding into the mechanisms of pathogenesis, much work has focused on the generation of targeted therapies for the treatment of CLL. Many of these targeted therapies involve the use of monoclonal antibodies targeting antigens present on the surface of cells, such as CD20. The success of this range of immunotherapies is dependent on the successful targeting of epitopes, or antigenic determinants, present within these surface antigens. Epitope mapping studies have revealed fundamental differences between the antigen epitopes that are recognised by immunotherapeutics and have aided in the highlighting of other potentially effective therapeutics (Klein, *et al.*, 2013) *(Niederfellner, et al.*, 2011). There have been two main immunotherapeutics used in the treatment of chronic lymphocytic leukaemia (CLL); anti-CD20

monoclonal antibody therapy and anti-CD52 monoclonal antibody therapy. As a therapy employed in the treatment of haematological malignancies, treatment with monoclonal anti-CD20 has proven most suitable in the majority of cases given its increased patient tolerability, when compared to treatment with monoclonal anti-CD52 where prolonged treatment may result in an increase in the likelihood of the development of systemic infections (Rieger *et al.,* 2004) (Lundin, *et al.,* 2002).

Within this part of the study it was important to determine a therapeutically relevant target that may be incorporated onto the surface of Fe_2O_3@APTES nanoparticles. This involved the use of flow cytometric analysis to investigate the presence and abundance of 4 surface antigens relevant in CLL: CD5, CD19, CD20 and CD52. Each of these markers are well established surface markers in CLL, with CD20 and CD52 having been utilised therapeutically, yielding good success (Adams & Weiner, 2005) (Albitar, *et al*., 2004) (Bagacean *et al.,* 2016) (Ginaldi, *et al.,* 1998) (Hillmen, *et al*., 2007). Here, using commercially-available monoclonal antibodies designed for flow cytometry, we assess the proof-of-concept use of these markers in the development of a nanotherapeutic. The specificity of these monoclonal antibodies and the relative expression in our model systems, including: the I-83 cell line, normal B cells, whole PBMCs and patient-derived CLL cells, was investigated. A more detailed description as to the relevance of each of these markers in CLL can be found in Chapter 1.3.2.

As demonstrated, here it was important to assess the interaction of functionalised nanoparticles with malignant B cells. This was conducted

using laser scanning confocal microscopy, with the results of this study then being compared to the results of that of uptake of bare Fe_2O_3 nanoparticles. The hypothesis being tested within this chapter is that appropriate functionalisation of our nanoparticles will increase the interactions of nanoparticles with malignant B cells. In addition to investigating the interactions of nanoparticles with these cell types on a qualitative level, quantification of this interaction and uptake is of vital importance. Knowledge of this level of uptake allows for a complete understanding of these interactions, allowing for the optimal development of a targeted therapeutic. In addition to the ability to accurately assess and quantify this uptake of nanoparticle into the cells, knowledge of the uptake mechanism employed by the cell type can provide useful data as to the mechanisms of action of these functionalised nanoparticles.

Macropinocytosis and clathrin-mediated endocytosis are pathways which have been studied extensively in the uptake of nanoparticles by different cell types (Engelberg *et al.,* 2018) (Sun, *et al.,* 2017) (Kou *et al.,* 2013) (Oh & Park, 2014). Macropinocytosis is an actin-dependent regulated form of endocytosis mediating the non-selective uptake of small molecules, nutrients and antigens, initiated from surface membrane ruffles that result in large endocytic vacuoles called macropinomes. It is a highly active form of uptake by macrophages and dendritic cells in the capture of antigens and plays a large role in the process of cell migration (Lim & Gleeson, 2011). Clathrin-mediated endocytosis, also known as receptor-mediated endocytosis, is the uptake of material into the cell from the surface, using clathrin-coated

vesicles. Clathrin-coated vesicles can be formed from many membranous compartments, but the term is usually used to refer to intake through vesicles formed from the plasma membrane. This form of endocytosis is used by all eukaryotic cells, with the pathway using a range of accessory adaptor proteins to package materials for uptake, depending upon the material (McMahon & Boucrot, 2011).

As discussed in Section 1.4.2, there are three main possible mechanisms of cell death induced by therapeutic antibodies: complement-dependent cytotoxicity (CDC), antibody-dependent cytotoxicity (ADCC) and induction of programmed cell death (PCD). Here, we investigate the effects of functionalised nanoparticles on the induction of PCD in both normal B cells and the I-83 cell line. Anti-CD20 monoclonal antibody therapy has been shown to induce apoptosis in both cell lines and patient-derived CLL cells via caspase activation. The induction of PCD in CLL cells has been mainly attributed to Type II anti-CD20 antibodies (further discussed in the Introduction). Previous studies have shown that treatment with monoclonal antibodies have the potential to induce significant apoptosis (above the levels of spontaneous apoptosis threshold of approximately 30%), and that this apoptosis was associated with an increase in the pro-apoptotic BCL2 proteins (Illidge, Cheadle, & Honeychurch, 2014). In order to fully maximise upon the potentials of any monoclonal antibody in the clinic, it is important to assess the effects of treatment with these therapeutics on the induction of apoptosis in cell models ahead of testing these therapeutics on the less dispensable patient-derived CLL cells.

Aims

Given the hypothesis laid out, the overall aim of this chapter was to develop, characterise, and assess the use of functionalised nanoparticles as a proof-of-concept therapeutic nanoparticle that can successfully target and reduce the viability of our CLL cell model, the I-83 cell line. This was achieved by:

- determination of the size of APTES coated Fe_2O_3 nanoparticles using both NTA and SEM, to ensure suitability for use within this study.

- identification of a suitable CLL cell surface marker for targeting with a functionalised nanoparticle using a flow cytometric panel of commonly assessed CLL surface markers.

- functionalisation of APTES-coated Fe_2O_3 nanoparticles with an appropriate monoclonal antibody, for the targeting of a CLL specific antigen on the surface of patient-derived CLL cells.

- qualitative and quantitative assessment of the interaction and uptake of this functionalised nanoparticle using fluorescence intensity measurements and laser scanning confocal microscopy.

- assessment of the level of toxicity exerted upon the I-83 cell line by functionalised nanoparticles.

4.2 Results

4.2.1 Nanoparticle Tracking Analysis of APTES-coated Fe$_2$O$_3$ nanoparticles

APTES-coated (Fe$_2$O$_3$@APTES) were prepared through the incubation of stock Fe$_2$O$_3$ nanoparticles with APTES solution for 24 hours at 4°C.

Similar to the characterisation of bare Fe$_2$O$_3$ nanoparticles described in Chapter 3, nanoparticle Tracking Analysis (NTA) was used to determine the Fe$_2$O@APTES nanoparticle size distribution and dispersion quality, establish the size of the nanoparticle suspended in ultrapure water and determine the aggregation/clustering state. Figure 4.1(A) shows the size distribution of the APTES-coated Fe$_2$O$_3$ nanoparticles, where the hydrodynamic diameter was determined to have a mode of 398.2 ± 16.7nm and a mean of 426.8 ± 13.5nm (n=6). As NTA measures the hydrodynamic diameter or radius of a nanoparticle, this larger size accounts for adsorption of solution to the nanoparticle surface whilst in suspension. As indicated by a red arrow, there is a secondary peak recorded at approximately 445nm (Figure 4.1(B)). Table 4.1 shows the additional parameters measured using NTA, including the total concentration of nanoparticles measured per frame and the average drift velocity of the nanoparticles.
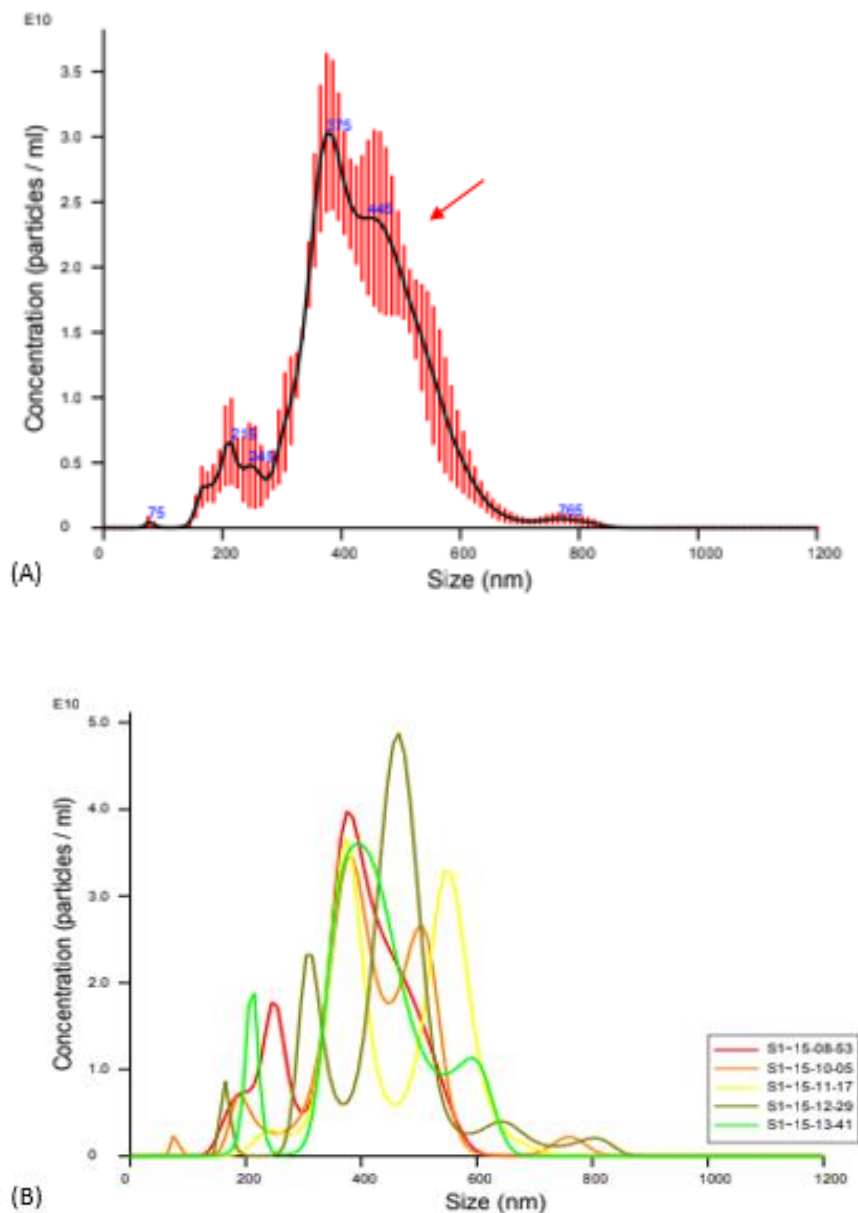
Figure 4.1: **NTA analysis of Fe₂O₃ nanoparticles following coating with APTES, in ultra-pure water.** 1mg/mL Fe₂O₃@APTES were dispersed in ultra-pure dH₂0 at 22°C and analysed by NTA. Six, 60 second videos were recorded per sample. Solid black line in Figure 4.1(A) represents the average of six 60 second videos. Primary peak shown at ~375nm and secondary aggregation is recorded at ~445nm (as indicated by red arrow). Red error bars indicate ± 1 SEM. Figure 4.1(B) illustrates each of the individual six 60 second video results that make up the collective average as seen in Figure 4.1(A). In each sample run, the primary peaks can be seen at ~375nm and secondary aggregation is recorded at ~445nm (n=6).

Table 4.1: T**he various parameters recorded during NTA analysis of Fe$_2$O$_3$ nanoparticles.** The recorded size of nanoparticles following coating with APTES. Recorded size of nanoparticles in suspension was consistent across readings (n=6)

Parameter	Result
Size distribution as measured by NTA (Mean)	426.8 ± 13.5nm
Size distribution as measure by NTA (Mode)	398.2 ± 16.7nm
Dilution factor	10,000
Total concentration per frame	21.9 ± 0.4 particles/frame
Total concentration per mL	6.62x10^{11} ± 1.31x10^{10} particles/mL
Average drift velocity	485 nm/s
Temperature	22.0°C

4.2.2 Scanning electron microscopy

Fe_2O_3@APTES nanoparticles were prepared through the incubation of stock Fe_2O_3 nanoparticles with APTES solution for 24 hours at 4°C. The morphology of the nanoparticles was investigated using scanning electron microscopy (SEM). Representative SEM images shown in Figure 4.2 demonstrate that Fe_2O_3@APTES display an approximate average diameter of 80nm and display a spherical morphology, as indicated by white arrows. Large aggregates and masses of nanoparticles were also observed in each specimen. Size was determined from the measurement of 10 Fe_2O_3@APTES nanoparticles in each field of view, across 3 samples.
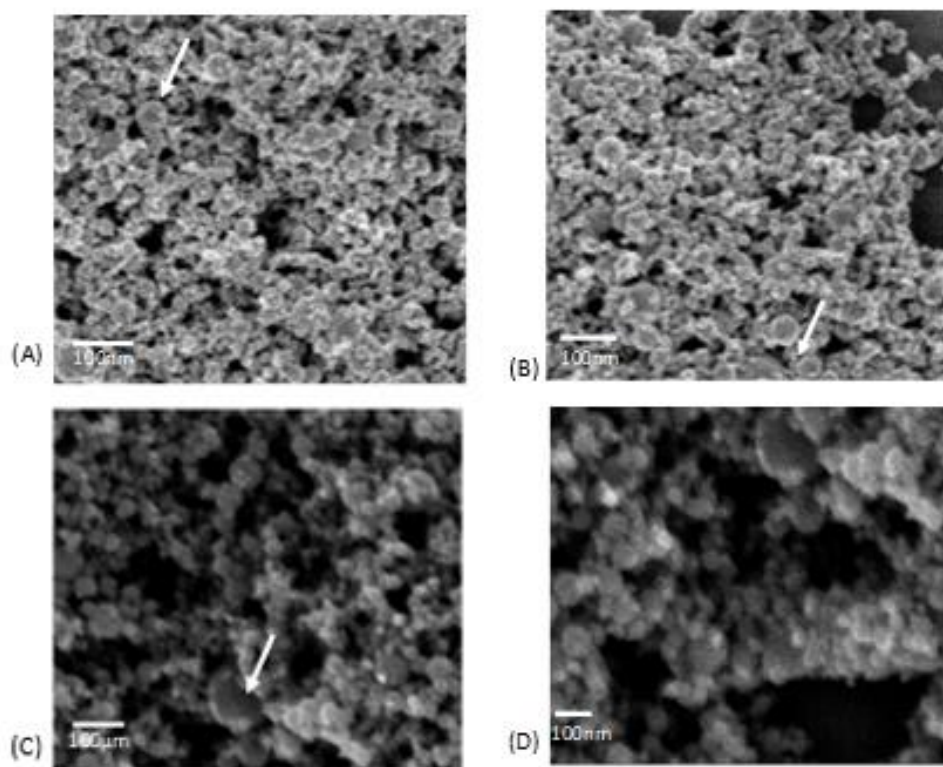
Figure 4.2: **Fe_2O_3@APTES nanoparticles visualised by scanning electron microscopy.** Fe_2O_3@APTES were prepared for SEM at a concentration of 1µg/mL nanoparticles suspended in isopropanol (dilation factor of 1:1000), dropped gently onto SEM imaging stub covered with carbon tab and allowed to dry. Silver paint was gently applied from the sample down to the metallic component of SEM stub to prevent overcharging. Representative scanning electron micrographs showing that Fe_2O_3@APTES nanoparticles have a spherical morphology and display an average size of ~80nm (indicated by white arrows and in Figure 3.2(A)(B). Figure panel (C) and (D) shows the degree of aggregation of nanoparticles with white arrows indicating larger aggregate, or cluster, of nanoparticles (n=3).

4.2.3 Determination of the expression of CD5, CD19, CD20 and CD52 on B cells and patient-derived CLL cells

The relative expression levels of CLL-specific surface markers on B cells from healthy donors, the I-83 cell line, and patient-derived CLL cells was analysed by flow cytometry using the BD Accuri C6, with monoclonal antibodies directed against CD5 (AlexaFluor647), CD19 (AlexFluor488), CD20 (AlexaFluor 488) and CD52 (AlexaFluor 647) (Figure 4.3). Expression levels of CD5 was found to be significantly lower in the I-83 cells and normal B cells compared to the patient-derived CLL cells ($p<0.001$). No difference in CD19 expression in the I-83 cells or normal B cells was observed; however, expression of CD19 in patient-derived CLL cells was variable with a range of 35,427.53-188,411.60 MFI and a mean of 97,144 ± 46,569 MFI (n=3).

Similar CD20 expression levels were found in each of the cell types analysed, however we did observe a non-significant lower expression within the patient-derived CLL cell population. We observed that expression levels of CD52 in the I-83 cell line and the patient-derived CLL cells were significantly higher compared to that of the normal B cells ($p<0.001$). Of note, there were no significant differences between expression of CD52 in the I-83 cell line and the patient-derived CLL cell (n=3). Representative flow cytometry scatter plots of each of CD5, CD19, CD20 and CD52 expression across each of the aforementioned cell types are shown in Figure 4.4 to Figure 4.7. 7 out of 8 patient-derived CLL samples were identified as >90% CD52 positive. Heterogeneity in expression of CD52 in patient-derived CLL samples was observed with mean MFI of 149,134 ± 41,930 MFI (n=8; Figure 4.8).

MFI of each cell surface marker was established in each celll type following previous determination of CD19-positivity for each cell type, as discussed in section 2.4.3.
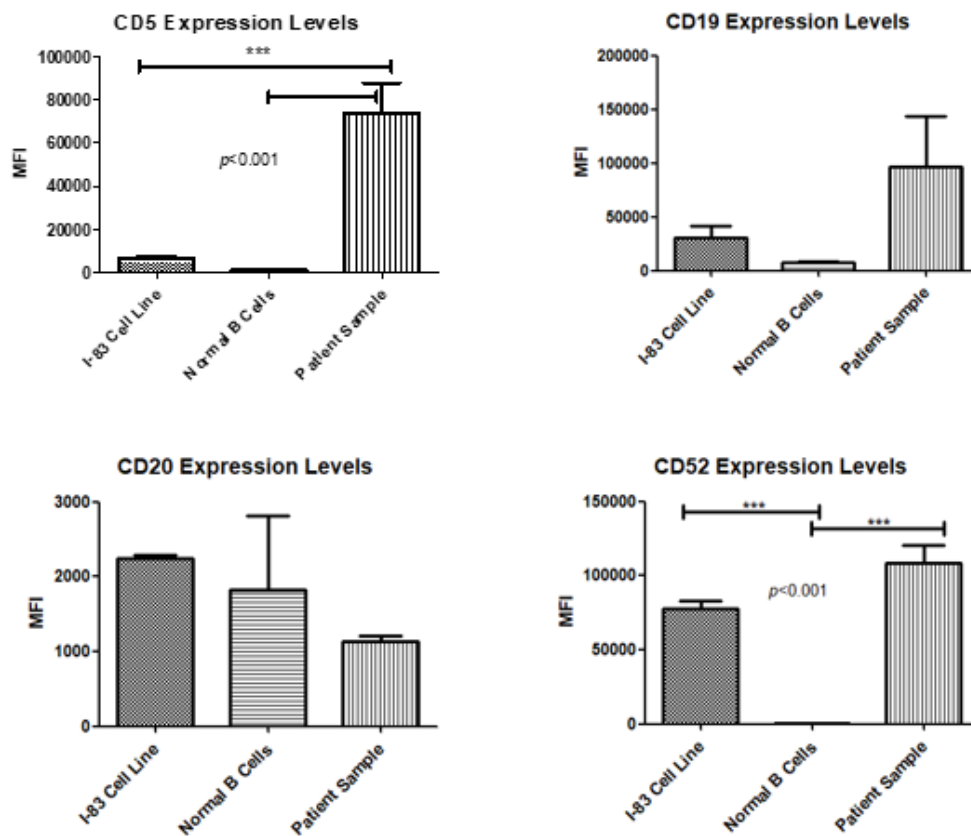
Figure 4.3: **Determination of a suitable CLL cell surface marker, using flow cytometric analysis.** 1×10^5 cells of each of the I-83 cell line, normal B cells and CLL patient samples were stained with each of CD5-AlexaFluor647, CD19-AlexaFluor488, CD20-AlexaFluor488 and CD52-AlexaFluor 647 monoclonal antibodies and analysed by flow cytometry on the BD Accuri C6. The mean MFI of expression levels of each surface marker, CD5, CD19, CD20 and CD52 in the I-83 cell line, normal B cells and patient-derived CLL cells (n=3 for each I-83, normal B cell; n=8 for patient-derived CLL cells) is presented. One-way ANOVA with Tukey post-test was used for statistical analysis.
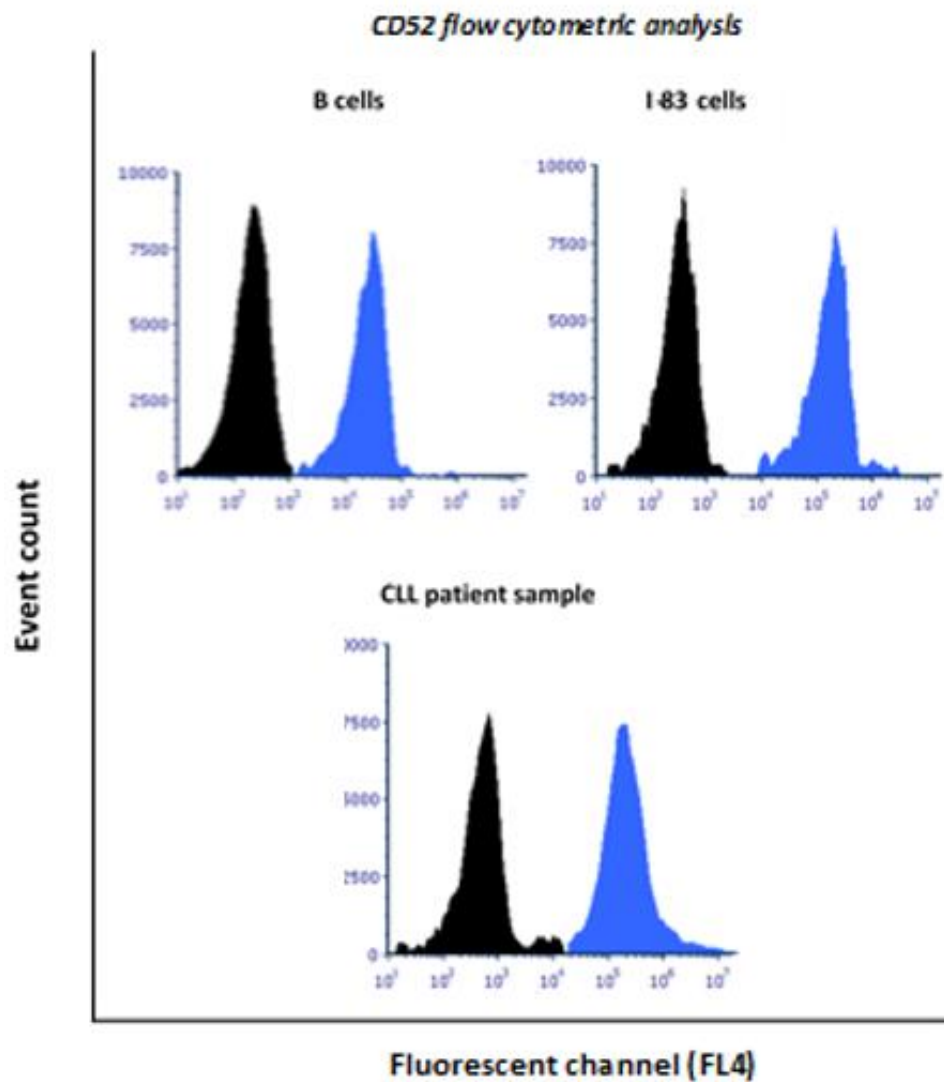
Figure 4.4: Flow cytometry histograms demonstrating the positivity for the cell surface marker, CD52 in each of the I-83 cell line, normal B cells and patient-derived CLL cells (CLL 8). Histograms depict the same number of events across each cell type (10,000 events; n=3 for each of normal B cells and I-83 cell line; n=8 for patient-derived CLL cells). In each analysis, lymphocytes were gated for as shown in Section 2.4.3. Percentage positivity for surface marker when compared to unstained control is depicted on each histogram, in addition to the MFI of each peak. Black peaks demonstrate the unstained population, with blue peaks representing the stained population.
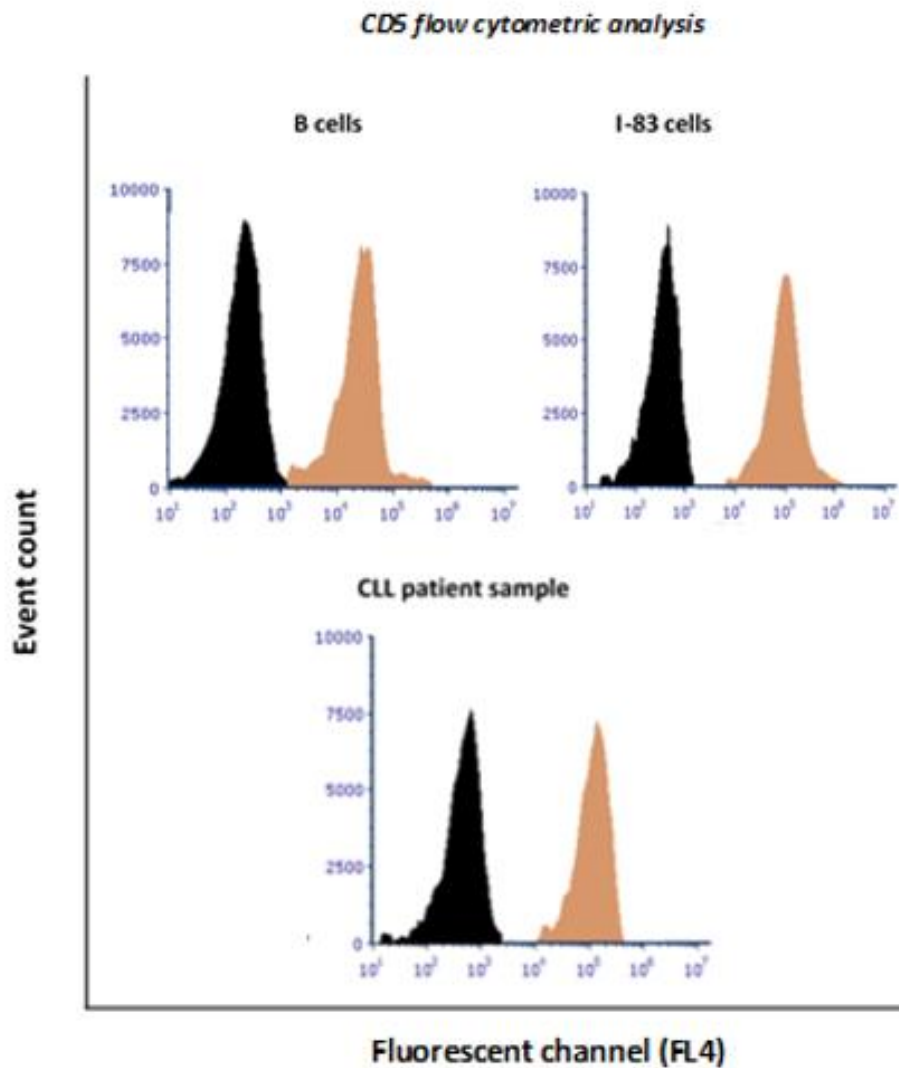
Figure 4.5: Flow cytometry histograms demonstrating the positivity for the cell surface marker, CD5 in each of the I-83 cell line, normal B cells and patient-derived CLL cells (CLL 2). Histograms depict the same number of events across each cell type (10,000 events; n=3 for each of normal B cells and I-83 cell line; n=8 for patient-derived CLL cells). In each analysis, lymphocytes were gated for as shown in Section 2.4.3. Percentage positivity for surface marker when compared to unstained control is depicted on each histogram, in addition to the MFI of each peak. Black peaks demonstrate the unstained population, with orange peaks representing the stained population.
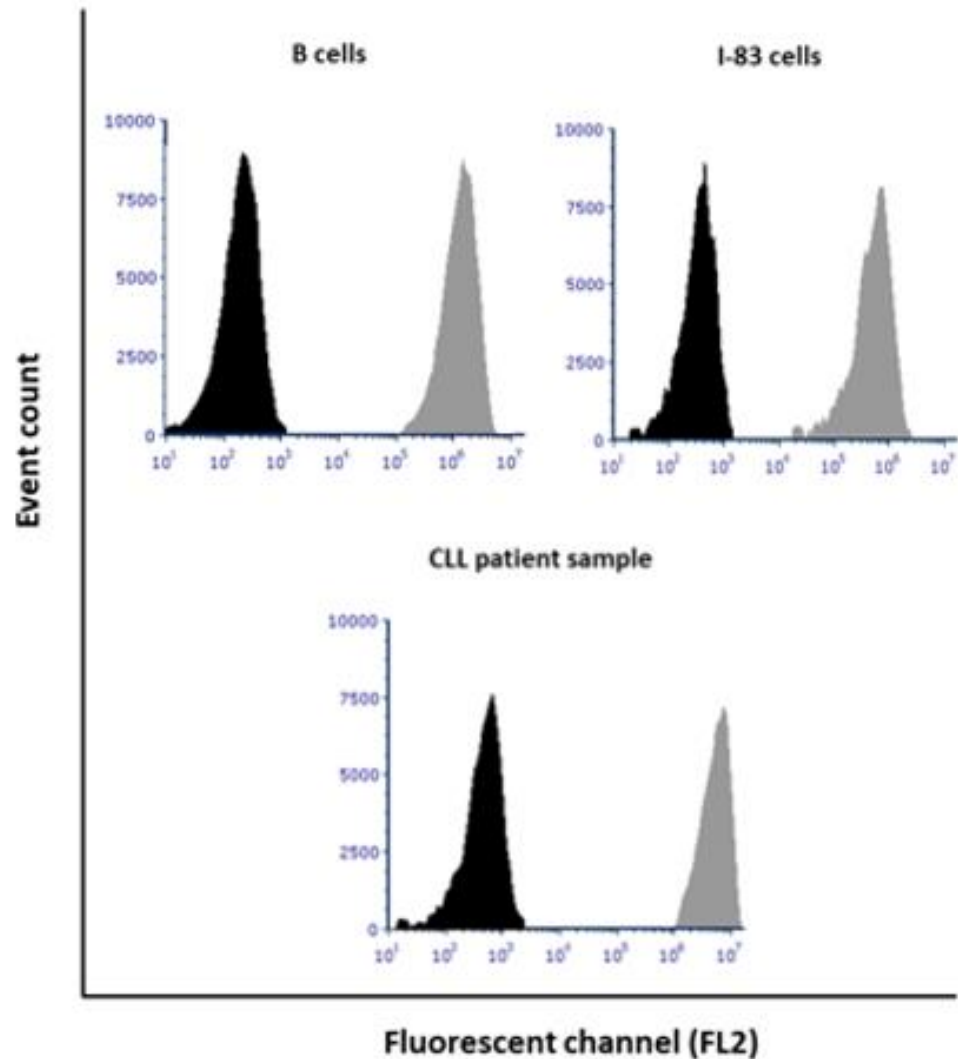
Figure 4.6: Flow cytometry histograms demonstrating the positivity for the cell surface marker, CD19 in each of the I-83 cell line, normal B cells and patient-derived CLL cells (CLL6). Histograms depict the same number of events across each cell type (10,000 events; n=3 for each of normal B cells and I-83 cell line; n=8 for patient-derived CLL cells). In each analysis, lymphocytes were gated for as shown in Section 2.4.3. Percentage positivity for surface marker when compared to unstained control is depicted on each histogram, in addition to the MFI of each peak. Black peaks demonstrate the unstained population, with grey peaks representing the stained population.
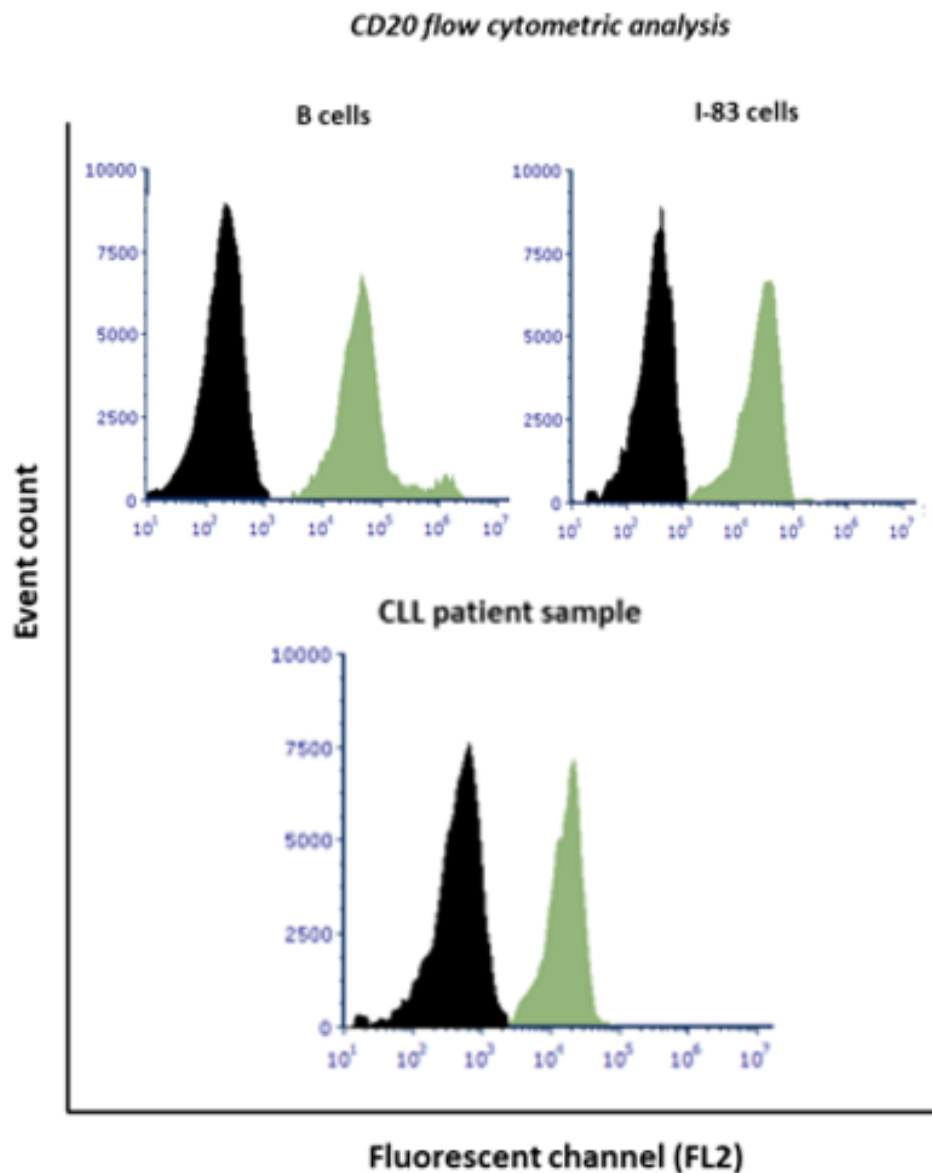
Figure 4.7: Flow cytometry histograms demonstrating the positivity for the cell surface marker, CD20 in each of the I-83 cell line, normal B cells and patient-derived CLL cells (CLL9). Histograms depict the same number of events across each cell type (10,000 events; n=3 for each of normal B cells and I-83 cell line; n=8 for patient-derived CLL cells). In each analysis, lymphocytes were gated for as shown in Section 2.4.3. Percentage positivity for surface marker when compared to unstained control is depicted on each histogram, in addition to the MFI of each peak. Black peaks demonstrate the unstained population, with green peaks representing the stained population.

Table 4.2: The percentage of positivity for monoclonal CD52-AlexaFluor647 cell surface antigen across eight patient-derived CLL cell.

Sample ID	% positivity for CD52 surface marker
CLL 4	92.0
CLL 5	99.9
CLL 6	99.9
CLL 7	41
CLL 8	99.2
CLL 9	98.1
CLL 10	99.6
CLL 11	91.2

Figure 4.8: Relative expression of CD52 in patient-derived CLL cells. $1x15^5$ patient-derived CLL cells from 8 patients were stained with anti-CD52 AlexaFluor 647 using flow cytometry on the BD Accuri C6. Cell Presented population was gated on CD19+ population, as described in section 2.4.3. Results indicate heterogeneity in expression of CD52 surface antigen across the patient samples.

4.2.4 Confirmation of successful functionalisation of Fe$_2$O$_3$@APTES nanoparticles

In the previous section, CD52 was identified as an appropriate marker for the development of a functional nanoparticle for the targeting of CLL due to its relatively high expression levels in the I-83 cell line and patient-derived CLL cells. Fe$_2$O$_3$@APTES nanoparticles were functionalised using anti-CD52 AlexaFluor 647. Anti-CD52 – AlexaFluor 647 was covalently incorporated to the surface of the nanoparticle (Fe$_2$O$_3$@CD52) and the fluorescent activity of the tag was measured using flow cytometry (Figure 4.9). Incorporation of anti-CD52-AlexaFluor 647 was shown to be efficient with 99.2 ± 0.6% of nanoparticles functionalised (n=3, Figure 4.9).

The Fe$_2$O$_3$@CD52 nanoparticle solution was analysed for stability and it was shown that Fe$_2$O$_3$@CD52 are stable for at least four weeks in solution at 4°C (data not shown). This stability assessment was performed for all batches of functionalised nanoparticles by flow cytometric analysis. Stability was defined as no loss of fluorescence as measured by flow cytometry, indicating antibody conjugation was retained.

Additionally, the level of antibody elution from the surface of Fe$_2$O$_3$@CD52 nanoparticle was determined in order to examine the stability and overall shelf-life of these nanoparticles. Following the collection of Fe$_2$O$_3$@CD52 nanoparticle supernatant over time periods of 2,4,6,8,24,48 and 72 hours, a bicinchoninic acid assay (BCA assay) was utilised to determine the levels of protein, and hence antibody, in

the supernatant. No protein was detected within the supernatant over this time period, within the sensitivity of this assay (protein levels of ≤10ng are undetectable using this assay) (n=3; results available in Appendix 8.3).
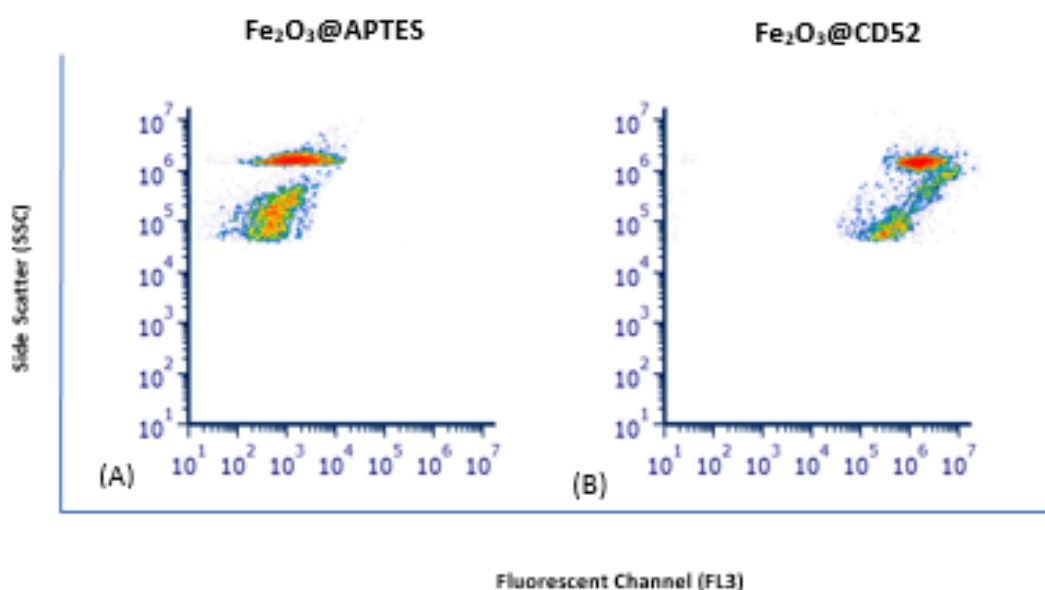
Figure 4.9: **Fe$_2$O$_3$@APTES nanoparticles can be successfully functionalised with anti-CD52 monoclonal antibody.** Representative density scatter plots showing successful functionalisation of Fe$_2$O$_3$@CD52 nanoparticles. Nanoparticles were covalently conjugated to anti-CD52 AlexaFlour 647 monoclonal antibody and analysed by flow cytometry. Plot (a) shows Fe$_2$O$_3$@APTES (non-functionalised NPs). Plot (b) shows successfully functionalised Fe$_2$O$_3$@CD52 nanoparticles. Plots indicate two populations in both non-functionalised and functionalised nanoparticles, aggregates and unaggregated; as would typically be observed in flow cytometric analysis of nanoparticles. Populations have been gated, excluding dust particles that may be in suspension and visible when in the nanoscale range (n=3).

4.2.5 Qualitative assessment of the interaction of CD52-functionalised Fe_2O_3 nanoparticles (Fe_2o_3@CD52) with B lymphocytes

Following on from the successful functionalisation of nanoparticles with anti-CD52 monoclonal antibody, patient-derived CLL cells were treated with 25µg/mL of either Fe_2O_3@APTES or Fe_2O_3@CD52, for 24 hours and subsequently prepared for LCSM as in Chapter 3.

We observed similar interaction of Fe_2O_3@APTES and Fe_2O_3@CD52 with normal B cells (Figure 4.10(A)-(C)). However, confocal Z-stacks indicate that Fe_2O_3@CD52 nanoparticles have an increased interaction with patient-derived CLL cells and are also internalised within the cell (Figure 4.10(D)(E)).

This qualitative study was performed in 6 different patient-derived CLL cells and all results displayed a similar increased interaction and uptake of Fe_2O_3@CD52 nanoparticles when compared to that of the Fe_2O_3@APTES.
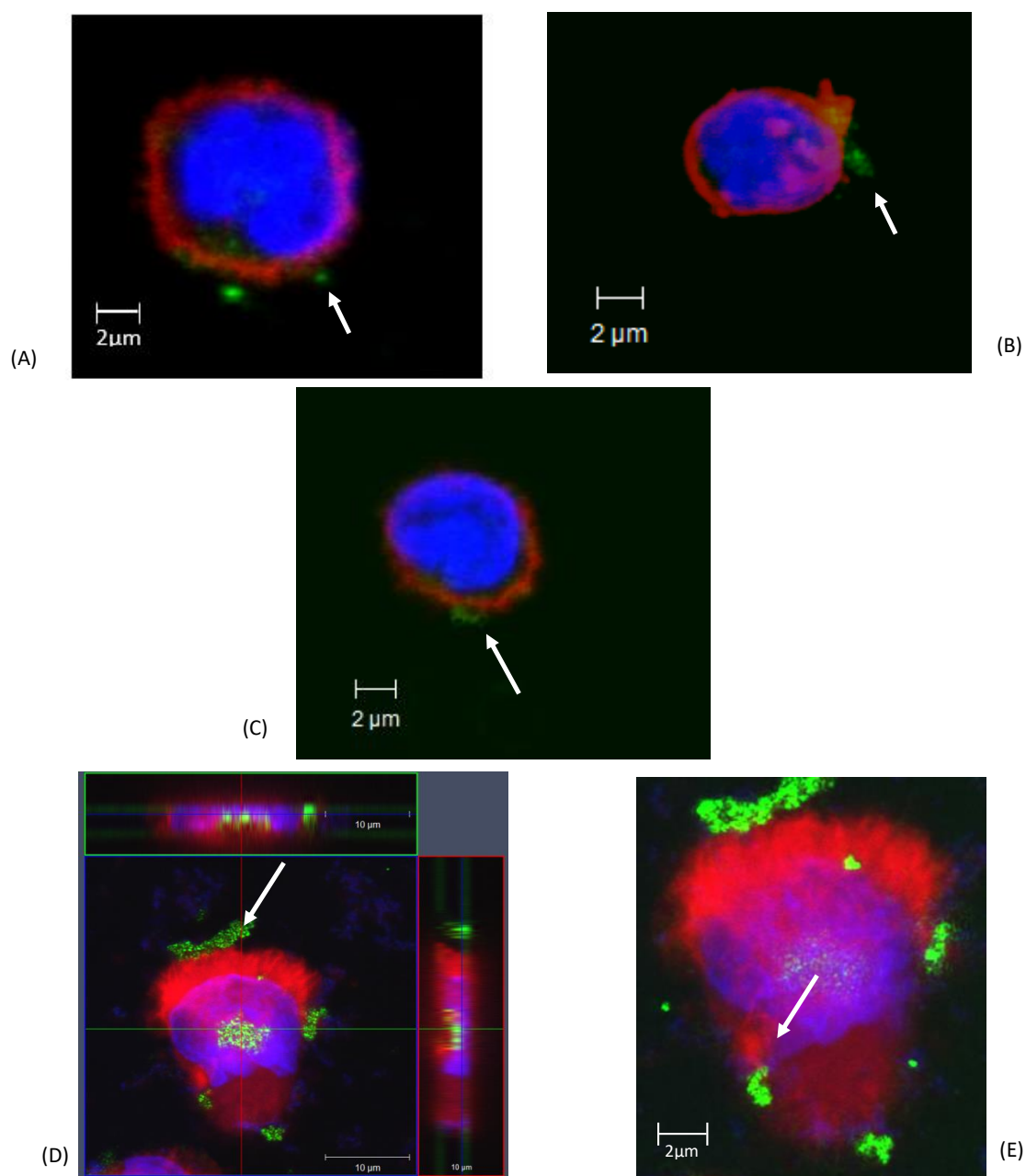
Figure 4.10: **Fe$_2$O$_3$@CD52 interacts with patient-derived CLL cells at an increased level to that of Fe$_2$O$_3$@APTES**. 2x10^5 patient-derived CLL cells were treated with 25μg/mL Fe$_2$O$_3$@APTES (A) or Fe$_2$O$_3$@CD52 (B)(C) nanoparticles for 24 hours and stained with Hoechst (nucleus, blue) and Rhodamine phalloidin (F-actin, red) and analysed by LSCM. Z-stack cross-sectional image showing the internalisation of Fe$_2$O$_3$@CD52 nanoparticle in a patient-derived CLL cell (D). Upper planar view of the same cell, demonstrating the interaction of Fe$_2$O$_3$@CD52 nanoparticle with the external surface of the cell (E). Images are representative of 6 patient-derived CLL cells, white arrows indicate the presence of respective nanoparticles interacting with the cells. Each treatment was conducted with 25μg/mL of respective nanoparticles. Red staining is that of F-actin using Rhodamine phalloidin, blue staining is that of the nucleus using Hoeschst and green in images represents the nanoparticles as captured using reflectance microscopy. Images are representative of patient-derived CLL cells CLL1, CLL4, CLL5, CLL8, CLL8, CLL9 and CLL14.

185

4.2.6 Assessment of the mechanism of internalisation of Fe₂O₃ nanoparticles by the I-83 cell line

Next, the mechanism of uptake of nanoparticles by CLL cells was assessed by fluorescence emitted by pH-sensitive bioconjugates on the surface of these nanoparticles. This protocol is based on the premise that the pH of cells decreases on a gradient from the surface of the cell to the internal compartments. I-83 cells were pre-treated with either amiloride to inhibit macropinocytosis, or chlorpromazine to inhibit clathrin-dependent endocytosis, and subsequent treatment of cells with a concentration range of 10, 25, 50 or 100μg/mL of Fe_2O_3@APTES or Fe_2O_3@CD52 for 24 hours. Uptake of both Fe_2O_3@APTES and Fe_2O_3@CD52 was assessed through the measurement of emitted fluorescence of pH-sensitive bioconjugate on the surface of the particles by a fluorescent plate reader. We observed a significant increase in uptake of Fe_2O3@CD52 nanoparticles compared to Fe_2O_3@APTES in the I-83 cell line at nanoparticle concentrations of 50 and 100μg/mL (Figures 4.11 and 4.12; $p<0.01$). Pre-treatment of the I-83 cell line with 50μM chlorpromazine had no effect on the cells ability to internalise Fe_2O_3@APTES, however pre-treatment with chlorpromazine did have a significant effect on the cells ability to internalise Fe_2O_3@CD52 at concentrations of 50μg/mL and 100μg/mL (Figure 4.11; n=3; $p<0.001$). Similarly, pre-treatment of I-83 cells with 100μM amiloride had no significant effect on the cells ability to internalise Fe_2O_3@APTES, however pre-treatment of with amiloride had a significant effect on the ability of the I-83 cells to internalise Fe_2O_3@CD52 at the nanoparticle concentration of 100μg/mL (Figure 4.12; n=3; $p<0.001$).

Figure 4.11: **Chlorpromazine significantly affects the levels of uptake of Fe₂O₃@CD52 in the I-83 cells.** 2×10^5 I-83 cells were pre-treated with 50µM chlorpromazine, followed by subsequent treatment with Fe₂O₃@APTES or Fe₂O₃@CD52 for 24 hours, and the effect of this pre-treatment on uptake of was assessed using a fluorescent plate reader assessing fluorescence (Biotek FLx800, at λ_{exc} = 505nm; λ_{emm} = 525nm) as discussed above (n=3; p<0.001; ANOVA with Tukey's post-test).

Figure 4.12: **Amiloride significantly effects the levels of uptake of Fe₂O₃@CD52 in the I-83 cells.** 2×10^5 I-83 cells were pre-treated with 100µM amiloride, followed by subsequent treatment with Fe₂O₃@APTES or Fe₂O₃@CD52 for 24 hours, and the effect of this pre-treatment on uptake of was assessed using a fluorescent plate reader assessing fluorescence (Biotek FLx800, at λ_{exc} = 505nm; λ_{emm} = 525nm) as discussed above (n=3; p<0.001; one-way ANOVA with Tukey's post-test).

4.2.7 Quantitative assessment of the interaction of CLL cells with fluorescent pH-sensitive doped Fe_2O_3 nanoparticles.

We next used a panel of CD52 antibodies (clones 097 and HI 186) and fluorophores (Table 4.3) to generate Fe_2O_3@CD52 nanoparticles to further characterise uptake in CLL cells. Functionalised nanoparticles were doped using pHRodo Green STP Ester and nanoparticle uptake was assessed by an increase in fluorescence as a result of the doped nanoparticles becoming exposed to lower pH within the lysosomes.

I-83 cells were treated with a concentration range of 10μg/mL, 25μg/mL, 50μg/mL and 100μg/mL of these fluorescent pH sensitive doped Fe_2O_3 nanoparticles for 24 hours. Nanoparticles functionalised with any of the three anti-CD52 antibody clones are internalised by the I-83 cell line significantly more than the isotype control (mouse IgM) or non-functionalised Fe_2O_3@APTES (n=3; $p<0.001$). Interestingly, Fe_2O_3@CD52 nanoparticles functionalised with anti-CD52 (clone 097)-AlexaFluor®647 were found to be internalised significantly more than nanoparticles functionalised with anti-CD52 (clone 097)-FITC ($p<0.001$; n=3).

We next investigated the internalisation of Fe_2O_3@CD52 nanoparticles (clone 097-AlexaFluor®647) in patient-derived CLL cells and normal B cells (Figure 4.14). Uptake of Fe_2O_3@CD52 nanoparticles was not observed in normal B cells; however, significantly increased uptake of Fe_2O_3@CD52 nanoparticles in the patient-derived CLL cells was observed (n=3; $p<0.001$).

Table 4.3: Illustrates the monoclonal antibody used in the generation of functionalised nanoparticles for these uptake studies and the purpose of including each of these antibodies in this body of work.

Monoclonal Antibody	Study Purpose
anti-CD52 (097) – AlexaFluor® 647	Uptake & interaction quantification
anti-CD52 (097) - FITC	Fluorophore control
anti-CD52 (097)	Fluorophore control
anti-CD52 (HI 186) - FITC	Clonality control
Mouse IgM	Non-specific antibody control
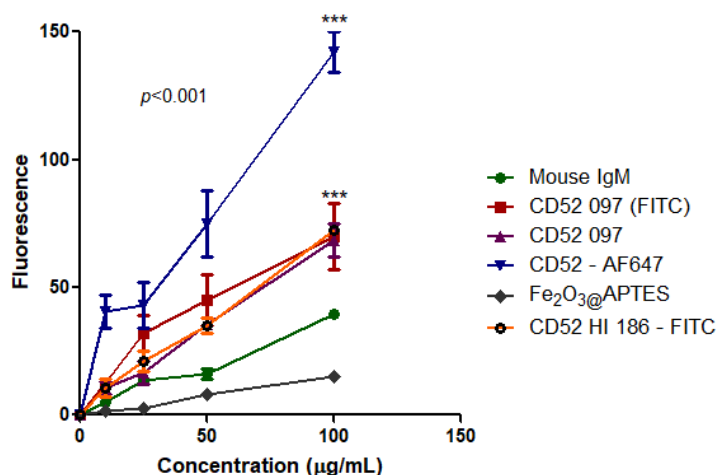
Figure 4.13: Fe$_2$O$_3$@CD52 functionalised nanoparticle are internalised in I-83 cells. Nanoparticles functionalised as indicated were doped with pHRodo Green STP Ester, which increases in fluorescence as the pH decreases (as the nanoparticles become internalised into the cell. 2x10^5 I-83 cells were incubated with functionalised nanoparticles for 24 hours and increased uptake of all Fe$_2$O$_3$@CD52 functionalised nanoparticles was observed when compared to Fe$_2$O$_3$@APTES and nanoparticles functionalised with mouse IgM. Increased uptake of CD52 (097) -AlexaFluor®647 vs. all other functionalised nanoparticles tested was noted (n=3; $p<0.001$; one-way ANOVA with Bonferonni post-test).
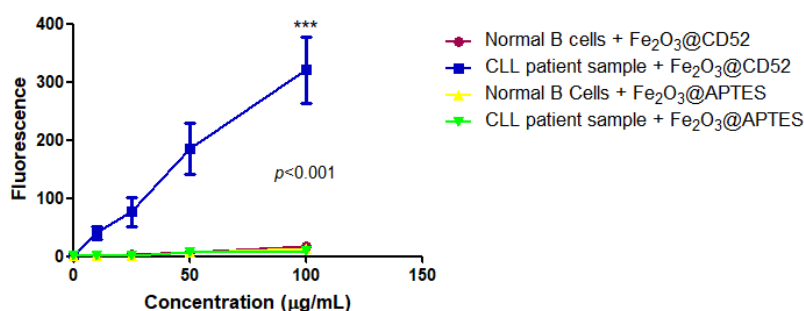
Figure 4.14: Preferential uptake of Fe$_2$O$_3$@CD52 by patient-derived CLL cells, compared to that of normal B cells. Nanoparticles functionalised as indicated were doped with pHRodo Green STP Ester, which increases in fluorescence as the pH decreases (as the nanoparticles become internalised into the cell). 2x10^5 I-83 cells were incubated with functionalised nanoparticles as indicated for 24 hours. Graph represents three patient-derived CLL cells (CLL1, CLL4, CLL9) and three normal donor B cell samples. Increased uptake of Fe$_2$O$_3$@CD52 (097) -AlexaFluor®647 in CLL cells was observed (n=3; $p<0.001$; one-way ANOVA with Bonferonni post-test).

4.2.8 Determination of toxicity of Fe_2O_3@CD52 nanoparticles on the I-83 cell line

We next assessed the levels of cytotoxicity in I-83 cells following treatment with Fe_2O_3@CD52 functionalised nanoparticles, cells were stained with ethidium bromide-acridine orange (EtO) cell stain following treatment over 24 hours and cell death levels were assessed using fluorescence microscopy.

A dose response in cytotoxicity can be seen following treatment with Fe_2O_3@CD52 nanoparticles, with a significant induction of cell death observed with treatment with >10µg/mL Fe_2O_3@CD52 nanoparticles, when compared to treatment with Fe_2O_3@APTES nanoparticles (Figure 4.15; n=3; $p<0.001$). The IC_{50} of Fe_2O_3@CD52 nanoparticles on I-83 cells over 24 hours was determined to be approximately 17.6 ± 3.17µg/mL, as determined using GraphPad Prism 5 software (range 13-100% cell death observed). No significant levels of cytotoxicity were detected with treatment up to 300µg/mL Fe_2O_3@APTES nanoparticles. Bare Fe_2O_3 nanoparticles demonstrated consistent levels of cytotoxicity as with earlier toxicity studies, with significant cytotoxicity being observed following treatment with 30µg/mL nanoparticles (n=3; $p<0.001$).

Fe$_2$O$_3$@CD52 nanoparticle treatment significantly impacts the cell viability of I-83 cells
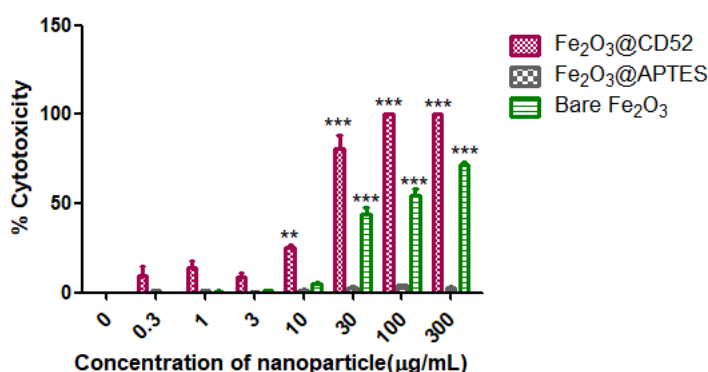
Figure 4.15: **I-83 cell viability is significantly affected by treatment with Fe$_2$O$_3$@CD52 nanoparticles, as measured by ethidium bromide-acridine orange staining**. 3×10^5 I-83 cells were treated with nanoparticles as indicated for 24 hours over a range of nanoparticle concentrations. Cells were recovered, and cytotoxicity was assessed using ethidium bromide-acridine orange staining followed by analysis using fluorescent microscopy. Significant levels of cytotoxicity was observed following treatment with 10µg/mL of Fe$_2$O$_3$@CD52 nanoparticles and 30µg/mL bare Fe$_2$O$_3$ with maximal levels occurring at 100µg/mL (n=3; $p < 0.001$; one-way ANOVA with Tukey post-test).

Next, we assessed whether the levels of cytotoxicity observed was as a result of apoptosis. For this, I-83 cells were treated with one of either bare Fe$_2$O$_3$ nanoparticles, Fe$_2$O$_3$@APTES or Fe$_2$O$_3$@CD52 for 8 hours and 24 hours, at a concentration range of 25, 50 and 100µg/mL. Following treatment, cells were recovered and stained with annexin-V PI flow cytometry stain and analysis on the flow cytometer for apoptosis levels, as described in Chapter 3 (Section 3.2.6).

Fe$_2$O$_3$@CD52 nanoparticle treatment over both timepoints resulted in a dose response induction of apoptosis in the I-83 cell line, with significant apoptosis levels being observed at treatment with 50µg/mL at 8 hours and 10ug/mL at 24 hours, as shown in Figure 4.16 and Figure 4.17 (n=3; $p < 0.001$), when compared to treatment with Fe$_2$O$_3$@APTES nanoparticles. Treatment with bare Fe$_2$O$_3$ nanoparticles was also found

to induce significant levels of apoptosis following treatment with 100µg/mL at 8 hours and 25µg/mL over 24 hours (n=3; $p<0.001$). However, apoptosis induced by Fe_2O_3@CD52 was greater than that induced by bare Fe_2O_3 nanoparticles at all concentrations (n=3; $p<0.001$). Treatment with Fe_2O_3@APTES was not found to induce any significant levels of apoptosis (n=3) at either 8 hours or 24 hours.

Following 8 hours of treatment with Fe_2O_3@CD52 nanoparticles, I-83 cells were found to predominantly be in the early apoptosis stage. Following 24-hour treatment with Fe_2O_3@CD52 nanoparticles, I-83 cells were found to be in both the early apoptosis and late apoptosis/necrosis stage, as can be seen by representative scatter pots below in Figure 4.18.
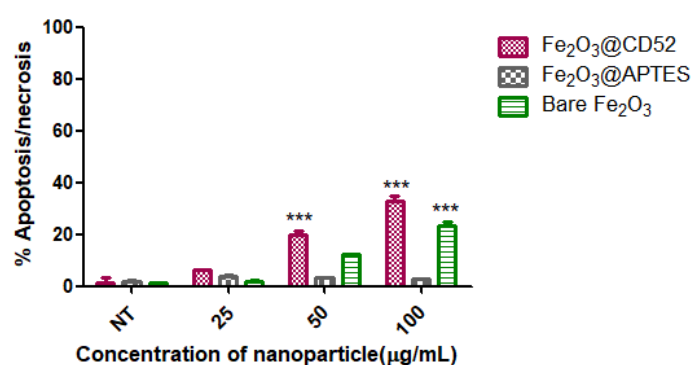
Figure 4.16: **Treatment with Fe_2O_3@CD52 nanoparticles induces significant levels of apoptosis/necrosis in I-83 cells, as measured by Annexin V-PI staining and flow cytometric analysis after 8 hours.** $3x10^5$ I-83 cells were treated as indicated for 8 hours. Cells were recovered, and apoptosis was assessed using Annexin V-PI staining and subsequent flow cytometric analysis. Significant apoptosis was observed following treatment with 50µg/mL of Fe_2O_3@CD52 nanoparticles. Significant apoptosis was observed following treatment with 100µg/mL bare Fe_2O_3. At each concentration, there was an increase in the levels of apoptosis by Fe_2O_3@CD52 compared to bare Fe_2O_3 (n=3; $p<0.001$; one-way ANOVA with Tukey post-test).

Fe₂O₃@CD52 nanoparticle treatment significantly impacts the cell viability of I-83 cells at 24 hours
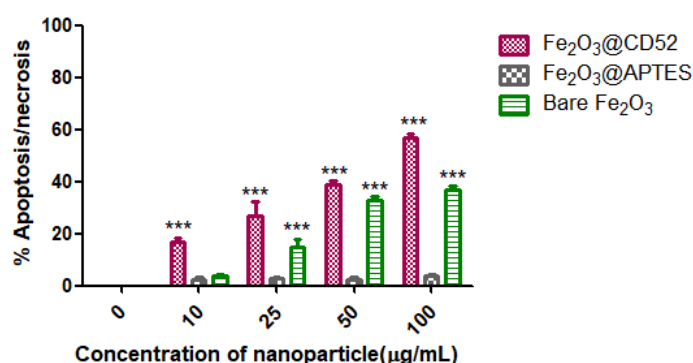
Figure 4.17: **Treatment with Fe₂O₃@CD52 nanoparticles induces significant levels of apoptosis/necrosis in I-83 cells, as measured by Annexin V-PI staining and flow cytometric analysis over 24 hours.** 3×10^5 I-83 cells as indicated for 24 hours. Cells were recovered, and apoptosis was assessed using Annexin V-PI staining and subsequent flow cytometric analysis. Significant apoptosis was observed following treatment with 10µg/mL of Fe₂O₃@CD52 nanoparticles, when compared to 25µg/mL of bare Fe₂O₃ nanoparticles. No significant induction of apoptosis was observed with Fe₂O₃@APTES. At each concentration, there was increase in apoptosis levels induced by Fe₂O₃@CD52 compared to bare Fe₂O₃ (n=3; $p<0.001$; one-way ANOVA with Tukey post-test).

Following the determination that CD52 functionalised nanoparticles significantly affected cell viability, we then aimed to determine whether or not the presence of anti-CD52, combined with an antibody directed at the pan-B cell marker CD19 (anti-CD19) might increase efficacy of the functionalised nanoparticle. Also included in this work was nanoparticles functionalised with anti-CD20, another commonly used monoclonal antibody therapeutic with B cell targeting capabilities. Results of this study found that the addition of another CLL surface target marker to the surface of the functionalised nanoparticle did not result in increased efficacy. Detailed results can be found in Appendix 8.4.
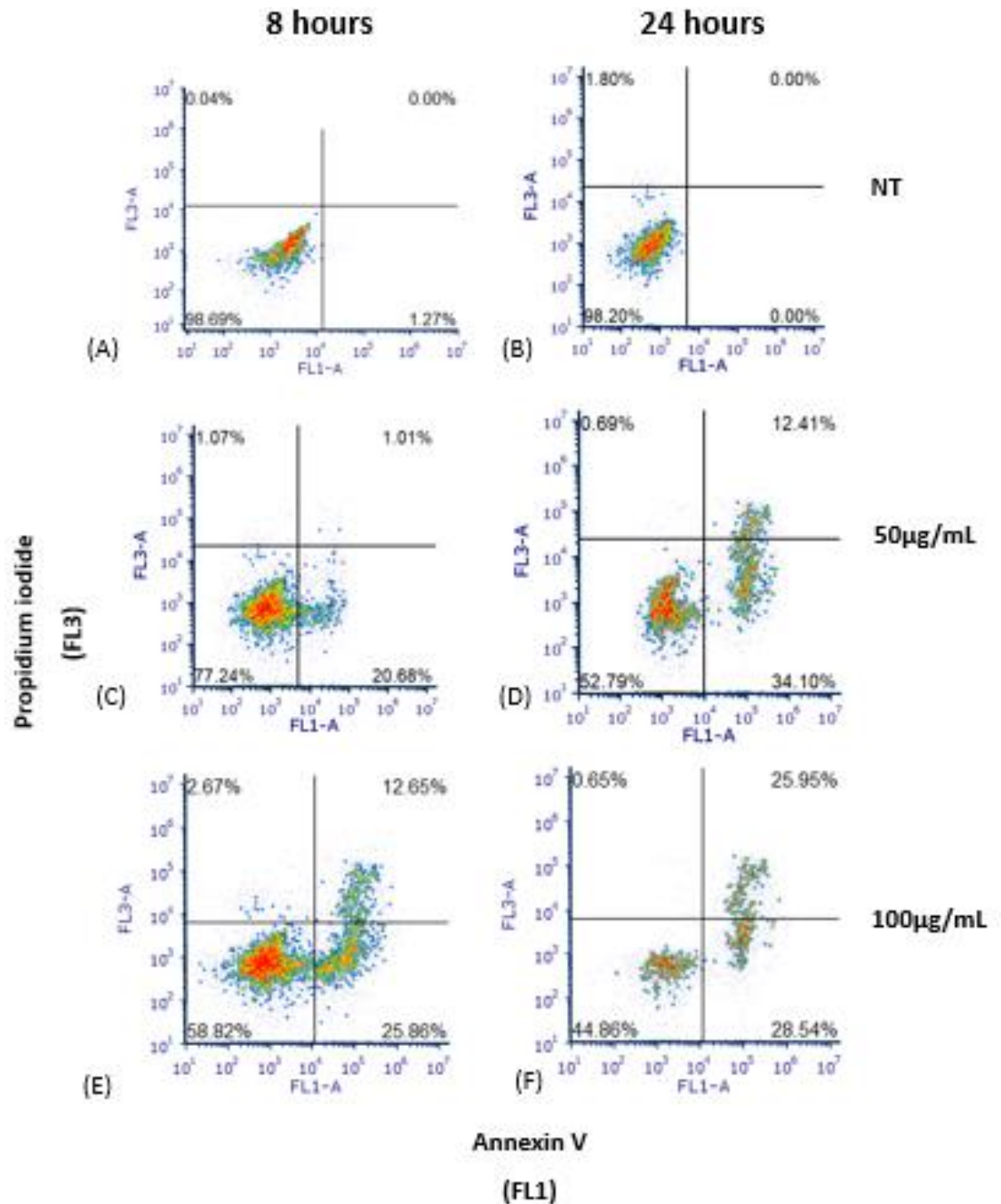
Figure 4.18: **Representative flow cytometric density plots of annexin V-propidium iodide staining of I-83 cells following treatment with Fe₂O₃@CD52 nanoparticles over 8 hours and 24 hours.** Levels of apoptosis in the no treatment control can be seen in Figure panels (A)(B). I-83 cells were treated with 50μg/mL Fe₂O₃ NPs for both 8 hours (panel C) and 24 hours (panel D). I-83 cells were treated with 100μg/mL Fe₂O₃ NPs for both 8 hours (panel (E) and 24 hours (panel F). Treatment with NPs resulted in the induction of apoptosis/necrosis at both timepoints, as indicated by an increase in annexin V-PI positive cells within the cell populations, when compared to the no treatment population (panel A). Flow cytometric plots show density plots of annexin V (X-axis) and PI (Y-axis) staining. In each plot, the lower right quadrant represents annexin V-PI negative cells. The lower left quadrant represents annexin V positive, PI negative cells; an indicator of early apoptosis. The upper right quadrant represents annexin V-PI positive cells; an indicator of late apoptosis/necrosis. The upper left quadrant represents annexin V negative, PI positive cells; an indicator of necrosis.

4.3 Discussion

The aim of this chapter was to identify a suitable cell surface target marker for the functionalisation of nanoparticles and to subsequently generate appropriately targeted nanoparticles and investigate both the toxicological effects and the interaction of these engineered functionalised nanoparticles with CLL cells. As discussed earlier, targeted therapies in the treatment of CLL have long been utilised with anti-CD52 and in particular, anti-CD20 therapies having shown much promise in clinical use (Badoux, *et al.*, 2011). Anti-CD20 monoclonal antibody therapy has become part of the standard of care regimen in the management of CLL, having been shown to improve patient outcome when combined with the chemotherapeutics fludarabine and cyclophosphamide, known as the FCR regimen (Badoux, *et al.*, 2011) (Byrd, *et al.*, 2005) (Byrd, *et al.,* 2001).

As discussed in Chapter 2.3, NTA is a robust technique used in the analysis of size and characterisation of stability of nanoparticle hydrodynamic size, by assessing the Brownian motion of these nanoparticles (Hole, *et al.*, 2013). Results of NTA here show the hydrodynamic radius of Fe_2O_3@APTES nanoparticles measuring at a mean of 426.8 ± 13.5nm. This increase in size of the nanoparticles is consistent with other reports, and can be attributed to hygroscopicity, or the adsorption and creation of a thin water film on the surface of the nanoparticles (Yesilbas & Boily, 2016) (Park, Kim, & Miller, 2009). Notably, this increase in size is consistent with the surface coating of APTES when comparing the substantial increase in size as measured

using NTA with the results of bare Fe_2O_3 nanoparticles as described in Chapter 3 (where uncoated nanoparticles were determined as ~210nm in radius) (Kim, *et al.*, 2017) (Bagwe, Hilliard, & Tan, 2006). Additionally, Fe_2O_3@APTES demonstrated stability consistent with the bare nanoparticles, with just one additional peak from the main population. This indicates a high level of nanoparticle stability within the sample, and therefore suitability for use in functionalisation reactions.

Next, we assessed the use of scanning electron microscopy to investigate the shape and uniformity of Fe_2O_3@APTES and therefore suitability for use in functionalisation reactions. SEM has long been used as a method for the visualisation and assessment of materials, and more recently used for the assessment of nanoparticle and nanomaterials. SEM results presented within this study demonstrate that coating of ~50nm Fe_2O_3 (size determined by supplier) with APTES (Fe_2O_3@APTES) increases the size of the nanoparticle by approximately 30nm, resulting in an average size of 80nm, and that typical morphology of spherical nanoparticles is retained. An understanding into the increase in size following coating of nanoparticles is an important factor into the subsequent understanding of the interactions and behaviour of these nanoparticles with their environment, whilst ensuring they remain below the optimal size of 100nm in size. As demonstrated here, there are a great number of advantages to assessing the size of a nanoparticle using a number of different approaches. As discussed earlier, NTA being a commonly used mechanism of size determination provides the hydrodynamic radius, which will be considerably larger than any measurement taken outside

of the aqueous environment, and alone may result in and inaccurate representation of size - a measurement which may prove important for further studies. A size of ~80nm will provide an adequate surface area for the subsequent functionalisation of these Fe_2O_3@APTES nanoparticles with targeting agents, with most antibodies measuring between 20 and 40nm in size, whilst still allowing for maximum interaction with cells in the environment (Chen *et al.,* 2004). This approximate size of nanoparticle has been used in multiple other studies for successful functionalisation with biologically-relevant agents (Cheng, *et al.*, 2006) (Neuberger, *et al.,* 2005). We observed aggregation of nanoparticles across the borosilicate surface of the sample, a common observation following the drying process necessary during the preparation of samples for SEM, and has been a popular discussion-point in the microscopy field with several published peer-reviewed publications in the last 3 years alone (Michen, *et al.*, 2015) (Kim, *et al.,* 2016) (Park, 2017). These data demonstrate that the aggregation state of nanoparticles is likely a result of SEM preparation employed and may therefore not be indicative of the behaviour and aggregation state of nanoparticles in aqueous solution but can be a useful tool in determining size and shape of the nanoparticle of interest.

There is increasing recognition of the use of biomarker-directed therapies in the realm of oncology. The benefits of such an approach have not only been demonstrated in solid tumours, (Adams & Weiner, 2005) but have been shown to be pivotal in the successful treatment of haematological malignancies, as demonstrated by the introduction of rituximab, the first therapeutic monoclonal antibody to make it to the

clinic (Badoux, *et al.*, 2011). When establishing a suitable model for the investigation of the utility of a nanoparticle-antibody conjugate, it is important to first understand the expression profile of the cell types of interest. In this instance, the interest was in the understanding of the expression profile of commonly expressed surface antigens across three main cell types; normal B cells, the CLL cell line I-83 and patient-derived CLL cells. CD5, CD19, CD20 and CD52 are commonly expressed surface markers in CLL, and therapies have already been developed targeting CD20 and CD52.

Results of analysis presented here demonstrate that CD52 was the cell surface marker found to be suitable for further investigation within this thesis. CD52 was expressed at similarly high levels, in both the I-83 cell line and patient-derived CLL cells, though with a wider variability of expression within the patient-derived CLL cell subset itself. The variability observed is consistent with other reports and assists to further substantiate the findings within this section (Klabusay, *et al.,* 2007). This means that optimisation of a targeted therapeutic using the I-83 cell line could yield results similar to that obtained in the patient-derived CLL cell, and that therefore the I-83 cell line could be a suitable cell-line model within this body of work. Additionally, CD52 expression levels in the normal B cells were significantly lower than in the I-83 and patient-derived CLL cell, allowing for potentially increased targeting specificity. Interestingly, the levels of CD52 in normal B cells were found to be slightly lower than that found within the literature (Rao, *et al.*, 2012) (Ginaldi, *et al.,* 1998). This may be due to the sample size chosen for investigation, or indeed the variability of our particular patient cohort, as

has previously been discussed by Klabusay *et al.* in 2007 (Klabusay *et al.,* 2007). There is wide variability reported in groups studying CD52 expression in both normal B cells and CLL cells. Klabusay *et al*. found that there was a significant difference in the levels of CD52 antigen expression on the surface of patient-derived CLL cells when compared to normal cells (Klabusay, *et al.,* 2007). In contrast to this, Rossmann *et al*. found that there was no statistically significant difference between the levels of CD52 expression in normal and malignant B cells, and that there were notable differences in the levels of expression between patient-derived CLL cells themselves (Rossmann, *et al.,* 2001). A third group reporting on CD52 expression in patient-derived CLL cells found that the levels of CD52 antigen varied between patient samples assessed, and their levels of expression more closely aligned with our findings within this body of work (Ginaldi, *et al*., 1998). These findings within the literature align to our findings that there will be variability between patient samples used within different studies, and that surface molecule expression, particularly that assessed using flow cytometric analysis is difficult to compare across multiple studies, owing to variations within the patient cohort itself, cryopreservation method employed, and procedures taken during the flow cytometry assessment.

Surface CD20 expression levels were found to be lower in the patient-derived CLL cells compared to the normal B cells, or the I-83 cell line. These finding are consistent with published works in this field, whereby CD20 expression levels have been found to be lower in CLL cells when compared to normal B lymphocytes (Prevodnik, *et al.,* 2011) (Ginaldi, *et al*., 1998). It is important to note when performing flow cytometry, that

the mean fluorescence intensity (MFI) of a fluorophore, a measurement commonly used to report on surface marker expression, cannot be compared against the MFI of another fluorophore, and should be used as a reference point only. The level of CD20 antigen expression is considerably lower in patient-derived CLL cell when compared to their normal counterpart, and it is postulated that this may directly relate to the earlier stage of maturation of the B-CLL cells when compared to the B cells of normal B cells and other B cell malignancies (Ginaldi, *et al.*, 1998) (Huh, *et al.,* 2001). We also found that levels of CD19 were found to be higher in the patient-derived CLL cell population than that of the other two cell types, and considerably more so than that of the normal B cells. This result was not unexpected, given that higher levels of CD19 in malignant cell types have been reported in the literature (Ginaldi, *et al.,* 1998). We observed that there was a significant patient variability in CD19 expression, as expected when studying any patient cohort, shown in Figure 4.3 (Ginaldi, *et al.*, 1998).

Although CD20 may be a preferable target due to its importance in current CLL therapies, CD20 expression levels were found to be relatively low within the patient-derived CLL cell analysed. As CD52 levels were found to be relatively high within the patient-derived CLL cells analysed, we determined that it would be most suitable for the development of a proof-of-concept targeted nanotherapeutic. However, a panel of functionalised nanoparticles were prepared using monoclonal anti-CD19, anti-CD20 antibodies which were not investigated in detail and will not be discussed further in this thesis.

This study also demonstrated the successful functionalisation of the population of nanoparticles in the preparation of Fe_2O_3@CD52. Within this study, a functionalisation rate of >98% as determined by flow cytometry was the threshold for successful nanoparticle functionalisation. This is an important distinction, as a low level of covalent antibody linkage to the surface of the nanoparticle could result in a lower level of cellular targeting, toxicity and subsequent overall viability as a potential model nanotherapeutic. Additionally, it is important to monitor the rate of nanoparticle functionalisation following each reaction, and prior to use, in order to ensure a level of consistency within the functionalisation process. This can be facilitated through the use of a robust and validated functionalisation protocol, such as the method employed in this study (section 2.1) (Jeong, *et al.*, 2017) (Bartczak & Kanaras, 2011) (Balasubramanian, *et al.*, 2009). Within this study, we determined that the rate of functionalisation was greater than 95% and therefore efficient and successful, based on the fluorescent shift of the Fe_2O_3@CD52 nanoparticle population, and the shift of >95% of the population indicates that at in the case of the functionalised population, at least one anti-CD52 antibody had been incorporated onto the surface of the nanoparticle. The use of fluorescence is one of the most common methodologies employed in the characterisation of antibody functionalised nanoparticles, through the use of either a shift in fluorescence as measured by flow cytometry (as in this study), or using a fluorescent plate reader (Balthasar, *et al.,* 2005) (Rodriguez, *et al.*, 2013) (Chen, *et al.*, 2008) (Akin, *et al.,* 2007).

We detected no antibody elution from the surface of the nanoparticles Fe_2O_3@CD52 nanoparticles, as described in Appendix 8.3, suggesting any elution was below the levels detectable by the assay (picogram levels). Levels of antibody elution from the surface of nanoparticles following on from functionalisation was an important consideration in determining the stability of functionalisation nanoparticles. Given that the greatest time point for the experiments performed within this study was 24 hours, a time point of 72 hours was chosen for antibody elution analysis for a robust assessment. It was important to determine whether antibody used in these functionalisation reactions would remain immobilised to the surface of nanoparticles or be free in suspension after a period of time, as this may have potential implications in the activity of the antibody in suspension. Additionally, it was important to ensure that the functionalised nanoparticles would remain immobilised throughout the course of toxicity studies, in order to confidently and reproducibly determine the appropriate concentration of functionalised nanoparticles to use. Whilst antibody elution from the surface of functionalised has been previously reported, the determination of the optimal stoichiometry of antibody and nanoparticle can overcome this issue (Li & Liu, 2012) (Sperling & Parak, 2010).

The uptake of our functionalised Fe_2O_3@CD52 nanoparticle in normal and malignant B cells was assessed qualitatively and compared uptake to that of Fe_2O_3@APTES. LSCM studies performed here demonstrate that bare nanoparticles do interact with and become internalised within both normal B cells and malignant B cells, but that interactions appear to be primarily localised to just the surfaces of the cells and do not

penetrate the nucleus. Treatment of patient-derived CLL cells with Fe_2O_3@CD52 results in a greater level of interaction, than with Fe_2O_3@APTES nanoparticles. Importantly, Fe_2O_3@CD52 nanoparticles were shown to have a greater interaction with CLL cells compared to normal B cells. Fe_2O_3@CD52 nanoparticles were also seen to be internalised within the cell body using Z-stack analysis. The considerably greater accumulation and internalisation of Fe_2O_3@CD52 by patient-derived CLL cells would indicate that the targeting capabilities of the functionalised nanoparticles was successful, indicating that Fe_2O_3@CD52 nanoparticles have a greater affinity for interacting with and becoming internalised by the patient-derived CLL cells, and was likely an active interaction. Following on from an understanding of the level of uptake of nanoparticles by these cell types, we then proceeded to investigate the mechanism of uptake of Fe_2O_3@CD52 by the I-83 cell line. In order to accurately assess this, a panel of inhibitors were used in order to assess the level of uptake. To investigate the inhibition of macropinocytosis, cells were pre-treated with amiloride hydrochloride, and for the inhibition of clathrin-dependent endocytosis, cells were pre-treated with chlorpromazine. These pathways were chosen as they have both been rigorously studied in the field of nanomedicine, and deemed to be the most common means of nanoparticle uptake by cells (Oh & Park, 2014) (Zhang, *et al.,* 2009) (Harush-Frenkel, *et al.,* 2007) (Zhao, *et al.*, 2011). We demonstrated that uptake of Fe_2O_3@CD52 was significantly greater than that of Fe_2O_3@APTES. This trend has also been demonstrated in CD52-targeted immunotherapeutic agents in Burkitt's Lymphoma models (Lapalombella, *et al.,* 2008). Pre-treatment

of the I-83 cell line chlorpromazine has a significant effect on the cells ability to internalise Fe_2O_3@CD52, and that uptake inhibition diminishes to almost that of the level of uptake of Fe_2O_3@APTES. Our findings are in keeping with previous work in this area, indicating that clathrin-dependent endocytosis play a key role in the uptake of nanoparticles, and are consistent with the findings of other publications (Zhang, *et al.,* 2009) (Harush-Frenkel, *et al.,* 2007). Pre-treatment of I-83 cells with amiloride had only a significant effect on the ability of the I-83 cells to internalise Fe_2O_3@CD52 at the highest nanoparticle treatment dose of 100µg/mL These data indicate that whilst uptake of Fe_2O_3@CD52 appears to be predominantly mediated by clathrin-dependent endocytosis, but that at very high treatment levels, macropinocytosis, a non-specific mechanism of uptake may also begin to become involved (Zhao, *et al.,* 2011). Our findings of uptake of nanoparticles of the similar approximate size of our nanoparticle are consistent with other reports in this area of study (Shang, *et al.,* 2014). In 2011, a group studied the mechanisms of uptake of polystyrene nanoparticles in a similar way and concluded that in all cases, polystyrene nanoparticles entered the cell in an energy dependent process, and that the use of inhibitors cold yield beneficial findings as to these processes (dos Santos, *et al.,* 2011).This study of the interaction and uptake of Fe_2O_3@CD52 by patient-derived CLL cells provides a greater understanding into the fundamental interactions of anti-CD52 in the context of CLL cell interactions and provides the basis and rationale for the use of an anti-CD52 functionalised nanoparticle as a proof of concept nanotherapeutic in the targeted treatment of CLL.

Next, we assessed the specificity of uptake of nanoparticles by these cell types. We utilised a number of functionalised nanoparticles, including the functionalised nanoparticle of choice, Fe_2O_3@CD52, and investigated their uptake in the I-83 cell line. These functionalised nanoparticles were chosen each as either a bare nanoparticle control, an isotype control, a fluorophore control and as a clonality control. Data show that each of the CD52 functionalised nanoparticles undergo a high level of uptake, with Fe_2O_3@CD52 (clone 097) displaying the greatest amount of uptake by the patient-derived CLL cells. This is likely as a result of the affinity of this anti-CD52 clone for the CD52 receptor on the surface of the patient-derived CLL cells, as has been discussed in previous publications of this clone (Hale, 1995). We demonstrated that neither clonality nor fluorophore has a significant effect on the uptake of functionalised nanoparticles, but that there was a significantly lower level of uptake of both bare nanoparticles and mouse IgM functionalised nanoparticles (the isotype control). These results are as expected and demonstrate specificity of anti-CD52 interaction with B cells. We then demonstrated that patient-derived CLL cells undergo a significant amount of Fe_2O_3@CD52 nanoparticle uptake, when compared to Fe_2O_3@CD52 nanoparticle uptake by normal B cells, potentially positioning Fe_2O_3@CD52 nanoparticle as a suitable targeting agent in the case of CLL. Here, we hypothesise that this significant increase in uptake is thought to be as a direct result of the significantly increased expression levels of CD52 on the surface of patient-derived CLL cells when compared to that of their normal counterpart, and it is likely that this increased expression of CD52 antigen on the surface of the patient-

derived CLL cells result in an increase in the number of Fe_2O_3@CD52 nanoparticle that interact with the patient-derived CLL cells surface, and in turn become internalised (Albitar, *et al.,* 2004) (Ginaldi, *et al.,* 1998). A future, detailed analysis of nanoparticle uptake and CD52 expression studies would be recommended in order to fully elucidate upon this.

One of the major areas of study within this thesis was an in-depth, robust study into the levels of apoptosis that may be induced in both the I-83 cell line, and normal B cells, using my novel functionalised nanoparticle. An initial investigation into the levels of cell death induced by Fe_2O_3@CD52 nanoparticle in the I-83 cell line, as measured using ethidium bromide/acridine orange staining, demonstrated that there is significant cytotoxicity induction following treatment Fe_2O_3@CD52 nanoparticles. The findings of our initial toxicity testing using ethidium bromide are consistent with the investigation of apoptosis/necrosis initiation following treatment with the same nanoparticles. This provides a robust rationale for the use of flow cytometric analysis of cells stained with Annexin V-PI as a measurement of toxicity of future nanoparticles. Much work has been conducted on the toxic effects of Fe_2O_3 nanoparticles, though few studies have focused on the effects of these nanoparticles on lymphocytes. Many cancer cell lines have been employed in these studies as *in vitro* toxicity models, however it is generally agreed that toxicity data generated can be conflicting and inconsistent, with many of these data generated being only applicable to other identical parameters studied (Bahadar, *et al.,* 2016). As discussed previously in Chapter 3, the findings we report here are consistent with the findings of the toxic effects of bare Fe_2O_3, with our

findings of an IC_{50} of 18.6µg/mL being lower than that of bare Fe_2O_3 reported in the literature (~25-200µg/mL), with this lower threshold likely attributing to the covalent linkage of the monoclonal antibody anti-CD52 (Jeng & Swanson, 2006) (Gaharwar, *et al.,* 2017). The relevance of the anti-CD52 antibody presence as it relates to toxicity in patient-derived CLL cells will be investigated in the next chapter.

Chapter 5: Functional effects of Fe$_2$O$_3$@CD52 on patient-derived CLL cells

5.1 Introduction

The translation of any proof-of-concept therapy from *in vitro* cell lines to *in vitro* patient-derived material is an important aspect translational research as presented within this thesis. Within previous chapters we have demonstrated the importance in choosing the most suitable cell surface marker in the development of an antigen-specific targeted therapeutic. As demonstrated in Chapter 4, we have assessed and demonstrated the efficacy of our engineered nanoparticle in the initiation of apoptosis/necrosis in the I-83 cell line and normal B cells, in addition to the ability of normal B cells and I-83 cells to interact with and internalise Fe_2O_3@CD52. We demonstrated a significant increase in the affinity of Fe_2O_3@CD52 for the I-83 cell line when compared normal B cells. Next, we assessed the functional effect of Fe_2O_3@CD52 nanoparticle on patient-derived CLL cells, the effect of Fe_2O_3@CD52 on the adhesion of CLL cells to endothelial cells under shear flow conditions and the ability of Fe_2O_3@CD52 to induce apoptosis/necrosis in CLL cells.

The induction of apoptosis or necrosis within patient-derived CLL cells was performed using Annexin V- propidium iodide (PI) staining of cell samples following treatment with both Fe_2O_3@APTES and Fe_2O_3@CD52. We also investigated if loading of fludarabine onto the surface of Fe_2O_3@CD52 would increase the efficacy of the functionalised nanoparticles by developing an early-stage proof-of-concept nanoparticle - Fe_2O_3@CD52-Fludarabine. Fludarabine has long been the mainstay in the treatment of CLL; having first been investigated in single agent therapy in patients with relapsed/refractory

CLL, with responses of up to 57%. Overall response rates in previously untreated patients have been seen to be as high as 70% (Skarbnik & Faderl, 2017)(Chang & Kahl, 2012).   The addition of rituximab, an anti-CD52 monoclonal antibody, to the FC regimen (then becoming the FCR regimen) has been shown to be highly efficacious in patients with relapsed/refractory CLL and previously untreated patients, with complete response rates of up to 30% and up to 70%, respectively. Interestingly, prior exposure to either rituximab or fludarabine did not affect responses in these patient populations negatively, though those patients did present intermediate response rates. Progression-free survival was also lower for patients who presented with high-risk cytogenetic abnormalities such as *del*17p and *del*11q (Tam, *et al.,* 2008). Studies such as these provided our rationale for the possibility of combining   our Fe_2O_3@CD52   nanoparticle   with   fludarabine. Alemtuzumab, the anti-CD52 monoclonal antibody, is indicated for use in patients who have failed to respond to fludarabine-containing first line therapy or who have a TP53 deletion/mutation. In this early-stage proof-of-concept study we aimed to determine whether the inclusion of fludarabine on the surface of Fe_2O_3@CD52 would demonstrate increased efficacy in CLL cells when compared to that of Fe_2O_3@CD52 or treatment with fludarabine alone, as has been seen with combinations of rituximab and other cytotoxic agents.

We also investigated the effect of the presence of well-established prognostic markers on Fe_2O_3@CD52 induced cytotoxicity in patient-derived CLL cells. The prognosis of patients with CLL is extremely variable, owing to the high levels of heterogeneity observed in CLL. In

addition to the classical approach of disease staging, there are many means that can be used to assess prognosis in CLL including a number of cytogenetic abnormalities, IGHV mutations, CD38, NOTCH1, *del*17p, *del*13q and CD49d. Binet staging for CLL is the staple staging system in Europe and is comprised of three stages. Binet stage A indicates that the patient has fewer than 3 groups of lymphoid enlargements, Binet stage B indicates greater than three groups of lymphoid enlargements with lymphocytosis and Binet stage C indicates enlarged lymph nodes or spleen, thrombocytopenia and lymphocytosis. These stages define early, intermediate and advanced disease stages, respectively, and can assist clinicians in predicting the best course of treatment for their patients (Nabhan & Rosen, 2014). Immunoglobulin variable region heavy chain (IGHV) mutational status identifies two distinct subgroups of CLL with differing clinical courses: indolent and aggressive. Patients presenting with mutated IGHV have been shown to display a better clinical course and therefore have a better prognosis. Patients with unmutated IGHV demonstrate a poorer clinical course and poorer prognosis. Approximately 60% of patients with CLL display a mutated IGHV (Oscier, *et al.*, 2002). CD38 is a marker on the surface of CLL cells whose expression has been shown to be of prognostic value. It was initially proposed that CD38 expression correlated with IGHV mutational status in that high CD38 expression correlated with poor disease progression. However, it has since been noted that CD38 expression is dynamic in CLL and tends to correlate with disease progression, with levels of CD38 increasing as the disease progresses (Patten, *et al.,* 2008). Up to 90% of patients with CLL will present with at

least one cytogenetic abnormality, dependent on the characteristics of the patient. Patients with *del*13q as a single abnormality display an excellent prognosis. Between 15 and 40% of patients will present with *del*13q as a single abnormality. Between 3 and 27% of patients will present with *del*17p. These patients will tend towards a very poor prognosis, with a rapidly evolving disease and minimal response to conventional therapies. These cytogenetic abnormalities can be used to identify groups of patients with differing progressions and survival: low risk (normal karyotype or *del*13q as a single abnormality) or high risk (patients with *del*17p) (Monserrat, 2006). Mutations in NOTCH1 present in approximately 10% of patients with CLL, with the frequency of NOTCH1 mutations being detected increasing with advanced disease. Mutations in NOTCH1 have been found to be mutually exclusive with *del*17p in the same patient and have been associated with a poor prognosis and an independent predictor of overall survival similar to that associated with *del*17p (Rossi, *et al.*, 2012). CD49d expression by CLL cells is associated with microenvironment-mediated proliferation of CLL cells and is an independent predictor of a progressive clinical course and short survival prognosis. Positivity for CD49d will be found in approximately 30% of patients assessed. Following on from toxicity studies in patient-derived CLL cells, we also assessed any noted correlation between responsiveness to Fe_2O_3@CD52 nanoparticles and cytogenetic profile was assessed, to determine the possible suitability of this proof-of-concept therapy in subgroups of CLL patient samples.

In this chapter we also examined the effects of Fe_2O_3@CD52 nanoparticles on the adhesion of CLL cells to endothelial cells in a

physiologically-relevant shear flow model, in order to more accurately investigate the effects of nanoparticle treatment on the diapedesis of CLL cells in the microenvironment. The CLL microenvironment is comprised of several different cell types including endothelial cells, mesenchymal stromal cells, nurse-like cells, T cells and lymphoma associated macrophages – each of which contribute to the CLL microenvironment signalosome. These cell types can stimulate CLL cells either directly or via mediators such as cytokines and chemokines across the blood, bone marrow and secondary lymphoid organs such as the lymph nodes and spleen (Friedberg, 2011) (Herishanu *et al.,* 2014) (Burger & Gribben, 2014). My interest was focused on that of the endothelial cells in the High Endothelial Venules (HEVs), which are post-capillary venules functioning as an entry point for lymphocytes into the lymph nodes. For the purposes of this study two cell types were utilised for study of this microenvironment: human umbilical vein endothelial cells (HUVECs) as a model for venous shear stress within the high endothelial venule capillary beds and human dermal lymphatic endothelial cells (HDLECs) as a model for lymphatic shear stress (stress generated from the contraction and relaxation of smooth muscle within the lymph nodes (Dixon, *et al.*, 2006).). HEVs are composed of endothelial cells that express ligands for the homing of lymphocytes (Martinet, *et al.,* 2012).

My aim was to investigate the effects of our nanoparticles on cellular adhesion to the endothelial monolayer as well as assessing nanoparticle induced cytotoxicity under static and shear flow conditions. The investigation of lymphocytes under only static conditions may not be

representative of the *in vivo* environment, therefore assessing the effects that shear stress may exert on lymphocytes is important (Lawrence & Springer, 1991) (Fan, *et al.,* 2016) (Fan, *et al.,* 2016) (Ni *et al.,* 2003). Cells undergoing haemodynamic forces are exposed to several important factors including signal transduction, activation and adhesion; with the endothelial monolayer serving as an important interface between blood cells and the tissues. The interactions between CLL cells and endothelial cells in high venules in capillary beds has been shown to be a key event in migration of CLL cells from the circulation to the lymph nodes and bone marrow environments (Herishanu *et al.,* 2014) (Hartmann, *et al.,* 2009). Typically, shear stress models *in vitro* use syringe-based pumps in order to generate a controllable flow, or force (Young & Simmons, 2010). These models generally involve the use of an endothelial monolayer in which cells are introduced under fluid shear flow conditions, to more accurately represent the dynamic environment *in vivo* (White & Frangos, 2007). Other experimental designs include using a vortex-based model in order to recreate the effects of shear force on specific cellular components such as the cell membrane and molecular adhesion, and the use of a haemodynamic shearing device, often employed in the study of platelet activation (Nobilli *et al.,* 2008). Work presented here aims to develop and optimise a shear flow assay, focusing on the use of a syringe-based pump, connected to an epifluorescent microscopy, for the visualisation of the effects of shear stress on B cells, specifically patient-derived CLL cells (see Section 2.4.15 for a detailed description of device set-up). Here we measured adherence of patient-derived CLL cells to the endothelial

monolayer and studied the effects that nanoparticle treatment plays on these interactions. Additionally, we measured the effects that shear stress can have on the toxicity of nanoparticles to the I-83 cell line.

In summary, within Chapter 5 we aimed to:

- Assess the effects of Fe_2O_3@CD52 nanoparticles on the interaction with and adherence of patient-derived CLL cells with the endothelial cells, using a customised microfluidics platform

- Assess the level of toxicity exerted upon patient-derived CLL cells by Fe_2O_3@CD52 nanoparticles

- Assess the effect of the presence of CLL prognostic factors on Fe_2O_3@CD52 induced cytotoxicity

5.2 Results

5.2.1 The effect of nanoparticles on the adherence of CLL patient samples to endothelial cells under shear flow conditions

The interaction of CLL cells with endothelial cells in HEV is important in the homing and trafficking of CLL cells from the peripheral blood to the lymph nodes. Here, we investigated the interaction of patient-derived CLL cells with an endothelial monolayer consisting of either HUVECs or HDLEC cells, using Cellix Vena8 Endothelial+ biochips and an in-house microfluidics syringe-based system, connected to an epifluorescent microscope (see Materials and Methods section 2.4.15). This allowed for visualisation and quantification of levels of adherence to the monolayer in order to determine adherence rates under differing rates of flow. HUVEC cells are human umbilical vein derived endothelial cells and are commonly used as a laboratory model for the study of endothelial cells. HDLEC cells are human dermal lymphatic endothelial cells and are used a laboratory model for the study of lymphatic endothelial cells and lymphatic vessel transport.

A flow rate of 0.5 Dynes/cm^2 and 0.25 Dynes/cm^2 rates were chosen to simulate venous shear stress and 0.08 Dynes/cm^2 was chosen in order to simulate lymphatic shear stress (Voyvodic, *et al.,* 2014) (Frueh, *et al.,* 2013) (Harker, *et al.,* 2014) (Woo, *et al.,* 2008).

Patient-derived CLL cell adherence to the endothelial monolayer (consisting of either HUVECs or HDLECs) was found to increase with time, reaching saturation at 15 minutes at each of the shear flow rates

of 0.5 Dynes/cm^2, 0.25 Dynes/cm^2 and 0.08 Dynes/cm^2, as shown in Figure 5.1 below.

Adherence of patient-derived CLL cells to the monolayer decreased with increased rates of shear flow, and cellular adherence of patient-derived CLL cells to the monolayer increased with increased timepoints. At 2 minutes and 15 minutes at a shear flow rate of 0.5 Dynes/cm^2 there was a mean adherence of 107.16 cells and 194.33 cells, respectively, to the HUVEC monolayer (n=6). At 2 minutes and 15 minutes at a shear flow rate of 0.25 Dynes/cm^2 there was a mean adherence of 162.83 cells and 224.83 cells, respectively, to the HUVEC monolayer (n=6). At 2 minutes and 15 minutes at a shear flow rate of 0.08 Dynes/cm^2 there was a mean adherence of 68.33 cells and 225.66 cells, respectively, to the HDLEC monolayer (n=3).

We then investigated the effects of treatment with bare Fe_2O_3 nanoparticles on the adherence of CLL cells to the endothelial monolayer. Treatment with 25µg/mL bare Fe_2O_3 nanoparticles demonstrated a significant effect on the adherence of CLL cells to the HUVEC monolayer at 0.5 Dynes/cm^2, with adherence decreasing by 50.4% at the 2 minute time point, and 42.1% at the 15 minute time point (n=6; $p<0.001$). Treatment with 25µg/mL Fe_2O_3 has a significant effect on the adherence of cells to the HUVEC monolayer at 0.25 Dynes/cm^2 (n=6; $p<0.001$), with adherence being seen to decrease by 46.5% at the 2 minute time point and 34% at the 15 minute time point. Treatment with 25µg/mL Fe_2O_3 has a significant effect on the adherence of cells to the HDLEC monolayer at 0.08 Dynes/cm^2 (n=6; $p<0.001$), with adherence being seen to decrease by 62.8% at the 2 minute time point

and 67.4% at the 15 minute time point. These data can be found in the Appendix 8.5. Additionally, we assessed the effect of shear flow rate on the cytotoxicity of nanoparticles in the I-83 cell line. We found that under shear flow rates of 0.5 Dynes/cm^2 and 0.25 Dynes/cm^2, there was no significant decrease in cell viability observed, in contrast to a significant decrease in cell viability under static conditions. Shear flow rates of 0.08 Dynes/cm^2 resulted in a significant decrease in cell viability ($p < 0.001$; n=3). These data can be found presented within the Appendix 8.6.

Next, we investigated the effect that Fe_2O_3@APTES, Fe_2O_3@CD52, and anti-CD52 monoclonal antibody alone, had on the adherence of patient-derived CLL cells to a HUVEC monolayer after 15 minutes at 0.5 Dynes/cm^2 (n=3). Treatment with Fe_2O_3@APTES was found to have no significant effect on patient-derived CLL cell adherence to the monolayer, with an adherence decrease of 16% (n=3). Treatment with Fe_2O_3@CD52 nanoparticles were found to have a significant effect on the adherence of patient-derived CLL cells to the monolayer (a decrease of approximately 49.5%), but treatment with anti-CD52 monoclonal antibody did not have any significant effect, with no decrease in patient-derived CLL cellular adherence to the monolayer being observed (see Figure 5.2), when compared to that of Fe_2O_3@APTES (n=3; $p < 0.001$). The same pattern of results was observed following assessment of the effect that Fe_2O_3@APTES, Fe_2O_3@CD52, and anti-CD52 monoclonal antibody alone on the adherence of patient-derived CLL cells to a HDLEC monolayer after 15 minutes at 0.08 Dynes/cm^2 (n=3). These results may be found in the Appendix 8.7. Figure 5.3 shows representative brightfield images as taken during one microfluidic run.

CLL cell adhesion to endothelial monolayer under fluid shear flow
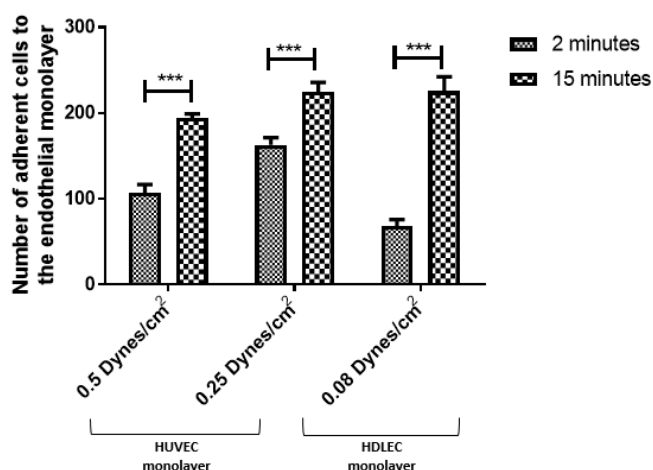
Figure 5.1: **Patient-derived CLL cell adherence to the endothelial monolayer increases with time**. 1×10^6 patient-derived CLL cells (n=6; CLL1, CLL3, CLL4) were introduced to the microfluidics system containing HUVEC and HDLEC monolayers under the flow rates as indicated. The number of adherent cells were recorded at 2 minutes and 15 minutes. CLL cell adherence was seen after 15 minutes. There was a significant increase in the number of adherent cells between the recorded timepoints of 2 minutes and 15 minutes ($p<0.001$; one-way repeated measures ANOVA, Dunnet's post-test).

Treatment with Fe_2O_3@CD52 nanoparticles reduce the adherence of CLL cells to the HUVEC monolayer at 0.5 Dynes/cm^2
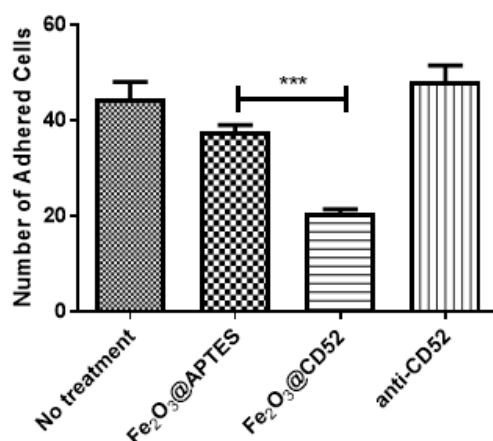
Figure 5.2: **Treatment with 25µg/mL Fe_2O_3@CD52 30 minutes prior results in significantly less adhesion of patient-derived CLL cells to HUVEC cells at a fluid shear flow rate of 0.5 Dynes/cm^2.** Patient-derived CLL cell (1×10^6) were treated with 25µg/mL Fe_2O_3@APTES, Fe_2O_3@CD52, and 10µg/mL of anti-CD52 for 30 minutes and adherence to HUVEC cells after 15 minutes under 0.5 Dynes/cm^2 shear flow was assessed (n=3). Treatment with Fe_2O_3@CD52 nanoparticles had a significant effect on cellular adherence, when compared to Fe_2O_3@APTES nanoparticles ($p<0.001$; ANOVA with Tukey post-test). Treatment with Fe_2O_3@APTES or 10µg/mL of anti-CD52 monoclonal antibody had no significant effect on adherence, when compared to that of no treatment. Data are illustrative of CLL patient samples CLL7, CLL15 and CLL16.
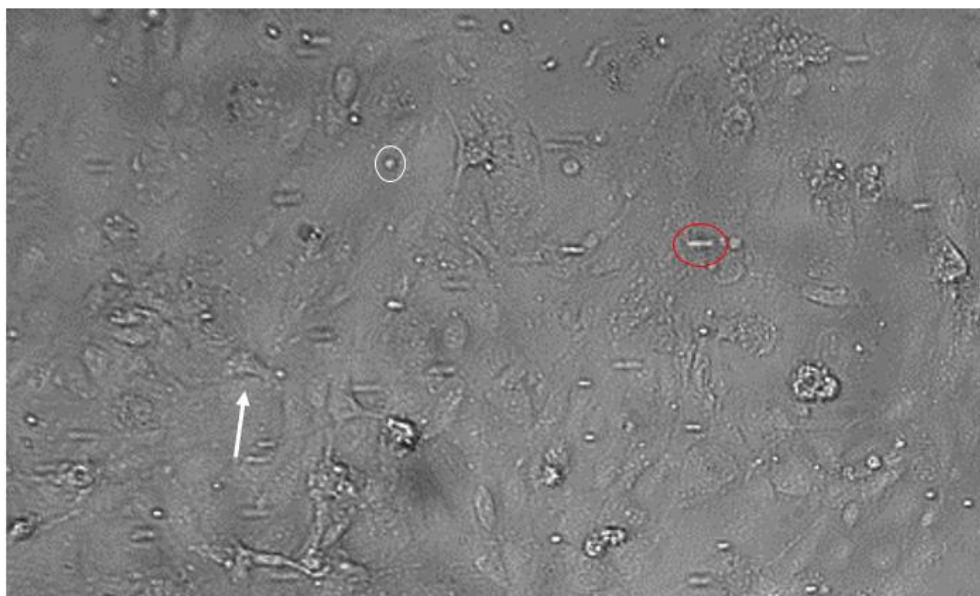
Figure 5.3: Representative image of CLL patient sample under a shear flow rate of 0.5 Dynes/cm², through a microchip coated with an endothelial monolayer of HUVECs. Patient-derived CLL cells that have become adhered to the endothelial monolayer can be seen encircled in white, whilst the HUVEC cell can be seen as per white arrow. CLL cells in flow across the monolayer (and as such appears as blurry) can be seen encircled in red.

5.2.2 Determination of toxicity of Fe_2O_3@CD52 nanoparticles on patient-derived CLL cells

Having shown that Fe_2O_3@CD52 nanoparticles induce apoptosis in the I-83 cell line, we next investigated the effect of treatment with the nanoparticle on a cohort of patient-derived CLL cells. $3x10^5$ patient-derived CLL patient samples were treated with either Fe_2O_3@APTES or Fe_2O_3@CD52 for 8 hours and 24-hour. Following treatment, CLL cells were recovered and were stained for annexin V and PI and analysed by flow cytometry analysis. The patient characteristics are shown in Table 2.2 and 5.1.

Table 5.1 Details of the clinical characteristics of CLL patient samples used within this study, and the parameters assessed.

CLL #	Binet stage	IGHV Mutation %	IGHV (M/UM)	NOTCH1 (M/UM)	CD38 (P/N)	CD49d (P/N)	*Del*13q (P/N)	*Del*17p (P/N)
1	C	99.5%	M	M	N	N	N	N
2	C	100%	UM	UM	P	N	P	N
4	A	94.17%	M	M	N	ND	P	N
5	A	100%	UM	UM	P	P	N	N
6	A	100%	UM	UM	N	N	P	N
7	A	ND	ND	UM	N	P	N	N
8	A	99.51%	UM	UM	N	P	N	P
9	A	ND	ND	ND	ND	N	ND	ND
10	A	100%	UM	M	N	ND	N	N
11	B	100%	UM	M	P	ND	N	N
12	C	95.79%	M	UM	N	P	ND	ND
13	B	100%	UM	M	P	P	N	P
14	C	100%	UM	M	P	ND	P	N
15	A	92%	M	UM	N	P	P	N
17	B	99.5%	UM	UM	P	ND	N	N

Following treatment of patient-derived CLL cells with 25, 50 and 100µg/mL Fe_2O_3@CD52 for 8 hours, there was a significant increase in apoptotic cells when compared to the no treatment control and all Fe_2O_3@APTES nanoparticle concentrations (n=15; $p<0.0001$) following treatment with 50µg/mL Fe_2O_3@CD52 and above, with a maximum level of apoptosis of 97% observed with cells treated with 100µg/mL Fe_2O_3@CD52. No significant increase in apoptosis was observed in CLL cells treated with Fe_2O_3@APTES or unbound anti-CD52 monoclonal antibody, though there was an increase in apoptosis induction observed with anti-CD52 monoclonal antibody treatment.

These data can be found below in Figure 5.4(A). Representative flow cytometric scatter plots of each treatment can be found in Figure 5.4(B) and below in Figure 5.9.

Following treatment of patient-derived CLL cells with 25, 50 and 100µg/mL Fe_2O_3@CD52 for 24 hours, there was a significant increase in apoptotic cells when compared to the no treatment control and all Fe_2O_3@APTES nanoparticle concentrations (n=15; $p<0.0001$) following treatment with 25µg/mL Fe_2O_3@CD52 and above, with a maximum level of apoptosis of 96.4% observed with cells treated with 100µg/mL Fe_2O_3@CD52. No significant increase in apoptosis was observed in CLL cells treated with Fe_2O_3@APTES or unbound anti-CD52 monoclonal antibody, though there was an increase in apoptosis induction observed with anti-CD52 monoclonal antibody treatment. These data can be found below in Figure 5.5 (A). Representative flow cytometric scatter plots of each treatment can be found in Figure 5.5 (B) and below in Figure 5.9.

CLL cells were also incubated with a preliminary proof-of-concept Fe_2O_3@CD52 nanoparticle functionalised with electrostatically-bound fludarabine (Fe_2O_3@CD52-Fludarabine). Results of this study indicate that the addition of fludarabine to the surface of our Fe_2O_3@CD52 nanoparticle resulted in no increase in apoptosis (Appendix 8.8).

A heterogenous response to Fe_2O_3@CD52 induced apoptosis was observed with a mean of 68.45% ± 5.406% after 8 hours and 78.83% ± 3.975% after 24 hours (Figure 5.6 (A)(B), respectively). No correlation was observed between responsiveness to treatment and percentage

expression of CD52 at either 8 hours (Figure 5.6 (C); $R^2=0.017$) or 24 hours (Figure 5.6 (D); $R^2=0.01$). Similarly, no correlation was observed between responsiveness to treatment and anti-CD52 AlexaFluor647 mean fluorescence intensity at either 8 hours (Figure 5.6 (E); $R^2=0.02$) or at 24 hours (Figure 5.6 (F); $R^2=0.04$).

A number of prognostic markers which are associated with poor outcome and resistance to chemotherapeutics are known for CLL, including Binet Stage, presence of unmutated IGHV genes, expression of CD38, expression of CD49d, mutations in NOTCH1 genes and deletions in chromosome 17p and 13q (Table 5.1). Overall, there was wide heterogeneity observed Fe_2O_3@CD52 induced apoptosis in each of Binet Stage A (n=8), Binet Stage B (n=3) and Binet Stage C (n=4) at both 8 hours (Figure 5.7 (A)) and 24 hours (Figure 5.7 (B)). There was minimally greater heterogeneity in Fe_2O_3@CD52 induced apoptosis found in samples identified in Binet Stage A and B samples, compared with that of Binet Stage C samples (range of 22.2-76.35%, 9.9-68.9% and 46.2-65.7%, respectively), though it was not statistically significant.

No significant difference in Fe_2O_3@CD52 induced mean apoptosis was observed between mutated IGHV (n=4) and mutated IGHV (n=9) after 8 hours and 24 hours (Figure 5.7 (C) and (D), respectively). However, greater heterogeneity in response was noted in patient samples with unmutated IGHV compared to mutated IGHV (range of 15-95% versus 71-82%, respectively) at 8 hours.

No significant difference was observed in Fe_2O_3@CD52 induced mean apoptosis between CD38 positive (n=6) or CD38 negative (n=8) CLL

cells at either 8 hours (Figure 5.7 (E)) or 24 hours (Figure 5.7 (F)). No significant difference was observed in Fe_2O_3@CD52 induced mean apoptosis between NOTCH1 mutated (n=6) or NOTCH1 unmutated (n=8) CLL cells at either 8 hours (Figure 5.8 (A)) or 24 hours (Figure 5.8 (B)).

A significant difference was found in Fe_2O_3@CD52 induced mean apoptosis between CD49d- patient-derived CLL cells (n=4), when compared to CD49d+ patient-derived CLL cells (n=6) following 8-hour treatment (range of 9.9-47.8% versus 49.8-61.1%, respectively; Figure 5.8 (C); $p<0.05$). However, no statistical difference was found in Fe_2O_3@CD52 induced mean apoptosis between CD49d- patient-derived CLL cells, when compared to CD49d+ patient-derived CLL cells following 24 hour treatment (Figure 5.8 (D)).

No significant difference was observed in Fe_2O_3@CD52 induced mean apoptosis between *del13q* positive (n=4) or *del13q* negative (n=9) CLL cells at either 8 hours (Figure 5.8 (E)) or 24 hours (Figure 5.8 (F)). No significant difference was observed in Fe_2O_3@CD52 induced mean apoptosis between *del17p* positive (n=2) or *del17p* negative (n=11) CLL cells at either 8 hours (Figure 5.8 (G)) or 24 hours (Figure 5.8 (H)).

Treatment with Fe$_2$O$_3$@CD52 induces significant apoptosis/necrosis in patient-derived CLL cells, over 8 hours

(A)

(B)
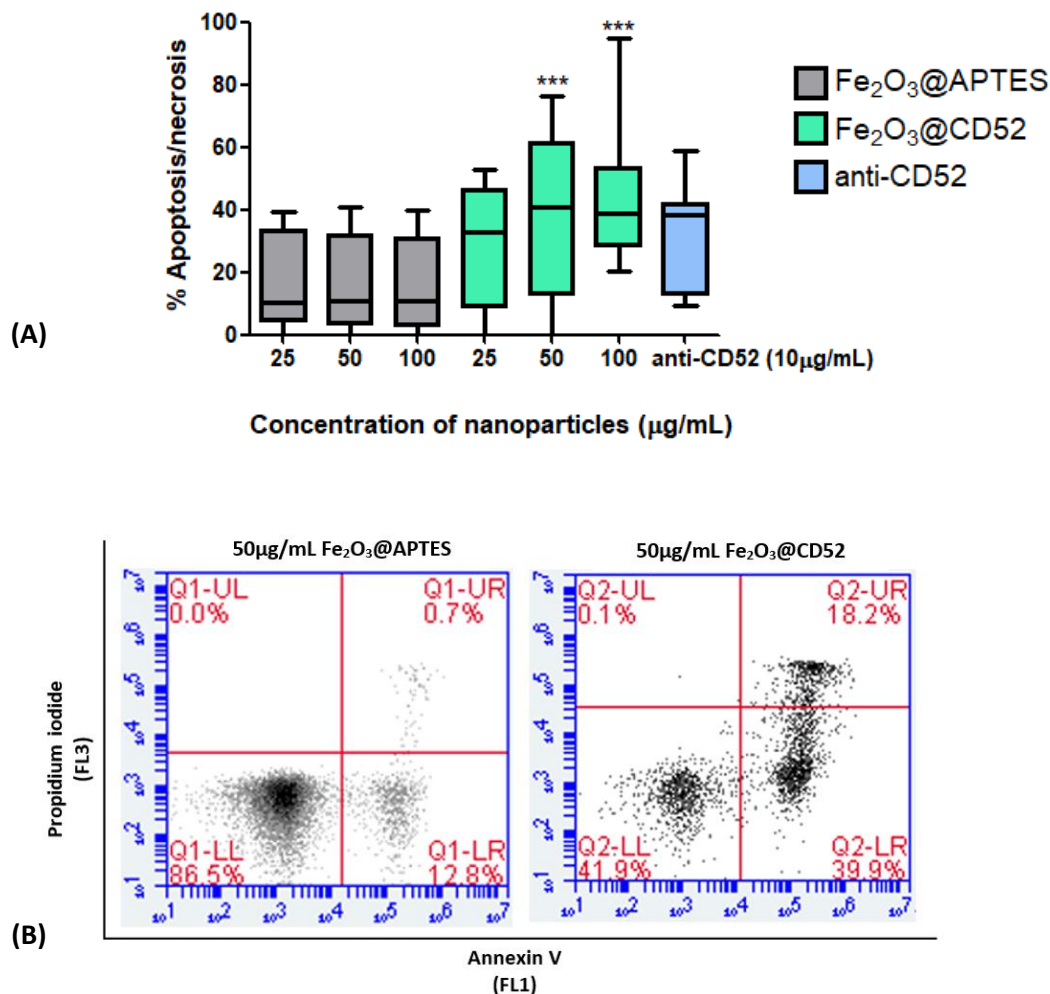
Figure 5.4: **Treatment with Fe$_2$O$_3$@CD52 nanoparticles over 8 hours induces significant apoptosis/necrosis in patient-derived CLL cells.** 3x15[5] patient-derived CLL cells were treated with Fe$_2$O$_3$@APTES, Fe$_2$O$_3$@CD52 or unbound anti-CD52 antibody at the indicated concentration for 8 hours. Cells were recovered, and cell viability assessed using Annexin-V P as discussed above. (A) These data show that Fe$_2$O$_3$@CD52 increases the levels of apoptosis significantly, when compared to the no treatment, and Fe$_2$O$_3$@APTES. There was no observed significant effect of unbound anti-CD52 when compared to the no treatment over this time period (n=15; $p < 0.0001$; one-way ANOVA with Tukey post-test). Figure panel (B) shows representative flow cytometry plots following 8-hour incubation at 50µg/mL treatment with indicated nanoparticles.

Figure 5.5: **Treatment with Fe$_2$O$_3$@CD52 nanoparticles over 24 hours induces significant apoptosis/necrosis in patient-derived CLL cells.** 3×10^5 patient-derived CLL cells were treated with Fe$_2$O$_3$@APTES, Fe$_2$O$_3$@CD52 or unbound anti-CD52 antibody at the indicated concentration for 24 hours. Cells were recovered, and cell viability assessed using Annexin-V P as discussed above. (A) These data show that Fe$_2$O$_3$@CD52 increases the levels of apoptosis significantly, when compared to the no treatment, and Fe$_2$O$_3$@APTES ($p<0.001$). There was an observed significant effect of unbound anti-CD52 when compared to the no treatment over this time period ($p<0.01$) (n=15; one-way ANOVA with Tukey post-test). Figure panel (B) shows representative flow cytometry plots following 24 hour incubation at 50µg/mL treatment with indicated nanoparticles.
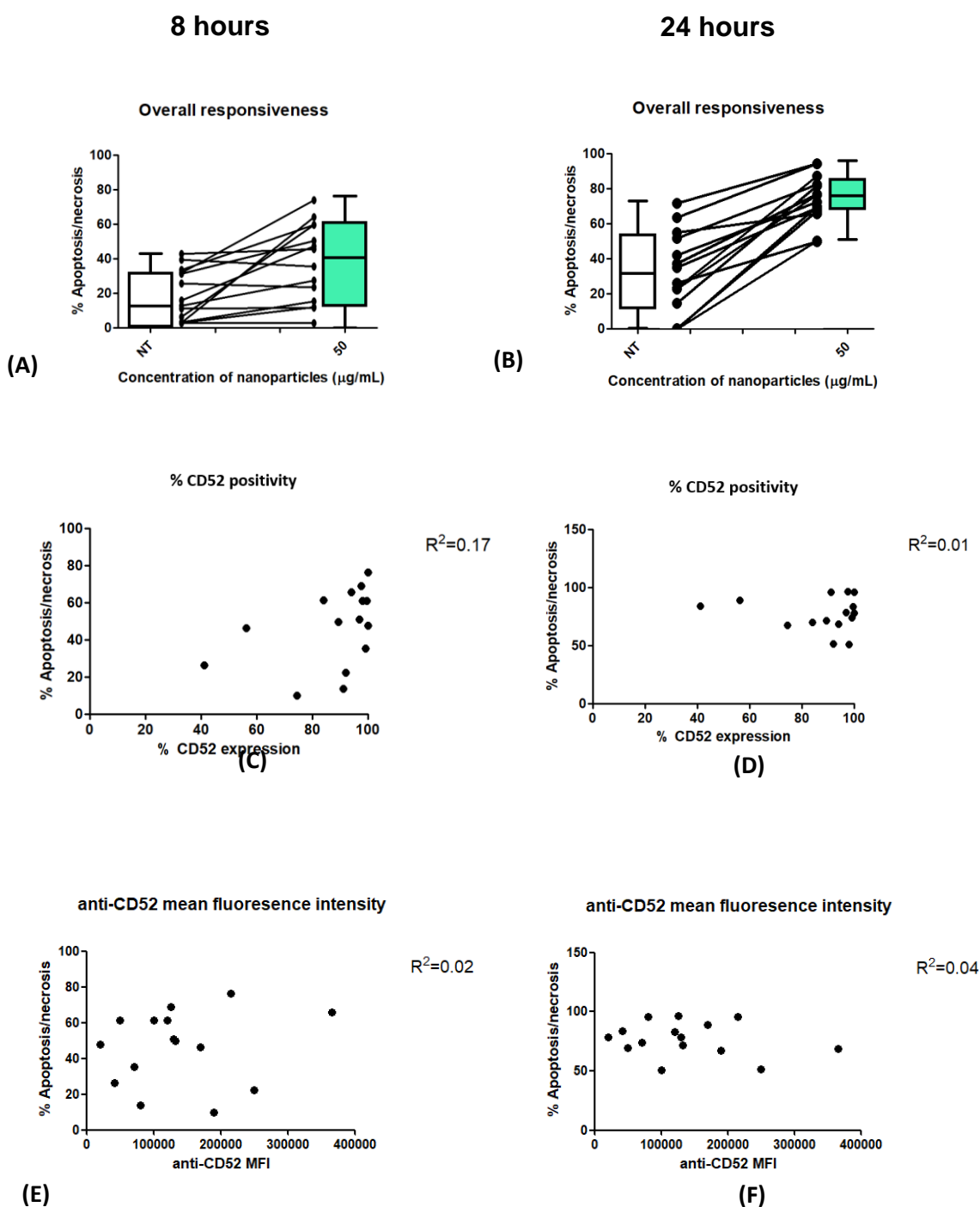
Figure 5.6: **Responsiveness to treatment with Fe₂O₃@CD52 in patient-derived CLL patient samples** 3×10^5 patient-derived CLL cells were treated with 50μg/mL Fe₂O₃@CD52 for the indicated timepoint. Cells were recovered, and apoptosis-necrosis levels were analysed using annexin V-PI staining and flow cytometry. (A) shows heterogeneity in overall responsiveness at 8 hours, with (B) showing a lack of heterogeneity in overall responsiveness at 24 hours. Data also presents no correlation between responsiveness to Fe₂O₃@CD52 treatment and either percentage CD52 expression ((C)(D)) or anti-CD52 AlexaFluor647 mean fluorescence intensity ((E)(F)) (n=15).

8 hours

24 hours
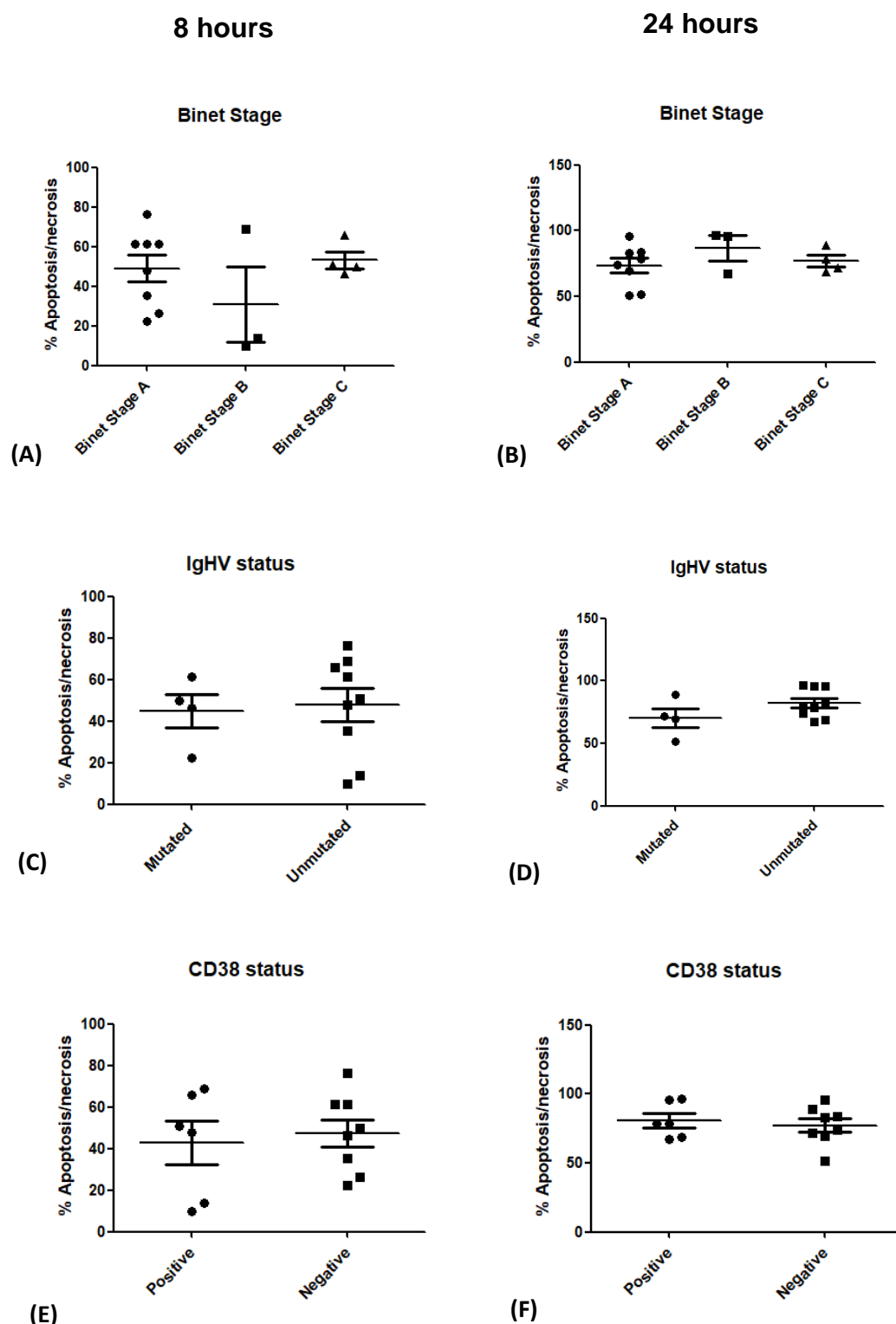
Figure 5.7: Responsiveness of patient-derived CLL cells to treatment with 50µg/mL Fe$_2$O$_3$@CD52 as categorised by Binet Stage, IGHV mutational status and CD38 status. 3x10^5 patient-derived CLL cells were treated with 50µg/mL Fe$_2$O$_3$@CD52 for the indicated timepoint. Cells were recovered, and apoptosis-necrosis levels were analysed using annexin V-PI staining and flow cytometry. A wide range of heterogeneity was observed across all Binet Stages at 8 hours (A) with minimal heterogeneity observed at 24 hours (B)(n=15). Similarly, a wide range of heterogeneity was observed in both IGHV mutated and unmutated at 8 hours (C) with minimal heterogeneity observed at 24 hours (D)(n=13). Similarly, a wide range of heterogeneity was observed in both CD38 positive and negative at 8 hours (E) with minimal heterogeneity observed at 24 hours (F)(n=14).
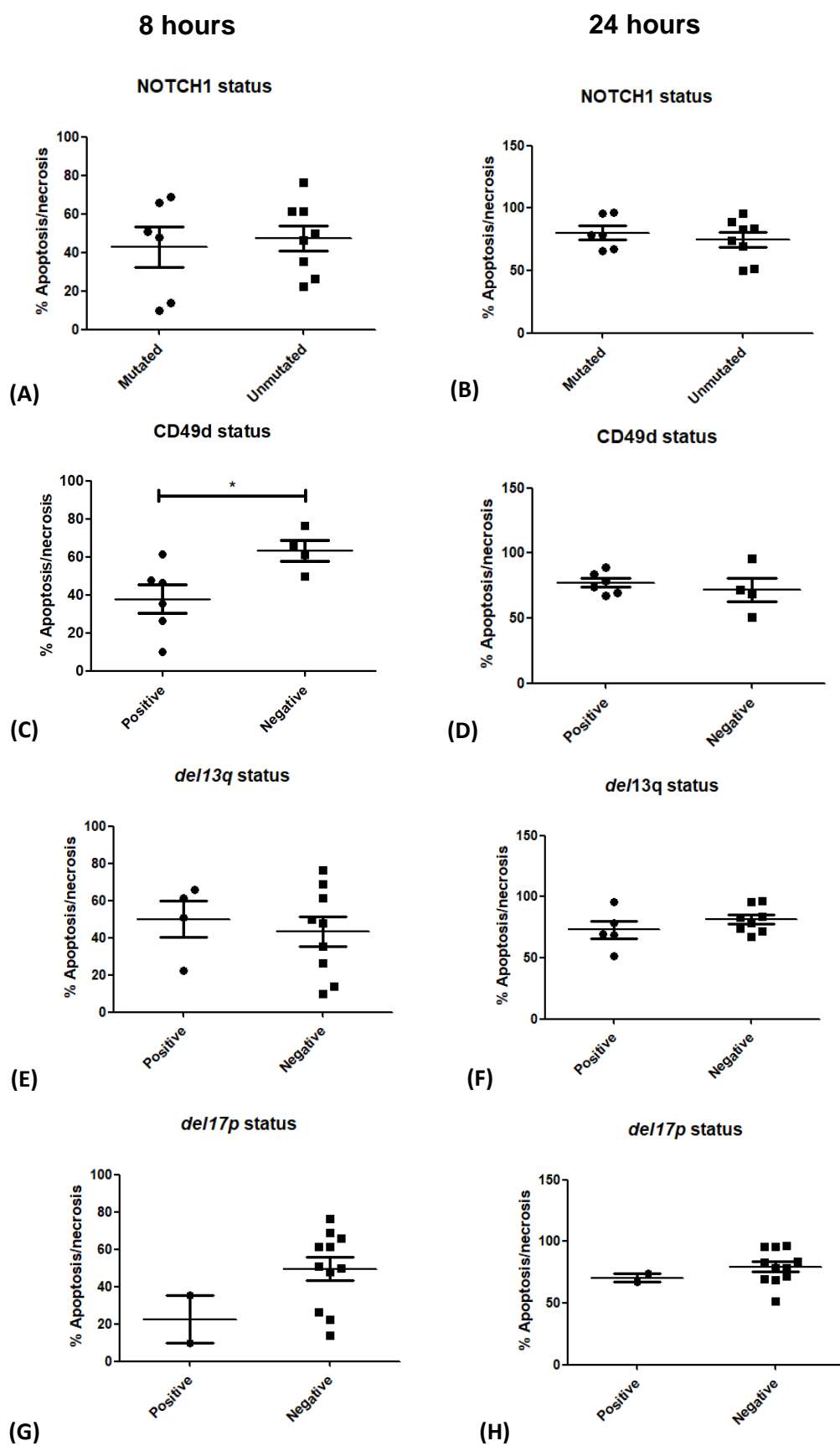
Figure 5.8: Responsiveness of patient-derived CLL cells to treatment with 50µg/mL Fe$_2$O$_3$@CD52 as categorised by NOTCH1, CD49d, del13q and del17p status. 3×10^5 patient-derived CLL cells were treated with 50µg/mL Fe$_2$O$_3$@CD52 for the indicated timepoint.

Cells were recovered, and apoptosis-necrosis levels were analysed using annexin V-PI staining and flow cytometry. A wide range of heterogeneity was observed in both NOTCH1 mutated and unmutated at 8 hours (A) with minimal heterogeneity observed at 24 hours (B)(n=14). There was a statistically significant difference between CD49d positive and CD49d negative at 8 hours (C) with minimal heterogeneity observed at 24 hours (D)(n=10). Similarly, a wide range of heterogeneity was observed in both *del13q* positive and negative at 8 hours (E) with minimal heterogeneity observed at 24 hours (F)(n=13). Again, a wide range of heterogeneity was observed in both *del17p* positive and negative at 8 hours (G) with minimal heterogeneity observed at 24 hours (H)(n=13).
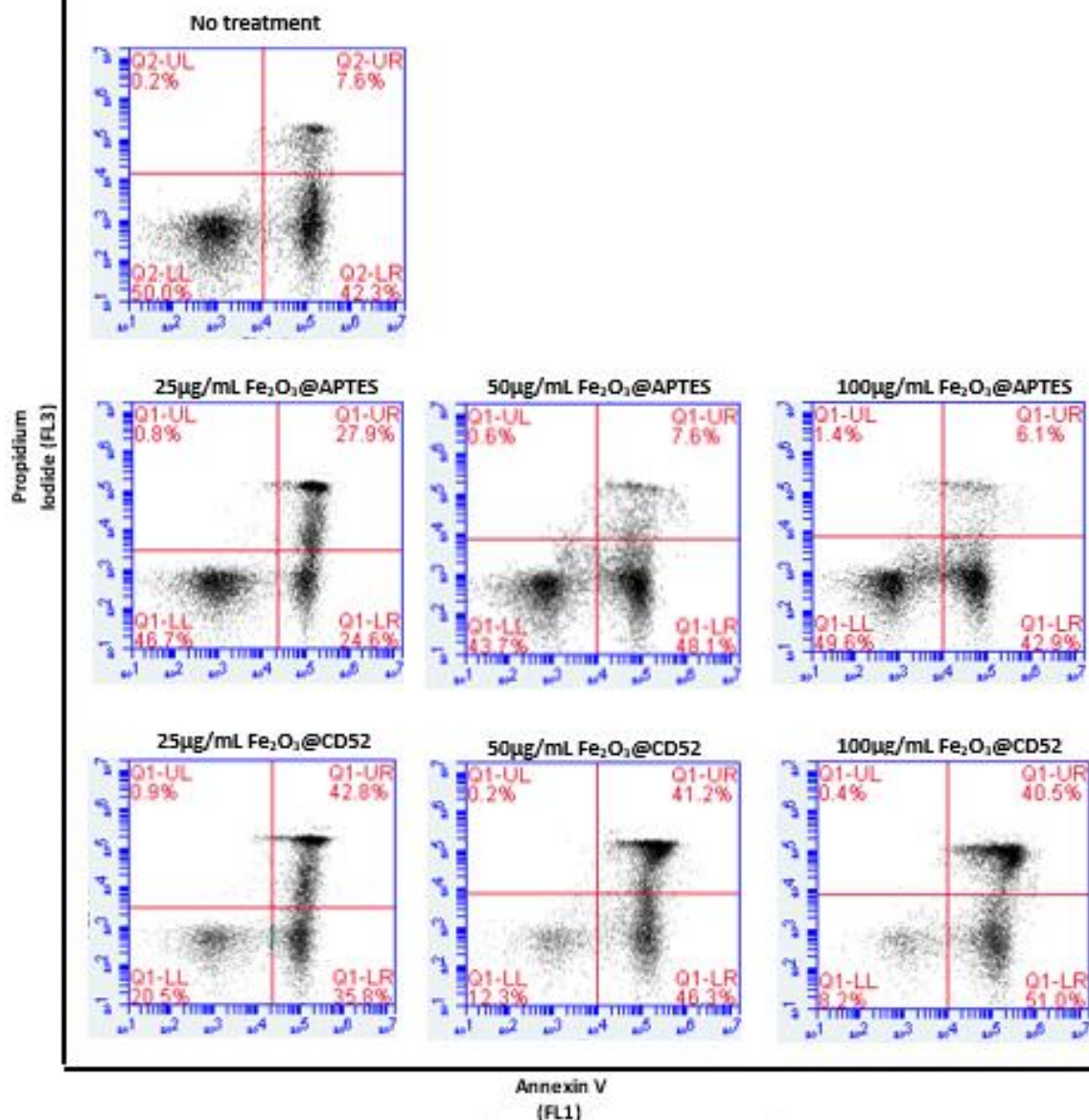
Figure 5.9: Representative flow cytometric scatter plots of one CLL patient sample showing the effects of Fe₂O₃@CD52 in contrast to no treatment and treatment with Fe₂O₃@APTES. Following treatment, cells were stained with Annexin V-PI, and levels of apoptosis/necrosis were analysed on the BD Accuri C6. The initial cell population can be seen in lower left quadrant (Q1-LL), and the shift to the lower right and upper right quadrants can be seen following treatment with nanoparticles indicated, as apoptosis/necrosis is detected. A shift to the lower right quadrant indicates early-stage apoptosis, with a shift to the upper left quadrant indicating late/stage apoptosis/necrosis. A double positive shift appears in the upper right quadrant (Q1-UR). As with other treatments, all nanoparticles were assessed for successful functionalisation ahead of treatment, and all CLL patient samples were previously tested for CD19+ ahead of use.

232

5.3 Discussion

The aim of this chapter was to assess the effect of anti-CD52 monoclonal antibody functionalised nanoparticles (Fe_2O_3@CD52) in a cohort of clinically and molecularly annotated patient-derived CLL cells. In particular, we assessed the effect of Fe_2O_3@CD52 on the interaction of CLL cells with endothelial cells under physiologically relevant fluids shear flow conditions and in the induction of cytotoxicity using annexin V/PI apoptosis assay.

The effect of shear stress on blood cells is of much research interest (White & Frangos, 2007) (Nobilli *et al.,* 2008). Here, we used a purpose-built microfluidics system to investigate the effects of shear stress on the adherence of CLL cells to endothelial cells under physiologically-relevant conditions and assess the effects of the interactions on these interactions. CLL cells undergo important interaction with their microenvironment and endothelial cells play important roles in the homing of CLL cells to the lymph nodes and bone marrow. These interactions happen under shear flow conditions, so it is critical to model these interactions under appropriate model systems (Fan, *et al.*, 2016) (Ni *et al.,* 2003).

Within this study, we utilised human umbilical vein endothelial cells (HUVECs) or human dermal lymphatic endothelial cells (HDLEC) cells, with three different flow rates. This study aimed to provide a further understanding of the interaction of patient-derived CLL cells with their endothelial environment *in vitro*, and whether treatment with nanoparticles could disrupt these interactions. CLL cells *in vivo* rely

heavily on the signals transduced from their microenvironment, and niches within this microenvironment can provide important protective sites for the CLL cells in order to evade standard chemotherapeutics (Frankel *et al.,* 2017). Shear flow rates of 0.5 Dynes/cm^2 and 0.25 Dynes/cm^2 were employed in the study of patient-derived CLL cells interacting with HUVEC monolayers. A shear flow rate of 0.08 Dynes/cm^2 was employed in order to investigate the interactions of CLL patient sample cells with the HDLEC monolayers. Data presented within this study demonstrate that there is an increase in CLL cell adhesion to the monolayer with increased time, and with saturation of CLL cell adherence being observed at approximately 15 minutes (data not shown). The levels of adherence of patient-derived CLL cells to the endothelial monolayer are also consistent with the findings by other groups (Fiorcari, *et al.*, 2013). We have shown previously (described in Chapter 3) that there is significant impact on cell viability in I-83 cells exposed to 25µg/mL of bare Fe_2O_3 nanoparticles under static conditions. However, following I-83 cell exposure to Fe_2O_3 nanoparticles under a shear flow rate of 0.5 Dynes/cm^2 there is no significant effect on cell viability. Interestingly, when cells are exposed to 0.08 Dynes/cm^2 shear flow rate, there is a significant effect on cell viability (data presented within the Appendix 8.6). It would be interesting to determine if a similar effect of shear flow on cell viability is observed with treatment with Fe_2O_3@ATPES or Fe_2O_3@CD52. Whilst we are unaware of any other studies looking at the effect of nanoparticles on CLL cell viability under shear flow conditions, we postulate that this increase in toxicity may be as a direct result of the increased interaction time given to the

cell suspension with the nanoparticles in their environment, as a result of the lower rate of flow. A study looking at a comparison of the toxic effects of gold nanoparticles on endothelial cells using both static and shear flow conditions found that there was a 20% reduction in the level of cell death under shear flow conditions (Fede, *et al.*, 2017). This study is consistent with our findings that at the 0.5 Dynes/cm^2 shear flow rate, there is a lower level of cellular toxicity in the cells undergoing shear flow when compared to the cells under static conditions (Appendix 8.6). Another study investigating the viability of the colon cancer cell line HCT116 under increasing rates of mimicked high wall shear flow found that with a slower shear flow rate, cell viability was decreased. As the shear flow rate was increased, this viability was found to be higher. Again, this study is consistent with our findings presented here (Fan, *et al.*, 2016).

Finally, the effect that Fe_2O_3@APTES, Fe_2O_3@CD52, and anti-CD52 monoclonal antibody alone, had on the adherence of cells to the HUVEC and HDLEC monolayer under shear flow was also investigated. There was no significant effect on the adherence of patient-derived CLL cells to their endothelial microenvironment following treatment with Fe_2O_3@APTES nanoparticles. The APTES coating of the nanoparticle may behave as a stabilising coating which may decrease the interactions of the nanoparticles with the surrounding cells and therefore prevent the inhibition of cellular adhesion. Similar such findings have recently been reported by groups assessing the use of APTES as a stabilising agent in polydimethylsiloxane (PDMS) – based microfluidic systems. Such research groups have found that the use of APTES as

an additional anchoring agent within their microfluidic systems have promoted longevity in cellular viability and aided adherence of various cell types when under shear stress (Siddique *et al.,* 2017) *(Chuah, et al.,* 2015). Treatment with Fe_2O_3@CD52 nanoparticles were found to result in a significant increase in the adherence of patient-derived CLL cells to the monolayer, which was not observed in CLL cells treated with anti-CD52 monoclonal antibody. This suggests that physical interaction of the Fe_2O_3@CD52 nanoparticles with CLL cells is required for inhibition of CLL adhesion to HUVEC cells under shear flow conditions. As demonstrated in Chapter 4, Fe_2O_3@CD52 are incorporated on the surface and are taken up by patient-derived CLL cells, which may have a mechanism for inhibition of adhesion to HUVEC cells of the patient-derived CLL cells with the monolayer. In addition, the nanoparticle themselves may interact with the endothelial monolayer and therefore prevent possible adherence of the CLL cell to the monolayer. Further investigations are warranted to decipher the mechanism of Fe_2O_3@CD52 induced inhibition of CLL cell adhesion to endothelial cells under shear flow conditions.

Results of this chapter again support the rationale for the development of a novel antibody based therapeutic. Results indicate that Fe_2O_3@CD52 nanoparticles decrease the interactions of patient-derived CLL cells with their microenvironment, potentially decreasing CLL cell trafficking to the lymph node microenvironment and induce cell death in CLL cells including those with poor prognostic indicators. A therapeutic based on this work could play a role in the management of

CLL and have potential clinical implications in the decrease of survival and homing of CLL cells.

Following on from a robust study into the validation of use of Fe_2O_3@CD52 in both normal B cells and the I-83 cell line in Chapter 4, we sought to determine the efficacy of this functionalised nanoparticle in patient-derived CLL cells through assessment of toxicity using annexin V-PI staining and flow cytometric analysis.

CLL patient samples were obtained from the SJH/TCD CLL biobank. This biobank contains cryopreserved CLL cells isolated from the peripheral blood of CLL patients and have been well annotated both clinically, immunophenotypically and molecularly (see Table 2.2). The use of these CLL patient samples provided considerably more valuable data on the efficacy of Fe_2O_3@CD52, than the use of cell line models alone.

Analysis of apoptotic events across this cohort of patient-derived CLL cells demonstrated that following incubation with Fe_2O_3@CD52, there is a significant dose response induction of apoptosis, when compared to the no treatment control, the unbound anti-CD52 antibody or Fe_2O_3@APTES. Whilst we are unaware of any other studies assessing the effectiveness of an anti-CD52 functionalised Fe_2O_3 nanoparticle in CLL to date, there has been substantial work undertaken to investigate the effectiveness of anti-CD52 therapy, alemtuzumab, on CLL cells. Currently, the mechanism of cell death employed by anti-CD52 monoclonal antibody therapy remains unclear, with *in vitro* studies having shown that each of complement-dependent cytotoxicity (CDC)

and antibody-dependent cellular cytotoxicity (ADCC) and programmed cell death induced by antibody binding are the mechanisms behind the induction of cell death (Zent, *et al.*, 2008). The CD52 monoclonal antibody clone used throughout this body of work (clone 097) has been shown in other studies to successfully initiate CDC in lymphocytes, providing long-term killing of colony-forming cells in bone marrow culture, and importantly, demonstrated similar effects in T cells are to that of alemtuzumab (Valentin, *et al.*, 1992).

Within this study of patient-derived CLL cells, we found toxicity of Fe_2O_3@CD52 to be seen at a significant level at treatment concentrations of 25µg/mL and above, and we used a control of free anti-CD52 monoclonal antibody at a concentration of 10µg/mL, a concentration commonly reported in the literature to obtain significant cell death (Mone, *et al.*, 2006) (Zent, *et al.*, 2008). This concentration of anti-CD52 monoclonal antibody is considerably higher than the hypothesised quantity of anti-CD52 monoclonal antibody loaded onto the surface of our nanoparticles, at any concentration (see Methods section 2, Table 2.5). We propose that the use of a nanoparticle carrier coupled to anti-CD52 monoclonal antibody therapy enhances the efficacy of the drug *in vitro.* This suggests that such a novel nanoparticle were to be translated to *in vivo* animal studies, a lesser concentration of antibody could be used to attain similar levels of cell death as with free antibody, resulting in potentially fewer systemic toxic effects than has been seen with free antibody itself (Christian & Lin, 2009) (Hiddemann, *et al.*, 1991). Additionally, the significant reduction in adherence of CLL cells to the endothelial monolayer following treatment with

Fe_2O_3@CD52 nanoparticles could have potential implications to the reduction in diapedesis and homing of CLL cells, further reducing systemic effects. We found that treatment with Fe_2O_3@CD52 nanoparticles results in significantly more apoptosis than that of any of the three controls, and that this finding can be observed following treatment with any of 25µg/mL, 50µg/mL and 100µg/mL. We only assessed direct toxicity induced by Fe_2O_3@CD52 nanoparticles and it should be noted that ADCC and CDC may contribute further to the effect of Fe_2O_3@CD52 on CLL cells.

As mentioned previously, we am aware of no data available on the use of anti-CD52 functionalised nanoparticles in CLL, to date. However, improved targeting and cytotoxicity in animal models and in CLL cell lines have been shown in biodegradable nanoparticles functionalised with anti-CD20 in addition to relatively high doses of hydroxychloroquine and chlorambucil, though it should be noted that the concentrations of functionalised nanoparticles used in this study for their *in vitro* work were considerably higher, at a nanoparticle concentration of 270µg/mL (Mezzaroba, *et al.*, 2013). Additionally, *in vivo* studies utilising polymeric nanoparticles functionalised with anti-CD20 antibody have been shown to be of great benefit in the imaging and diagnosis of CLL, with the incorporation of anti-CD20 to the surface of these nanoparticles significantly increasing targeting of CLL cells (Capolla, *et al.,* 2015). These studies support our hypothesis that the generation of a proof-of-concept anti-CD52 functionalised nanoparticle for the targeting and killing of CLL cells is a novel approach and will be of benefit in further research towards the generation of a targeted

therapeutic for CLL. Additionally, we assessed the use of an early-stage proof-of-concept model of Fe_2O_3@CD52 with the purine analogue fludarabine electrostatically-bound to the surface (Fe_2O_3@CD52-Fludarabine). A detailed breakdown of these results can be found in Appendix 8.8. Within this study we found that across both time points assessed, no significant difference was found in levels of apoptosis between either Fe_2O_3@CD52 or Fe_2O_3@CD52-Fludarabine, indicating that within this model, there is no significant toxicity benefit to be gained from the inclusion of fludarabine on the surface of functionalised nanoparticles. However, it is important to note that a full spectroscopic study of the successful electrostatic functionalisation of fludarabine to the surface of these nanoparticles was not performed and could potentially form interesting future work. Here, we use a high concentration of fludarabine (20µM) for inclusion to the surface of the nanoparticle and within our control studies, when compared to concentrations that are often found within the literature (0.3-30µM) (Di Raimondo, *et al.*, 1995) (Fonte, *et al.*, 2013). The purpose of this was to ensure that the concentration remaining on the surface of the nanoparticles throughout the timepoints remains high enough for successful induction of cytotoxicity. However, it is possible that there was little fludarabine left remaining on the surface of the nanoparticles at the time of targeting of the cell as a result of diffusion into the surrounding media or during the short time of storage, hence not contributing to cell death. However, should the fludarabine have diffused into the surrounding cellular media, apoptotic events would still have been initiated and therefore would have been recorded in our

apoptosis/necrosis assays. Fludarabine has been associated with a number of adverse events, including opportunistic systemic infections, blood and lymphatic disorders, immunosuppression and benign and malignant neoplasms (Hiddemann, *et al.*, 1991). It would be interesting to investigate this delivery of a therapeutic agents using more targeted agents with less currently being used clinically in CLL such as ibrutinib and venetoclax.

We observed a heterogeneous response to Fe_2O_3@CD52 across each of the CLL patient samples tested. This finding was as expected, as there will likely always be heterogeneity across any patient-derived CLL cell sample cohort, and levels of responsiveness to any chemotherapeutic will likely demonstrate a diverse response given that not all patients samples will demonstrate the same clinical, immunophenotypical or molecular characteristics (Guièze & Wu, 2015) (Wu, 2012). There was a notable heterogeneity in responsiveness to therapy in patients classed as Binet Stage A and B, with minimal heterogeneity in responsiveness noted in Binet Stage C. This is an interesting finding, as it would indicate that if observed in a larger cohort size, this proof-of-concept nanoparticle could yield predictable results in patients with an advanced disease stage. In order to investigate this heterogeneity further we assessed the responses of patient-derived CLL cells to the Fe_2O_3@CD52 nanoparticle based the presence of prognostic factors in Table 5.1. There was no significant difference in response to Fe_2O_3@CD52 in patients with other favourable prognostic markers compared to those with poor prognostic markers, including unmutated IGVH, CD38+, *del17p*, and mutated NOTCH1. We noted a

statistically significant difference in response of CLL cells to treatment with Fe_2O_3@CD52 in patients identified as CD49d negative, an indicator of a better clinical outcome and favourable clinical outcome, when compared to those CD49d positive, after 8 hours. This could mean that this subset of patients could possibly fair favourably following receipt of our proof-of-concept nanotherapeutic. These prognostic markers are associated with disease progression, poor outcomes and, in the case of *del17p*, resistance to chemoimmunotherapy. These findings indicate equipotent activity of Fe_2O_3@CD52 nanoparticle in patients with poor and favourable prognostic markers, suggesting further translational studies of this novel potential therapeutic is warranted.

6. General Discussion and future work

6.1 General summary and discussion

6.1.1   Summary

Within this thesis, we have addressed each of the points outlined in the Aims and Objectives reported in Chapter 1. In summary, we have presented the following:

1. Characterisation of both non-functionalised and functionalised Fe_2O_3 nanoparticles using a range of techniques including NTA, SEM, DLS and flow cytometry, and determination of chosen nanoparticle as suitable in size.

2. Identification of CD52 as a suitable cell surface marker for targeting CLL cells with functionalised Fe_2O_3 nanoparticles from a panel of commonly assessed B cell surface markers, using flow cytometry,

3. Functionalisation of Fe_2O_3 nanoparticles with anti-CD52 monoclonal antibodies, as well as Fe_2O_3 nanoparticles functionalised with anti-CD19 and anti-CD20 monoclonal antibodies, and electrostatic conjugation of Fe_2O_3@CD52 with the purine analogue, fludarabine for increased efficacy.

4. Both qualitative and quantitative assessment of interactions of CLL cells with Fe_2O_3@CD52 nanoparticles, specificity of these interactions in CLL cells compared to normal B cells, and preferential interaction of CLL cells with Fe_2O_3@CD52 compared to non-functionalised nanoparticles or nanoparticles functionalised with differing CD52 clones or control isotype antibodies.

5. Determination of clathrin-dependent uptake as the possible mechanism of uptake of Fe_2O_3@CD52 nanoparticles, mediated through nanoparticle/CD52 antigen interaction on the cell surface.

6. The reduction in adherence of patient-derived CLL cells following treatment with both non-functionalised and functionalised nanoparticles to endothelial monolayers under physiologically-relevant shear flow conditions, as assessed using a custom-built microfluidics system.

7. The ability of Fe_2O_3@CD52 nanoparticles to induce significant levels of apoptosis in both the I-83 cell line and patient-derived CLL cells, including CLL cells harbouring poor prognostic markers.

6.1.2 General Discussion

The core objective of this thesis was the successful development of a proof-of-concept nanotherapeutic, demonstrating targeting capabilities towards chronic lymphocytic leukaemia (CLL) cells. The field of nanotherapeutics is growing rapidly and has been for over two decades, furthered with the FDA approval for the use of ferumoxytol as an Fe_2O_3-based MRI contrast agent in 2009 (McCullough *et al.,* 2012). Since 2013, the number of clinical trials involving a nanoparticle constituent has increased three-fold, highlighting the extent of interest in this evolving field (Etheridge, *et al.,* 2013) (Bobo *et al.,* 2016). As presented in Chapter 1, several solutions have been presented and translated into clinical practice. However, there remain a large number of disease areas and disease states that could benefit from the inclusion of nanotechnology, and work presented within this thesis offers an opportunity to resolve some of these unmet clinical needs.

The first nanomedicine product to be approved for the treatment of cancer was Doxil, a formulation of doxorubicin encapsulated within a nanoscale liposome, receiving an indication for the treatment of Kaposi's sarcoma in patients with HIV (Safra, *et al.*, 2000). Over 20 years after approval, Doxil is still widely used for its original indication, as well as under its new indication of ovarian cancer, metastatic breast cancer and multiple myeloma (Barenholz, 2012). Commonly, nanoparticles are conjugated to an existing drug in order to increase the pharmacokinetics or pharmacodynamics of the drug, such as is the case in Doxil (Senapati, *et al.,* 2018), yielding a nanomedicinal product or nanodrug. Additionally, there is much on-going research into the

development of targeted nanotherapeutics, with the aim of targeting specific cells, or cell-surface receptors. This approach is generally conducted through the immobilisation of a targeting ligand to the surface of the nano-structure (Senapati *et al.,* 2018), and has been shown to potentially result in an increase in the accumulation of the nanotherapeutic on or within the cell type, as a result of a phenomenon known as enhanced permeability and retention (EPR). EPR is characterised primarily by the presence of what are known as fenestrations, or small pores, in the tumour vasculature enabling the passive accumulation of nanoparticles in tumours (Matsumura & Maeda, 1986). To date, there has been only one targeted nanomedicine to receive approval by the FDA; Ontak® (Denileukin diftitox). Advancements in nanomedicine such as those described within this thesis, in addition to the unmet needs in the advancements of treatment of blood cancers, have provided the rationale for the development of a novel, proof-of-concept, targeted nanotherapeutic for the treatment of CLL.

CLL is a malignancy of B cells characterised by the accumulation of small, mature in appearance CD5+ lymphocytes in the blood, bone marrow and lymphoid tissues. There are several factors that can contribute to the pathogenesis of CLL, these include aberrant signalling via surface immunoglobulin constituting a large proportion of the B cell receptor, in addition to the many different possible molecular and genetic alterations that can be seen in CLL. These genetic alterations include *del*13q, *del*17p (TP53 mutation), somatic hypermutation of

IGHV, NOTCH1 mutations, as well as expression of cell surface molecules CD38 and CD49d.

In addition to a variety of prognostic factors, the interactions of CLL cells with their tumour microenvironmental components such as endothelial cells, stromal cells, T cells and nurse-like cells in the lymph nodes can play pivotal roles in the progression of CLL. The CLL microenvironment has been shown to be a key modulator in the progression of the disease course, with CLL cells relying heavily on environmental cues and stimuli for proliferation and survival (Fiorcari, *et al.*, 2013). Additionally, BMSCs have been shown to provide a protective niche for CLL cells in circulation, providing both shelter from toxic agents and abundant attachment sites. These cells have also been shown to be of importance in the migratory behaviour of CLL cells in aggressive disease states. These adhesive properties of CLL cells have been the topic of much discussion in recent years (Fiorcari, *et al.*, 2013) (Hartmann, *et al.,* 2009). The homing of CLL cells to the lymph nodes and bone marrow and the complexity of this cross-talk, as well as the mechanisms of drug resistance and treatment failure still need to be better defined and are the subject of much investigation (ten Hacken & Burger, 2016). The use of static *in vitro* experimental approaches does not highlight the importance of the interaction of CLL cells with endothelial cells under shear flow conditions, and therefore the use of an *in vitro* microenvironmental simulator such as the microfluidics system described within this thesis, could be of great benefit (Farahani *et al.,* 2015).

Typically, treatment for CLL is initiated in patients with advanced disease or active, symptomatic disease, with treatment then often being decided based on the patient's clinical condition. Alemtuzumab is a monoclonal antibody targeting CD52 on the surface of CLL cells and is indicated as a second-line therapy for the treatment of CLL. Monotherapy with alemtuzumab has been shown to produce response rates of 33-53%, with a median duration of response ranging from 8.7 to 15.4 months in patients with advanced CLL who were previously treated with an alkylating agent. Additionally, it has shown to have proven effects in patients who have high-risk genetic markers such as *del(11q)* or *del(17p)*, and TP53 mutations; meaning that anti-CD52 monoclonal therapy may be a suitable treatment option for patients with poor prognostic features. However, due to the presence of CD52 on the surface of so many immune cells, high levels of cytotoxicity have been observed with anti-CD52 therapies; a side-effect which further accelerates the need for a more targeted approach in the treatment of CLL **(**Ginaldi, *et al.*,1998)**.**

The interaction of nanoparticles with the biological environment is largely dependent on the properties of the nanoparticle of choice. The particle size, shape and surface chemistry are key in determining the potential use of a nanoparticle as a nanotherapeutic. These characteristics can affect the degree of protein adsorption, the cellular uptake of the nanoparticle, their biodistribution and their clearance *in vivo* (Cisterna, *et al.*, 2016) (Nel, *et al.*, 2009). It is for these reasons that a pivotal first step in the assessment of a nanoparticle for use as a nanotherapeutic is a thorough characterisation of size and shape. Within

this work, we assessed the characteristics of commercially-available non-functionalised Fe_2O_3 nanoparticles using three robust characterisation techniques: nanoparticle tracking analysis (NTA), scanning electron microscopy (SEM) and dynamic light scattering (DLS). Fe_2O_3 was chosen for use in this study as it is a well-studied nanoparticle and has gained FDA approval as an MRI contrast agent, in addition to the inherent biocompatibility of Fe_2O_3 fostered by the natural iron metabolism processes *in vivo*. Fe_2O_3 nanoparticles used in this study had been previously characterised by Sigma Aldrich using BET analysis, a method used in the size determination of nanoparticles, and were deemed to be of 50nm in size. Our findings using NTA demonstrated that the bare Fe_2O_3 nanoparticles had a hydrodynamic radius of approximately 250nm. It would be expected that within even ultra-pure water, Fe_2O_3 nanoparticles would have a larger radius due to the accumulation of water molecules on the surface of the nanoparticle (Zhu, *et al.*, 2011)(Hole, *et al.*, 2013). SEM demonstrated that Fe_2O_3@APTES nanoparticles had a diameter of approximately 80nm in size, with the increase in diameter (from the size of 50nm determined by the manufacturer) being attributed to the coating on the surface of the nanoparticles. A size of ~80nm will provide an adequate surface area for the subsequent functionalisation of these Fe_2O_3@APTES nanoparticles with targeting agents, whilst still allowing for maximum interaction with cells in the environment. This approximate size of nanoparticle has been used in multiple other studies for successful functionalisation with biologically-relevant agents, proving a suitable scaffold for the development of a functionalised nanotherapeutic for the

treatment of CLL (Cheng, *et al.*, 2006) (Neuberger *et al.,* 2005). Additionally, my findings correspond with the BET analysis of the Sigma Aldrich certified Fe_2O_3 nanoparticles, and the increase in size corresponds with available literature (Hole*, et al.,* 2013).

Within this study, CD52 was chosen as an appropriate cell surface marker for targeting with functionalised Fe_2O_3 nanoparticles. This analysis was conducted through a flow cytometric screening panel assessing the expression of CD5, CD19, CD20 and CD52 by the I-83 CLL cell line, normal B cells and patient-derived CLL cells. From my analysis, we found that CD52 was highly expressed across both the I-83 cell line and the CLL patient samples, and at comparable levels to each other. This resulted in great benefit, as the I-83 cell line was therefore adopted as a suitable cell line CLL model during the development of a CD52 functionalised nanoparticle. Expression of CD20 across the I-83 cell line and patient-derived CLL cells were found to be low. It is expected that CD20 expression would be low in CLL patient samples, as this has been repeatedly reported in the literature, and speaks to the reduced efficacy of rituximab when compared to more novel anti-CD20 therapies such as ofatumumab and obinutuzumab (Bagacean *et al.,* 2016) (Tobinai *et al.,* 2017) (Coiffier, *et al.*, 2008). Given the findings of my panel of surface markers assessed, it was identified that the generation of an anti-CD52 functionalised nanoparticle was the most appropriate for this study. Notably, the findings observed in my work for each of the four surface markers investigated are consistent with other findings within the field (Bashford-Rogers, *et al.*, 2017) (Klabusay *et al.,* 2007) (Scheuermann & Racila,

1995) (Wang *et al.,* 2012). Thus, in line with the biomarker response, the successful functionalisation of these Fe_2O_3@CD52 was confirmed using flow cytometric analysis.

We demonstrated that using HIM it is possible to visualise the successful interaction of nanoparticles with the surface of B cells, a finding more difficult to interpret using more commonly used electron microscopy tools such as SEM owing to the need for sputter-coating of these samples. This finding has further promoted my use of nanoparticles in the targeting of B cells. Additionally, HIM determined that the morphology of normal B cells differed to that of the patient-derived CLL cells in that CLL cells appear to be smoother and more spherical, when compared to that of the normal B cell. In addition to this finding, normal B cells were observed to display microvilli on their cell surface. To date, we are unaware of any other reports of helium ion microscopy of B cells, or other lymphocytes, but this could indicate the potential for cell-cell communication or perhaps as a cellular anchoring mechanism. Such microvilli have been shown by SEM to be present on the surface of circulating lymphocytes. Here we show findings similar to that which can be found within the literature, though with perhaps more prominent evidence of these microvilli on the cell surface (Majstoravich, *et al.,* 2004), and work presented herein could indicate that the use of advanced tools such as HIM could allow for the visualisation of surface structures in greater detail. It has long been accepted that the cytoskeletal organisation of CLL cells is different to that of normal B cells, with lower detectable levels of F-actin and less cytoskeletal integrity than that of normal B cells, a finding which was substantiated

in our LCSM findings, where F-actin was minimally detected in comparison to what is seen in adherent cell types. In light of these morphological differences, cell interaction and uptake studies were carried out where we investigated differences between normal B cells and malignant B cells when exposed to functionalised nanoparticle (Fe$_2$O$_3$@CD52). The findings presented here demonstrate a considerable increase in the interaction and uptake of Fe$_2$O$_3$@CD52 by both the I-83 cell line and patient-derived CLL cells, when compared to normal B cells, and when compared to Fe$_2$O$_3$@APTES. We also demonstrate that neither clonality nor the presence of a fluorophore have any significant effect on the uptake of nanoparticles by malignant B cells. Once we had assessed the interaction of these nanoparticle types with CLL cells and determined the level of uptake of these nanoparticles by CLL cells, we then deemed it important to assess the possible mechanism of uptake of functionalised nanoparticles. We determined that whilst uptake of Fe$_2$O$_3$@CD52 appears to be predominantly mediated by clathrin-dependent endocytosis, at high treatment levels (100µg/mL) macropinocytosis, a non-specific mechanism of uptake, may also begin to become involved (Zhao, *et al.*, 2011). These findings again contribute to the successful development of a targeted nanotherapeutic, as knowledge of the uptake mechanisms employed in the cell type can potentially be exploited in future studies and work (Xu *et al.,* 2013). Our findings are in keeping with previous work in this area, indicating that clathrin-dependent endocytosis play a key role in the uptake of nanoparticles, and are consistent with the findings of other publications (Zhao, *et al.*, 2011).

An important additional aspect to this thesis that enabled further understanding of the CLL dynamic interaction with the HEV microenvironment, was the generation of a microfluidic system, for the assessment of the interactions of nanoparticles with CLL cells, under shear flow. The generation of such a system required extensive optimisation to determine the most appropriate dynamic physiological parameters such as cell co-culture and optimal seeding density, integrin activation and shear flow rate. Following on from the setting up of this experimental system, the results obtained enabled me to determine that treatment of CLL cells with bare and functionalised nanoparticles significantly impacts the rate of CLL cellular adherence to the endothelial cells under physiologically relevant shear flow conditions. This could have potential implications in the prevention of CLL cell homing, should such a targeted therapeutic progress to *in vivo* testing, given that CLL cells *in vivo* rely heavily on the microenvironmental signalling, and the niches within their microenvironment can provide important protective sites for the CLL cells in order to evade standard chemotherapeutics (Frankel *et al.,* 2017) (Frueh, *et al.*, 2013) (Hartmann, *et al.,* 2009). We hypothesise that, as has been demonstrated with other chemotherapeutics as discussed above, it is possible that these nanoparticles become entrenched within these protective niches of the microenvironment, preventing CLL cell adherence to the endothelial monolayer. Findings of this study demonstrated that, under a higher rate of shear flow (0.5 Dynes/cm^2), treatment of the I-83 cell line with bare nanoparticles resulted in significantly decreased toxicity when compared to that of static

experimentation. This is an interesting finding and indicates that the presence of nanoparticles under static conditions may illicit a toxic response due to the increased interaction of the nanoparticles with the cells as part of the sedimentation of the nanoparticles in 2D cultured cell monolayer, and that a reduction in this interaction time as seen in the dynamic experimental model may lead to a decreased toxicity. The supporting evidence of this hypothesis was acquired when an increase in cellular toxicity was observed in cells treated with nanoparticles under a lower shear flow rate of 0.08 Dynes/cm^2. We propose that this increase in interaction time as a result of the lower rate of shear flow could offer the potential for nanoparticles to induce higher cellular toxicity, however further investigations are needed.

The most pivotal aspect to this thesis was the assessment of toxicity of functionalised nanoparticles on CLL patient samples. We demonstrated that Fe_2O_3@CD52 induced significant apoptosis, when compared to no treatment and controls of the unbound anti-CD52 antibody or Fe_2O_3@APTES, in a clinically and molecularly annotated CLL sample cohort. We propose that the use of a nanoparticle carrier coupled to anti-CD52 monoclonal antibody therapy enhances the efficacy *in vitro*, possibly by allowing the cells to be targeted by the antibody on the surface and illicit this toxic response, ahead of the interaction and internalisation of the nanoparticles by the cells. We then propose that it is possible that the internalisation of the nanoparticles by the cells following successful targeting and binding by the cell surface antigen could result in the possible degradation of the APTES coating (which acts as a biocompatible layer in in nanoparticles which are non-

functionalised) and potentially illicit further toxicity, as presented in Chapter 3. This finding could have several beneficial implications in the generation of this proof-of-concept nanotherapeutic, including the requirement of reduced antibody in *in vivo* animal studies resulting in potentially fewer systemic toxic effects compared with free antibody (Christian & Lin, 2009) (Hiddemann, *et al.*, 1991).

Assessment of responsiveness of CLL patient samples to treatment with Fe_2O_3@CD52 demonstrated high levels of patient heterogeneity in response across both timepoints assessed. Again, given the responses to anti-CD52 monoclonal antibody alone (Ginaldi, *et al.*, 1998) (Hillmen, *et al.*, 2007), this was an expected result, as there will likely always be heterogeneity across any CLL patient cohort, and levels of responsiveness to any chemotherapeutic will likely demonstrate a diverse response given that not all patients samples will demonstrate the same clinical characteristics (Guièze & Wu, 2015) (Wu, 2012). Assessment of the responses to the nanoparticle based on prognostic markers showed Fe_2O_3@CD52 was equipotent in inducing apoptosis in CLL cells with favourable and poor prognostic markers, including unmutated IGHV, *del17p*, mutated NOTCH1, and expression of CD38 and CD49d. This could be of great benefit as it suggests that this proof-of-concept nanoparticle may have potential for the treatment of patients with poor predicted outcomes and chemoresistant disease, should such a nanotherapeutic become translated to the clinic. be suitable in the management of advanced disease stage, it could also act as a predictor of drug responsiveness and applicable to patients presenting with both

a poor and a favourable predicted disease outcome; should such a nanotherapeutic become translated to the clinic.

In summary, here we report a thorough, in-depth examination of a proof-of-concept nanotherapeutic and its interaction with normal and malignant B cells. Our findings here contribute to the on-going work into the development of a novel therapeutic for blood cancers and offer a valid proof-of-concept hypothesis as a potential platform for future work.

6.2 Future directions

The future of nanomedicines is an area undergoing rapid expansion and has been for the last two decades. Treatment with anti-CD52 monoclonal antibody has been shown to have great benefits in the treatment of CLL, however this has been removed for use as a first-line therapy given its implications in severe generalised toxicity and systemic infections, thus the adoption of a nanotechnological formulation, as a drug delivery system has potential. The work undertaken in my thesis demonstrates a significant stride towards the knowledge required towards the development of a nanotherapeutic for the management of CLL, including the interactions of CLL cells with nanoparticles in *in vitro* and the potential toxicity of a nanotherapeutic functionalised with an anti-CD52 monoclonal antibody.

As with any body of work, there remains area for future work. The orientation of antibody to the surface of the nanoparticle would be an interesting observation which would require extensive biochemistry and analytical characterisation, which was out of the scope for this thesis. The orientation of the antibody to the surface of the nanoparticle could have implications to its bioavailability, but the control of this orientation

would usually be conducted after a proof-of-concept investigation has shown potential. Should the binding region of the antibody be the area of the antibody that has been covalently linked to the surface of the nanoparticle, it would render this antibody inactive. Whilst the conjugation method employed within this study has been accepted by the field, and well reported within the literature, novel methods as to the conjugation of antibodies in a controlled manner have been investigated (Treerattrakoon *et al.* 2017). Similarly, as from the latest direction taken in comprehensive characterisation assessment by the Nanomedicine group in TTMI, the determination of the extent of electrostatic functionalisation of fludarabine to the surface of Fe_2O_3@CD52 (Fe_2O_3@CD52-fludarabine) would be an interesting observation for future studies, and would be required should that engineered nanoparticle be used for an extensive proof-of-concept study such as is presented here.

The investigation of some of the developed functionalised nanoparticle in other B cell malignancies; and T cell malignancies, given the presence of CD52 in these malignancies would be of great interest also. It would be of great interest to observe levels of apoptosis in other B and T cell malignancies, particularly in those that remain difficult to treat; such as is the case with cutaneous T cell lymphoma (CTCL) (Bagot, 2017) (Hildyard *et al.,* 2017).

References

Adams, G., & Iiner, L. (2005). Monoclonal antibody therapy of cancer. *Nat Biotech, 23*, 1147-1157.

Aghanejad, A., *et al.* (2018). Mucin-1 aptamer-armed superparamagnetic iron oxide nanoparticles for targeted delivery of doxorubicin to breast cancer cells. *Bioimpacts, 8*(2), 117-127.

Akin, D., *et al.* (2007). Bacteria-mediated delivery of nanoparticles and cargo into cells. *Nat Nanotech, 2*, 441-449.

Albitar, M., *et al.* (2004). Free circulating soluble CD52 as a tumor marker in chronic lymphocytic leukemia and its implication in therapy with anti-CD52 antibodies. *Cancer, 101*(5), 999-1008.

Alduaij, W., & Illidge, T. (2011). The future of anti-CD20 monoclonal antibodies: are I making progress? *Blood, 117*, 2993-3001.

Alexander, E., Sanders, S., & Braylan, R. (1976). Purported difference between human T- and B-cell surface morphology is an artefact. *Nature, 261*(5557), 239-241.

Ali, A., *et al.* (2016). Synthesis, characterization, applications, and challenges of iron oxide nanoparticles. *Nanotechnol Sci Appl., 9*, 49-67.

Alivisatos, A., *et al.* (1996). Organisation of "nanocrystal molecules" using DNA. *Nature, 382*(6592), 609-611.

Allen, T., & Cullis, P. (2004). Drug delivery systems: entering the mainstream. *Science, 303*(5665), 1818-1822.

Askari, S., *et al.* (2016). The anticancer effects of biodegradable nanomagnetic dual natural components on the leptin gene expression in lung cancer. *Artif Cells Nanomed Biotechnol, 44*(7), 1753-1763.

Ayache, J., *et al.* (2010). Artifacts in Transmission Electron Microscopy. In *Sample Preparation Handbook for Transmission Electron Microscopy* (pp. 125-170). Springer.

Badoux, X., *et al.*. (2011). Fludarabine, cyclophosphamide, and rituximab chemoimmunotherapy is highly effective treatment for relapsed patients with CLL. *Blood, 117*(11), 3016-3024.

Bae, Y., & Park, K. (2012). Targeted drug delivery to tumors: Myths, reality and possibility. *J Control Release, 153*(3), 198-205.

Bagacean, C., *et al.* (2016). Anti-CD20 monoclonal antibodies in chronic lymphocytic leukemia: from uncertainties to promises. *Immunotherapy, 8*(5), 569-81.

Bagot, M. (2017). New Targeted Treatments for Cutaneous T-cell Lymphomas. *Indian J Dermatol , 62*(2), 142-145.

Bagl, R., Hilliard, L., & Tan, W. (2006). Surface modification of silica nanoparticles to reduce aggregation and non-specific binding. *Langmuir, 22*(9), 4357-4362.

Bahadar, H., *et al*. (2016). Toxicity of Nanoparticles and an Overview of Current Experimental Models. *Iran Biomed J, 20*(1), 1-11.

Balasubramanian, *et al*. (2009). A Detection System Based on Giant Magnetoresistive Sensors and High-Moment Magnetic Nanoparticles Demonstrates Zeptomole Sensitivity: Potential for Personalized Medicine. *Angew Chem Int Ed Engl, 48*(15), 2764-2767.

Balthasar, S., *et al*. (2005). Preparation and characterisation of antibody modified gelatin nanoparticles as drug carrier system for uptake in lymphocytes. *Biomaterials, 26*(15), 2723-2732.

Banobre-Lopez, M., Teijeiro, A., & Rivas, J. (2013). Magnetic nanoparticle-based hyperthermia for cancer treatment. *18*(6), 397-400.

Barenholz, Y. (2012). Doxil®--the first FDA-approved nano-drug: lessons learned. *J Control Release, 160*(2), 117-134.

Bartczak, D., & Kanaras, A. (2011). Preparation of Peptide-Functionalized Gold Nanoparticles Using One Pot EDC/Sulfo-NHS Coupling. *Langmuir, 27*(16), 10119-10123.

Barua, S., & Mitragotri, S. (2014). Challenges associated with Penetration of Nanoparticles across Cell and Tissue Barriers: A Review of Current Status and Future Prospects. *Nano Today, 9*(2), 223-243.

Bashford-Rogers, R., *et al*. (2017). Dynamic variation of CD5 surface expression levels within individual chronic lymphocytic leukemia clones. *Exp Hematol, 46*, 31-37.

Bates, D., *et al*. (2014). Development and characterization of an antibody-labeled super-paramagnetic iron oxide contrast agent targeting prostate cancer cells for magnetic resonance imaging. *PLoS One, 9*(5), e97220.

Behzadi, S., *et al*. (2017). Cellular uptake of nanoparticles: journey inside the cell. *Chem Soc Rev, 46*(14), 4218-4244.

Bell, D. (2009). Contrast Mechanisms and Image Formation in Helium Ion Microscopy. *Microsc Microanal, 15*(2), 147-153.

Beum, P., *et al*. (2008). Complement activation on B lymphocytes opsonized with rituximab or ofatumumab produces substantial

changes in membrane structure preceding cell lysis. *J Immunol, 181*(1), 822-832.

Bini, R., *et al*. (2012). Synthesis and functionalization of magnetite nanoparticles with different amino-functional alkoxysilanes. *J Magn Magn Mater, 324*, 534-539.

Bishop, G., *et al*. (2003). Antigen-Specific B-Lymphocyte Activation. *Crit Rev Immunol, 23*(3), 149-197.

Bleesing, J., & Oliveira, J. (2013). Assessment of functional immune responses. In *Clinical Immunology (Fourth Edition)* (pp. 1172-1182). Elsevier.

Bobo, D., *et al*. (2016). Nanoparticle-Based Medicines: A Review of FDA-Approved Materials and Clinical Trials to Date. *Pharm Res, 33*(10), 2373-2387.

Bourdage, J., *et al*. (2007). An Affinity Capture Elution (ACE) assay for detection of anti-drug antibody to monoclonal antibody therapeutics in the presence of high levels of drug. *J Immunol Methods, 327*(1-2), 10-17.

Bozzuto, G., & Molinari, A. (2015). Liposomes as nanomedical devices. *Int J Nanomedicine, 10*, 975-999.

Braig, F., *et al*. (2017). Resistance to anti-CD19/CD3 BiTE in acute lymphoblastic leukemia may be mediated by disrupted CD19 membrane trafficking. *Blood, 129*, 100-104.

Brown, K., & Natan, M. (1998). Hydroxylamine Seeding of Colloidal Au Nanoparticles in Solution and on Surfaces. *Langmuir, 14*(4), 726-728.

Buger, J., & O'Brien, S. (2018). Evolution of CLL treatment - from chemoimmunotherapy to targeted and individualised therapy. *Nat Rev Clin Oncol , 15*(8), 510-527.

Bulbake, U., *et al*.. (2017). Liposomal Formulations in Clinical Use: An Updated Review. *Pharmaceutics, 9*(2), E12.

Burger, J., & Chiorazzi, N. (2013). B cell receptor signaling in chronic lymphocytic leukemia. *Trends Immunol, 34*(12), 592-601.

Busbee, B., Obare, S., & Murphy, C. (2003). An improved synthesis of high-aspect ratio gold nanorods. *Adv Mater, 15*, 414-416.

Butt, H., Wolff, E., Gould, S., Dixon Northern, B., Peterson, C., & Hansma, P. (1990). Imaging cells with the atomic force microscope. *J Struct Biol, 105*(1-3), 54-61.

Byrd, J., *et al*. (2014). Ibrutinib versus ofatumumab in previously treated chronic lymphoid leukemia. *N Engl J Med, 371*(3), 213-223.

Byrd, J., *et al.* (2015). Three-year follow-up of treatment-naïve and previously treated patients with CLL and SLL receiving single-agent ibrutinib. *Blood, 125*, 2497-2506.

Byrd, J., *et al.* (2001). Rituximab using a thrice Iekly dosing schedule in B-cell chronic lymphocytic leukemia and small lymphocytic lymphoma demonstrates clinical activity and acceptable toxicity. *J Clin Oncol, 19*(8), 2153-2164.

Byrd, J., *et al.* (2005). Addition of rituximab to fludarabine may prolong progression-free survival and overall survival in patients with previously untreated chronic lymphocytic leukemia: an updated retrospective comparative analysis of CALGB 9712 and CALGB 9011. *Blood, 105*(1), 49-53.

Caligaris-Cappio, F., & Hamblin, T. (1999). B-Cell Chronic Lymphocytic Leukemia: A Bird of a Different Feather. *J Clin Oncol, 17*, 399-408.

Caligaris-Cappio, F., *et al.* (1986). Cytoskeleton Organization Is Aberrantly Rearranged in the Cells of B Chronic Lymphocytic Leukaemia and Hairy Cell Leukaemia. *Blood, 67*(1), 233-239.

Carrasco, Y., & Batista, F. (2006). B-cell activation by membrane-bound antigens is facilitated by the interaction of VLA-4 with VCAM-1. *EMBO J, 25*(4), 889-899.

Cartron , G., *et al.* (2014). Obinutuzumab (GA101) in relapsed/refractory chronic lymphocytic leukemia: final data from the phase 1/2 GAUGUIN study. *Blood, 124*(14), 2196-2202.

Caruso, F., *et al.* (2012). Nanomedicine. *Chem Soc Rev, 41*(7), 2537-2538.

Chappell, C. *et al.* (2017). CD22 is required for formation of memory B cell precursors within germinal centers. *PLoS One, 12*(3), e0174661.

Chaves, N., *et al.* (2017). Exploring cellular uptake of iron oxide nanoparticles associated with rhodium citrate in breast cancer cells. *Int J Nanomedicine, 12*, 5511-5523.

Chen, H., *et al.* (2008). Preparation and characterization of PE38KDEL-loaded anti-HER2 nanoparticles for targeted cancer therapy. *J Control Release, 128*(3), 209-216.

Chen, Y., *et al.* (2004). Atomic force bio-analytics of polymerization and aggregation of phycoerythrin-conjugated immunoglobulin G molecules. *Mol Immunol, 41*(12), 1247-1252.

Chen C & Puvvada S. (2016). Prognostic Factors for Chronic Lymphocytic Leukemia. *Curr Hematol Malig Rep,* 11(1), 37-42.

Cheney, C., *et al.* (2014). Ocaratuzumab, an Fc-engineered antibody demonstrates enhanced antibody-dependent cell-mediated cytotoxicity in chronic lymphocytic leukaemia. *mAbs, 6*(3), 748-754.

Cheng, J., *et al.* (2006). Formulation of functionalized PLGA–PEG nanoparticles for in vivo targeted drug delivery. *Biomaterials, 28*(5), 869-876.

Chiorazzi , N., & Ferrarini, M. (2011). Cellular origin(s) of chronic lymphocytic leukemia: cautionary notes and additional considerations and possibilities. *Blood, 117*(6), 1781-1791.

Cho, K., *et al.* (2008). Therapeutic Nanoparticles for Drug Delivery in Cancer. *Clin Cancer Res., 14*(5), 1310-1316.

Christian, B., & Lin, T. (2009). Antibody Therapy for CLL. *Semin Hematol, 45*(2), 95-103.

Cisterna, B., *et al.* (2016). Targeted nanoparticles for colorectal cancer. *Nanomedicine, 11*(18), 2443-2456.

Coiffier, B., *et al.* (2008). Safety and efficacy of ofatumumab, a fully human monoclonal anti-CD20 antibody, in patients with relapsed or refractory B-cell chronic lymphocytic leukemia: a phase 1-2 study. *Blood, 111*(3), 1094-1100.

European Commission (2011, October 20). *Commission Recommendation of 18 October 2011 on the definition of nanomaterial Text with EEA relevance.* Retrieved November 2018, from European Commission - EUR-Lex: http://data.europa.eu/eli/reco/2011/696/oj

Electronic Medicines Compendium (2017). Lemtrada Summary of Product Characteristics.

Cooper, M. (2015). The early history of B cells. *Nat Rev Immunol, 15*, 191-197.

Cooper, M., Peterson, R., & Good, R. (1965). Delineation of the thymic and bursal lymphoid systems in the chicken. *Nature, 205*, 143-146.

Cummings, B., Wills, L., & Schnellmann, R. (2004). Measurement of Cell Death in Mammalian Cells. *Curr Protoc Pharmacol, 25*(1), 12.8.1-12.8.22.

Davids, M., & Burger, J. (2012). Cell Trafficking in Chronic Lymphocytic Leukemia. *Open J Hematol, 3*(S1), -3.

Dearden, DE., *et al.,* (2011). Alemtuzumab therapy in T-cell prolymphocytic leukemia: comparing efficacy in a series treated intravenously and a study piloting the subcutaneous route, *Blood* 118(22), 5799-5802.

de Iers, M., *et al.* (2011). Daratumumab, a Novel Therapeutic Human CD38 Monoclonal Antibody, Induces Killing of Multiple Myeloma and Other Hematological Tumors. *J Immunol, 186*(3), 1840-1848.

Dighiero, G., *et al.* (1998). Chlorambucil in indolent chronic lymphocytic leukemia. French Cooperative Group on Chronic Lymphocytic Leukemia. *N Eng J Med, 338*(21), 1506-1514.

dos Santos, T., *et al.* (2011). Effects of Transport Inhibitors on the Cellular Uptake of Carboxylated Polystyrene Nanoparticles in Different Cell Lines. *PLoS ONE, 6*(9), e24438. doi:10.1371/journal.pone.0024438

Duan, X., & Li, Y. (2013). Physicochemical Characteristics of Nanoparticles Affect Circulation, Biodistribution, Cellular Internalization, and Trafficking. *Small, 9*(9-10), 1521-1532. doi:10.1002/smll.201201390

Ebrahimi , E., *et al..* (2016). Novel drug delivery system based on doxorubicin-encapsulated magnetic nanoparticles modified with PLGA-PEG1000 copolymer. *Artif Cells Nanomed Biotechnol, 44*, 290-297.

Egerton, R. (2005). *Physical principles of electron microscopy: An introduction to TEM, SEM and AEM.* Springer US.

Ehrlich, P. (1901-1921). Nobel Lecture, 1909. *Nobel lectures, Physiology or Medicine.*

Eibel, H. (2015). Early B Cell Development. In A. Plebani, & V. Lougaris, *Agammaglobulinemia. Rare Diseases of the Immune System* (Vol. 4, pp. 1-99). Springer.

Eichhorst , B., *et al.* (2016). First-line chemoimmunotherapy with bendamustine and rituximab versus fludarabine, cyclophosphamide, and rituximab in patients with advanced chronic lymphocytic leukaemia (CLL10): an international, open-label, randomised, phase 3, non-inferiority trial. *Lancet Oncol, 17*(7), 928-942.

Eichhorst , B., *et al.* (2015). Chronic lymphocytic leukaemia: ESMO Clinical Practice Guidelines for diagnosis, treatment and follow-up. *Ann Oncol, Suppl 5*, 78-84.

El-Boubbou, K. (2018). Magnetic iron oxide nanoparticles as drug carriers: preparation, conjugation and delivery. *Nanomedicine.* doi:10.2217/nnm-2017-0320

Elechiquerra, J., Burt, J., Morones, J., Camacho-Bragado, A., Gao, X., Lara, H., & Yacaman, M. (2005). Interaction of silver nanoparticles with HIV-1. *J Nanobiotechnology, 3*, 6.

Elmore, S. (2007). Apoptosis: A Review of Programmed Cell Death. *Toxicol Pathol, 35*(4), 495-516.

Eltoum, I., Fredenburgh, J., & Grizzle, W. (2001). Advanced Concepts in Fixation: 1. Effects of Fixation on Immunohistochemistry, Reversibility of Fixation and Recovery of Proteins, Nucleic Acids, and other Molecules from Fixed and Processed Tissues. 2. Developmental Methods of Fixation. *J Histotechnol, 24*(3), 201-210.

Eltoum, I., Fredenburgh, J., Myers, R., & Grizzle, W. (2001). Introduction to the theory and practice of fixation of tissues. *J Histotechnol, 24*(1), 173-190.

Engelberg, S., *et al*. (2018). Cancer cell-selective, clathrin-mediated endocytosis of aptamer decorated nanoparticles. *Oncotarget, 9*(30), 20993-21006.

Engin, A., *et al*. (2017). Mechanistic understanding of nanoparticles' interactions with extracellular matrix: the cell and immune system. *Part Fibre Toxicol, 14*(22). doi:10.1186/s12989-017-0199-z

Etheridge, M., *et al*. (2013). The big picture on nanomedicine: the state of investigational and approved nanomedicine products. *Nanomed Nanotechnol Biology and Med, 9*(1), 1-14.

Fagraeus, A. (1948). The plasma cellular reaction and its relation to the formation of antibodies in vitro. *J Immunol, 58*, 1-13.

Fan, R., *et al*. (2016). Circulatory shear flow alters the viability and proliferation of circulating colon cancer cells. *Sci Rep, 6*, 27073.

Farahani, M., *et al*. (2015). CLL Exosomes Modulate the Transcriptome and Behaviour of Recipient Stromal Cells and Are Selectively Enriched in miR-202-3p. *PLoS ONE, 10*(10), e0141429.

Fassina, G., *et al*. (1998). Immunoglobulin specificity of TG19318: a novel synthetic ligand for antibody affinity purification. *J Molec Recognition, 11*(1-6), 128-133.

Faure, B., *et al*. (2013). Dispersion and surface functionalization of oxide nanoparticles for transparent photocatalytic and UV-protecting coatings and sunscreens. *Sci Technol Adv Mater, 14*(2), 023001.

Ferrari, M. (2008). Nanogeometry: beyond drug delivery. *Nat Nanotechnol, 3*, 131-132.

Feugier, P. (2015). A review of rituximab, the first anti-CD20 monolconal antibody used in the treatment of B non-Hodgkins lymphomas. *Future Oncol, 11*(9), 1327-1342.

Feynman, R. (1960). There's plenty of room at the bottom: An invitation to enter a new field of physics. *Engeineering and Science*, 22-36.

Filipe, V., *et al.* (2010). Critical evaluation of nanoparticle tracking analysis (NTA) by NanoSight for the measurement of nanoparticles and protein aggregates. *Pharm Res, 27*(5), 796-810.

Fiorcari, S., *et al.* (2013). The PI3-Kinase Delta Inhibitor Idelalisib (GS-1101) Targets Integrin-Mediated Adhesion of Chronic Lymphocytic Leukemia (CLL) Cell to Endothelial and Marrow Stromal Cells. *PLOS One, 8*(12), e83830.

Flias, A., & Tsourkas, A. (2009). Imaging circulating cells and lymphoid tissues with iron oxide nanoparticles. *Hematology,* 1, 720-726.

Foa, R., *et al.* (2013). Clinical implications of the molecular genetics of chronic lymphocytic leukemia. *Haematologica*, 98(5), 675-685.

Food and Drug Administration (FDA). (2017, December). *Drug Products, Including Biological Products, that Contain Nanomaterials - Guidance for Industry.* Retrieved November 2018, from FDA.gov: https://www.fda.gov/downloads/Drugs/GuidanceComplianceRegulatoryInformation/Guidances/UCM588857.pdf

Forconi, F. (2015). Three years of ibrutinib in CLL. *Blood, 125*, 2455-2456.

Foss, F. (2000). DAB389IL-2 (Denileukin Diftitox, ONTAK): A New Fusion Protein Technology. *Clin Lymphoma Myeloma Leuk, 1*(Suppl 1), S27-S31.

Franca, A., *et al.* (2014). Macrophage scavenger receptor A mediates the uptake of gold colloids by macrophages in vitro. *Nanomedicine, 6*(7), 1175-1188. doi:10.2217/nnm.11.41

Frankel, T., *et al.* (2017). The Role of Tumor Microenvironment in Cancer Immunotherapy. *Adv Exp Med Biol, 1036*, 51-64.

Frenkel, J., & Doefman, J. (1930). Spontaneous and Induced Magnetisation in Ferromagnetic Bodies. *Nature, 126*(3173), 274-275.

Frens, G. (1973). An experiment concerning the dispersion forces between very small metal spheres. *Physical Letters A, 44*(3), 208-210.

Friedman, A., *et al.* (2015). Precision medicine for cancer with next-generation functional diagnostics. *Nat Rev Cancer, 15*(12), 747-756.

Frueh, J., *et al.* (2013). Systems biology of the functional and dysfunctional endothelium. *Cardiovasc Res, 99*(2), 334-341.

Gaharwar, U., *et al.* (2017). Iron oxide nanoparticles induced cytotoxicity, oxidative stress and DNA damage in lymphocytes. *J Appl Toxicol, 37*(10), 1232-1244.

Georgiadis, P., *et al.* (2017). Evolving DNA methylation and gene expression markers of B-cell chronic lymphocytic leukemia are present in pre-diagnostic blood samples more than 10 years prior to diagnosis. *BMC Genomics, 18*, 728.

Ghia, P., & Hallek, M. (2014). Management of chronic lymphocytic leukaemia. *Haematologica, 99*(6), 965-972.

Ginaldi, L., *et al.* (1998). Levels of expression of CD19 and CD20 in chronic B cell leukaemias. *J Clin Pathol, 51*, 364-369.

Ginaldi, L., *et al.* (1998). Levels of expression of CD52 in normal and leukemic B and T cells: correlation with in vivo therapeutic responses to Campath-1H. *Leuk Res, 22*(2), 185-191.

Gioria, S., *et al.* (2018). Are existing standard methods suitable for the evaluation of nanomedicines: some case studies. *Nanomedicine, 13*(5), 539-554.

Gobbo, O., *et al.* (2015). Magnetic Nanoparticles in Cancer Theranostics. *Theranostics, 5*(11), 1249-1263.

Goede, V., *et al.* (2014). Obinutuzumab plus chlorambucil in patients with CLL and coexisting conditions. *N Engl J Med, 370*(12), 1101-1110.

Gordon, R., *et al.* (1979). Intracellular hyperthermia. A biophysical approach to cancer treatment via intracellular temperature and biophysical alterations. *Med Hypotheses, 5*(1), 83-102.

Gribben, JG. (2010). How I treat CLL up front. *Blood*, 115(2), 187-197.

Guièze, R., & Wu, C. (2015). Genomic and epigenomic heterogeneity in chronic lymphocytic leukemia. *Blood, 126*, 445-453.

Gupta, A., & Gupta, M. (2005). Synthesis and surface engineering of iron oxide nanoparticles for biomedical applications. *Biomaterials, 26*(18), 3995-4021.

Hagedorn, M., *et al.* (2006). Optimized fixation and immunofluorescence staining methods for Dictyostelium cells. *Methods Mol Biol, 346*, 327-338.

Hale, G. (1983). The CD52 antigen and development of the CAMPATH antibodies. *Cytotherapy*, 3(3), 137-143.

Hale, G. (1995). Synthetic peptide mimotope of the CAMPATH-1 (CD52) antigen, a small glycosylphosphatidylinositol-anchored glycoprotein. *Immunotechnology, 1*(3-4), 175-187.

Hale, G., & Waldmann, H. (2000). From Laboratory to Clinic: The Story of CAMPATH-1. *Methods Mol Med, 40*, 243-266.

Hallden, G., *et al.* (1989). A new membrane permeabilization method for the detection of intracellular antigens by flow cytometry. *J Immunol Methods, 124*(1), 103-109.

Hallek, M. (2017). Chronic lymphocytic leukemia: 2017 update on diagnosis, risk stratification, and treatment. *Am J Haematol, 92*(9), 946-965.

Hallek, M., *et al.* (2008). Guidelines for the diagnosis and treatment of chronic lymphocytic leukemia: a report from the International Workshop on Chronic Lymphocytic Leukemia updating the National Cancer Institute-Working Group 1996 guideline. *Blood, 111*(12), 5446-5456.

Hamblin , T., *et al.* (1999). Unmutated Ig V(H) genes are associated with a more aggressive form of chronic lymphocytic leukemia. *Blood, 94*, 1848-1854.

Harker, K., *et al.* (2014). Shear Forces Enhance Toxoplasma gondii Tachyzoite Motility on Vascular Endothelium. *mBio, 5*(2), e01111-01114.

Harris, D., *et al.* (2000). Reciprocal regulation of polarized cytokine production by effector B and T cells. *Nat Immunol, 1*, 475-482.

Hartmann, T., *et al.* (2009). Circulating B-cell chronic lymphocytic leukemia cells display impaired migration to lymph nodes and bone marrow. *Cancer Res, 69*(7), 3121-3130.

Harush-Frenkel, O., *et al.* (2007). Targeting of nanoparticles to the clathrin-mediated endocytic pathway. *Biochem Biophys Res Commun, 353*(1), 26-32.

Hazrin-Chong, N., & Manefield, M. (2012). An alternative SEM drying method using hexamethyldisilazane (HMDS) for microbial cell attachment studies on sub-bituminous coal. *J Microbiol Methods, 90*(2), 96-99.

Herberman, R., *et al.* (1979). Augmentation by interferon of human natural and antibody-dependent cell-mediated cytotoxicity. *Nature, 277*, 221-223.

Herishanu, Y., *et al.* (2014). Biology of Chronic Lymphocytic Leukemia in Different Microenvironments: Clinical and Therapeutic Implications. *Hematol Oncol Clin North Am, 27*(2), 173-206.

Hiddemann, W., *et al.* (1991). Treatment of advanced chronic lymphocytic leukemia by fludarabine. *Annal Haematol Oncol, 63*(1), 1-4.

Hildyard, C., *et al.* (2017). Toward a Biology-Driven Treatment Strategy for Peripheral T-cell Lymphoma. *Clin Med Insights Blood Disord, 10*. doi:10.1177/1179545x17705863

Hillmen, P., *et al.* (2007). Alemtuzumab Compared With Chlorambucil As First-Line Therapy for Chronic Lymphocytic Leukemia. *J Clin Oncol, 25*, 5616-5623.

Hoffman, W., *et al.* (2016). B Cells, Antibodies, and More. *Clin J Am Soc Nephrol, 11*(1), 137-154.

Hole, P., *et al.* (2013). Interlaboratory comparison of size measurements on nanoparticles using nanoparticle tracking analysis (NTA). *J Nanopart Res, 15*, 2101.

Hoshyar, N., *et al.* (2016). The effect of nanoparticle size on in vivo pharmacokinetics and cellular interaction. *Nanomedicine, 11*(6), 673-692.

Huang, K., *et al.* (2012). Size-Dependent Localization and Penetration of Ultrasmall Gold Nanoparticles in Cancer Cells, Multicellular Spheroids, and Tumors in Vivo. *ACS Nano, 6*(5), 4483-4493.

Huh, Y., *et al.* (2001). Higher Levels of Surface CD20 Expression on Circulating Lymphocytes Compared With Bone Marrow and Lymph Lymphocytes Compared With Bone Marrow and Lymph Nodes in B-Cell Chronic Lymphocytic Leukaemia. *Am J Clin Pathol, 116*(3), 437-443.

Hussain, S., *et al.* (2005). In vitro toxicity of nanoparticles in BRL 3A rat liver cells. *Toxicol In Vitro, 19*(7), 975-983.

Hutchinson, C., *et al.* (2014). Lymphocytes from chronic lymphocytic leukaemia undergo ABL1-linked amoeboid motility and homotypic interaction as an early adaptive change to ex vivo culture. *Exp Hematol Oncol, 3*(7), 1-14.

Islam, W., *et al.* (2018). Augmentation of the Enhanced Permeability and Retention Effect with Nitric Oxide-Generating Agents Improves the Therapeutic Effects of Nanomedicines. *Mol Cancer Ther*. doi:10.1158/1535-7163.MCT-18-0696

Jain, P., *et al.* (2007). Au nanoparticles target cancer. *Nano Today, 2*(2), 16.

Jain, P., *et al.* (2008). Noble metals on the nanoscale: optical and photothermal properties and some applications in imaging, sensing, biology and medicine. *Acc Chem Res., 41*(12), 1578-1586.

Janas, E., *et al.* (2005). Rituxan (anti-CD20 antibody)-induced translocation of CD20 into lipid rafts is crucial for calcium influx and apoptosis. *Clin Exp Immunol, 139*(3), 439-446.

Jantus Lewintre, E., *et al.* (2004). Treatment of B-CLL Cells with Bortezomib and Rituximab Reduces Cell Viability In Vitro. *Blood, 104*, 2798.

Jeng, H., & Swanson, J. (2006). Toxicity of metal oxide nanoparticles in mammalian cells. *J Environ Sci Health A Tox Hazard Subst Environ Eng, 41*(12), 2699-2711.

Jeong, S., *et al.* (2017). Highly robust and optimized conjugation of antibodies to nanoparticles using quantitatively validated protocols . *Nanoscale, 9*, 2548-2555.

Jiang, W., *et al.* (2008). Nanoparticle-mediated cellular responses is size-dependent. *Nat Nanotechnol, 3*(3), 145-150.

Joens, M., *et al.* (2013, December 17). Helium Ion Microscopy (HIM) for the imaging of biological samples at sub-nanometer resolution. *Scientific Reports, 3*(3514), 1-7. doi:10.1038/srep03514

Jonkman, J., & Brown, C. (2015). Any Way You Slice It—A Comparison of Confocal Microscopy Techniques. *J Biomol Tech, 26*(2), 54-65.

Jurkowitz-Alexander, M., *et al.* (1992). Cell sIlling, blebbing, and death are dependent on ATP depletion and independent of calcium during chemical hypoxia in a glial cell line (ROC-1). *J Nuerochem, 59*(1), 344-352.

Kang, B., *et al.* (2010). Nuclear targeting of gold nanoparticles in cancer cells induces DNA damage, causing cytokine arrest and apoptosis. *J Am Chem Soc, 132*(5), 1517-1519.

Kang, J., *et al.* (2015). High Resolution Live Cell Raman Imaging Using Subcellular Organelle-Targeting SERS-Sensitive Gold Nanoparticles with Highly Narrow Intra-Nanogap. *Nano Lett, 15*(3), 1766-1772.

Karlsson, H., *et al.* (2008). Copper Oxide Nanoparticles Are Highly Toxic: A Comparison between Metal Oxide Nanoparticles and Carbon Nanotubes. *Chem Res Toxicol, 21*(9), 1726-1732.

Kaufmann, S. (2017). Remembering Emil von Behring: from Tetanus Treatment to Antibody Cooperation with Phagocytes. *mBio, 8*(1), e00117.

Kay, N., *et al.* (2006). Chronic lymphocytic leukemia: current and emerging treatment approaches. *Clin Adv Hematol Oncol, 4*(11), 11-12.

Keller, A., *et al.* (2010). Stability and Aggregation of Metal Oxide Nanoparticles in Natural Aqueous Matrices. *Environ Sci Technol, 44*(6), 1962-1967.

Kim, J., *et al.* (2006). Toxicity and tissue distribution of magnetic nanoparticles in mice. *Toxicol Sci, 89*(1), 338-347.

Kim, K., *et al.* (2017). Surface treatment of silica nanoparticles for stable and charge-controlled colloidal silica. *Int J Nanomedicine, 9*(Suppl 2), 29-40.

Kim, S., *et al.* (2016). Structural Development of Nanoparticle Dispersion during Drying in Polymer Nanocomposite Films. *Mcaromolecules, 49*(23), 9068-9079.

Kim, Y., *et al.* (2000). B-cell chronic lymphocytic leukemia/small lymphocytic lymphoma involving bone marrow with an interfollicular pattern. *Am J Clin Pathol, 114*(1), 41-46.

Kinashi, T. (2005). Intracellular signalling controlling integrin activation in lymphocytes. *Nat Rev Immunol*, 5, 546-559.

Kipps, T., *et al.* (2017). Chronic lymphocytic leukaemia. *Nat Rev Dis Primers, 3*(16096). doi:10.1038/nrdp.2016.96

Kishore, U., & Reid, K. (2000). C1q: structure, function, and receptors. *Immunopharmacology, 49*(1-2), 159-170.

Klabusay, M., *et al.* (2007). Different Levels of CD52 Antigen Expression Evaluated by Quantitative Fluorescence Cytometry are Detected on B-Lymphocytes, CD 34+ Cells and Tumor Cells of Patients with Chronic B-cell Lymphoproliferative Diseases. *Cytometry B Clin Cytom, 72B*(5), 363-370.

Klein, C., *et al.* (2013). Epitope interactions of monoclonal antibodies targeting CD20 and their relationship to functional properties. *MAbs, 5*(1), 22-23.

Klein, C., et al. (2013). Epitope interactions of monoclonal antibodies targeting CD20 and their relationship to functional properties. *MAbs, 5*(1), 22-33.

Klein, U., *et al.* (2010). The DLEU2/miR-15a/16-1 cluster controls B cell proliferation and its deletion leads to chronic lymphocytic leukemia. *Cancer Cell, 17*(1), 28-40.

Kolhatkar, A., *et al.* (2013). Tuning the Magnetic Properties of Nanoparticles. *Int J Mol Sci, 14*(8), 15977-16009.

Kong, T., *et al.* (2008). Enhancement of Radiation Cytotoxicity in Breast-Cancer Cells by Localized Attachment of Gold Nanoparticles. *Small, 4*(9), 1537-1543.

Kontani, K., *et al.* (1993). NAD glycohydrolase specifically induced by retinoic acid in human leukemic HL-60 cells. Identification of the NAD glycohydrolase as leukocyte cell surface antigen CD38. *J Biol Chem,* 268(23), 16895-16898.

Kono, M., *et al.* (2013). Non-activated T and B lymphocytes become morphologically distinguishable after detergent treatment. *Cytometry A, 83*(4), 396-402.

Koshovets, O., & Ganichev, N. (2016). Nanotechnology contribution to innovation-driven growth: Hype or Hope? *Economy & Business, 10*, 546-561.

Kossatz, S., *et al.* (2015). Efficient treatment of breast cancer xenografts with multifunctionalized iron oxide nanoparticles combining magnetic hyperthermia and anti-cancer drug delivery. *Breast Cancer Res, 17*, 66.

Kou, L., *et al.* (2013). The endocytosis and intracellular fate of nanomedicines: Implication for rational design. *AJPS, 8*(1), 1-10.

Kujipers, TW., *et al.* (2010) CD20 deficiency in humans results in impaired T cell–independent antibody responses. *JCI,* 120(1), 214-222.

Kumar Gupta, A., & Gupta, M. (2005). Synthesis and surface engineering of iron oxide nanoparticles for biomedical applications. *Biomaterials, 26*(18), 3995-4021.

Kumar, S., *et al.* (2008). Directional conjugation of antibodies to nanoparticles for synthesis of multiplexed optical contrast agents with both delivery and targeting moieties. *Nature Protocols, 3*, 314-320.

Laffon, B., *et al.* (2018). Cellular and Molecular Toxicity of Iron Oxide Nanoparticles. *Adv Exp Med Biol, 1048*, 199-213.

Lammers, T., *et al.* (2012). Drug targeting to tumors: principles, pitfalls and (pre-) clinical progress. *J Control Release, 161*(2), 175-187.

Lapalombella, R., *et al.* (2008). A novel Raji-Burkitt's lymphoma model for preclinical and mechanistic evaluation of CD52-targeted immunotherapeutic agents. *Clin Cancer Res, 14*(2), 569-578.

Laurent, S., *et al.* (2008). Magnetic Iron Oxide Nanoparticles: Synthesis, Stabilization, Vectorization, Physicochemical Characterizations, and Biological Applications. *Chem Rev, 108*(6), 2064-2110.

Lawrence, M., & Springer, T. (1991). Leukocytes Roll on a Selectin at Physiologic Flow Rates: Distinction from and Prerequisite for Adhesion through Integrins. *Cell, 65*(5), 859-873.

LeBien, T., & Tedder, T. (2008). B lymphocytes: how they develop and function. *Blood, 112*(5), 1570-1580.

Li, H., *et al.* (2016). Stimuli-responsive clustered nanoparticles for improved tumor penetration and therapeutic efficacy. *Proc Natl Acad Sci USA, 113*(15), 4164-4169.

Li, K., & Liu, B. (2012). Polymer encapsulated conjugated polymer nanoparticles for fluorescence bioimaging. *J Mater Chem, 22*, 1257-1264.

Li, K., *et al.* (2017). Next-generation superparamagnetic iron oxide nanoparticles for cancer theranostics. *Drug Discov Today, 22*(9), 1421-1429.

Lim, J., & Gleeson, P. (2011). Macropinocytosis: an endocytic pathway for internalising large gulps. *Immunol Cell Biol, 89*, 836-843.

Lima-Tenorio, M., *et al.* (2015). Magnetic nanoparticles: in vivo cancer diagnosis and therapy. *Int J Pharm*(493), 313-327.

Lin, P., *et al.* (2014). Techniques for physicochemical characterization of nanomaterials. *Biotechnol Adv., 32*(4), 711-726.

Lu, A., *et al.* (2007). Magnetic Nanoparticles: Synthesis, Protection, Functionalization, and Application. *Angew Chem Int Ed, 46*(8), 1222-1244.

Ludwig, DL., *et al.* (2003). Monoclonal antibody therapeutics and apoptosis. *Oncogene*, 22(56)9097-9106.

Lundin, J., *et al.* (2002). Phase II trial of subcutaneous anti-CD52 monoclonal antibody alemtuzumab (Campath-1H) as first-line treatment for patients with B-cell chronic lymphocytic leukemia (B-CLL). *Blood, 100*(3), 768-773.

Luo, W., *et al.* (2018). B Cell Receptor and CD40 Signaling Are Rewired for Synergistic Induction of the c-Myc Transcription Factor in Germinal Centre B cells. *Immunity, 48*, 313-326.

Mahdavi, M., *et al.* (2013). Synthesis, Surface Modification and Characterisation of Biocompatible Magnetic Iron Oxide Nanoparticles for Biomedical Applications. *Molecules, 18*(7), 7533-7548.

Majstoravich, S., *et al.* (2004). Lymphocyte microvilli are dynamic, actin-dependent structures that do not require Wiskott-Aldrich syndrome protein (WASp) for their morphology. *Blood, 104*, 1396-1403.

Maude, S. *et al.* (2015) CD19-targeted chimeric antigen receptor T cell therapy for acute lymphoblastic leukaemia. *Blood, 125*, 4017-4023.

Malavasi, F., et al. (2011). CD38 and chronic lymphocytic leukemia: a decade later. *Blood, 118*(3), 3470-3478.

Malavasi, F, et al. (2008). Review Evolution and function of the ADP ribosyl cyclase/CD38 gene family in physiology and pathology. *Physiol Rev, 88*(3), 841-886.

Maouyo, D., *et al.* (2000). pH heterogeneity at intracellular and extracellular plasma membrane sites in HT29-C1 cell monolayers. *Am J Physiol Cell Physiol, 278*(5), 973-981.

Marcus, M., *et al.* (2016). Iron oxide nanoparticles for neuronal cell applications: uptake study and magnetic manipulations. *J Nanobiotech, 14*(37), 1-12.

Marghussain, V. (2015). Magnetic Properties of Nano-Glass Ceramics. In M. V, *Nano-Glass Ceramics: Processing, Properties and Applications* (pp. 181-223).

Global Markets (2018, May). *Global Nanotechnology Market Outlook 2018 - 2024.* Retrieved November 2018, from Research and Markets Report: https://www.researchandmarkets.com/reports/4536705/global-nanotechnology-market-outlook-2018-2024

Marshall, M., *et al.* (2017). Therapeutic Antibodies: What Have I Learnt from Targeting CD20 and Where Are I Going? *Front Immunol, 8*, 1245.

Martin, P.J., *et al.* (1980). A new human T-cell differentiation antigen: Unexpected expression on chronic lymphocytic leukaemia cells. *Immunogenetics*, 11, 429-439.

Martinet, L., *et al.* human solid tumors contain high endothelail venules: association with T and B lymphocyte infiltration and favourable prognosis in breast cancer. *Cancer Res*, 71, 5678-5687.

Masuda, K., & Kishumoto, T. (2016). CD5: A New Partner for IL-6. *Immunity, 44*, 720-722.

Matsumura, Y., & Maeda, H. (1986). A new concept for macromolecular therapeutics in cancer chemotherapy: mechanism of tumoritropic accumulation of proteins and the antitumor agent smancs. *Cancer Res, 46*(12), 6387-6392.

Mauricio, M., *et al.* (2018). Nanoparticles in Medicine: A Focus on Vascular Oxidative Stress. *Oxid Med Cell Longev*, 6231482.

McCullough, B., *et al.* (2012). Ferumoxytol in clinical practice: Implications for MRI. *J Magn Reson Imaging, 37*(6), 1476-1479.

McLeod, S., *et al.* (1998). Activation of the Rap1 GTPase by the B cell antigen receptor. *J Biol Chem, 273*(44), 29218-29223.

McMahon, H., & Boucrot, E. (2011). Molecular mechanism and physiological functions of clathrin-mediated endocytosis. *Mol Cell Biol, 12*, 517-533.

McWilliams, A. (2016). *The Maturing Nanotechnolgy Market: Products and Applications.* BBC Research.

Melan, M., & Sluder, G. (1992). Redistribution and differential extraction of soluble proteins in permeabilized cultured cells. Implications for immunofluorescence microscopy. *J Cell Sci, 101*(4), 731-743.

Michen, B., *et al.* (2015). Avoiding drying-artifacts in transmission electron microscopy: Characterizing the size and colloidal state of nanoparticles. *Sci Rep, 5*, 9753.

Mody, V., *et al.* (2010). Introduction to metallic nanoparticles. *J Pharm Bioallied Sci, 2*(4), 282-289.

Mone, A., *et al.* (2006). Alemtuzumab induces caspase-independent cell death in human chronic lymphocytic leukemia cells through a lipid raft-dependent mechanism. *Leukaemia, 20*, 272-279.

Moore, T., *et al.* (2015). Nanoparticle colloidal stability in cell culture media and impact on cellular interactions. *Chem Soc Rev, 44*, 6287-6305.

Mossner, E., *et al.* (2010). Increasing the efficacy of CD20 antibody therapy through the engineering of a new type II anti-CD20 antibody with enhanced direct and immune effector cell-mediated B-cell cytotoxicity. *Blood, 115*(22), 4393-4402.

Mu, K., *et al.* (2015). Monoclonal Antibody–Conjugated Superparamagnetic Iron Oxide Nanoparticles for Imaging of Epidermal Growth Factor Receptor–Targeted Cells and Gliomas. *Molecular Imaging, 14*, 1-12.

Mu, Q., *et al.* (2015). Anti-HER2/neu peptide-conjugated iron oxide nanoparticles for targeted delivery of paclitaxel to breast cancer cells . *Nanoscale, 7*(43), 18010-18014.

Mukherjee, P., *et al.* (2007). Potential therapeutic application of gold nanoparticles in B-chronic lymphocytic leukaemia (BCLL): enhancing apoptosis. *J Nanobiotechnology, 5*, 4.

Murdock, R. *et al.* (2008). Characterization of Nanomaterial Dispersion in Solution Prior to In Vitro Exposure Using Dynamic Light Scattering. *Toxicological Sciences, 101*(2), 239-253. doi:10.1093/toxsci/kfm240

Muzquiz-Ramos, E., *et al.* (2015). Synthesis and characterization of maghemite nanoparticles for hyperthermia applications. *Ceram Int, 41*(1), 397-402.

Naddafi, F., & Davami, F. (2015). Anti-CD19 Monoclonal Antibodies: a New Approach to Lymphoma Therapy. *Int J Mol Cell Med, 4*(3), 143-151.

Nadler, LM., *et al.* (1983). B4, a human B lymphocyte-associated antigen expressed on normal, mitogen-activated, and malignant B lymphocytes. *J Immunol,* 131(1), 244-250.

Naserzadeh, P., *et al.* (2018). Single-walled carbon nanotube, multi-walled carbon nanotube and Fe2O3 nanoparticles induced mitochondria mediated apoptosis in melanoma cells. *Cutan Ocul Toxicol, 37*(2), 157-166.

Nel, A., *et al.* (2009). Understanding biophysicochemical interactions at the nano–bio interface. *Nat Mater, 8*, 543-557.

Neuberger, T., *et al.* (2005). Superparamagnetic nanoparticles for biomedical applications: Possibilities and limitations of a new drug delivery system. *J Magn Magn Mater., 293*(1), 483-496.

Nguyen, V., & Lee, B. (2017). Protein corona: a new approach for nanomedicine design. *Int J Nanomedicine, 12*, 3137-3151.

Ni, C., *et al.* (2003). Shear flow attenuates serum-induced STAT3 activation in endothelial cells. *J Biol Chem, 278*(22), 19702-19708.

Nicholson, L. (2016). The immune system. *Essays Biochem, 60*(3), 275-301.

Nie, S. (2010). Understanding and overcoming major barriers in cancer nanomedicine. *Nanomedicine , 5*(4), 523-528.

Niederfellner, G., *et al.* (2011). Epitope characterization and crystal structure of GA101 provide insights into the molecular basis for type I/II distinction of CD20 antibodies. *Blood, 118*(2), 358-367.

Nobilli, M., *et al.* (2008). Platelet Activation Due to Hemodynamic Shear Stresses: Damage Accumulation Model and Comparison to In Vitro Measurements. *ASAIO J, 54*(1), 64-72.

Nowack, B., *et al.* (2011). 120 years of Nanosilver History: Implications for Policy Makers. *Environmental Science and Technology, 45*, 1177-1183.

Nuckel, H., *et al.* (2005, May 9). Alemtuzumab induces enhanced apoptosis in vitro in B-cells from patients with chronic lymphocytic leukemia by antibody-dependent cellular cytotoxicity. *514*(2-3), 217-224. doi:10.1016/j.ejphar.2005.03.024

Nune, S., *et al.* (2009). Nanoparticles for biomedical imaging. *Expert Opin Drug Deliv, 6*(11), 1175-1194.

Oh, N., & Park, J. (2014). Endocytosis and exocytosis of nanoparticles in mammalian cells. *Int J Nanomedicine, 9*((Suppl 1)), 51-63.

Onoue, S., *et al.* (2014). Nanodrugs: pharmacokinetics and safety. *Int J Nanomedicine, 9*, 1025-1037.

Oscier, D., *et al.* (2016). The morphology of CLL revisited: the clinical significance of prolymphocytes and correlations with prognostic/molecular markers in the LRF CLL4 trial. *Br J Haematol, 174*(5), 767-775.

Paddock, S. (2000). Principles and practices of laser scanning confocal microscopy. In *Molecular Biotechnology* (Vol. 16, pp. 127-149). Springer.

Paddock, S., & Eliceiri, K. (2013). Laser Scanning Confocal Microscopy: History, Applications, and Related Optical Sectioning Techniques. In P. S. (eds), *Methods in Molecular Biology* (Vol. 1075, pp. 9-47). Humana Press.

Parambath, A. (Ed.). (2018). *Engineering of Biomaterials for Drug Delivery Systems: Beyond Polyethylene Glycol.* Elsevier.

Park, K. (2017). Prevention of nanoparticle aggregation during freeze-drying. *J. Control. Release, 248*, 153.

Park, K., *et al.* (2009). A study on effects of size and structure on hygroscopicity of nanoparticles using a tandem differential mobility analyzer and TEM. *J Nanoparticle Res, 11*(1), 175-183.

Park, Y., *et al.* (2015). Upconverting nanoparticles: a versatile platform for wide-field two-photon microscopy and multi-modal in vivo imaging. *Chem Soc Rev, 44*(6), 1302-1317.

Patil, R., *et al.* (2018). Comprehensive cytotoxicity studies of superparamagnetic iron oxide nanoparticles. *Biochem Biophys Rep, 13*, 63-72.

Patten, P., *et al.* (2012). IGHV-unmutated and IGHV-mutated chronic lymphocytic leukemia cells produce activation-induced deaminase protein with a full range of biologic functions. *Blood, 120*(24), 4802-4811.

Pawluczowycz, A., *et al.* (2009). Binding of submaximal C1q promotes complement-dependent cytotoxicity (CDC) of B cells opsonized with anti-CD20 mAbs ofatumumab (OFA) or rituximab (RTX): considerably higher levels of CDC are induced by OFA than by RTX. *J Immunol, 183*(1), 749-758.

Pecora, R. (1985). *Dynamic Light Scattering: Applications of Photon Correlations Spectroscopy.* Plenum Press.

Pepper, C., et al. (2007). Highly purified CD38+ and CD38- sub-clones derived from the same chronic lymphocytic leukemia patient

have distinct gene expression signatures despite their monoclonal origin. *Leukemia, 21*(4), 687-696.

Pettijohn, E., & Ma, S. (2017). Targeted Therapy in Chronic Lymphocytic Leukemia (CLL). *Curr Hematol Malig Rep, 12*(1), 20-28.

PoIrs, K., *et al.* (2007). Characterization of the size, shape, and state of dispersion of nanoparticles for toxicological studies. *Nanotoxicology, 1*(1), 42-51.

Prevodnik, V., *et al.* (2011). The predictive significance of CD20 expression in B-cell lymphomas. *Diagn Pathol, 6*(33).

Prina-Mello, A., *et al.* (2013). Multiparametric toxicity evaluation of SPIONs by high content screening technique: identification of biocompatible multifunctional nanoparticles for nanomedicine. *IEEE Transactions on Magnetics, 49*(1), 377-382.

Rajiv, S., *et al.* (2016). Comparative cytotoxicity and genotoxicity of cobalt (II, III) oxide, iron (III) oxide, silicon dioxide, and aluminum oxide nanoparticles on human lymphocytes in vitro. *Hum Exp Toxicol, 35*(2), 170-183.

Ranmadugala, D., *et al.* (2017). Impact of 3–Aminopropyltriethoxysilane-Coated Iron Oxide Nanoparticles on Menaquinone-7 Production Using B. subtilis. *Nanomaterials, 7*(11), 350.

Rao, S., *et al.* (2012). Human peripheral blood mononuclear cells exhibit heterogeneous CD52 expression levels and show differential sensitivity to alemtuzumab mediated cytolysis. *PloS One , 7*(6), e39416.

Raveche, E. (1990). Possible immunoregulatory role for CD5 + B cells. *Clin Immunol Immunopathol, 56*(2), 135-150.

Revia, R., & Zhang, M. (2016). Magnetite nanoparticles for cancer diagnosis, treatment, and treatment monitoring: recent advances. *Mater Today, 19*(3), 157-168.

Rieger, K., *et al.* (2004). Efficacy and Tolerability of Alemtuzumab (CAMPATH-1H) in the Salvage Treatment of B-Cell Chronic Lymphocytic Leukemia—Change of Regimen Needed? *Leuk Lymphoma , 45*(2), 345-349.

Riley, J., & Sliwkowski, M. (2000). CD20: a gene in search of a function. *Semin Oncol, 27*((Supple 6)), 17-24.

Rock, K., & Kono, H. (2011). The inflammatory response to cell death. *Annu Rec Pathol, 3*, 99-126.

Rodriguez, P., *et al.* (2013). Minimal "Self" Peptides That Inhibit Phagocytic Clearance and Enhance Delivery of Nanoparticles. *Science, 339*(6122), 971-975.

Romer, I., *et al.* (2011). Aggregation and dispersion of silver nanoparticles in exposure media for aquatic toxicity tests. *J Chromatogr A, 1218*(27), 4226-4233.

Rosen, S.D. (2004). Ligands for L-selectinhoming, inflammation, and beyond. *Ann Rev Immunol*, 22, 129-156.

Rosenblum, D., *et al.* (2018). Progress and challenges towards targeted delivery of cancer therapeutics. *Nat Commun, 9*(1), 1410.

Rossi, D., & Gaidan, G. (2016). The clinical implications of gene mutations in chronic lymphocytic leukaemia. *Br J Cancer, 114*(8), 849-854.

Rossi, D., *et al.* (2013). Integrated mutational and cytogenetic analysis identifies new prognostic subgroups in chronic lymphocytic leukemia. *Blood, 121*, 1403-1412.

Rossmann, E., *et al.* (2001). Variability in B-cell antigen expression: implications for the treatment of B-cell lymphomas and leukemias with monoclonal antibodies. *Hematol J, 2*(5), 300-306.

Rothen-Ruthishauser, B., *et al.* (2014). Quantification of gold nanoparticle cell uptake under controlled biological conditions and adequate resolution. *Nanomedicine, 9*(5), 607-621.

Rowan, W., *et al.* (1998). Cross-linking of the CAMPATH-1 antigen (CD52) mediates growth inhibition in human B- and T-lymphoma cell lines, and subsequent emergence of CD52-deficient cells. *Immunology, 95*, 427-436.

Ruck, T., *et al.* (2015). Alemtuzumab in Multiple Sclerosis: Mechanism of Action and Beyond. *Int J Mol Sci, 16*(7), 16414-16439.

Sabale, S., *et al.* (2017). Recent developments in the synthesis, properties, and biomedical applications of core/shell superparamagnetic iron oxide nanoparticles with gold. *Biomater Sci, 5*(11), 2212-2225.

Saeed, M., *et al.* (2018). Therapeutic Applications of Iron Oxide Based Nanoparticles in Cancer: Basic Concepts and Recent Advances. *Biomater Sci*. doi:10.1039/C7BM00999B

Safi, M., *et al.* (2011). The effects of aggregation and protein corona on the cellular internalization of iron oxide nanoparticles. *Biomaterials, 32*(35), 9353-9363.

Safra, T., *et al.* (2000). Pegylated liposomal doxorubicin (doxil): Reduced clinical cardiotoxicity in patients reaching or exceeding cumulative doses of 500 mg/m2 . *Annal Oncol, 11*(8), 1029-1033.

Salisbury, J., *et al.* (1980). Role of coated vesicles, microfilaments, and calmodulin in receptor-mediated endocytosis by cultured B lymphoblastoid cells. *J Cell Biol, 87*(1), 132.

Samir, A., *et al.* (2015). Nanotechnology applications in hematological malignancies (Review). *Oncol Rep, 34*(3), 1097-1105.

Sanna, V., *et al.* (2014). Targeted therapy using nanotechnology: focus on cancer. *Int J Nanomedicine, 9*, 467-483.

Sanvicens, N., & Pilar Marco, M. (2008). Multifunctional nanoparticles – properties and prospects for their use in human medicine. *Trends Biotechnol, 26*(8), 425-433.

Sarvaria, A., *et al.* (2017). B cell regulation in cancer and anti-tumor immunity. *Cell Mol Immunol, 14*, 662-674.

Sawas, A., *et al.* (2017). A phase 1/2 trial of ublituximab, a novel anti-CD20 monoclonal antibody, in patients with B-cell non-Hodgkin lymphoma or chronic lymphocytic leukaemia previously exposed to rituximab. *Br J Haematol, 117*(2), 243-253.

Scheuermann, R., & Racila, E. (1995). CD19 antigen in leukemia and lymphoma diagnosis and immunotherapy. *Leuk Lymphoma, 18*(5-6), 385-397.

Schroeder, H., & Cavacini, L. (2013). Structure and Function of Immunoglobulins. *J Allergy Clin Immunol, 125*(2(2)), S41-S52.

Schlighofer, C., & Indtner, C. (2010). First-line treatment of chronic lymphocytic leukemia: role of alemtuzumab. *Onco Targets Ther, 24*(3), 53-67.

Scielzo, C., *et al.* (2010). How the microenvironment shapes chronic lymphocytic leukemia: the cytoskeleton connection. *Leukaemia and Lymphoma, 51*(8), 1371-1374.

Seifert, M., *et al.* (2013). Origin and Pathogenesis of B Cell Lymphomas. *Methods in Molecular Biology, 971*, 1-25.

Selinummi, J., *et al.* (2009). Bright Field Microscopy as an Alternative to Whole Cell Fluorescence in Automated Analysis of Macrophage Images. *PLoS ONE, 4*(10), e7497.

Senapati, S., *et al.* (2018). Controlled drug delivery vehicles for cancer treatment and their performance. *Signal Transduct Target Ther, 16*(3), 10.1038/s41392-017-0004-3. doi:10.1038/s41392-017-0004-3

Shang, L., *et al.*. (2014). Engineered nanoparticles interacting with cells: size matters. . *J Nanobiotech, 12*(5). doi:10.1186/1477-3155-12-5.

Sharma, A., *et al.* (2008). Prevention of MDR Development in Leukemia Cells by Micelle-Forming Polymeric Surfactant. *J Control Release, 131*(3), 220-227.

Simon, J., & ESTRASORB Study Group. (2006). Estradiol in micellar nanoparticles: the efficacy and safety of a novel transdermal drug-delivery technology in the management of moderate to severe vasomotor symptoms. *Menopause, 13*(2), 222-231.

Singh, N., *et al.* (2010). Potential toxicity of superparamagnetic iron oxide nanoparticles (SPION). *Nano Reviews, 1*(1), 5358.

Sperling, R., & Parak, W. (2010). Surface modification, functionalization and bioconjugation of colloidal inorganic nanoparticles. *Phil Trans R Soc, 368*(1915), 1333-1383.

Steurer, *et al.* (2006). Single-agent purine analogues for the treatment of chronic lymphocytic leukaemia: a systematic review and meta-analysis. *Cancer Treat Rev, 32*(5), 377-389.

Stopforth, R., *et al.* (2016). Regulation of Monoclonal Antibody Immunotherapy by FcγRIIB. *J Clin Immunol, 36*, 88-94.

Strober, W. (2001). Trypan blue exclusion test of cell viability. *Curr Protoc Immunol, 3*, Appendix 3B.

Sun, J., *et al.* (2017). A Distinct Endocytic Mechanism of Functionalized-Silica Nanoparticles in Breast Cancer Stem Cells. *Sci Rep, 7*, 16236.

Sykes, E., *et al.* (2016). Tailoring nanoparticle designs to target cancer based on tumor pathophysiology. *PNAS, 113*(9), e1142-1151.

Taniguchi, N. (1974). On the Basic Concept of Nanotechnology. *Proceedings of the International Conference on Production Engineering*, 18-23.

Tedder, TF., *et al.* (1988). Heterogeneity in the B1 (CD20) cell surface molecule expressed by human B-lymphocytes. *Mol Immunol*, 25, 1321-1330.

ten Hacken, E., & Burger, J. (2016). Microenvironment interactions and B-cell receptor signaling in Chronic Lymphocytic Leukemia: Implications for disease pathogenesis and treatment. *Biochim. Biophys. Acta, 1863*(3), 401-413.

Thompson, P., & Wierda , W. (2016). Eliminating minimal residual disease as a therapeutic end oint: working toward cure for patients with CLL. *Blood, 127*, 279-286.

Thompson, R., et al. (2016). An introduction to sample preparation and imaging by cryo-electron microscopy for structural biology. *Methods, 100*, 3-15.

Tiselius, A., & Kabat, E. (1939). An electrophoretic study of immune sera and purified antibody preparations. *J Exp Med, 69*, 119-131.

Tiwari, G., *et al.* (2012). Drug delivery systems: An updated review. *Int J Pharm Investig, 2*(1), 2-11.

Tobinai, K., *et al.* (2017). A Review of Obinutuzumab (GA101), a Novel Type II Anti-CD20 Monoclonal Antibody, for the Treatment of Patients with B-Cell Malignancies. *Adv Ther, 34*(2), 324-356.

Tong, R., *et al.* (2013). Photoswitchable nanoparticles for in vivo cancer chemotherapy. *Proc Natl Acad Sci USA, 110*, 19048-19053.

Tong, R., *et al.* (2012). Photoswitchable nanoparticles for triggered tissue penetration and drug delivery. *J Am Chem Soc, 134*, 8848-8855.

Tran, S., *et al.* (2017). Cancer nanomedicine: a review of recent success in drug delivery. *Clin Transl Med, 6*(1). doi:10.1186/s40169-017-0175-0

Treerattrakoon, K., *et al.* (2017). Oriented conjugation of antibodies against the epithelial cell adhesion molecule on fluorescently doped silica nanoparticles for flow-cytometric determination and in vivo imaging of EpCAM, a biomarker for colorectal cancer. *Microchimica Acta, 184*(7), 1941-1950.

Treuel, L., *et al.* (2013). New views on cellular uptake and trafficking of manufactured nanoparticles. *J R Soc Interface, 10*(82), 20120939.

Tsao, T., *et al.* (2011). Origin, separation and identification of environmental nanoparticles: a review. *J Environ Monit, 13*(5), 1156-1163.

Turkevich, J., *et al.* (1954). The colour of colloidal gold. *Journal of Colloidal Science, 9*, 26-35.

Turner, M., *et al.* (2016). Characterization of a CD52 Knockout Mouse to Investigate the Function of CD52. *Neurology, 86*(16 Supplement), P5.323.

ud Din, F., *et al.* (2017). Effective use of nanocarriers as drug delivery systems for the treatment of selected tumors. *Int J Nanomedicine, 12*, 7291-7309.

Uthaman, S., *et al.* (2015). Polysaccharide-Coated Magnetic Nanoparticles for Imaging and Gene Therapy. *Biomed Res Int*, 959175.

Umemoto, E., *et al.* Nepmucin; a novel HEV sialomucin, mediates L-selectin-dependent lymphocyte rolling and promotes lymphocyte adhesion under flow. *J Exp Med*, 203, 1603-1614.

Valle, J., *et al.* (2011). A phase 2 study of SP1049C, doxorubicin in P-glycoprotein-targeting pluronics, in patients with advanced adenocarcinoma of the esophagus and gastroesophageal junction. *Invest new Drugs, 29*(5), 1029-1037.

Velasquez, M., & Gottschalk, S. (2016). Targeting CD19: the good, the bad, and CD81. *Blood, 129*, 9-10.

Vences-Catalan, F., *et al.* (2012). The CD19/CD81 complex physically interacts with CD38 but is not required to induce proliferation in mouse B lymphocytes. *Immunology*, 137(1), 48-55.

Ventola, CL. (2017). Progress in Nanomedicine: Approved and Investigational Nanodrugs. *PT* 42(12), 742-755.

Verma, A., & Stellacci, F. (2010). Effect of Surface Properties on Nanoparticle–Cell Interactions. *Small, 6*(1), 12-21.

Villa, C., *et al.* (2016). Red blood cells: Supercarriers for drugs, biologicals, and nanoparticles and inspiration for advanced delivery systems. *Adv Drug Deliv Rev, 106*(A), 88-103.

Vinhas, R., *et al.* (2017). Nanoparticles—Emerging Potential for Managing Leukemia and Lymphoma. *Front Bioeng Biotechnol, 5*, 79.

Vojdeman, F., *et al.* (2017). Soluble CD52 is an indicator of disease activity in chronic lymphocytic leukemia. *Leuk Lymphoma, 58*(10), 2356-2362.

Von Behring, E., & Kitasato, S. (1890). Ueber das Zustandekommen der Diphtherie-Immunitat und der Tetanus-Immunität bei Thieren. *Dtsch Med Wochenschr (in German), 16*, 1113-1114.

Voyvodic, P., *et al.* (2014). Loss of Syndecan-1 Induces a Pro-inflammatory Phenotype in Endothelial Cells with a Dysregulated Response to Atheroprotective Flow. *J Biol Chem, 289*, 9547-9559.

Wagner, V., *et al.* (2006). The emerging nanomedicine landscape. *Nat Biotech, 24*(10), 1211-1217.

Wang, J., *et al.* (2016). Nanoparticle drug delivery systems: an excellent carrier for tumor peptide vaccines. *Drug Delivery, 25*(1), 1319-1327.

Wang, K., *et al.* (2012). CD19: a biomarker for B cell development, lymphoma diagnosis and therapy. *Exp Hematol Oncol, 1*, 36.

Wang, W., *et al.* (2015). NK Cell-Mediated Antibody-Dependent Cellular Cytotoxicity in Cancer Immunotherapy. *Front Immunol, 6*, 368.

Warner, J., & Arnason, J. (2012). Alemtuzumab use in relapsed and refractory chronic lymphocytic leukemia: a history and discussion of future rational use. *Ther Adv Hematol, 3*(6), 375-389.

Watson, T. (1997). Fact and Artefact in Confocal Microscopy. *Adv Dent Res, 11*(4), 433-441.

White, C., & Frangos, J. (2007). The shear stress of it all: the cell membrane and mechanochemical transduction. *Philos Trans R Soc Lond B Biol Sci, 362*(1484), 1459-1467.

Wierda, W., *et al.* (2017). NCCN Guidelines Insights: Chronic Lymphocytic Leukemia/Small Lymphocytic Leukemia, Version 1.2017. *J Natl Compr Canc Netw, 15*(3), 293-311.

Woo, K., *et al.* (2008). Fluid flow induces mechanosensitive ATP release, calcium signalling and Cl− transport in biliary epithelial cells through a PKCζ-dependent pathway. *J Physiol, 586*(11), 2779-2798.

Wu, C. (2012). CLL clonal heterogeneity: an ecology of competing subpopulations. *Blood, 120*, 4117-4118.

Wu, W., *et al.* (2015). Recent progress on magnetic iron oxide nanoparticles: synthesis, surface functional strategies and biomedical applications. *Sci Technol Adv Mater, 16*, 023501.

Xu, S., *et al.* (2013). Targeting receptor-mediated endocytotic pathways with nanoparticles: rationale and advances. *Adv Drug Deliv Rev, 65*(1), 121-138.

Yang J., *et al.* (2007). Multifunctional magneto-polymeric nanohybrids for targeted detection and synergistic therapeutic effects on breast cancer. *Angew Chem Int Ed Engl,* 46(46):8836-9.

Yesilbas, M., & Boily, J. (2016). Particle Size Controls on Water Adsorption and Condensation Regimes at Mineral Surfaces. *Sci Rep, 6*, 32136.

Yong, K., *et al.* (2009). Multifunctional Nanoparticles as Biocompatible Targeted Probes for Human Cancer Diagnosis and Therapy. *J Mater Chem, 19*(27), 4655-4672.

Young, E., & Simmons, C. (2010). Macro- and microscale fluid flow systems for endothelial cell biology. *Lab Chip, 10*(2), 143-160.

Yu, B., *et al.* (2013). Targeted drug delivery and cross-linking induced apoptosis with anti-CD37 based dual-ligand immunoliposomes in B chronic lymphocytic leukemia cells. *Biomaterials, 34*(26), 6185-6193.

Zaimy, M., *et al.* (2017). New methods in the diagnosis of cancer and gene therapy of cancer based on nanoparticles. *Cancer Gene Ther, 24*(6), 233-243.

Zent, C., *et al.* (2004). Alemtuzumab (CAMPATH 1H) does not kill chronic lymphocytic leukemia cells in serum free medium. *Leuk Res, 28*, 495-507.

Zhang, L., *et al.* (2008). Nanoparticles in Medicine: Therapeutic Applications and Developments. *Clin Pharmacol Ther, 83*(5), 761-769.

Zhang, S., *et al.* (2009). Size-Dependent Endocytosis of Nanoparticles. *Adv Mater, 21*(4), 419-424.

Zhang, Y., *et al.* (2017). Quantitating morphological changes in biological samples during scanning electron microscopy sample preparation with correlative super-resolution microscopy. *PLoS One, 12*(5), e0176839.

Zhao, F., *et al.* (2011). Cellular Uptake, Intracellular Trafficking, and Cytotoxicity of Nanomaterials. *Small, 7*(10), 1322-1337.

Zhou, R., *et al.* (2017). Magnetic separation of microparticles by shape. *Lab on a Chip, 17*(3), 401-406.

Zhou, X., *et al.* (2008). The Role of Complement in the Mechanism of Action of Rituximab for B-Cell Lymphoma: Implications for Therapy. *The Oncologist, 13*(9), 954-966.

Zhu, Y., *et al.* (2011, June 24). Carbon-Based Supercapacitors Produced by Activation of Graphene. *Science, 332*(6037), 1537-1541. doi:10.1126/science.1200770.

8． Appendices

8.1 Dynamic light scattering of Fe_2O_3 nanoparticles

Size Quality Report
v2.0

Malvern Instruments Ltd – © Copyright 2008

Malvern

Sample Name:	GC4010_LK_I2
SOP Name:	GC Size Fe2O3 DMEM.sop
File Name:	GC4010.dts
Record Number:	68
Measurement Date and Time:	31 January 2016 19:17:35
Temperature (°C):	25.0

RESULT DOES NOT MEET QUALITY CRITERIA

Multimodal fit error high
* Data quality too poor for distribution analysis
* Sample too polydisperse for distribution analysis

Cumulant fit error high
* Data quality too poor for cumulant analysis
* Sample too polydisperse for cumulant analysis

In range figure is low (72%)
* Presence of large or sedimenting particles
* Sample fluorescence
* Sample absorbance (coloured samples)

Polydispersity Index is very high (.751)
* Sample is very polydisperse and may not be suitable for DLS measurements
* Sample contains large particles/aggregates/dust
* Wrong measurement position selected

Raw Correlation Data

Size Distribution by Intensity
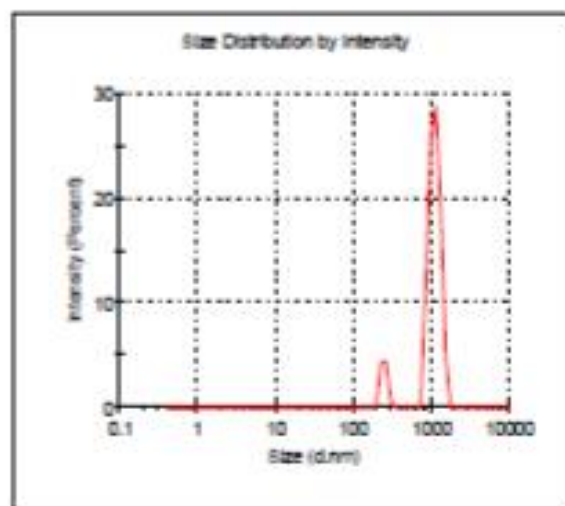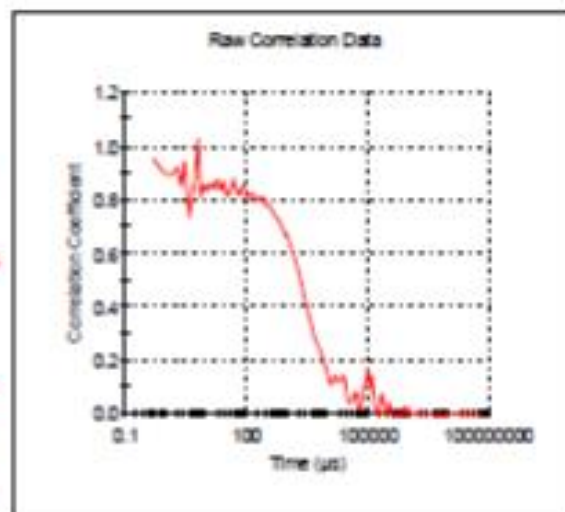
8.2 BET analysis of Sigma Fe₂O₃ nanoparticles

SIGMA-ALDRICH®

Product Specification

Product Name:
Iron(III) oxide – nanopowder, <50 nm particle size

Product Number:	**544884**	Fe_2O_3
CAS Number:	1309-37-1	
MDL:	MFCD00011008	
Formula:	Fe2O3	
Formula Weight:	159.69 g/mol	

TEST	Specification
Appearance (Color)	Conforms to Requirements
Red-Brown to Brown	
Appearance (Form)	Powder
X-Ray Diffraction	Conforms to Structure
Titration by Na2S2O3	68.2 - 71.7 %
% Fe	
Size	≤ 50 nm

Specification: PRD.0.ZQ5.10000017007

1 of 1

8.3 Monoclonal antibody elution from the surface of Fe₂O₃ nanoparticles following covalent linkage
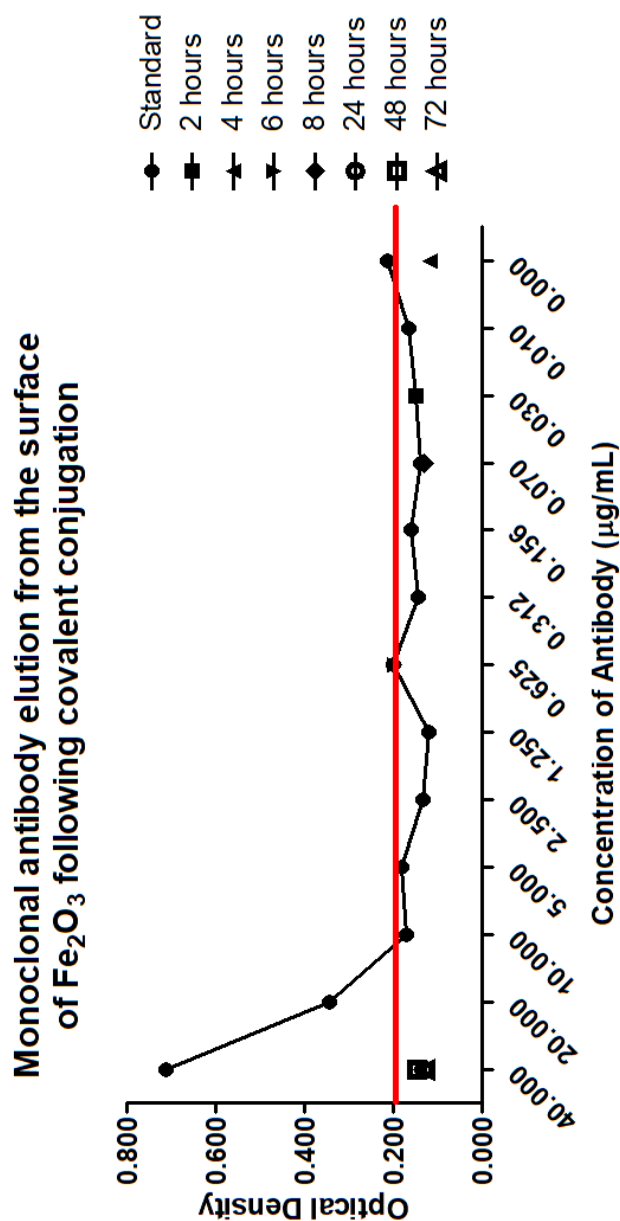
Figure 8.3: Antibody elution from the surface of Fe₂O₃ nanoparticles following covalent conjugation. Samples of Fe₂O₃@CD52 nanoparticles were incubated at 4°C for 72 hours. At each time point indicated, samples were collected, and nanoparticles removed from suspension using magnetic separation (as discussed in section 2.2). BCA (bicinchoninic acid assay) was then performed as per manufacturer's instructions for the detection of protein (monoclonal antibody) in collected supernatant. Across each time point measured levels of protein (antibody) in the supernatant were below the detectable threshold (OD 0.2, protein levels of ≤10ng are undetectable using this assay) indicating little to no elution of monoclonal antibody over the indicated time points (n=3).

8.4 The effects of a range of functionalised nanoparticles on the I-83 cell line
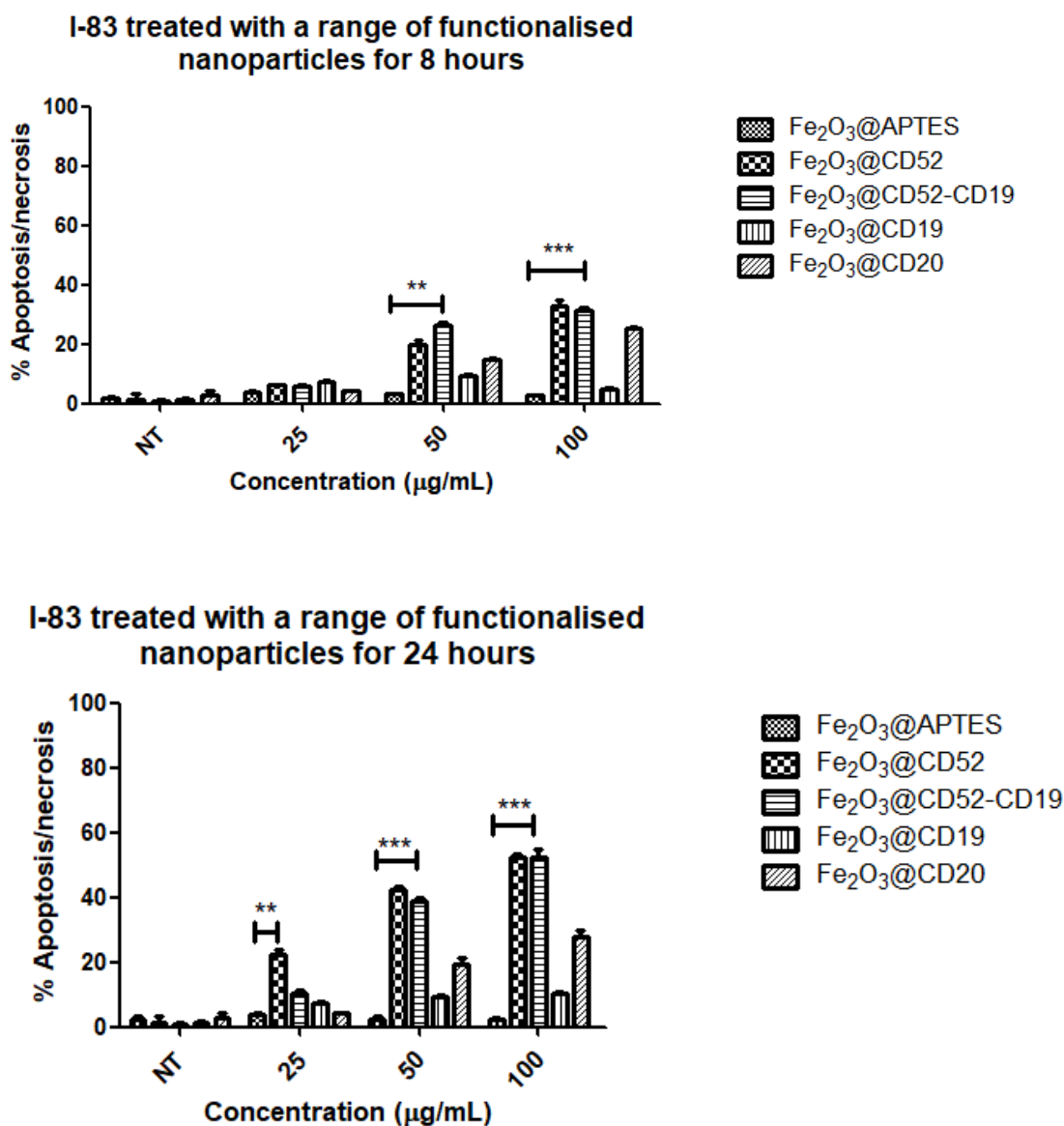
Figure 8.4: I-83 cells treated with a range of functionalised nanoparticles for 8 and 24 hours. 3×10^5 I-83 cells were treated with a range of functionalised nanoparticles over 8 and 24 hours at concentrations indicated above. Cell viability was assessed using Annexin V-PI. Graphs shows that both $Fe_2O_3@CD52$ and $Fe_2O_3@CD52$-CD19 had a significant effect on cell viability, when compared to $Fe_2O_3@APTES$ (n=3; $p<0.001$), but that there was no significant difference in the effect on cell viability between the two NPs. $Fe_2O_3@CD20$ induced significant cell death when compared to that of $Fe_2O_3@APTES$ (n=3; $p<0.001$), though to a lesser extent than that of $Fe_2O_3@CD52$. $Fe_2O_3@CD19$ had no significant effect on cell viability. One-way ANOVA with Tukey post-test was used for statistical analysis.

8.5 The effect of Fe_2O_3 nanoparticle treatment on the adherence of CLL cells to the endothelial monolayer

Treatment with Fe_2O_3 nanoparticles reduce the adherence of CLL cells to the HUVEC monolayer at 0.5 Dynes/cm^2
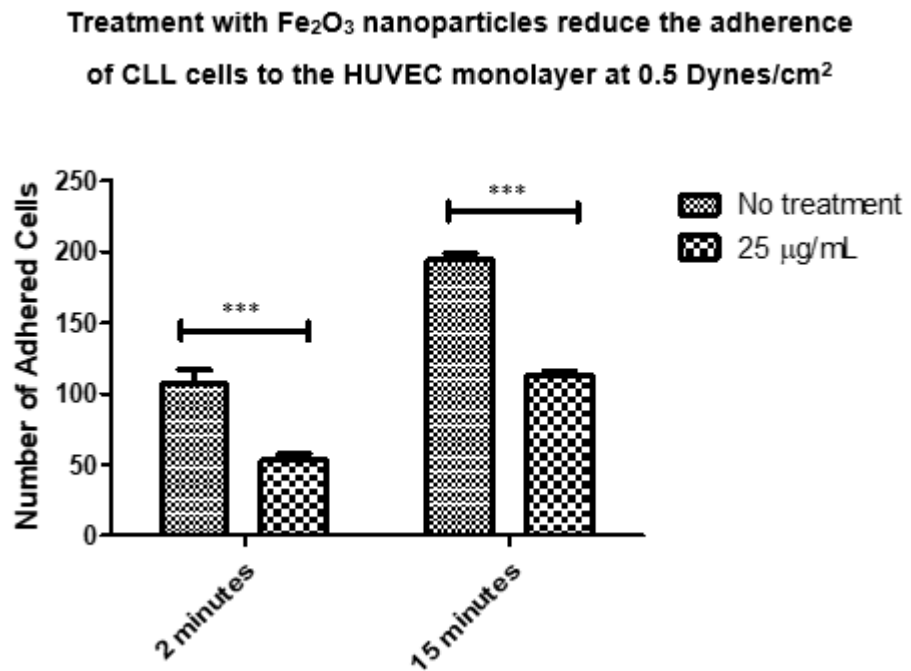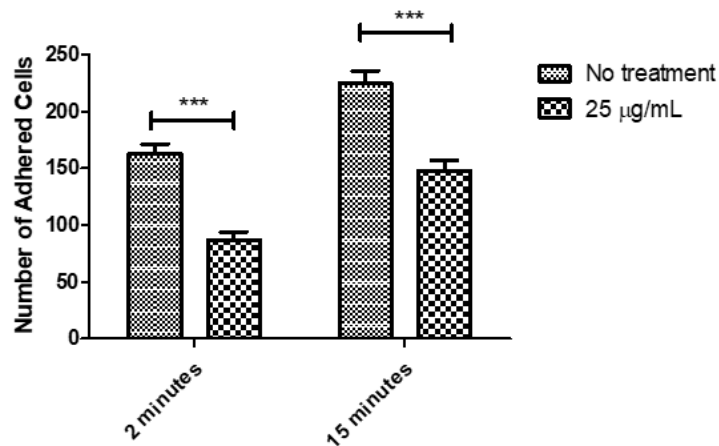
Figure 8.5.1: The effect of Fe_2O_3 nanoparticle treatment on CLL cell adherence to the endothelial monolayer at 0.5 Dynes/cm^2. Treatment with nanoparticles at both time points has a significant effect on cellular adherence ($p<0.001$), with adherence decreasing by 50.4% at 2 minutes and 42.1% at 15 minutes (n=6; one-way repeated measures ANOVA, Dunnet's post-test).

Treatment with Fe₂O₃ nanoparticles reduce the adherence of CLL cells to the HUVEC monolayer at 0.25 Dynes/cm²
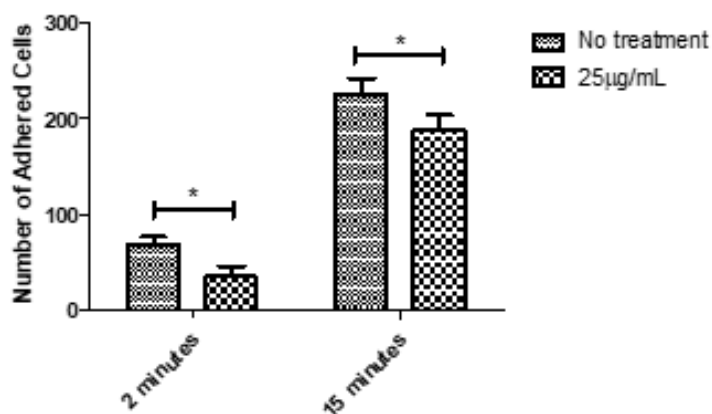

Figure 8.5.2: **The effect of Fe₂O₃ nanoparticle treatment on CLL cell adherence to the endothelial monolayer at 0.25 Dynes/cm².** Treatment with nanoparticles at both time points has a significant effect on cellular adherence ($p<0.001$), with adherence decreasing by 46.5% at 2 minutes and 34% at 15 minutes (n=6, one-way repeated measures ANOVA, Dunnet's post-test).

Treatment with Fe₂O₃ nanoparticles reduce the adherence of CLL cells to the HDLEC monolayer at 0.08 Dynes/cm²

Figure 8.5.3: **The effect of Fe₂O₃ nanoparticle treatment on CLL cell adherence to the endothelial monolayer at 0.08 Dynes/cm².** Treatment with nanoparticles at both time points has a significant effect on cellular adherence ($p<0.05$), with adherence decreasing by 49.8% after 2 minutes and by 16.9% after 15 minutes (n=3; one-way repeated measures ANOVA, Dunnet's post-test).

8.6 The effects of shear flow rate on the viability of the I-83 cell line following treatment with 25µg/mL Fe_2O_3 nanoparticles for 30 minutes.

The effect of shear flow rate on the viability of the I-83 cell line after 30 minutes.
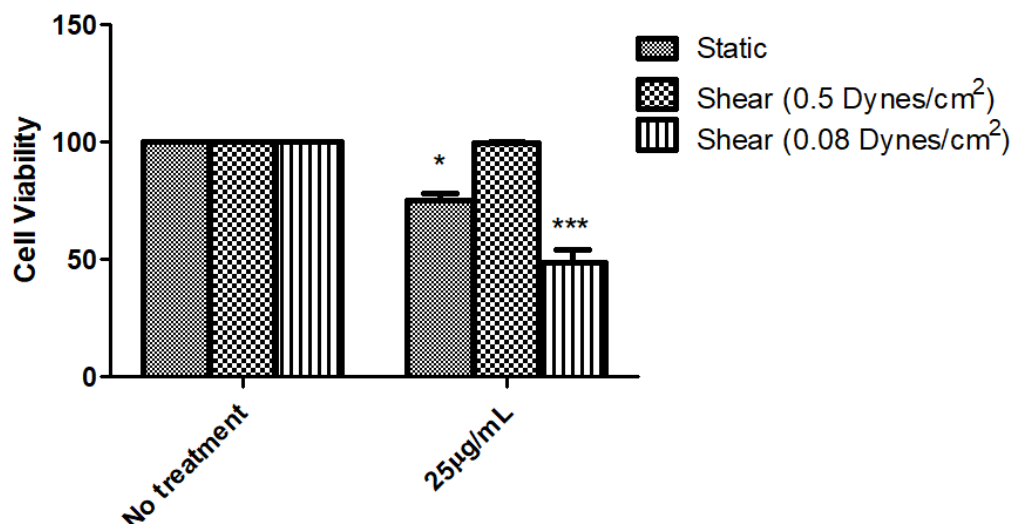
Figure 8.6: The effects of shear flow rates on cell viability following treatment with Fe_2O_3 nanoparticles, as assessed using Trypan Blue staining. Following treatment with 25µg/mL Fe_2O_3 nanoparticles and 30 minutes of flow through the microfluidics platform, cells were collected, and viability was assessed using Trypan Blue exclusion staining. As expected, a significant effect on cell viability was noted following static incubation ($p<0.05$; n=3). There was no significant effect on cell viability following shear flow of 0.5 Dynes/cm^2, but a significant effect on cell viability was noted following shear flow rate of 0.08 Dynes/cm^2 ($p<0.001$; n=3; one-way ANOVA with Tukeys post-test).

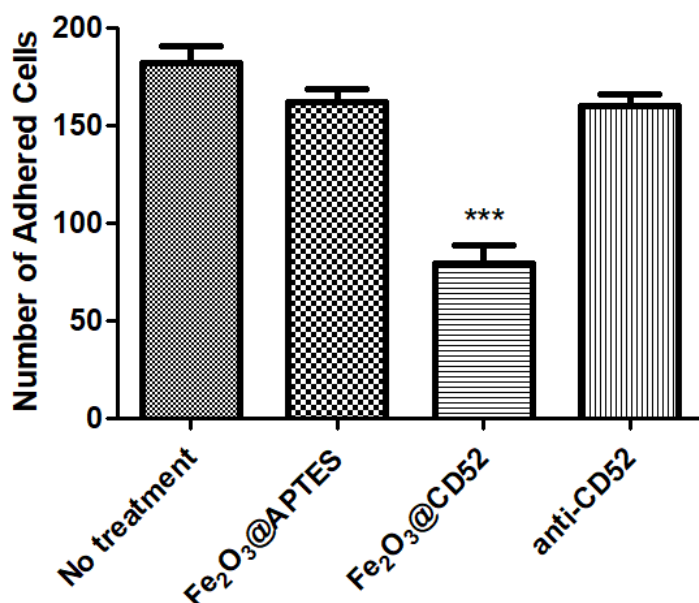## 8.7. The effect of Fe$_2$O$_3$@CD52 on CLL cell adhesion to the HDLEC monolayer under a shear flow rate of 0.08 Dynes/cm^2.

Figure 8.7: **Treatment with 25µg/mL Fe$_2$O$_3$@CD52 30 minutes prior results in significantly less adhesion of patient-derived CLL cells to HDLEC cells at a fluid shear flow rate of 0.08 Dynes/cm^2.** Patient-derived CLL cell (1x10^6) were treated with 25µg/mL Fe$_2$O$_3$@APTES, Fe$_2$O$_3$@CD52, and 10µg/mL of anti-CD52 for 30 minutes and adherence to HDLEC cells after 15 minutes under 0.08 Dynes/cm^2 shear flow was assessed (n=3). Treatment with Fe$_2$O$_3$@CD52 nanoparticles had a significant effect on cellular adherence, when compared to Fe$_2$O$_3$@APTES nanoparticles (p<0.001; ANOVA with Tukeys post-test). Treatment with Fe$_2$O$_3$@APTES or 10µg/mL of anti-CD52 monoclonal antibody had no significant effect on adherence, when compared to that of no treatment. Data are illustrative of CLL patient samples CLL7, CLL15 and CLL16.

8.8. The effect of treatment with the novel, early-stage, proof-of-concept nanoparticle functionalised with anti-CD52 monoclonal antibody and the purine analogue fludarabine on the induction of apoptosis/necrosis in CLL cells

The effect of treatment with a Fe_2O_3@CD52-Fludarabine on the induction of apoptosis/necrosis in patient-derived CLL cells, at 8 hours
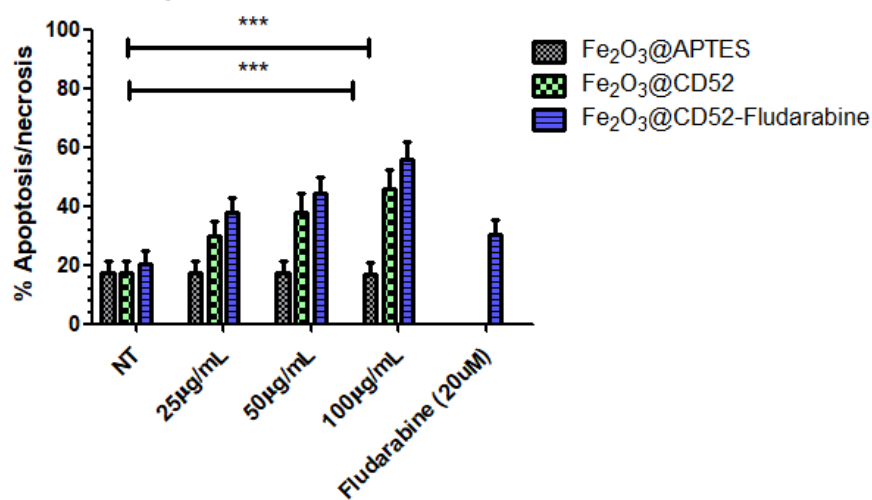
Figure 8.8.1: The addition of fludarabine to the surface of Fe_2O_3@CD52 nanoparticles does not significantly increase the induction of apoptosis/necrosis in patient-derived CLL cells. 3×10^7 patient-derived CLL cells were treated with Fe_2O_3@APTES, Fe_2O_3@CD52 Fe_2O_3@CD52-Fludarabine or unbound fludarabine at the indicated concentration for 8 hours. Cells were recovered, and cell viability assessed using Annexin-V PI. These data show that Fe_2O_3@CD52 increases the levels of apoptosis significantly, when compared to the no treatment, and Fe_2O_3@APTES. There was no observed significant effect of unbound fludarabine when compared to the no treatment over this time period. There was no significant increase in the levels of apoptosis/necrosis in cells treated with Fe_2O_3@CD52-Fludarabine compared to those treated with Fe_2O_3@CD52 (n=15; $p<0.0001$ functionalised nanoparticles versus Fe_2O_3@APTES; one-way ANOVA with Tukeys post-test).
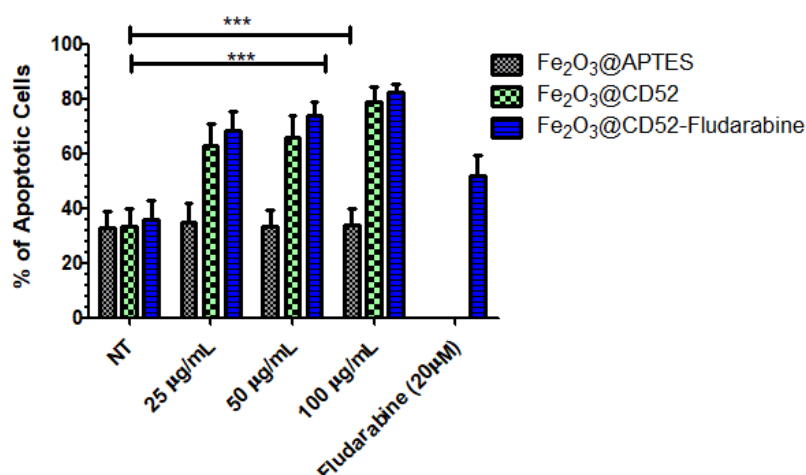
Figure 8.8.2: The addition of fludarabine to the surface of Fe$_2$O$_3$@CD52 nanoparticles does not significantly increase the induction of apoptosis/necrosis in patient-derived CLL cells. 3×10^7 patient-derived CLL cells were treated with Fe$_2$O$_3$@APTES, Fe$_2$O$_3$@CD52 Fe$_2$O$_3$@CD52-Fludarabine or unbound fludarabine at the indicated concentration for 24 hours. Cells were recovered, and cell viability assessed using Annexin-V PI. These data show that Fe$_2$O$_3$@CD52 increases the levels of apoptosis significantly, when compared to the no treatment, and Fe$_2$O$_3$@APTES. There was no observed significant effect of unbound fludarabine when compared to the no treatment over this time period. There was no significant increase in the levels of apoptosis/necrosis in cells treated with Fe$_2$O$_3$@CD52-Fludarabine compared to those treated with Fe$_2$O$_3$@CD52 (n=15; $p<0.0001$ functionalised nanoparticles versus Fe$_2$O$_3$@APTES; one-way ANOVA with Bartlett's post-test).